ABSTRACT

Title of Dissertation: THE FORMATION OF METAL-FREE POPULATION III STARS IN X-RAY AND LYMAN-WERNER RADIATION BACKGROUNDS

Jongwon Park
Doctor of Philosophy, 2024

Dissertation Directed by: Professor Massimo Ricotti
Department of Astronomy

Metal-free Population III (or Pop III) stars are instrumental in shaping the early universe, influencing the formation of the first galaxies. The formation of Pop III stars depends on the fraction of molecular hydrogen (H_2), which is regulated by X-ray and Lyman-Werner (LW) radiation backgrounds. Therefore, gaining insight into the impact of these radiation backgrounds is essential for unraveling the mysteries surrounding Pop III star formation and their impacts on the first galaxies. In this dissertation, I investigate the interaction between X-ray/LW backgrounds and the formation of Pop III stars.

To conduct this investigation, I employed the radiative hydrodynamics code RAMSES-RT. I implemented various physical processes governing Pop III star formation, such as primordial chemistry, radiation background, secondary ionization/heating, and self-shielding. Performing a grid of simulations covering a large parameter space of X-ray/LW intensity, I systematically explored the effects of radiation backgrounds on Pop III stars. I found that a moderate X-ray

background boosts the H_2 fraction in dark matter halos, facilitating Pop III star formation in low-mass halos. In contrast, a LW background dissociates H_2 and prevents star formation in low-mass halos. This result suggests that the number of Pop III supernovae detected by the JWST is enhanced by an X-ray background. Furthermore, I discovered that an X-ray background reduces the characteristic mass and multiplicity of Pop III stars. This leads to a top-heavier initial mass function and may have a potential impact on galaxy formation.

Moreover, I made further improvements to the simulations by incorporating radiative feedback from Pop III protostars. This study confirmed previous works that radiation from protostars suppresses their growth, thereby playing a significant role in determining the mass of Pop III stars theoretically. I also found that hierarchical binaries (binaries of binaries), eccentric orbits, and outward migration are common occurrences in Pop III star formation. Eccentric orbits induce variability of Pop III protostars and this is observable by the JWST when light is magnified through gravitational lensing. In a follow-up study, I investigated the origin of outward migration and found that the gas disks around the protostars accrete gas with high angular momentum and transfer the angular momentum to the binary stars through torques. This finding paves the way for studies of migration behaviors across different stellar populations.

Finally, I explored the X-ray effects on the number of Pop III stars using cosmological simulations. Developing methods to calculate the intensity of the radiation background on the fly and realistically accounting for the X-ray feedback loop, I found that a weak X-ray background develops and this background ionizes the intergalactic medium, thereby moderately increasing the number density of Pop III stars (by a factor of ~ 2). This rise in the number of Pop III stars due to X-ray radiation lowers the star formation rate of metal-enriched Pop II stars, highlighting the significance of the X-ray background in galaxy formation.

This thesis covers various aspects of Pop III star formation and the effect of X-ray radiation backgrounds which has been overlooked by previous studies. It lays a foundation for future research aimed at connecting the theoretical understanding of Pop III star formation and observations targeting Pop III stars and the first galaxies.

THE FORMATION OF METAL-FREE POPULATION III STARS IN X-RAY AND LYMAN-WERNER RADIATION BACKGROUNDS

by

Jongwon Park

Dissertation submitted to the Faculty of the Graduate School of the
University of Maryland, College Park in partial fulfillment
of the requirements for the degree of
Doctor of Philosophy
2024

Advisory Committee:
Professor Massimo Ricotti, Chair/Advisor
Professor Alberto Bolatto
Professor Benedikt Diemer
Professor Carter Hall, Dean's Representative
Dr. Massimo Stiavelli, External Examiner

Preface

This thesis comprises five papers in a series of X-ray effects on Pop III star formation. Chapters 2 through 5 contain the published papers, while Chapter 6 presents the preliminary results intended for publication. The published works are as follows.

- Park, J., Ricotti, M., & Sugimura, K., 2021, *Population III star formation in an X-ray background: I. Critical halo mass of formation and total mass in stars*, MNRAS, 508, 6176

- Park, J., Ricotti, M., & Sugimura, K., 2021, *Population III star formation in an X-ray background: II. Protostellar discs, multiplicity and mass function of the stars*, MNRAS, 508, 6193

- Park, J., Ricotti, M., & Sugimura, K., 2023, *Population III star formation in an X-ray background: III. Periodic radiative feedback and luminosity induced by elliptical orbits*, MNRAS, 521, 5334

- Park, J., Ricotti, M., & Sugimura, K., 2024, *The origin of outward migration of Population III star*, MNRAS, 528, 6895

Chapter 1 of this thesis is an introduction to metal-free Pop III stars and relevant physics, including molecular hydrogen and radiation background. Chapter 2 presents the findings of Park et al. (2021a) concerning the mass of minihalos for star formation and the total mass of Pop III

stars affected by X-ray and Lyman-Werner radiation background. Chapter 3 discusses the results of Park et al. (2021b) regarding the X-ray effect on disk fragmentation and the multiplicity of Pop III stars. Chapter 4 is derived from Park et al. (2023), focusing on the radiative feedback effect and periodic modulation of the luminosity of Pop III protostar binaries. Chapter 5 is a published work on the origin of outward migration (Park et al., 2024). Chapter 6 is based on ongoing work, focusing on the X-ray effect and Pop III star formation in cosmological simulations, with expected substantial changes upon submission to peer-reviewed journals. Finally, in Chapter 7, the results are summarized, and future works are introduced.

Dedication

To my parents.

Acknowledgments

I am deeply indebted to Professor Massimo Ricotti for his guidance and support throughout my research journey. His mentorship has been invaluable, and I am grateful beyond words for his contributions to this thesis.

I extend my appreciation to Alberto Bolatto and Benedikt Diemer for their insightful feedback and guidance as members of my thesis committee. Their advice has greatly enriched my work. I also thank Carter Hall and Massimo Stiavelli for serving as committee members and spending their time on my thesis. My special thanks go to my collaborator Kazuyuki Sugimura for introducing this field of research to me. I also thank KwangHo Park for facilitating my connection with Massimo Ricotti and the University of Maryland. Without him, I would not have had the opportunity to work with such esteemed colleagues. I thank ChongChong He for sharing his insight from time to time. I would like to express my gratitude to my former colleague Rory Smith. Additionally, I thank my former advisor Sukyoung Yi, especially for helping me look for positions in South Korea, and Taysun Kimm for offering me a position.

I am thankful to all the faculty and staff members in the department. Their roles helped me directly and indirectly focus on my research. Special thanks to department chair Andy Harris for leadership and valuable advice on issues outside my research. I also extend my appreciation to Olivia Dent, Barbara Hansborough, and Lauren Miles for their assistance with administrative matters. I am grateful to Cole Miller and Stuart Vogel for their collaboration on ASTR 120/121,

which broadened my perspective on astronomy beyond the realm of Population III stars. I also thank Douglas Hamilton for sharing fascinating stories about planets, and Richard Mushotzky, Chris Hunt, Melissa Hayes-Gehrke, Derek Richardson, and all others members in the department for their kindness.

마지막으로 이 곳 까지 올 수 있도록 지지해주고 기다려 준 가족들과 친적분들께 감사의 말씀을 드립니다. 저의 성공을 기원하고 기다려주는 엄마와 동생, 하늘나라에서 지켜보고 있을 아빠, 응원해주시고 지원해주시는 이모들, 제가 하는 일에 관심 가져주고 친절하게 대해주는 친구, 지인들 모두 감사하고 사랑합니다.

Table of Contents

Preface ii

Dedication iv

Acknowledgements v

Table of Contents vii

List of Tables xi

List of Figures xii

List of Abbreviations xv

Chapter 1: Introduction 1
- 1.1 Population III Stars . . . 1
- 1.2 Molecular Hydrogen . . . 4
  - 1.2.1 Cooling . . . 4
  - 1.2.2 Difference from Metal Cooling . . . 6
  - 1.2.3 Formation of Molecular Hydrogen . . . 7
  - 1.2.4 HD . . . 9
- 1.3 Radiation Background . . . 10
- 1.4 Properties of Population III Stars . . . 14
  - 1.4.1 Critical Mass of Halo . . . 14
  - 1.4.2 Mass . . . 15
  - 1.4.3 Multiplicity . . . 18
- 1.5 Thesis Outline . . . 18
- 1.6 A summary of software and facilities . . . 19

Chapter 2: Population III Star Formation in an X-ray Background - I. Critical Halo Mass of Formation and Total Mass In Stars 20
- 2.1 Introduction . . . 21
- 2.2 Simulation . . . 24
  - 2.2.1 Chemistry . . . 26
  - 2.2.2 Radiation Background and Secondary Photo-electrons from X-ray Ionization . . . 30
  - 2.2.3 Tracking Clumps . . . 34

2.3 Results - I. Critical Minihalo Mass for Pop III Formation . . . 35
2.4 Results: II. Total Mass in Pop III Stars . . . 44
2.5 Summary and Discussion . . . 54

Chapter 3: Population III Star Formation in an X-ray Background - II. Protostellar Discs, Multiplicity, and Mass Function of the Stars 59
3.1 Introduction . . . 60
3.2 Simulation . . . 63
3.3 Results: I. Properties of Protostellar Discs . . . 68
3.4 Multiplicity and Migration of Population III stars . . . 79
3.5 Discussion . . . 87

Chapter 4: Population III Star Formation in an X-ray Background - III. Periodic Radiative Feedback and Luminosity Induced by Elliptical Orbits 93
4.1 Introduction . . . 94
4.2 Simulation . . . 98
4.2.1 Grid of Cosmological Initial Conditions and Zoom-in Simulations . . . 98
4.2.2 Primordial H_2 and HD Chemistry and Cooling . . . 103
4.2.3 Self-shielding of Background Radiation . . . 103
4.2.4 Sink Formation and Accretion . . . 105
4.2.5 Photon Injection . . . 107
4.2.6 Radiative Transfer . . . 109
4.3 Result . . . 111
4.3.1 Formation of Protostars in Primordial Discs . . . 111
4.3.2 Roles of FUV and EUV Radiation Feedback . . . 115
4.3.3 Modulation of the Accretion Rate and Feedback due to Eccentricity of the Orbits . . . 117
4.3.4 Pop III Masses and Multiplicity in Different X-ray Backgrounds . . . 121
4.3.5 Results for a Smaller Mass Halo . . . 124
4.4 Effect of HD Cooling . . . 127
4.5 Discussion . . . 129
4.6 Summary . . . 138

Chapter 5: On the Origin of Outward Migration of Population III Stars 142
5.1 Introduction . . . 143
5.2 Method . . . 147
5.2.1 Simulations . . . 147
5.2.2 Torque . . . 151
5.2.3 Orbital Energy . . . 155
5.3 Origin of Outward Migration . . . 156
5.3.1 Typical Formation Scenario . . . 156
5.3.2 Source of Angular Momentum of Sinks . . . 159
5.3.3 Source of Angular Momentum of Disc . . . 166
5.3.4 Efficiency of Angular Momentum Accretion . . . 171
5.3.5 Origin of Eccentric Orbits . . . 176

5.4 Cases without Outward Migration . . . 178
5.5 Discussion . . . 186
5.6 Summary . . . 189

Chapter 6: Population III Star Formation in an X-ray Background: IV. On-the-fly Calculation of an X-ray Radiation Background and the X-ray Effects on the Critical Mass for Star Formation 193
6.1 Introduction . . . 194
6.2 Simulation . . . 197
6.2.1 Pop III Star Formation . . . 200
6.2.2 Pop II Star Formation . . . 203
6.2.3 Effect of Background Radiation . . . 203
6.2.4 On-the-fly Calculation of Radiative Background . . . 206
6.3 Results . . . 212
6.3.1 X-ray Background, Heating, and Ionization . . . 212
6.3.2 Pop III Star Density and Critical Mass . . . 217
6.3.3 X-ray Effects on the Formation of the Second-generation Stars . . . 223
6.4 Discussion . . . 225
6.4.1 Future Work . . . 227

Chapter 7: Conclusion 228
7.1 Summary . . . 228
7.1.1 Critical Mass of Halos for Star Formation . . . 228
7.1.2 Mass of Pop III Stars . . . 229
7.1.3 Disk Fragmentation and Multiplicity . . . 229
7.1.4 Initial Mass Function . . . 230
7.1.5 Radiative Feedback from Protostars . . . 230
7.1.6 Migration . . . 231
7.1.7 X-ray Effects in a Cosmological Context . . . 233
7.2 Future Work . . . 234
7.2.1 Structure of Bipolar H II Region around Pop III Stars at AU Scales . . . 235
7.2.2 Formation of Extremely Metal-poor Stars . . . 237
7.2.3 Effect of X-rays on the Transition from Pop III to Pop II Star Formation . . . 238
7.3 Concluding Remarks . . . 238

Appendix A: Appendices for Chapter 2 241
A.1 Validation of Primordial Chemistry and Cooling in RAMSES . . . 241
A.2 Number of Pop III Stars . . . 243

Appendix B: Appendices for Chapter 3 244
B.1 Effect of X-ray Shielding . . . 244

Appendix C: Appendices for Chapter 4 250
C.1 Radiative Transfer Recipes . . . 250
C.1.1 Importance of X-ray Self-Shielding . . . 250

C.1.2 Protostar Formation Recipes . . . 251
C.1.3 Sink Formation Threshold and Radius . . . 253
C.1.4 Ionizing and LW Photon Emission from Sink Particles . . . 255
C.1.5 Resolution Study . . . 257
C.1.6 Reduced Speed of Light Approximation . . . 259
C.2 Relative Importance of EUV vs FUV Feedback . . . 260
C.3 Sink Merger . . . 260

Appendix D: Appendices for Chapter 5 262
D.1 Sink Particle Recipes . . . 262
D.1.1 Sink Radius . . . 262
D.1.2 Softening Length . . . 263
D.1.3 Accretion of Angular Momentum . . . 265
D.2 Non Quasi-steady State Accretion . . . 269
D.3 Reference Frame . . . 269

Bibliography 272

List of Tables

2.1 Summary of the simulations 25

3.1 Summary of the simulations 65
3.2 Parameters of Mass Functions 87

4.1 Summary of simulations. 100
4.2 Energy bins. 108
4.3 Parameters of equation (4.10). 133

5.1 Summary of simulations 148
5.2 Parameters of the logarithmic polar grid 164

6.1 Parameters of the cosmological simulations 199
6.2 Energy bins. 202

List of Figures

1.1 Effect of metal cooling . . . 8
1.2 Ionization cross-sections and mean-free paths . . . 11
1.3 Profiles of primordial gas in a DM halo . . . 17

2.1 Snapshots of the gas density in Halo 1, Halo 2, and Halo 3 for the case without radiation backgrounds . . . 26
2.2 Halo mass as a function of redshift . . . 27
2.3 Spectra of LW and X-ray radiation background . . . 32
2.4 Halo 2 in a LW-only simulation and one including X-ray effects . . . 35
2.5 Redshift of collapse (z_α) to a density 10^α for Halo 1 as a function of $\mathrm{J_{LW,21}}$ and $\mathrm{J_{X0,21}}$ . . . 37
2.6 Redshift of collapse z_α to density 10^α for Halo 2 and Halo 3 . . . 39
2.7 Schematic diagrams of Fig. 2.5 and 2.6 . . . 42
2.8 Properties of the gas in Halo 1 within 100 pc at the time when the central density reaches 10^7 H cm^{-3} . . . 46
2.9 Minimum gas temperature $T_{\rm min}$ and $M_{\rm final}$ as a function of X-ray intensity $\mathrm{J_{X0,21}}$ . . . 48
2.10 The accretion rate on the protostellar core and final mass in Pop III stars as a function of $T_{\rm min}$ . . . 50
2.11 Evolution of the total mass of clumps (the protostar) since the formation of the first one in three haloes . . . 52
2.12 The dimensionless ratio η of two accretion rates in equation (2.21) . . . 53

3.1 Halo mass as a function of redshift . . . 64
3.2 Surface density and Toomre Q parameter of the face-on circumstellar disc . . . 69
3.3 Fragmentation time as a function of the minimum gas temperature $T_{\rm min}$ . . . 70
3.4 Disc of Halo 2 in the absence of a radiation background . . . 71
3.5 Same as Fig. 3.4 but for a disc irradiated by an X-ray background with intensity $\mathrm{J_{X0,21}} = 10^{-2}$ and $\mathrm{J_{LW,21}} = 0$ . . . 72
3.6 The radius, thickness, mass and average Toomre Q parameter of discs as a function of time . . . 77
3.7 Masses and distances from the centre (bottom panels) of individual clumps . . . 80
3.8 Maximum distance of a clump as a function of the gas accretion rate at $n_{\rm H} = 10^7$ H cm^{-3} and $\mathrm{d}M/\mathrm{d}t|_{\rm cr}$ . . . 81

3.9 Histogram of the distances of Pop III stars from the centre-of-mass in a weak and strong X-ray background . . . 82
3.10 Panel (a): Total number of clumps when the total mass exceeds $M_{\rm final}$, including clumps that merged with others . . . 84
3.11 Mean mass function per halo and distribution of the multiplicity of stars in each halo . . . 86
3.12 The mass functions of compact remnants (NS and BHs) in the two samples . . . 92

4.1 Redshift of collapse to a hydrogen number density $n_{\rm H} = 10^7$ H cm^{-3} as a function of LW and X-ray background intensities . . . 99
4.2 Hydrogen number density (top) and temperature (bottom) slices of the initial conditions for the simulations in Table 4.1 . . . 102
4.3 Rendered image of a nearly equal mass binary Pop III protostar and disc . . . 112
4.4 Snapshots of Run F at different times . . . 113
4.5 Radiative feedback creating outflow . . . 116
4.6 Mass, accretion rate, and distance from CoMin Run A . . . 118
4.7 Left: Same as Fig. 4.6 but for $\rm J_{X0,21} = 10^{-4}$ (Run C) . . . 122
4.8 Left: Same as Fig. 4.6 but for Halo3 with $\rm J_{X0,21} = 0$ and $\rm J_{X0,21} = 10^{-5}$ . . . 125
4.9 Accretion rate and separation of selected binaries . . . 126
4.10 Top left: Phase diagram of Run E (solid line) and Run E˙noHD (dashed line) . . . 128
4.11 Total mass of protostars . . . 130
4.12 The final mass and star formation timescale as a function of accretion rate . . . 131
4.13 The IMFs in weak and strong X-ray background . . . 133
4.14 Apparent magnitudes of protostars in two JWST NIRCam bands: F140M and F322W2 . . . 136
4.15 Separation and eccentricity of S01-S02 binary in Run A . . . 139

5.1 Hierarchical binary . . . 157
5.2 Trajectories of stars . . . 158
5.3 Evolution of Fiducial-Outward binary . . . 160
5.4 Evolution of Fiducial-Outward binary . . . 162
5.5 Distribution of gravitational torque on the binary . . . 165
5.6 Folded torque map and its radial profile . . . 167
5.7 Angular momentum of the minidiscs as a function of time . . . 169
5.8 Properties of the Fiducial-Outward binary as a function of time . . . 170
5.9 Specific angular momentum of the Fiducial-Outward binary . . . 172
5.10 Specific angular momentum of the Fiducial-Outward binary right after its formation 175
5.11 Toomre-Q parameter of Fiducial-Outward . . . 176
5.12 Time evolution of the orbital eccentricities . . . 177
5.13 Same as Fig. 5.3 but for the Fiducial-Inward binary . . . 179
5.14 Evolution of Fiducial-Inward binary . . . 180
5.15 Gas density maps and density profiles of Fiducial-Inward . . . 181
5.16 Same as Fig. 5.8 but for the Fiducial-Inward binary case . . . 184
5.17 Presence of the secondary circumstellar disc . . . 185

6.1 Dark matter density map . . . 198
6.2 Snapshot of zoom-in simulation R2X at $z = 9$ . . . 201
6.3 Time-dependent spectrum of a Pop II star particle . . . 204
6.4 Schematic diagram of the on-the-fly background calculation . . . 208
6.5 Spectrum of a single Pop III star . . . 210
6.6 The intensity of the radiation background . . . 211
6.7 Snapshots of a cosmological zoom-in simulation at $z = 9$ . . . 213
6.8 Snapshots of Region 2 at $z = 9$ (2) . . . 214
6.9 Volume-weighted mean temperature, electron fraction, and H_2 fraction . . . 215
6.10 The number of Pop III stars in X-ray and non-X-ray simulations . . . 219
6.11 Mass functions at $z = 9$ . . . 220
6.12 Schematic diagram illustrating the definition of the critical . . . 221
6.13 Mass functions of halos hosting Pop III stars and the critical mass at different redshifts. . . . 222
6.14 Star formation rate density of Pop III and Pop II stars . . . 224
6.15 Volume filling factors of ionized gas and metal-enriched gas . . . 225

7.1 Protostellar feedback effect in an eccentric binary . . . 232
7.2 Schematic diagrams of radiative feedback prescriptions in the literature . . . 236

A.1 Phase diagram for a one-zone calculation . . . 242
A.2 Same calculations as in Figure A.1 but showing the H_2 and electron fraction . . . 242

B.1 Phase diagrams of test simulations . . . 246
B.2 Same as Figure B.1 but showing the H_2 fraction as a function of the hydrogen number density . . . 248
B.3 Same as Figure B.1, but showing the electron fraction as a function of hydrogen number density . . . 249

C.1 Effect of X-ray self-shielding on the total mass . . . 251
C.2 Change with the improvement of the simulation . . . 252
C.3 Dependence of results on the assumed sink radii . . . 254
C.4 Test with different photon injection criteria and sub-sink recipes . . . 256
C.5 Resolution study . . . 258
C.6 Total mass in sinks in Run F affected by EUV (red), FUV (blue) and both (black solid) . . . 260
C.7 Masses and separations in Run E with different assumptions on mergers . . . 261

D.1 Separation and total mass with different sink radii . . . 263
D.2 Separation with different sink softening lengths . . . 265
D.3 Numerical tests with different accretion schemes . . . 266
D.4 $\mathrm{d}\ln a_\mathrm{b}/\mathrm{d}\ln M_\mathrm{b}$ of Fiducial-Outward (top) and Fiducial-Inward (bottom) . . . 270

List of Abbreviations

AMR	Adaptive Mesh Refinement
AU	Astronomical Unit
BBH	Binary Black Hole
BH	Black Hole
DM	Dark Matter
FUV	Far Ultraviolet
H_2	Molecular hydrogen
HD	Hydrogen deuteride
HMXB	High-mass X-ray Binary
HN	Hypernova
IGM	Intergalactic Medium
IMBH	Intermediate-Mass Black Hole
IMF	Initial Mass Function
JWST	James Webb Space Telescope
LW	Lyman-Werner
MW	Milky Way galaxy
NRST	Nancy Grace Roman Space Telescope
PISN	Pair-instability Supernova Pop I star Population I star
Pop II star	Population II star
Pop III star	Population III star
Pop III star	Population III star
PS	Press-Schechter
RHD	Radiative Hydrodynamics

SMBH	Supermassive Black Holes
SN	Supernova

Chapter 1: Introduction

1.1 Population III Stars

The advancement of observational technologies has brought increasing attention to the study of the first galaxies, black holes, and stars in the early universe. With the remarkable capability of the JWST, we are able to explore the distant and early universe, uncovering the first galaxies (Finkelstein et al., 2022, 2023; Curtis-Lake et al., 2023). Furthermore, the VIRGO/LIGO gravitational wave (GW) observatories have detected GW signals from the mergers of binary black holes (BBHs) (Abbott et al., 2016, 2017), potentially originating from the first stars (Hartwig et al., 2016). There is also anticipation that the explosions of these first stars could be detected using the JWST and the next-generation telescope Nancy Grace Roman Space Telescope (NRST) (Whalen et al., 2014). Understanding these observations necessitates the study of metal-free Population/Pop III stars (or the first stars).

Studying Pop III stars is crucial for several reasons, particularly in light of recent observations. Firstly, Pop III stars play a pivotal role in the formation of the second-generation stars, which serve as the building blocks of the first galaxies. Their strong UV radiation heats and ionizes the surrounding medium, regulating the process of star formation. Additionally, Pop III supernovae (SNe) events evacuate gases from the host dark matter (DM) halos (Wise and Abel, 2008), thereby delaying the formation of the second-generation stars (Jeon et al., 2014b). More-

over, Pop III stars are responsible for producing the first heavy elements (metals) through nuclear fusion reactions. When these stars explode, they disperse these heavy elements into space, enriching the pristine gas composed primarily of hydrogen and helium (Ricotti et al., 2002b; Greif et al., 2010; Wise et al., 2012; Safranek-Shrader et al., 2014; Chiaki et al., 2018; Abe et al., 2021). Secondly, due to their large masses ($M \sim 100$ $\mathrm{M}_{\odot}$), Pop III stars have the potential to form intermediate-mass black holes (IMBHs) ($\sim$ a few 10 $\mathrm{M}_{\odot}$, Heger and Woosley, 2002)[1] which are typically more massive than stellar-mass black holes (BHs) observed in the present universe. This connection is particularly relevant given recent observations of binary black holes detected by VIRGO/LIGO. The total masses of these black holes are ~ 60 $\mathrm{M}_{\odot}$ (Abbott et al., 2016, 2017) and thus they could have formed from Pop III stars (Hartwig et al., 2016). Furthermore, massive Pop III stars explode as hypernovae (HNe) or pair-instability supernovae (PISNe), which are significantly brighter ($\sim 10-100$ times) than normal supernovae (Heger and Woosley, 2002). These events can be detected even in the distant universe, providing valuable insights into the properties of the first stars (Whalen et al., 2014). Therefore, studying Pop III stars is not only timely but also crucial for understanding these observations. Despite their significance, however, the formation of the first stars remains poorly understood and requires further research to fully grasp their implications for the early universe and subsequent galaxy formation.

One of the main challenges in studying Pop III stars stems from the lack of direct observations. Observing these stars in the present or local universe is exceptionally difficult due to their short lifetimes (Schaerer, 2002). Consequently, researchers must look to the early and distant universe to find Pop III stars. However, current telescope capabilities are insufficient to observe individual distant stars unless they are magnified by a foreground galaxy cluster (Diego, 2019;

[1] In this thesis they refer to BHs with $10\ \mathrm{M}_{\odot} \lesssim M \lesssim 100\ \mathrm{M}_{\odot}$.

Welch et al., 2022a,b). As a result, Pop III stars remain hypothetical objects, with their existence inferred from other populations of stars found in the local universe.

In the Milky Way, Population I (Pop I) stars, located in the galactic disk, are characterized by their richness in metals ($Z \sim Z_{\odot}$)[2]. Pop II stars, found in the galactic bulge and stellar halo, exhibit lower metallicity levels ($Z \sim 0.01-0.1Z_{\odot}$). The term "Population III" refers to stars with zero metallicity, although extremely low metallicity stars ($Z \lesssim 10^{-4}\ Z_{\odot}$) are also often classified as Pop III stars in the literature (Ricotti et al., 2016; Kimm et al., 2017; Katz et al., 2017; Jeon and Bromm, 2019; Katz et al., 2023). This classification is due to the suppression of gas cloud fragmentation, resulting in the formation of massive stars at low metallicities ($Z \sim 10^{-4}\ Z_{\odot}$ Bromm et al., 2002). In this thesis, the focus is specifically on the formation of metal-free ($Z = 0$) Pop III stars, aiming to contribute to our understanding of the earliest stages of stellar evolution in the universe.

In astronomy, elements heavier than hydrogen and helium are collectively referred to as "metals." Their mass fraction, denoted as metallicity Z, is relatively small compared to hydrogen and helium. For instance, in the case of the Sun, the mass fractions of hydrogen, helium, and metals are $X = 0.74$, $Y = 0.24$, and $Z = Z_{\odot} = 0.014$, respectively (Asplund et al., 2009). Despite metals making up only about $\sim 1-2\ \%$ in the local universe, they play a crucial role in cooling gas clouds efficiently, which is essential for the formation of stars. In the absence of metals, gas cooling relies on a less efficient coolant, molecular hydrogen (H_2) (Tegmark et al., 1997; Bromm et al., 2002). Therefore, understanding the formation of H_2 and other factors that regulate its formation is critical for understanding the formation of Pop III stars. Investigating these processes is key to unraveling the mechanisms underlying the formation of the earliest stars

[2] Z denotes the metallicity and z denotes the redshift.

in the universe.

1.2 Molecular Hydrogen

1.2.1 Cooling

In the process of star formation, a gas cloud with a significant extent ($R \sim 100$ pc) must undergo contraction to scales of sub-AU size under the influence of its self-gravity. However, this contraction is resisted by the internal pressure of the cloud, creating a balance with the inward force of gravity. For star formation to occur, this balance must be disrupted, allowing gravity to overcome the outward pressure gradient unless additional mass is introduced into the system. The disruption of this balance is achieved through the loss of energy from the system, enabling gravity to prevail over the pressure forces. Radiative cooling is the fundamental process by which this energy loss occurs in star formation. Through radiative cooling, the gas cloud sheds thermal energy, facilitating its collapse under the influence of gravity and eventually leading to the formation of stars.

The energy of a gas cloud is extracted through radiative cooling. In a gas cloud, particles move with speeds corresponding to the temperature of the cloud, characterized by the kinetic energy ($(3/2)k_{\rm B}T \sim (1/2)m\langle v^2\rangle$). As these particles collide with each other, some collisions result in the excitation of particles from lower energy quantum states to higher ones. This excitation can lead to an increase in electron energy and rotational/vibrational energy in the case of a molecule. Over time, the excited particles return to their lower energy states and emit photons with energy corresponding to the energy difference between the two states. During this process, the kinetic energy of the particles is converted into electromagnetic energy. As this radiative emission occurs

throughout the gas cloud, the system gradually loses its thermal energy in the form of radiation, thereby reducing the temperature and pressure of the cloud.

In the early universe, where heavy elements are scarce, hydrogen is the primary coolant in gas clouds. Atomic hydrogen cooling occurs through the transitions between the ground state of the electron energy level and the excited states. This cooling process is most effective at $T \sim 10^4$ K. However, only gas within massive halos can achieve a temperature high enough for atomic cooling. The gas temperature of a virialized halo is,

$$T_{\rm vir} \approx 10^3 \left(\frac{M_{\rm h}}{10^6\ {\rm M}_\odot}\right)^{2/3} \left(\frac{1+z}{10}\right)\ {\rm K}, \tag{1.1}$$

where $M_{\rm h}$ is the mass of the halo and z is the redshift. For instance, at $10 \lesssim z \lesssim 30$, the virial temperature of a DM halo with $M \sim 10^7\ {\rm M}_\odot$ is $\sim 10^4$ K. However, since massive halos are relatively rare, atomic hydrogen cooling is not the primary cooling mechanism for most regions. Furthermore, atomic hydrogen cooling leads to rapid gas accretion and the formation of direct-collapse black holes (DCBHs, Begelman et al., 2006) instead of Pop III stars. Therefore, atomic hydrogen cooling plays a lesser role in the formation of Pop III stars. As a side note, atomic helium cooling is also insignificant because it occurs at an even higher temperature. On the other hand, what significantly influences the formation of Pop III stars is H_2 cooling, which occurs at lower temperatures. At temperatures between ~ 200 and 10^4 K, rotationally and vibrationally excited H_2 molecules extract the energy from the gas cloud, facilitating the collapse and eventual formation of Pop III stars.

1.2.2 Difference from Metal Cooling

H_2 plays an important role as the main coolant in metal-free primordial gas, driving the formation of Pop III stars. The unique properties of H_2 contribute to the distinct characteristics of Pop III stars compared to other stellar populations. Firstly, the rotation energies of H_2 molecules are spaced more widely compared to other diatomic molecules. Classically, the rotational energy of a H_2 molecule is

$$E_{\rm rot} = \frac{J(J+1)\hbar^2}{2\mu r_0^2}, \tag{1.2}$$

where J is the rotation quantum number[3], μ is the reduced mass, $\hbar = h_{\rm P}/2\pi$ is the reduced Planck constant, and r_0 is the interparticle separation. The small moment of inertia (μr_0^2) results in large energy differences between rotational states. As a result, high kinetic energies of the particles are required for excitation. Secondly, H_2 lacks a permanent dipole moment, which means that the rotational transition with $\Delta J = \pm 1$ is not allowed by the selection rule. Instead, these transitions can occur through quadrupole transition ($\Delta J = \pm 2$). However, quadrupole transitions have low Einstein A coefficients and are slow processes (Hollenbach and McKee, 1979), reducing the efficiency of H_2 cooling. Additionally, H_2 cooling is inefficient at lower temperatures and can only effectively extract energy from gas clouds with temperatures ranging from ~ 100 K to $\sim 10^4$ K. Below this temperature range, H_2 cooling becomes ineffective. In contrast, heteronuclear diatomic molecules like CO have permanent dipole moments. This property allows metal-enriched molecules containing CO to cool at lower temperatures ($T \sim 10$ K).

The complex atomic structures of metals allow more efficient radiative cooling through

[3]From Chapter 2 to 4, J indicates the intensity of a radiation background. In Chapter 5, $\boldsymbol{J}$ refers to the angular momentum vector.

a number of fine structure transitions. These transitions, characterized by narrowly spaced energy levels, facilitate cooling below $T \sim 10^4$ K. The rate of radiative cooling due to metals is proportional to the metallicity of the cloud (Smith et al., 2008). This implies that there exists a critical metallicity below which H_2 cooling predominates over metallic line cooling, significantly altering the properties of star formation. Numerical studies conducted by Bromm et al. (2002) demonstrated that gas clouds with two different metallicities ($Z = 10^{-3}\ Z_\odot$ and $Z = 10^{-4}\ Z_\odot$) evolve differently. In their study, the cloud with higher metallicity fragments, while fragmentation is suppressed in the cloud with lower metallicity. The effect of metals on star formation is depicted in Fig. 1.1. At low metallicity (left panel), gas fragmentation is inhibited, resulting in the formation of a few massive stars. However, as metallicity increases (moving from left to right in the figure), turbulence within the gas cloud develops, leading to fragmentation and the formation of multiple stars.

1.2.3 Formation of Molecular Hydrogen

The formation of molecular hydrogen (H_2) is a crucial process in primordial gas cooling and the formation of Pop III stars. In a metal-enriched environment, H_2 forms on the surface of dust grains, and the rate of formation is influenced by the metallicity of the cloud. This relationship is evident in the bottom panels of Fig. 1.1, where the H_2 fraction increases as the metallicity of the cloud increases from left to right. However, in the early universe where metallicity is essentially zero, dust grains did not exist. Therefore, H_2 cannot form on dust grains but primarily

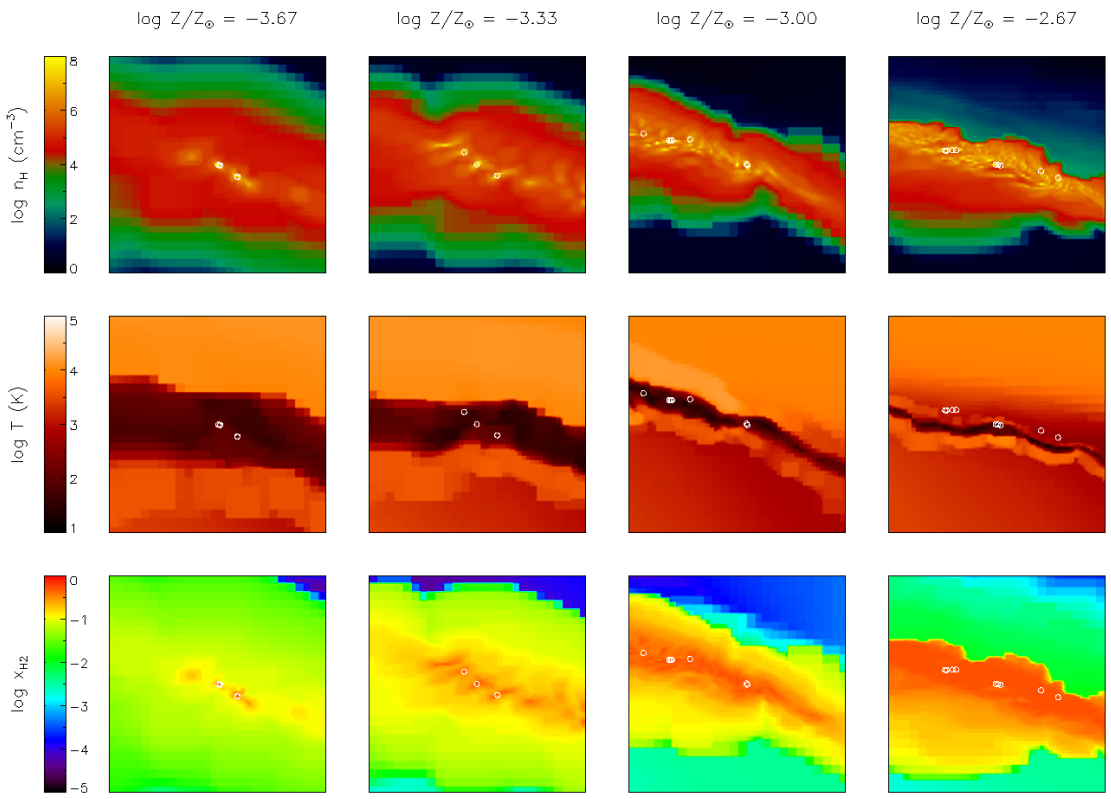

Figure 1.1: Hydrogen density (top), temperature (middle), and H_2 fraction (bottom) of a star-forming gas cloud with varying metallicities, arranged from left to right. The white circles within each box represent stars. To establish the initial conditions for the simulations, I utilized the outcomes of a cosmological zoom-in simulation of Garcia et al. (2023). As the metallicity of the gas cloud increases (from left to right), the cloud becomes more turbulent and fragmentation becomes more active.

forms in the gas phase via the H^- channel,

$$\begin{aligned} H + e^- &\longrightarrow H^- + \gamma \\ H + H^- &\longrightarrow H_2 + e^-. \end{aligned} \tag{1.3}$$

In this process, H^- serves as a catalyst. The rate of H_2 formation depends on the fraction of free electrons (e^-). This reaction is particularly dominant at low densities. At high density ($n_H \gtrsim$

10^8 H cm^{-3}) three-body interaction becomes the dominant channel for H_2 formation,

$$3\,\mathrm{H} \longrightarrow \mathrm{H_2} + \mathrm{H}, \tag{1.4}$$

and,

$$2\,\mathrm{H} + \mathrm{H_2} \longrightarrow 2\,\mathrm{H_2}. \tag{1.5}$$

1.2.4 HD

Another crucial factor in Pop III star formation is the presence of deuterium hydride (HD). Unlike symmetric H_2, HD has a small dipole moment, allowing for dipole transitions that occur at lower temperatures ($T \lesssim 100$ K). However, HD alone is insufficient to trigger the collapse of primordial gas within a virialized halo where temperatures are $T \sim 10^3$ K. Additionally, the abundance of HD is much lower compared to H_2 (Yoshida et al., 2007).

Although HD is not the primary coolant of primordial gas due to its lower abundance, there are situations where HD cooling becomes significant and plays a critical role in Pop III star formation. When the gas temperature reaches $T \sim 150$ K, HD cooling becomes effective in further cooling the gas, altering the properties of Pop III stars. This scenario can occur, for instance, when a gas ionized by neighboring Pop III stars recombines. With a high ionization fraction, the H_2 fraction remains high, leading to an increase in the HD fraction. Ultimately, this process results in a reduction in the mass of Pop III stars. In Chapter 4, the focus will be on investigating the effect of X-rays on the global ionization and subsequent formation of Pop III stars. X-rays can significantly impact the ionization state of the gas, influencing the formation and abundance of HD and, consequently, the properties of Pop III stars.

1.3 Radiation Background

Pop III star formation is primarily driven by H_2 cooling, and the rate of cooling depends on the H_2 fraction of the gas cloud. Consequently, radiation backgrounds that regulate the formation of H_2 play a crucial role in shaping Pop III star formation. For instance, H_2 formation via the H^- channel (equation (1.3)) is contingent upon the electron fraction, which can be influenced by an ionizing radiation background. Intense ionizing radiation can enhance the formation of H_2, potentially altering the properties of Pop III stars. Furthermore, UV radiation in the Lyman-Werner (LW) band can have a significant impact on H_2 by dissociating it. Many authors have highlighted the role of LW radiation in influencing Pop III star formation (Haiman et al., 2000; Omukai, 2001; Regan et al., 2020). Therefore, when studying Pop III star formation, it is imperative to consider the effects of radiation backgrounds, as they can significantly influence the formation and abundance of H_2, subsequently shaping the properties of Pop III stars.

Several authors have emphasized the significance of X-ray radiation in ionizing the gas and enhancing the gas-phase H_2 formation (Haiman et al., 2000; Oh et al., 2001; Venkatesan et al., 2001; Ricotti, 2016). This perspective is supported by two key aspects of X-rays. First, X-ray photons possess the capability to traverse considerable distances in the early universe. The intergalactic medium (IGM) in the early universe ($z \gtrsim 10$) is nearly neutral before being ionized at $z \sim 6 - 10$ (Fan et al., 2006). Therefore, the IGM is opaque to ionizing radiation especially UV emitted by main-sequence Pop III stars. Unlike UV photons, which are readily absorbed due to their large ionization cross-sections, X-ray photons exhibit smaller cross-sections and can travel greater distances without being absorbed by the neutral medium. This is illustrated in the left panel of Fig. 1.2, which displays the ionization cross-sections of H I, He I, and He II as a

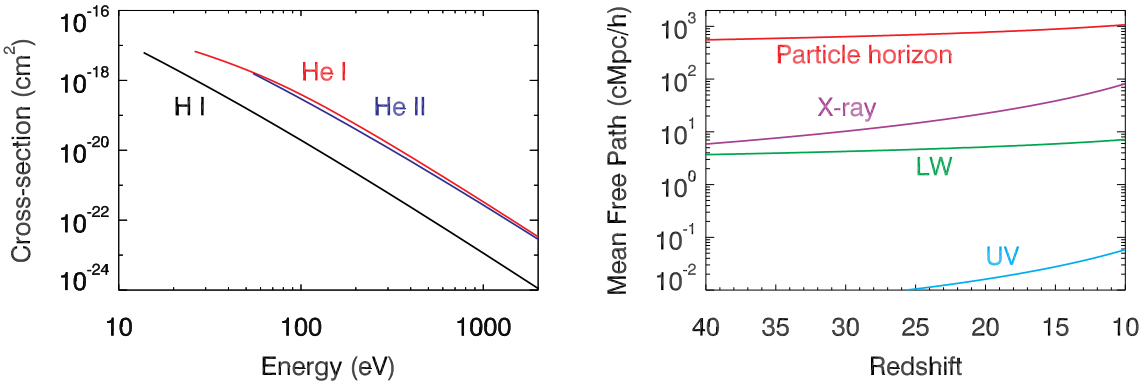

Figure 1.2: Left: Ionization cross-sections of H I (black), He I (red), and He II (blue). Right: Particle horizon (red, $c \times t_{\rm age}$), X-ray mean free path (purple, 500 eV), LW mean free path (green), and UV mean free path (cyan, 54.4 eV). The average LW mean free path is 150th of the particle horizon (Ricotti et al., 2001; Ricotti, 2016).

function of photon energy. X-ray photons ($E \gtrsim 200$ eV) are less absorbed by the local medium compared to ionizing UV photons, allowing them to penetrate deeper into the IGM as depicted by the purple and cyan lines in the right panel of the figure. Second, X-rays are efficient at ionizing the IGM. When a high-energy X-ray photon ($E_{\rm ph} \gtrsim 0.2$ keV) ionizes a hydrogen atom, the resulting photoelectron possesses significant kinetic energy ($E_{\rm el} = E_{\rm ph} - I_{\rm H}$, $I_{\rm H} = 13.6$ eV is the ionization potential of a hydrogen atom). In a neutral medium, the electron collides with other hydrogen atoms, leading to a secondary ionization effect (Shull, 1979; Shull and van Steenberg, 1985). For instance, one soft X-ray photon ($E_{\rm ph} \sim 0.2$ keV) can ionize ~ 30 neutral hydrogen atoms in the medium (Park et al., 2021a). Consequently, a moderate X-ray background can ionize the IGM, thereby promoting the formation of H_2 and facilitating the formation of Pop III stars (Ricotti, 2016; Park et al., 2021a). However, it is essential to acknowledge that X-rays also have negative feedback by inducing heating Jeon et al. (2014a). Therefore, when studying Pop III stars, it is important to consider both positive and negative feedback mechanisms associated with X-ray radiation.

High-energy X-ray photons play a significant role, yet their sources differ from main-sequence Pop III stars. While Pop III stars are indeed hot, their contribution to X-ray emissions is limited. For instance, the surface temperature of a massive Pop III star typically reaches $\sim 10^5$ K, corresponding to a peak wavelength of ~ 300 nm and a photon energy of ~ 40 eV. Consequently, while massive Pop III stars are bright in UV, they emit relatively faint X-rays. However, the remnants and phenomena associated with Pop III stars are potent sources of X-ray photons. First, supernova remnants (SNRs) are robust X-ray emitters due to the shock-heating of gas during the explosive event, resulting in high temperatures ($T \gtrsim 10^7$ K, Lopez et al., 2011). This hot plasma emits high-energy photons through thermal bremsstrahlung radiation. Moreover, if Pop III stars end their lives as PISNe or HNe, which are significantly more energetic ($10-100$ times) than typical SNe (Heger and Woosley, 2002), they can emit copious amounts of X-ray photons. Second, Pop III BHs are potential sources of X-ray emissions. Pop III stars within a specific mass range may collapse into BHs (Heger and Woosley, 2002). These Pop III BHs, owing to their massive progenitors, are larger than stellar-mass BHs in the present universe and can thus emit substantial X-ray radiation. If a Pop III binary evolves into a high-mass X-ray binary (HMXB), it becomes a source of hard X-ray photons ($E \gtrsim 2$ keV), influencing the surrounding medium through heating (Jeon et al., 2014a). Additionally, wandering IMBHs accreting material in the first galaxies may emit strong X-ray radiation, as suggested by theoretical studies (Park and Ricotti, 2011; Sugimura and Ricotti, 2020). Finally, active galactic nuclei (AGNs) are expected to contribute significantly to the buildup of an X-ray background in the early universe. Recent observations predicted high fractions of AGNs at $z \sim 10$ (Juodžbalis et al., 2023; Fujimoto et al., 2023), underscoring the importance of studying their effects in the early universe. In summary, given the presence of various X-ray sources in the early universe, it is essential to consider the effects of X-ray radiation

in studies of Pop III star formation.

X-rays play a role in ionizing the IGM and increasing the fraction of H_2, while LW radiation directly dissociates H_2, thereby decreasing its fraction. In the LW band, when an H_2 absorbs a photon, it undergoes an excitation of an electron energy state. Subsequently, when the excited molecule emits a photon, some of the energy is converted into vibrational energy. With $\approx 15\,\%$ of the time, this vibrational energy is sufficient to break molecular bonds and dissociate H_2 (Draine, 2011). Unlike the ionization of an atom, this dissociation process is a line process and therefore only photons with certain energies are absorbed. Examples of these lines are presented in Haiman et al. (2000) and Ricotti et al. (2001). However, factors such as the expansion of the universe, hydrodynamics, and peculiar motions of DM halos alter the frequencies of photons, complicating the modeling H_2 dissociation by LW photons. On average LW photons have significantly larger mean free paths compared to ionizing UV photons in the early universe. For instance, the effective mean free path of LW photons is ~ 150 times smaller than the horizon (Ricotti et al., 2001; Ricotti, 2016). This is depicted in the right panel of Fig. 1.2, where the comparison with the mean free path with ionizing UV and X-ray photons is illustrated. Consequently, LW radiation emerges as a crucial radiation background in the opaque early universe. An intense LW background can potentially delay the formation of Pop III stars. When DM halos are irradiated by LW radiation, they grow in mass without forming Pop III stars. If the virial temperature of the gas within the halos exceeds $\sim 10^4$ K, atomic hydrogen cooling becomes prominent. In such cases, massive BH seeds ($M \sim 10^5\,\mathrm{M}_\odot$) appear, making these halos potential sites for the formation of supermassive black holes (SMBH) (Regan et al., 2020).

1.4 Properties of Population III Stars

1.4.1 Critical Mass of Halo

The formation of Pop III stars initiates with the cooling of virialized gas within a DM halo. This cooling process occurs when the gas undergoes ionization through particle collisions, leading to the formation of a sufficient quantity of H_2 via the H^- channel (equation 1.3). If the gas collapses rapidly with a significant presence of H_2, Pop III stars can form. Tegmark et al. (1997) demonstrated that the first Pop III stars emerge at $z \sim 30$ within minihalos of mass $\sim 10^6$ $M_\odot$. However, if a halo possesses a mass lower than this threshold, the gas within it is not sufficiently ionized by collisional processes, resulting in an insufficient electron fraction to generate the required amount of H_2. This critical mass of the halo, above which Pop III stars can form, stands as a pivotal aspect of Pop III star formation and carries significant implications. Firstly, the critical mass is intricately linked to the detection of PISNe by instruments such as JWST and NRST (*e.g.*, Whalen et al., 2014). A lower critical mass implies that even relatively small DM halos have the potential to host Pop III stars, consequently increasing the number of Pop III stars per unit volume. By analyzing observations to estimate the number of Pop III stars, insight into the factors influencing the critical mass can be gleaned. Secondly, the number of Pop III stars may hold significance in the context of the formation of the first galaxies. Pop III stars generate heavy elements and contaminate the primordial gas. Subsequent generations of stars form within this contaminated gas, serving as the foundational components of the first galaxies. Therefore, comprehending the critical mass is necessary for advancing our understanding of galaxy formation processes.

While Tegmark et al. (1997) initially proposed a critical mass of $\sim 10^6\ \mathrm{M}_\odot$, Ricotti (2016) demonstrated that an X-ray background could potentially reduce the critical mass. This reduction is feasible because a virialized gas undergoes ionization by a moderate X-ray background as well as collisional ionization. This enhances the formation of H_2 via H^- channel (equation 1.3), consequently lowering the critical mass and allowing smaller halos to foster the formation of Pop III stars. For example, Ricotti (2016) predicted that in a weak X-ray background, the number density of Pop III stars would be $\sim\ 10$ per $(1\ \mathrm{Mpc}/h)^3$ volume. However, the presence of a moderate X-ray background could elevate this number by a factor of ~ 10.

1.4.2 Mass

In star formation theory, the Jeans mass is a fundamental concept used to assess whether a gas cloud can contract and potentially form stars. It also helps estimate the masses of the stars that form in the cloud. The Jeans length is a critical parameter in this context, and it is defined as,

$$\begin{aligned} \lambda_\mathrm{J} &= t_\mathrm{ff} c_\mathrm{s} \\ &= \frac{c_\mathrm{s}}{\sqrt{G\rho}}, \end{aligned} \tag{1.6}$$

where $t_\mathrm{ff} = 1/\sqrt{G\rho}$ is the free-fall time, G is the gravitational constant, ρ is the density, and c_s is the sound speed. The mass enclosed within the Jeans length is called the Jeans mass and it is,

$$\begin{aligned} M_\mathrm{J} &= \frac{4\pi}{3}\lambda_\mathrm{j}^3 \rho \\ &\sim \frac{k_\mathrm{B}^{1.5}(T/\mathrm{K})^{1.5}}{G^{1.5} m_\mathrm{H}^2} \frac{1}{\sqrt{(n/\mathrm{cm}^3)}} \\ &\sim 17\ \mathrm{M}_\odot\ \frac{(T/\mathrm{K})^{1.5}}{\sqrt{(n/\mathrm{cm}^3)}}, \end{aligned} \tag{1.7}$$

where $k_{\rm B}$ is the Boltzmann constant, T is the gas temperature, $m_{\rm H}$ is the hydrogen mass, and n is the number density. The above Jeans criterion ($R > \lambda_{\rm J}$) indicates that a gas cloud may undergo collapse if the enclosed mass within a certain scale exceeds the Jeans mass ($M_{\rm enc} > M_{\rm J}$).

The Jeans mass is contingent upon both temperature and density (equation 1.7), thereby exhibiting variations as the gas cloud experiences cooling/heating or collapse/expansion. The variation is often elucidated by the polytropic equation-of-state $P = K\rho^{\gamma}$ and,

$$\begin{aligned} M_{\rm J} &\propto \rho\lambda_{\rm J}^3 \\ &\propto \rho c_{\rm s}^3 \frac{1}{\rho^{3/2}} \\ &\propto \rho^{\frac{1}{2}(3\gamma-4)}, \end{aligned} \tag{1.8}$$

where γ is determined by the characteristics of the coolant. If $\gamma > \frac{4}{3}$, $M_{\rm J}$ increases with ρ (contraction). Conversely, if $\gamma < \frac{4}{3}$ the Jeans mass decreases as the cloud contracts. In this case, the gas cloud may fragment when the enclosed masses around density peaks exceed the local Jeans mass.

In a giant molecular cloud enriched with metals, characterized by temperatures $T \sim 10$ K and densities $n \sim 10^2$ cm^{-3}, the Jeans mass is ~ 50 M$_\odot$. Considering these clouds typically have masses $\sim 10^5$ M$_\odot$, they have the potential to collapse and form multiple stars. As the gas cloud evolves, it fragments, giving rise to a cluster of low-mass stars, thereby leading to a bottom-heavy initial mass function (IMF). In contrast, for primordial gas (zero-metallicity) in a virialized halo of mass of $\sim 10^6$ M$_\odot$, $T \sim 10^3$ K and $n \sim 1$ cm^{-3}. At these conditions, the Jeans mass is estimated to be $M_{\rm J} \sim 5 \times 10^5$ M$_\odot$ while the mass within the halo is $\sim 10^5$ M$_\odot$, assuming the cosmic baryon-DM density ratio. With H_2 cooling reducing the gas temperature to $T \sim 200$ K

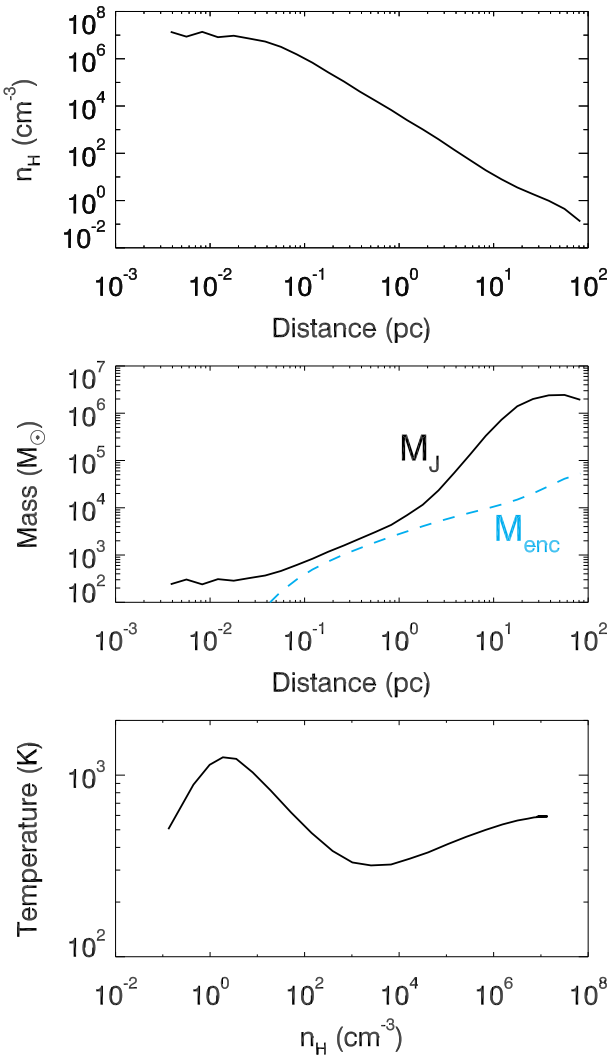

Figure 1.3: Profiles of primordial gas in a DM halo (Park et al., 2023). Top: Density profile. Middle: The Jeans mass (black) and enclosed mass (cyan). Bottom: n vs T phase diagram.

at $n \sim 10^4$ cm^{-3}, the Jeans mass decreases to $M_{\rm J} \sim 100 - 1000$ M$_\odot$. This is illustrated in the middle panel of Fig. 1.3. Initially, at the virial radius ($r \sim 10^2$ pc), the enclosed mass significantly falls below the Jeans mass. However, as the gas cloud cools via H_2, the Jeans mass decreases. On a scale of $r \sim 10^{-1} - 10^0$ pc, two mass scales become comparable, and subsequent evolution proceeds with self-gravity within this radius. The Jeans mass on this scale is ~ 100 M$_\odot$, leading to the formation of Pop III stars with similar masses, thus rendering the IMF top-heavy.

1.4.3 Multiplicity

Early theoretical and numerical investigations (Abel et al., 2002; Bromm et al., 2002) initially posited that a primordial gas cloud would not fragment, leading to the formation of a single massive Pop III star. However, with advancements in simulation resolution, it became apparent that as the density increases, a gas disk forms, subsequently fragmenting to give rise to multiple stars (Clark et al., 2011a; Susa et al., 2014; Stacy et al., 2016; Sugimura et al., 2020). Despite this fragmentation, Pop III stars are believed to be massive, resulting in a top-heavy IMF, in contrast to the bottom-heavy Salpeter or Chabrier IMF observed in stars within the local universe (Salpeter, 1955; Chabrier, 2003). This result suggests that the formation of massive Pop III binaries, which, upon evolution into BBH, could merge and emit strong GW signals through various channels (Michaely and Perets, 2019; Liu and Bromm, 2020).

1.5 Thesis Outline

In this thesis, I investigate the formation of metal-free Pop III stars under the influence of X-ray/LW radiation backgrounds. Across multiple chapters, I address various facets of this topic. Chapter 2 delves into the impact of X-ray and LW backgrounds on the critical mass of halos for Pop III star formation, employing an extensive set of simulations of halos irradiated by X-ray/LW backgrounds with various intensities. In addition, the characteristic mass of Pop III stars affected by X-ray radiation is explored. Chapter 3 examines how X-rays affect disk fragmentation and the multiplicity of Pop III stars. Chapter 4 introduces radiative feedback from Pop III protostars and evaluates its implications on several properties. Additionally, I suggest that the variability of eccentric binaries can be observed. In Chapter 5, I explore the origin of outward

migration frequently observed in Pop III star formation simulations, analyzing torques and angular momentum to understand how the angular momentum is transferred from the envelope to the binaries. Furthermore, Chapter 6 revisits the concept of critical mass within a cosmological framework, incorporating on-the-fly calculation of X-ray/LW radiation backgrounds to capture feedback loop effects. Lastly, Chapter 7 summarizes the findings and outlines potential avenues for future research.

1.6 A summary of software and facilities

Computational resources:

1. The Deepthought2 and Zaratan HPC cluster of the University of Maryland supercomputing resources[4]
2. Student workstations of the Department of Astronomy, University of Maryland[5]

Software:

1. RAMSES-RT (Teyssier, 2002; Rosdahl et al., 2013; Bleuler and Teyssier, 2014)

[4] https://www.glue.umd.edu/hpcc/
[5] https://www.astro.umd.edu/twiki/bin/view/AstroUMD/StudentWorkstations

Chapter 2: Population III Star Formation in an X-ray Background - I. Critical Halo Mass of Formation and Total Mass In Stars

The first luminous objects forming in the universe produce radiation backgrounds in the FUV and X-ray bands that affect the formation of Population III stars. Using a grid of cosmological hydrodynamics zoom-in simulations, we explore the impact of the LW and X-ray radiation backgrounds on the critical DM halo mass for Population III star formation and the total mass in stars per halo. We find that the LW radiation background lowers the H_2 fraction and delays the formation of the Population III stars. On the other hand, X-ray irradiation anticipates the redshift of collapse and reduces the critical halo mass, unless the X-ray background is too strong and gas heating shuts down gas collapse into the haloes and prevents star formation. Therefore, an X-ray background can increase the number of DM haloes forming Pop III stars by about a factor of ten, but the total mass in stars forming in each halo is reduced. This is because X-ray radiation increases the molecular fraction and lowers the minimum temperature of the collapsing gas (or equivalently the mass of the quasi-hydrostatic core) and therefore slows down the accretion of the gas onto the central protostar.

2.1 Introduction

A better understanding of the formation of the first stars (Pop III) star and their impact on second-generation stars is timely and important. First, they have an important role in the formation of the first galaxies and black holes (Bromm and Yoshida, 2011; Bromm, 2013, for review). They produce the heavy elements required for the formation of the second-generation stars (*e.g.*, Greif et al., 2010; Wise et al., 2012; Safranek-Shrader et al., 2014; Chiaki et al., 2018; Abe et al., 2021), but their formation rate is uncertain because it is self-regulated by complex chemical and radiative feedback loops (Ricotti et al., 2002b; Wise and Abel, 2008). For instance, the radiation backgrounds they produce affect their formation rate on cosmological scales (Ricotti, 2016, hearafter R16). Secondly, although there has been significant progress in detecting high-z galaxies (*e.g.* Bouwens et al., 2019; Finkelstein et al., 2022), our understanding of their formation is still limited to the brightest galaxies at redshifts below $z \sim 6 - 10$. With the JWST, however, we will be able to look further and learn more about the formation processes of the first objects. Moreover, Pop III stars are of particular interest because the formation of the first IMBH remnants with stellar origin is also poorly understood, and Pop III remnants are possible candidates for the formation of black hole mergers detected by LIGO and Virgo gravitational wave experiments (Abbott et al., 2016, 2017) due to their high masses (order of $10 - 100$ $\mathrm{M}_{\odot}$, Heger and Woosley, 2002).

The first Pop III stars form in DM haloes of $\sim 10^6$ $\mathrm{M}_{\odot}$ (called minihaloes) at $z \sim 30$ (Tegmark et al., 1997; Bromm et al., 2002; Abel et al., 2002; Yoshida et al., 2008). In the early Universe, there are no heavy elements that can cool the gas in virialized minihaloes with $T_{\rm vir} < 10^4$ K (corresponding roughly to minihalo masses $< 10^8$ $\mathrm{M}_{\odot}$). Therefore, the formation of Pop III

stars relies on molecular hydrogen (H_2) formation via the H^- catalyst. This implies that the radiation regulating the amount of H_2 is crucial to their formation. For instance, FUV radiation in the LW bands ($11.2 - 13.6$ eV) emitted by Pop III stars dissociates H_2 (Haiman et al., 2000; Omukai, 2001), suppressing gas cooling in minihaloes. The mean free path of LW radiation in the IGM is roughly ~ 150 times smaller than the particle horizon (Ricotti et al., 2001, R16), and much greater than the mean free path of ionizing UV radiation (≥ 13.6 eV). Therefore, LW photons can travel far and build a radiation background that dominates the radiation from local sources, and it is able to delay or suppress the formation of Pop III stars (Haiman et al., 2000; O'Shea and Norman, 2008; Johnson et al., 2013; Regan et al., 2020). Another radiation background that affects the H_2 fraction is the X-ray radiation ($\gtrsim 0.2$ keV, Haiman et al., 2000; Venkatesan et al., 2001; Xu et al., 2016). The IGM is relatively transparent to photons in this energy range. An X-ray radiation background partially ionizes the pristine gas and increases the amount of H_2 that forms via $H + H^- \longrightarrow H_2 + e^-$ channel. In the early Universe, HMXBs, accreting IMBHs, or supernova/hypernova explosions of Pop III stars are possible sources of an X-ray radiation background (Jeon et al. 2014a; Xu et al. 2016; R16).

The role of the X-ray background in regulating the formation of Pop III stars is still debated. Using zoom-in simulations, Jeon et al. (2014a) studied the effect of X-ray radiation emitted by local sources and found negligible effects on the Pop III star formation rate. On the other hand, through self-consistent modeling of sources and the background they produce on IGM scales, R16 found that X-ray emission from the first sources has positive feedback on the number of Pop III stars because of the enhanced H_2 formation and cooling. However, when the mean X-ray emission per source is above a critical value, the number of Pop III stars per comoving volume is reduced because X-ray heating of the IGM becomes the dominant feedback effect. At the critical

X-ray luminosity per source, the number of Pop III stars per comoving Mpc/h^3 at $z \sim 15$ is ~ 400, that is far larger than ~ 10 Pop III stars found in the same volume without X-rays (*i.e.*, with only LW radiation background). The limit of this model is that it considers global feedback loops but neglects local feedback effects and galaxy-scale gas dynamics.

The IMF of Pop III stars is also an important open question in Pop III star formation theory and has been studied numerically by many authors (Hirano et al., 2014; Susa et al., 2014; Stacy et al., 2016). Using a number of RHD simulations, Hirano et al. (2014) and Hirano et al. (2015, hearafter HR15) explored the final masses of Pop III stars, taking into account photodissociation of H_2 by LW background, but neglecting the effect of X-ray radiation. Simulating a large sample of minihaloes, they found correlations between the final mass of Pop III stars and properties of gas cloud or host halo, such as the gas accretion rate. Hummel et al. (2015, hereafter HM15) explored the role of an X-ray background in determining the number of Pop III stars and their final masses.

In this work, the first in a series, we investigate how the X-ray and LW radiation backgrounds affect the formation of Pop III stars using a set of zoom-in cosmological simulations of minihaloes. First, we study the impact of the backgrounds on the redshift of collapse and therefore the critical mass of the DM minihalo when Pop III stars form. This is tightly related to the number of Pop III stars and PISNe that will be able to be detected with JWST and the NRST (Whalen et al., 2014). Furthermore, we explore how the total mass in Pop III stars depends on the intensity of the radiation backgrounds. In a companion paper (Park et al., 2021b, hereafter, Paper II), we study the effect of X-ray irradiation on the properties and fragmentation of protostellar discs, the multiplicity, mass function and separation of Pop III stars.

The paper is organized as follows. In Section 2.2 we introduce our simulations and meth-

ods. In Section 2.3 and 2.4 we discuss how a radiation background affects the minimum mass of minihaloes forming Pop III stars, and the final masses of Pop III stars, respectively. In Section 2.5 we provide a discussion and a summary.

2.2 Simulation

We use the RHD cosmological code RAMSES-RT (Rosdahl et al., 2013). Its original version RAMSES (Teyssier, 2002) is an N-body + hydrodynamic code using an AMR technique. In order to simulate the growth of haloes, gas collapse, and development of discs from cosmological initial conditions, we perform zoom-in simulations. First, we run two DM-only simulations of 1 and 2 Mpc/h^3 boxes. We select two haloes (Halo 1 and Halo 3) from the 1 Mpc/h^3 box and one halo (Halo 2) from the other. Halo 1 is at the centre of a group while Halo 2 and Halo 3 are in sparsely populated regions.

Inside each zoom-in region, the mass of DM particles is $\sim 800\ \mathrm{M}_\odot$. The cells within the zoom-in regions are refined if they contain at least 8 DM particles or if their Jeans lengths are not resolved with at least N_J cells. For the latter condition, a widely adopted value is $N_\mathrm{J} = 4$ (Truelove et al., 1997), but we adopt the value of N_J adaptively. At small scales where the circumstellar disc fragments and stars form (cell size smaller than $\sim 1\ \mathrm{pc}/h$, comoving), we adopt $N_\mathrm{J} = 16$ in order to prevent any possible artificial fragmentation and better resolve possible turbulent motions. If the size of a cell is greater than $\sim 30\ \mathrm{pc}/h$ (comoving), we adopt $N_\mathrm{J} = 4$ to save computational time. Any cells between these two scales are refined with $N_\mathrm{J} = 8$. The size of a smallest cell is $0.00375\ \mathrm{pc}/h$ (comoving). At $z = 20$, this corresponds to a physical size of $2.63 \times 10^{-4}\ \mathrm{pc}$ (or 54 au). The corresponding AMR levels are shown in Table 2.1. The initial

Table 2.1: Summary of the simulations.

	$M_{\rm vir}$ ($z = 15.7$)	$M_{\rm DM}$ (zoom-in)	Box size	$l_{\rm max}$
Halo 1	7.9×10^6 M$_\odot$	800 M$_\odot$	1 Mpc/h^3	28
Halo 2	4.4×10^6 M$_\odot$	800 M$_\odot$	2 Mpc/h^3	29
Halo 3	7.0×10^5 M$_\odot$	800 M$_\odot$	1 Mpc/h^3	28

conditions of the DM-only and zoom-in simulations are generated with MUSIC (Hahn and Abel, 2011). The assumed cosmological parameters are $h = 0.674, \Omega_{\rm m} = 0.315, \Omega_\Lambda = 0.685, \Omega_{\rm b} = 0.0493, \sigma_8 = 0.811$ and $n_{\rm s} = 0.965$ (Planck Collaboration et al., 2020). The initial abundances of electrons and H_2 are $\sim 2 \times 10^{-4}$ and 2×10^{-6}, respectively.

Snapshots of the haloes are presented in Fig. 2.1 and a summary of the three simulations is given in Table 2.1. In Fig. 2.2 we plot the virial masses of the haloes as a function of redshift. Halo 1 is more massive than the other two, and its mass reaches $\sim 2 \times 10^7$ M$_\odot$ at $z \sim 15$. Halo 2 and Halo 3 end up being haloes of $\sim 7 \times 10^6$ and 2×10^6 M$_\odot$ at $z \sim 10$. In a strong LW radiation background, the collapse of the gas is delayed to when the mass of the minihalo is $\gtrsim 10^7$ M$_\odot$, close to the critical mass at which Ly α cooling becomes dominant and approaching a regime thought to be the main formation channel of direct-collapse-black holes (*e.g.*, Omukai 2001; Bromm and Loeb 2003; Regan and Haehnelt 2009; Shang et al. 2010; Latif et al. 2011; Hosokawa et al. 2012; Sugimura et al. 2014; Chon et al. 2016; Regan et al. 2020; see also Inayoshi et al. 2020 for a review). Excluding this extreme case, the formation of Pop III stars in our simulations occurs when the masses of the minihaloes are between 10^5 M$_\odot$ and $\sim 2 \times 10^6$ M$_\odot$. In this range, the masses of the three haloes grow in different ways. Halo 1 grows rapidly between redshift $z \sim 30$ to $z \sim 22$ and Pop III star formation happens during this time. Halo 3 also grows rapidly from $z \sim 19$ to $z \sim 17$ and the redshift of star formation in many simulations falls in this range.

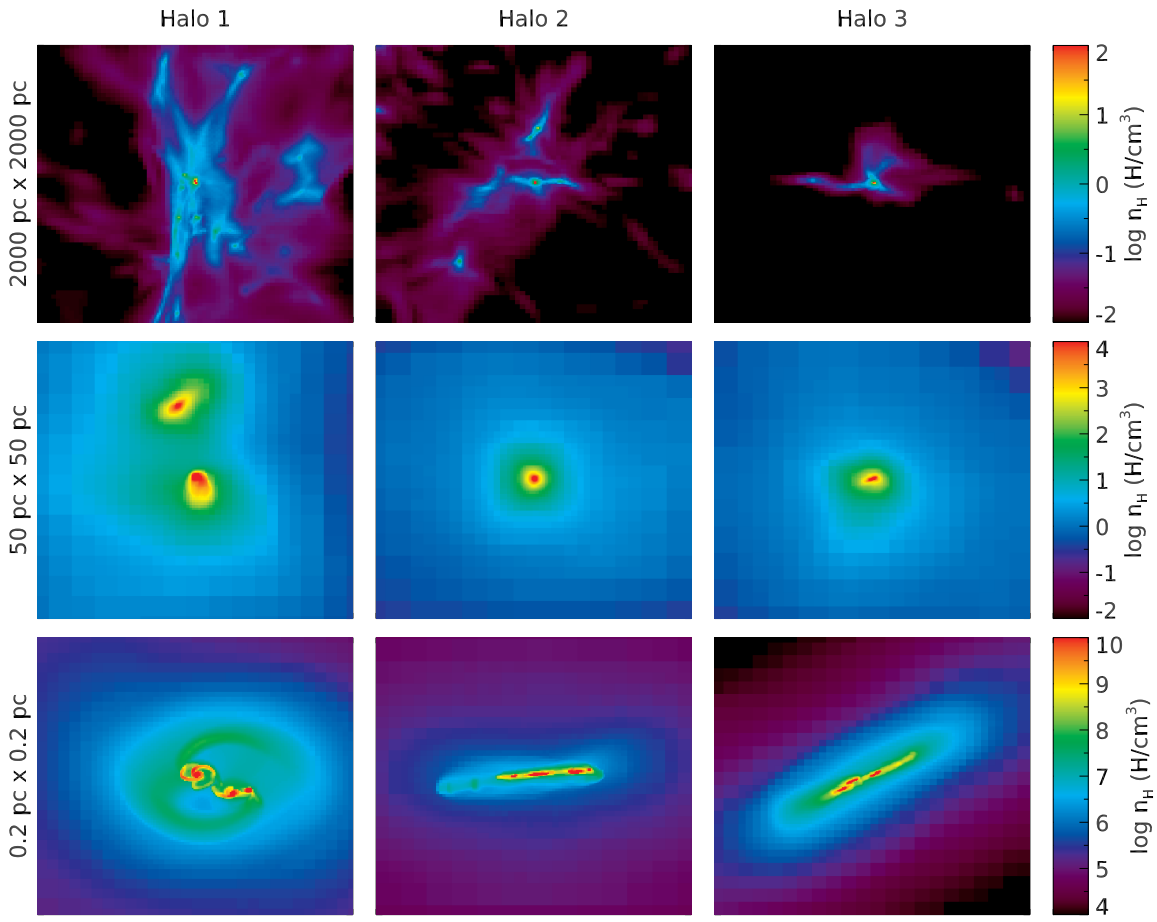

Figure 2.1: Snapshots of the gas density in Halo 1, Halo 2, and Halo 3 (columns from left to right, respectively) for the case without radiation backgrounds. Each row shows the gas density at three different scales (see label on the left).

On the other hand, the mass of Halo 2 increases slowly, by a factor of two from $z \sim 25$ and 20, and most of the star formation happens during this time.

2.2.1 Chemistry

RAMSES-RT incorporates the chemistry of hydrogen/helium ions and molecular hydrogen. In this study, the formation and destruction of H_2 are treated following Katz et al. (2017) with some modifications. Our revised model is accurate up to gas densities $n_{\rm H} \sim 10^{12}$ H cm^{-3}. Improvements and validation of the primordial chemistry/cooling model with respect to the original

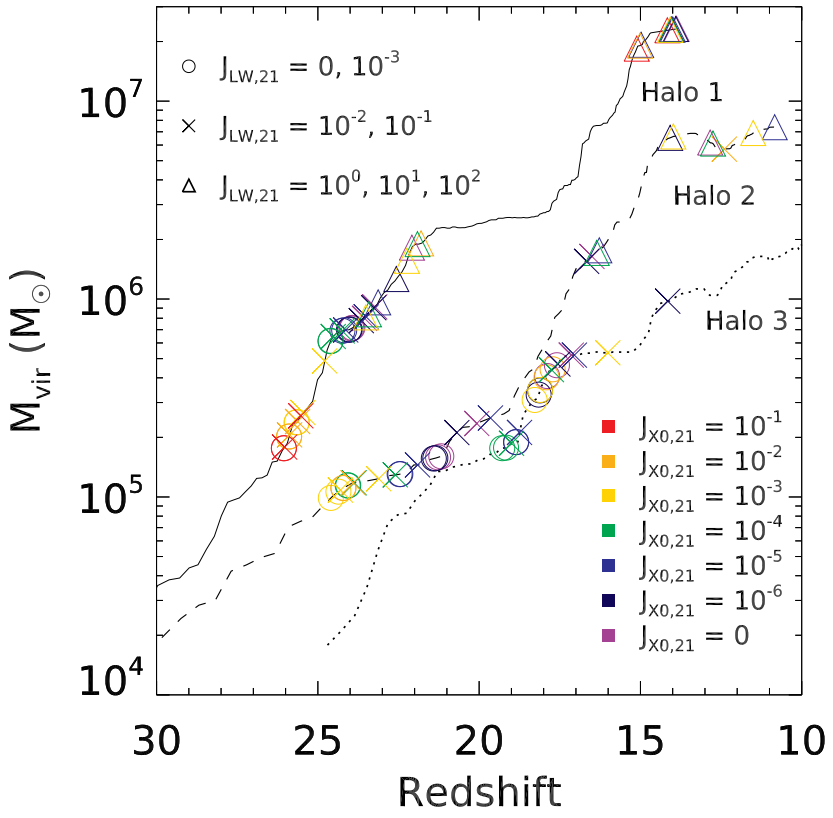

Figure 2.2: Halo mass as a function of redshift. The virial masses of Halo 1, Halo 2, and Halo 3 are shown with different lines. The positions of symbols refer to the redshift of the formation of Pop III stars and the masses of their host minihaloes. Different symbols and colors indicate the intensity of LW and X-ray backgrounds as indicated by the legend (see Section 2.2.2). Strong X-rays reduce the critical mass of Halo 1 (red and orange) and moderate X-rays reduce that of Halo 2 and Halo 3 (green and yellow). On the other hand, strong LW backgrounds delay Pop III star formation in all haloes (triangles).

RAMSES version are shown in Appendix A.1. The H_2 formation rate is,

$$\frac{\mathrm{d}x_{\mathrm{H2}}}{\mathrm{d}t} = -C_{\mathrm{coll}} x_{\mathrm{H2}} - k_{\mathrm{photo}} x_{\mathrm{H2}} + R n_{\mathrm{HI}}, \tag{2.1}$$

where x_{H2} is the H_2 fraction, n_{HI} is the H I number density, C_{coll} is the collisional dissociation rate, k_{photo} is the photodissociation rate and R is the production rate. The term C_{coll} is the sum of the collisional dissociation rates of H_2 colliding with H, H_2, e^-, He and H^+ (Glover and Abel,

2008; Glover et al., 2010). Its definition is

$$C_{\rm coll} = \sum_{\rm i} k_{\rm coll,i} n_{\rm i} \tag{2.2}$$

where i means one of five chemical species ($\rm H$, $\rm He$, $\rm e^-$, $\rm H^+$ and $\rm H_2$). The term $k_{\rm coll,i}$ is the collisional dissociation rate for species i and $n_{\rm i}$ is its number density. The photodissociation rate is,

$$k_{\rm photo} = 4\pi \int_{\rm 11.2eV/h_P}^{\rm 13.6eV/h_P} \frac{\rm J_\nu}{h_{\rm P}\nu} \sigma_{\rm LW} {\rm d}\nu. \tag{2.3}$$

$h_{\rm P}$ is the Planck constant, $\rm J_\nu$ is the intensity and $\sigma_{\rm LW}$ is the effective cross-section,

$$\sigma_{\rm LW} = 2.47 \times 10^{-18} f_{\rm shd}\ {\rm cm}^2, \tag{2.4}$$

where $f_{\rm shd}$ is the shielding factor. To compute $f_{\rm shd}$, we adopt the formulae in Wolcott-Green and Haiman (2019):

$$\begin{aligned} f_{\rm shd} = & \frac{0.965}{(1+x/b_5)^{\alpha(n,T)}} \\ & + \frac{0.035}{(1+x)^{0.5}} \times \exp\left[-8.5 \times 10^{-4} (1+x)^{0.5}\right], \end{aligned} \tag{2.5}$$

where

$$\begin{aligned} \alpha(n,T) &= A_1(T) \times \exp\left(-0.2856 \times \log(n/{\rm cm}^{-3})\right) + A_2(T), \\ A_1(T) &= 0.8711 \times \log(T/{\rm K}) - 1.928, \\ A_2(T) &= -0.9639 \times \log(T/{\rm K}) + 3.892. \end{aligned} \tag{2.6}$$

Here, $x \equiv N_{\rm H2}/5 \times 10^{14}$ cm^2, where $N_{\rm H2}$ is the H_2 column density. One difference from the formula in Gnedin et al. (2009) is the Doppler broadening factor $b_5 = b/10^5$ cm s^{-1}. For each cell, the value of b is computed with $b = (b_{\rm turb}^2 + b_{\rm thermal}^2)^{1/2}$, where $b_{\rm turb} = 7.1 \times 10^5$ cm s^{-1} is the turbulent broadening factor (Krumholz, 2012) and $b_{\rm thermal} = (2k_{\rm B}T/m_{\rm H2})^{1/2}$ is the thermal broadening factor (Richings et al., 2014). For the latter, $m_{\rm H2}$ is the mass of an H_2 molecule, T is the temperature of the cell, and $k_{\rm B}$ is the Boltzmann constant. The rate of production of H_2 is,

$$R = \frac{k_1 k_2 x_{\rm e}}{k_2 + k_5 x_{\rm HII} + k_{13} x_{\rm e}} + (R_{3,1} n_{\rm HI} x_{\rm HI} + R_{3,2} n_{\rm H2} x_{\rm HI}), \tag{2.7}$$

where $x_{\rm HII}$ is the ionized H fraction, $x_{\rm e}$ is the electron fraction and $n_{\rm H2}$ is the H_2 number density. The first term on the right-hand side of the equation is the production rate through the H^- channel. In this work, contrary to the other species, we do not track the out-of-equilibrium H^- abundance, instead we calculate the equilibrium value using the four reaction rates of H^- formation (k_1, k_2, k_5 and k_{13} from Glover et al., 2010) as in Katz et al. (2017). At densities higher than 10^8 H cm^{-3}, the three-body interaction (the second term in equation (2.7)) is the dominant channel of H_2 formation. $R_{3,1}$ is the production rate from the reaction $3\,{\rm H} \longrightarrow {\rm H_2} + {\rm H}$ (Forrey, 2013) and $R_{3,2}$ is that from $2\,{\rm H} + {\rm H_2} \longrightarrow 2\,{\rm H_2}$ (Palla et al., 1983).

We make use of the results of Glover and Abel (2008) and Glover (2015) to calculate the gas cooling rate due to the collisions of H_2 with H, H_2, e^-, He and H^+. The low-density limit follows equation (37) and Table 8 of Glover and Abel (2008) and we adopt equation (30) of Glover (2015) to calculate the LTE limit. The rate of cooling by H_2 is,

$$\Lambda = \frac{\Lambda_{\rm H_2,LTE}}{1 + \Lambda_{\rm H_2,LTE}/\Lambda_{{\rm H_2},n\to 0}}, \tag{2.8}$$

where $\Lambda_{\rm H_2,LTE}$ is the LTE limit and $\Lambda_{\rm H_2,}n\to0$ is the low density limit.

At high density, H_2 line emission is trapped by the optically thick gas, so the cooling rate is affected by the escape probability of the radiation. The cooling rate is multiplied by the following factor.

$$\bar{f}_{\rm esc} = \frac{1}{(1+N_{\rm H2}/N_{\rm c})^{\alpha}}. \tag{2.9}$$

The equation and parameters ($N_{\rm c}$ and α) are defined in Fukushima et al. (2018).

2.2.2 Radiation Background and Secondary Photo-electrons from X-ray Ionization

In RAMSES, the ionization and heating by a radiation background can be calculated for redshifts $z < 15$ by reading a table of background spectra at different redshifts (Haardt and Madau, 2012). In this work, however, we are interested in the radiation background in the earlier Universe at $z \sim 30-15$, hence we must follow a different approach.

The evolution of the radiation background and Pop III star formation rate that produces it are regulated by feedback loops acting on cosmological scale (see, R16). In this study, however, we focus on the formation of Pop III stars in a single halo using zoom-in simulations. This prevents us from tracking the number of X-ray sources that contribute to the background. Moreover, the physics regulating the formation of possibly important X-ray sources in the early Universe (*e.g.*, HMXRBs, SN/HN, accreting IMBHs, miniquasars) is not well constrained, therefore the radiation background they build is somewhat uncertain. For this reason, we use a simple approach. We run a large grid of simulations for each halo, with different radiation background models. Each of the models consists of a LW ($11.2-13.6$ eV) band background, and a soft X-ray

($0.2 - 2.0$ keV) background. Other studies (HM15; Jeon et al., 2014a; Xu et al., 2016) focus on the role of HMXBs which emit harder X-ray photons ($1 - 10$ keV), but here we limit our interest to soft X-rays, mostly produced by accreting IMBHs and supernova/hypernovae explosions and remnants (R16). We assume that the specific intensity of the LW background ($J_{LW,21}$, in units of 10^{-21} erg s^{-1} cm^{-2} Hz^{-1} sr^{-1}) is constant with the frequency between $11.2 - 13.6$ eV, while the X-ray background is a power law with slope 1.5: $J_{X,21} = J_{X0,21}(E/E_0)^{-1.5}$, where $J_{X0,21}$ is the intensity at $E_0 = 200$ eV (Inayoshi and Omukai, 2011). For the sake of simplicity, we assume the intensity of the background is constant as a function of time in physical units (not comoving). However, note that X-ray feedback may change the number of X-ray sources (R16) and the accretion rate of gas onto an IMBH (Jeon et al., 2012), producing a time-dependent X-ray background. We explore a grid of $7 \times 7 = 49$ different combinations of LW and X-ray backgrounds: $J_{LW,21} = 0, 10^{-3}, 0.01, 0.1, 1, 10, 100$ and $J_{X0,21} = 0, 10^{-6}, 10^{-5}, 10^{-4}, 10^{-3}, 0.01, 0.1$. These models may represent radiation backgrounds with local and cosmological origins (Jeon et al. 2014a; HM15; R16; Regan et al. 2020). HM15 shows HMXBs can generate an X-ray background corresponding to our most intense case ($J_{X0,21} = 0.1$) and a LW background with $J_{LW,21} = 1$ may delay Pop III star formation until the atomic cooling regime (Regan et al., 2020). Throughout this paper, we categorize X-ray backgrounds with $J_{X0,21} \geq 10^{-3}$ as "strong" X-ray backgrounds. As a reference to previous works, $J_{X0,21} \sim 10^{-2}$ corresponds to the strong X-ray case in R16, in which Pop III star formation can be suppressed by IGM heating. A value $J_{X0,21} \sim 10^{-4}$ roughly corresponds to the fiducial scenario in R16, in which the number of Pop III stars is maximized, and it is also similar to the value of the X-ray background adopted by Xu et al. (2016). A sketch of the spectra is shown in Fig. 2.3.

If a high-energy X-ray photon ionizes a hydrogen atom, the resultant photo-electron also

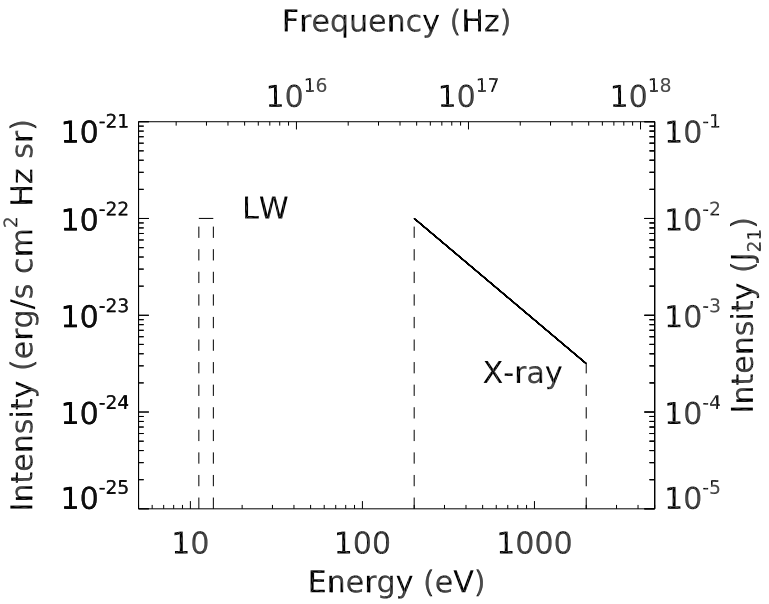

Figure 2.3: Spectra of LW and X-ray radiation background. The intensity in cgs unit and J are shown. The intensity of the LW background is constant and that of the X-ray background is proportional to $\nu^{-1.5}$ (Inayoshi and Omukai, 2011). We assume that ionizing UV photons (13.6 eV - 0.2 keV) cannot build a radiation background so the intensity in this range is zero. In this example, $\mathrm{J_{LW,21}} = 10^{-2}$ and $\mathrm{J_{X0,21}} = 10^{-2}$.

has large kinetic energy. This electron may produce secondary ionizations by colliding with other neutral hydrogen atoms or be thermalized and heat the gas by colliding with other electrons. We model the secondary ionization/heating following Shull and van Steenberg (1985) and Ricotti et al. (2002a). The ionization rate of species i is:

$$\begin{aligned} -\frac{\mathrm{d}x_\mathrm{i}}{\mathrm{d}t} &= x_\mathrm{i}\zeta^\mathrm{i} + \sum_{\mathrm{j=H\ I,He\ I}} \frac{n_\mathrm{j}}{n_\mathrm{i,tot}} \zeta^\mathrm{j} \left\langle \Phi^\mathrm{i}(E_0^\mathrm{j}, x_\mathrm{e}) \right\rangle , \\ &= (1 + f_\mathrm{ion,i})\zeta^\mathrm{i}, \end{aligned} \tag{2.10}$$

where $f_\mathrm{ion,i}$ is the secondary ionization fraction of species i, $E_0^\mathrm{i} = h_\mathrm{P}\nu - I_\mathrm{i}$ is the photo-electron energy and $\left\langle \Phi^\mathrm{i}(E_0^\mathrm{j}, x_\mathrm{e}) \right\rangle$ is the average number of secondary ionization per primary electron of

species j (see Ricotti et al., 2002a). $I_{\rm i}$ is the ionization potential and $\zeta^{\rm i}$ is the photo-ionization rate

$$\zeta_{\rm i} = 4\pi \int_{I_{\rm i}/h_{\rm P}}^{\infty} \frac{{\rm J}_\nu}{h_{\rm P}\nu}\, \sigma_{\rm i}\, d\nu, \tag{2.11}$$

where $\sigma_{\rm i}$ is the ionization cross-section of i (Verner et al., 1996). The rate of heating due to species i is

$$\begin{aligned} \frac{{\rm d}e}{{\rm d}t} &= 4\pi \int_{I_{\rm i}/h_{\rm P}}^{\infty} \frac{{\rm J}_\nu}{h_{\rm P}\nu}\, \sigma_{\rm i} E_{\rm h}(E_0^{\rm i}, x_{\rm e})\, d\nu \\ &= f_{\rm heat,i}\Gamma_{\rm i}. \end{aligned} \tag{2.12}$$

where e is the internal energy. A fraction of the energy of photo-electrons is used to ionize the gas and therefore the heating of the gas is less efficient (Ricotti et al., 2002a). This effect is considered with the factor $E_{\rm h}(E_0^{\rm i}, x_{\rm e})$. The photoheating rate neglecting secondary photo-electron ionization is

$$\Gamma_{\rm i} = 4\pi \int_{I_{\rm i}/h_{\rm P}}^{\infty} \frac{{\rm J}_\nu}{h_{\rm P}\nu}(h_{\rm P}\nu - I_{\rm i})\, \sigma_{\rm i}\, d\nu. \tag{2.13}$$

The secondary ionization fraction $f_{\rm ion,i}$ is large (*e.g.* $f_{\rm ion,H\ I} \sim 17.3$) when the gas is almost neutral and its value converges to zero with increasing $x_{\rm e}$. On the contrary, the heating fraction $f_{\rm heat,i}$ is low in a neutral gas (close to 0.1) and converges to 1 with increasing $x_{\rm e}$. This can be understood as in a neutral gas (low $x_{\rm e}$), most of the photo-electrons collide with neutral hydrogen and ionize the gas, while in a highly ionized gas, photo-electrons collide with other electrons and thermalize.

2.2.3 Tracking Clumps

We impose that the Jeans length is resolved with at least $N_{\rm J} = 16$ cells up to the maximum AMR level near the halo centre. Once the maximum level is reached, however, we cannot refine them further. In order to prevent artificial fragmentation at the maximum refinement level caused by a decreasing Jeans length, we suppress the cooling of cells with the maximum refinement level following the method in Hosokawa et al. (2016). This is done by multiplying the cooling function by the factor

$$C_{\rm limit} = \exp\left[-\left(\frac{\xi - 1}{0.1}\right)^2\right] \quad (\text{if } \xi > 1), \tag{2.14}$$

where $\xi = f_{\rm limit}(\Delta x/\lambda_{\rm J})$ with the cell size Δx and Jeans length $\lambda_{\rm J}$. We assume $f_{\rm limit} = 12$ as in Hosokawa et al. (2016).

To investigate the growths of protostars and the initial mass function, many studies employ sink particles/cells and calculate the gas accretion onto and radiative feedback from them (*e.g.*, HR15; Sugimura et al., 2020, hereafter S20). In this study, we do not use sink particles, hence we neglect accretion and feedback physics associated with them. Our goal is to perform many simulations for various external radiation backgrounds to capture the effects of X-rays on the collapse and fragmentation. Instead of using sink particles, we flag cells with $C_{\rm limit} < 10^{-4}$ in each run. Using a friends-of-friends algorithm, we link neighboring cells together to identify dense clumps. Each clump represents a quasi-hydrostatic core that would collapse to form a star if we did not impose limitations on the cooling rate and the resolution. Throughout this article, we use each clump as a proxy for a single Pop III star.

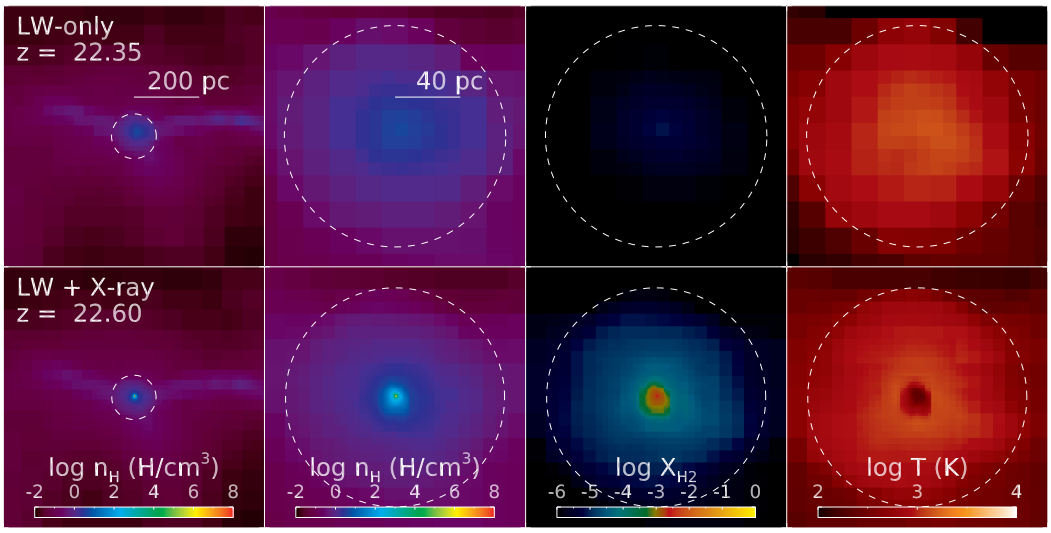

Figure 2.4: Halo 2 in a LW-only simulation (the top panels) and one including X-ray effects (the bottom panels). The first two columns show the hydrogen number density at different scales (shown in the top panels). The third and forth panels show the H_2 fraction and gas temperature, respectively (the scale is the same as in the second panel from the left). The intensity of the LW radiation is the same in both simulations ($J_{LW,21} = 10^{-1}$). The intensities of X-ray backgrounds are $J_{X0,21} = 0$ and 10^{-4}, respectively. The white circle indicates the virial radius of the halo. When irradiated by a moderate X-ray background, the gas core in the halo has a higher H_2 fraction (third column) and can cool to a lower temperature (fourth column). Hence the gas in the X-ray irradiated halo can collapse to a higher density than the case with the same LW background but without X-rays (second column), allowing the formation of Pop III stars.

2.3 Results - I. Critical Minihalo Mass for Pop III Formation

In a gas of primordial composition, the formation of H_2 is inefficient in minihaloes below a critical mass due to the low electron fraction produced by collisional ionization during virialization (Tegmark et al., 1997). However, pristine gas can cool more efficiently, even in small mass minihaloes, if an X-ray radiation background enhances the electron fraction. Fig. 2.4 demonstrates the effectiveness of the X-ray background in promoting Pop III star formation. When the halo is irradiated by a constant (as a function of time) LW background (top panels), the maximum gas density in the minihalo at redshift $z = 22.6$ is below 10 H cm^{-3}, and the gas collapses to form a dense core at $z \sim 16.5$, when the mass of the minihalo is 1.6×10^6 $M_\odot$. If the halo is

exposed to the same LW background but also an X-ray background (bottom panels), the gas at the halo centre cools efficiently (the right panels shows the temperature) thanks to the enhanced H_2 fraction (see the third panel from the left). The cooling enables the formation of a dense core at $z = 22.6$, when the halo mass is $\sim 1.5 \times 10^5$ $M_\odot$, a critical mass about ten times lower than the case without X-ray irradiation.

To quantify the effect of the X-ray background we define the critical mass as the mass of a minihalo at the redshift when the Pop III star forms. To this end, we define the parameter z_α, that is the redshift at which the central gas density reaches 10^α H cm^{-3}. For example, if the central gas density reaches 10^1 H cm^{-3} at $z = 25$ and 10^8 H cm^{-3} at $z = 23$, $z_1 = 25$ and $z_8 = 23$, respectively. In this section, we assume that Pop III stars form at z_{10}. From the time of formation of the protostellar core, it takes roughly $10^4 - 10^5$ years for feedback to halt gas accretion and reach the final Pop III star mass (S20). This time scale is much shorter than the typical variations of the formation time caused by different intensities of the LW or X-ray radiation backgrounds. The later phases of evolution of the gas ($n_{\rm H} > 10^{10}$ H cm^{-3}), when a protostellar disc is formed, are discussed later in Section 2.4 and Paper II (Chapter 3).

The three panels in Fig. 2.5 show z_1, z_3 and z_{10}, respectively, for Halo 1 for the 7×7 grid of radiation backgrounds. The middle and right panels are nearly identical, meaning that once the gas reaches a density above 10^3 H cm^{-3}, for the range of backgrounds considered here, the collapse cannot be halted and proceeds rapidly to densities $\sim 10^{10}$ H cm^{-3}. The panel on the left shows that the gas density reaches 10 H cm^{-3} by $z \sim 24$ for any value of the LW background unless the X-ray intensity is larger than $J_{\rm X0,21} > 10^{-3}$ and $J_{\rm LW,21} > 10$. This is because the core gas density of Halo 1 at virialization is ~ 10 H cm^{-3} even without any core contraction due to gas cooling (see Ricotti, 2009, for the calculation of the core gas density assuming an isothermal

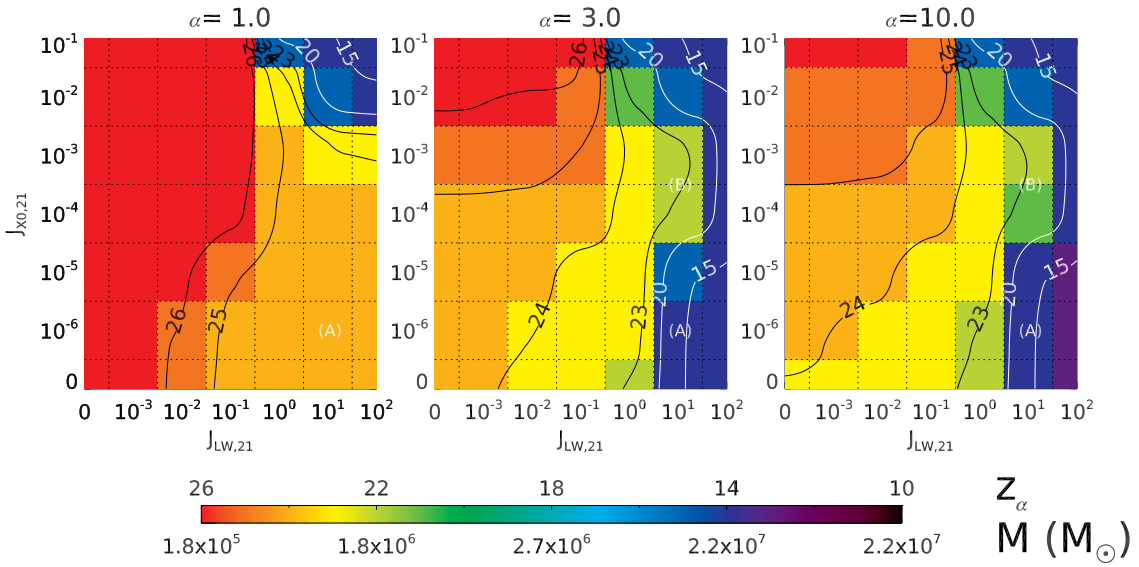

Figure 2.5: Redshift of collapse (z_α) to a density 10^α for Halo 1 as a function of $\mathrm{J_{LW,21}}$ and $\mathrm{J_{X0,21}}$. From left to right, α is 1, 3 and 10. The smoothed iso-contours for $z_\alpha = 15$, 20, 23, 24, 25, and 26 are drawn on the top of the color map. Under the color bar, the mass of the halo at a particular redshift is shown. The locations in each panel marked by letter labels are used for a more detailed explanation of the results in the text. The center and right panels show that X-rays have net positive feedback in the sense of anticipating the formation of Pop III stars (and hence reducing the critical halo mass for star formation) and generally counteracting the negative feedback effect of a strong LW radiation background. The effect in reducing the critical mass is most pronounced in a weak or moderate LW background ($\mathrm{J_{LW,21}} \leq 10^{-1}$) with strong X-ray irradiation ($\mathrm{J_{X0,21}} \geq 10^{-3}$).

equation of state and $T \approx T_{\rm vir}$). Therefore z_1 is always reached by Halo 1 unless the X-ray background is strong enough ($\mathrm{J_{X0,21}} > 10^{-3}$) to heat the IGM to $T_{\rm IGM} > T_{\rm vir}$ and cooling from H_2 formation (that is increased by X-ray photo-ionization) does not offset significantly the X-ray heating ($\mathrm{J_{LW,21}} > 10$).

Let's now focus on the right panel, showing the redshift of Pop III star formation. In a zero background (the bottom left corner), the Pop III star forms at $z \sim 24$ when the halo mass is $\sim 7 \times 10^5$ $\mathrm{M_\odot}$. Increasing the LW background intensity to $\mathrm{J_{LW,21}} \sim 10$ delays Pop III formation to $z \sim 14$ when the halo mass exceeds 2×10^7 $\mathrm{M_\odot}$ (label A). The figure also shows that z_{10} increases and the critical mass decreases, with increasing X-ray intensity. This is consistent with

HM15 which also finds an earlier onset of gas collapse in an X-ray background. We find that the X-ray background is particularly effective in offsetting the negative feedback effect of a strong LW background. In a weak X-ray background, LW intensity $J_{LW,21} \sim 10$ delays the formation of Pop III stars to $z \sim 14$ (label A in the figure), but if an X-ray background $J_{X0,21} \sim 10^{-4} - 10^{-3}$ is present, the central gas can collapse to form Pop III stars at $z \sim 22$ (label B) when the mass of the halo is below 1.8×10^6 $M_\odot$. Compared to 2×10^7 $M_\odot$ at $z \sim 14$, this is a reduction of the critical mass by one order of magnitude. In a cosmological context, a reduction of the critical mass by an order of magnitude implies that the number of minihaloes that are able to form Pop III stars will increase by roughly the same factor. As a side note, Regan et al. (2020) found that LW radiation backgrounds with $J_{LW,21} \sim 0.1 - 10$ suppresses the formation of Pop III stars and allows direct-collapse-black holes to form in atomic cooling haloes (with mass $> 10^8$ $M_\odot$). Our results suggest that a strong X-ray background may offset this effect enabling Pop III star formation even in a strong LW background.

Fig. 2.6 shows the same results as Fig. 2.5, but for Halo 2 and Halo 3, respectively. At all redshifts, Halo 2 is smaller in mass than Halo 1, and Halo 3 is the smallest halo (see Fig. 2.2). The results for these two haloes are qualitatively similar to Halo 1, with some quantitative differences explained below. For these smaller mass haloes, when both the LW and X-ray intensity are large, the gas density fails to reach 10 H cm^{-3} (label A in the figure). This is because, due to their lower masses and virial temperatures, the core densities of these haloes at virialization are $<$ 10 H cm^{-3}, hence sufficiently rapid cooling is necessary to reach that density. A LW background $J_{LW,21} \geq 10^{-1}$ is sufficient to suppress cooling and prevent the gas from reaching 10 H cm^{-3} before $z \sim 16$. The collapse of gas to higher densities (from $\alpha = 3$ to 10) follows the same trend as that of Halo 1. An increase in the LW intensity suppresses the formation of H_2 and

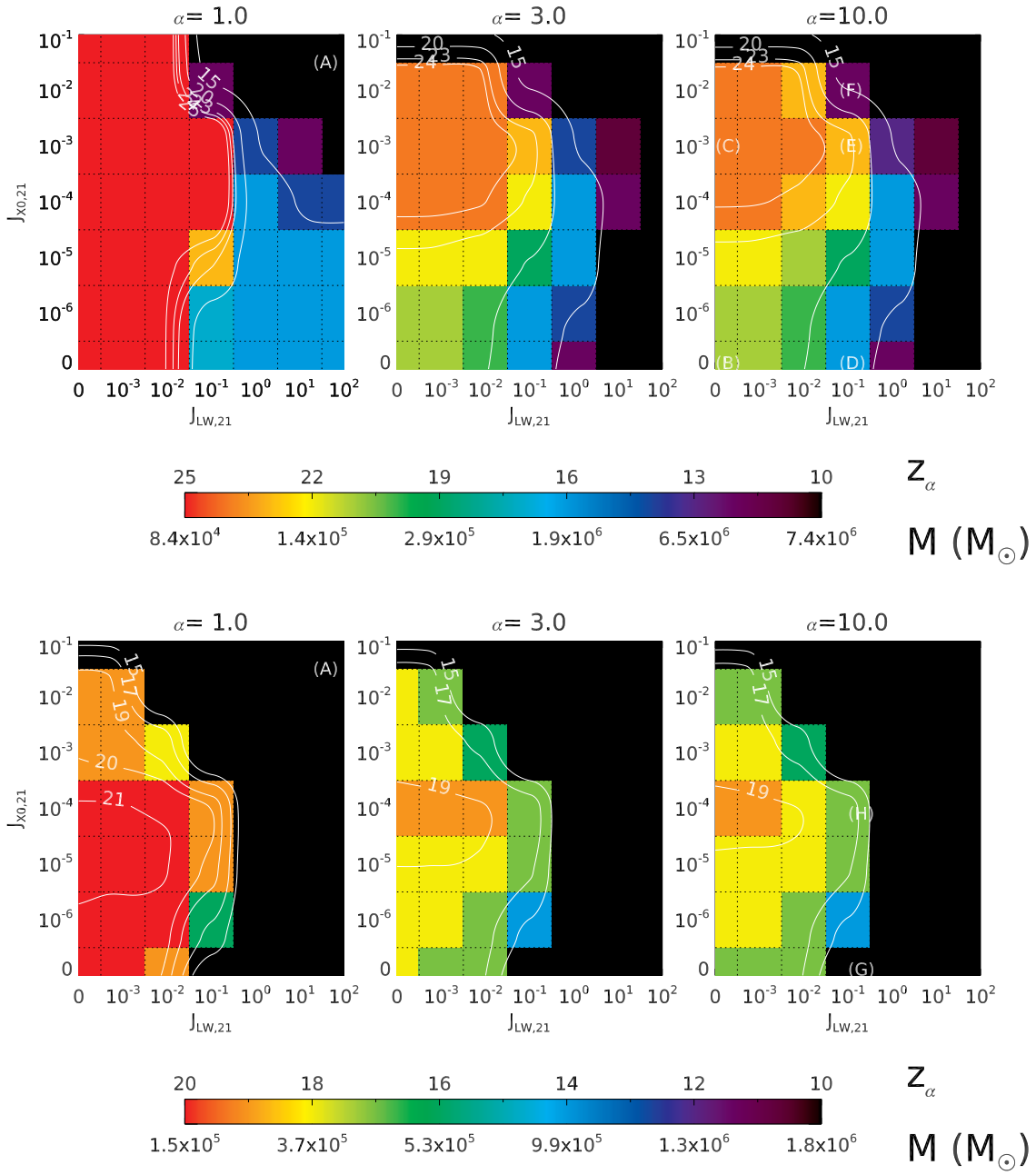

Figure 2.6: Redshift of collapse z_α to density 10^α for Halo 2 (top panels) and Halo 3 (bottom panels). The meaning of the labels and contour plots is the same as in Fig. 2.5. Note that for Halo 3 the iso-contour lines are at $z = 15, 17, 19, 20$, and 21. Unlike the case of Halo 1, that has the largest mass among our simulated haloes, here positive feedback from X-rays is most significant for moderate X-ray irradiation, at $\mathrm{J_{X0,21}} \sim 10^{-4} - 10^{-3}$, because for strong X-ray irradiation the heating of IGM prevents the gas from condensing in these smaller mass haloes.

delays Pop III star formation. Compared to Halo 1, however, a significant delay of Pop III star formation occurs for a weaker LW radiation background. For instance, z_{10} of Halo 1 decreases dramatically between $\mathrm{J_{LW,21}} = 1$ and 10 while this occurs between $\mathrm{J_{LW,21}} = 0.1$ and 1 for Halo 2 and $\mathrm{J_{LW,21}} = 0.01$ and 0.1 for Halo 3. In a strong LW background, Pop III stars fail to form before $z \sim 13$ ($z \sim 10$) for Halo 2 (Halo 3).

The positive feedback by an X-ray background is also observed in Halo 2 and Halo 3. Without any LW or X-ray radiation backgrounds $z_{10} = 21.27$ (18) in Halo 2 (Halo 3) and the critical mass is $\sim 1.5 \times 10^5$ $\mathrm{M_\odot}$ (location B). In a strong X-ray background ($\mathrm{J_{X0,21}} = 10^{-3}$, location C), $z_{10} = 24.6$ (~ 31 Myr earlier) in Halo 2 and the critical mass decreases to 9.5×10^4 $\mathrm{M_\odot}$ (while it decreases by a factor of ~ 3 for Halo 3). When LW radiation is stronger ($\mathrm{J_{LW,21}} \sim 0.1$), the effect of X-rays becomes more pronounced: in Halo 3 Pop III star does not form without X-ray irradiation (location G) and in Halo 2 the critical mass is 1.6×10^6 $\mathrm{M_\odot}$ ($z_{10} = 16.50$, location D). Adding X-ray radiation (location E and H), the critical mass is lower by more than a factor of 10 for Halo 2 (1.2×10^5 $\mathrm{M_\odot}$, $z_{10} = 23.11$) and is about $\sim 3.0 \times 10^5 - 10^6$ $\mathrm{M_\odot}$ for Halo 3.

If the X-ray intensity increases further, however, the heating of the IGM becomes the dominant feedback mechanism, suppressing the formation of Pop III star as in the analytic models of R16. Increasing the X-ray intensity by a factor of 10 (location F) suppresses gas collapse and Pop III star formation does not occur until $z = 12.60$ when the halo mass is 6.6×10^6 $\mathrm{M_\odot}$. If $\mathrm{J_{X0,21}} = 0.1$, the heating by a radiation background shuts down gas collapse completely and the formation of a Pop III star is suppressed until $z = 10$.

In all the haloes the reduction of the critical minihalo mass produced by an increasing X-ray background is largest in an intense LW background. This can be readily understood because

no matter how strong is the boosting of H_2 formation by X-rays, there is a floor to the lowest critical mass, that is dictated by the inefficient cooling rate of H_2 in gas with temperature below $\sim 100 - 200$ K. Hence, virialized gas in minihaloes with $T_{\rm vir} < 100 - 200$ K cannot cool rapidly even if the gas has high molecular fraction. A rough estimate of this floor critical mass of DM minihaloes is,

$$M_{\rm cr}({\rm min}) \approx 10^5 \, {\rm M}_\odot \left(\frac{1+z_{\rm vir}}{20} \right)^{-3/2}, \tag{2.15}$$

where we have assume $T_{\rm vir} = 200$ K. This limiting minimum mass could be significantly reduced by HD cooling, which is neglected in our work.

In order to better understand the common qualitative features described above for the three haloes, in Fig. 2.7 we show a sketch of the region on the grid in which Pop III stars can form. The sketch on the left is based on the analytical model in R16, while the sketch on the right illustrates the results of this study based on hydrodynamical simulations.

When an X-ray background is intense (top line in the sketch), gas photo-heating is the dominant feedback process. In this case, the temperature of the IGM ($T_{\rm IGM}$) and the halo virial temperature ($T_{\rm vir}$) determine the formation of Pop III stars. If $T_{\rm vir} < T_{\rm IGM}$ the gas in the halo cannot collapse until the halo mass grows enough and $T_{\rm vir}$ exceeds $T_{\rm IGM}$. R16 assumed that only haloes with $T_{\rm vir} > T_{\rm IGM}$ can form Pop III stars and this is represented as a horizontal line in the left panel. In the hydrodynamics simulations, however, the formation of Pop III stars in strong X-ray radiation shows a dependence on the intensity of the LW radiation and thus this line is slanted. We speculate that this is due to the additional cooling by H_2 in the absence of a strong LW background. The position of the line on the diagram is shifted upward (to higher $J_{\rm X0,21}$) if the halo is more massive and has a higher virial temperature.

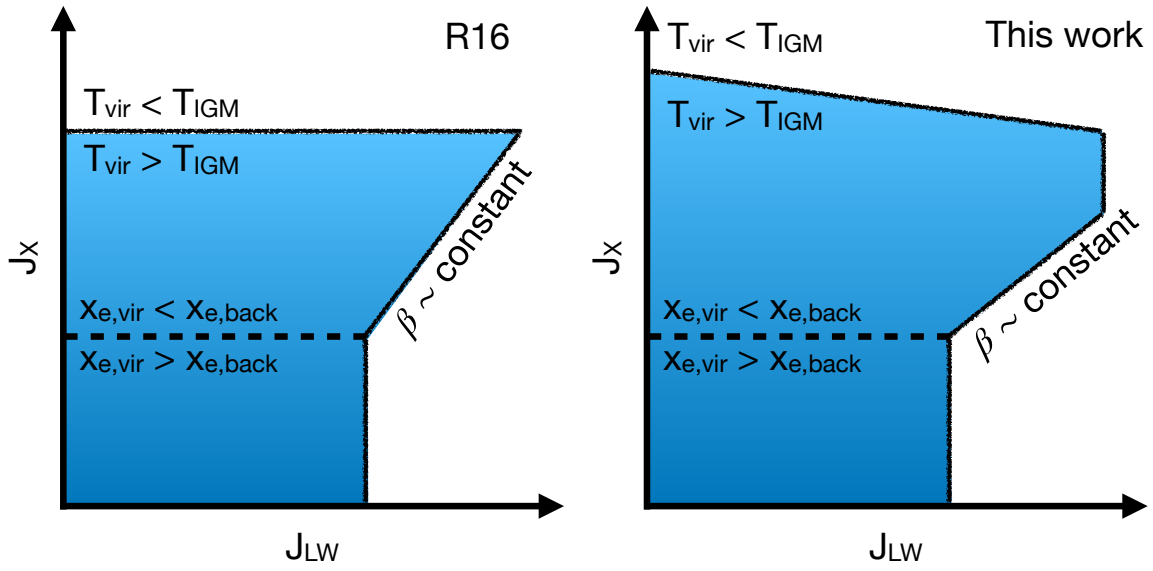

Figure 2.7: Schematic diagrams of Fig. 2.5 and 2.6. The colored regions represent the region on the grid where the formation of Pop III is allowed. The left panel shows the region expected by the model in R16, and the right one simplifies the trend of our simulations. $T_{\rm vir}$ and $T_{\rm IGM}$ indicate the temperatures of a virialized halo and the IGM, respectively. $x_{\rm e,vir}$ is the electron fraction of the halo in the absence of an X-ray background and $x_{\rm e,back}$ is the fraction of electrons due to additional ionization by the X-ray background radiation. The parameter β, related to the mean spectral energy distribution of the first sources of light, is the ratio of the integrated energy in the X-ray band and the LW band (see R16).

The lower part of the diagram can be understood considering the degree of X-ray ionization and H_2 formation. If the X-ray radiation is weak (below the dashed line) the fraction of electrons produced by X-ray photoionization ($x_{\rm e,back}$) is lower than the residual electron fraction from the epoch of recombination and the electron fraction produced by collisional ionization in the virialized halo ($x_{\rm e,vir}$). In this region the positive feedback by the X-ray background is negligible. The position of the line is mostly determined by the growth rate of the halo. Halo 1, that grows quickly and becomes more massive than the other two, has higher virial temperature and thus higher collisional ionization rate. In addition, the halo is irradiated for a shorter period of time before the formation of Pop III stars. Therefore, the intensity of the X-ray background must be higher ($\rm J_{X0,21} \sim 10^{-5}$ for Halo 1, see Fig. 2.5) to increase sufficiently $x_{\rm e,back}$ and have an

influence on the critical mass of the halo. On the other hand, the position of the dashed line is lower for Halo 2 and 3 ($J_{X0,21} \sim 10^{-6}$, Fig. 2.6) because they are irradiated by X-rays for a longer time, hence weaker X-ray background is sufficient to produce $x_{e,back} > x_{e,vir}$.

Above the dashed line the X-ray photoionization is the dominant positive feedback. In this region of the parameter space, the increased H_2 fraction from X-ray ionization compensates for the H_2 dissociation by the LW background, making the formation of Pop III stars possible in a stronger LW background. The slanted line on the right side of the region shows this trend. The slope of the isocontour lines in this region is roughly linear: $J_{X0,21} \propto J_{LW,21}$. This can be understood in the context of the R16 model in which the critical mass was found to depend on the parameter β, that is the ratio of the energies in two energy bins in the mean spectrum of the sources $\beta \equiv E_X/E_{LW} \sim J_X/J_{LW}$.

In conclusion, considering the finite sampling in the $J_{LW,21} - J_{X0,21}$ plane due to the limited number of simulations in this work, our results are in good qualitative agreement with the analytic model in R16, although the simulations show that the R16 model neglects some physical processes that are important when the X-ray irradiation is strong, and/or when minihalo masses grow rapidly. In the absence of radiation backgrounds, the critical halo mass we find is in agreement with R16 (about 10^6 $M_\odot$). We note that in R16 the smallest mass halo in which Pop III stars can form is $\sim 3 \times 10^4$ $M_\odot$, obtained when a strong X-ray irradiation is considered at very high redshift. In this work we find a minimum mass about three times larger ($\sim 10^5$ $M_\odot$). This is in agreement with the estimate of the minimum critical mass in equation (2.15), given that the analytical work considers also very rare haloes forming at $z > 30$.

2.4 Results: II. Total Mass in Pop III Stars

Our simulations follow the formation of protostars for $5 \times 10^4 - 10^5$ years after the time of formation, defined here when the core density reaches $\sim 10^{10} - 10^{11}$ H cm^{-3}. However, we neglect radiation feedback from the accreting protostars that can dissociate H_2 (FUV radiation) and produce winds powered by photo-heating from hydrogen and helium ionization. Therefore the masses of the Pop III stars at the end of our simulations are (in most cases) overestimated and provide an upper limit to the Pop III mass. Without radiation feedback, the masses of the Pop III stars grow at a nearly constant rate from the time of formation. Radiation feedback is expected to both reduce the accretion rate and halt the accretion after $\sim 2 \times 10^4$ years (see S20).

In order to estimate the effect of radiation feedback in reducing the final masses of Pop III stars, we use an empirical relationship based on previous work by HR15 that includes UV radiation feedback. HR15 provides a relation between the final mass of Pop III star and the accretion rate onto the protostellar core

$$M_{\rm final} = 250\ {\rm M}_\odot \left(\frac{{\rm d}M/{\rm d}t|_{\rm cr}}{2.8 \times 10^{-3}\ {\rm M}_\odot\ {\rm yr}^{-1}} \right)^{0.7}, \tag{2.16}$$

where $M_{\rm final}$ is the final mass and ${\rm d}M/{\rm d}t|_{\rm cr}$ is the accretion rate at the characteristic radius. We define the characteristic radius consistently with the definition in HR15: when the central gas density reaches 10^7 H cm^{-3}, we compute the enclosed mass ($M_{\rm enc}(r)$) and the Bonnor-Ebert mass (Ebert, 1955; Bonnor, 1956) as a function of the radius, r:

$$M_{\rm BE}(r) \approx 1050\ {\rm M}_\odot \left(\frac{T}{200\ {\rm K}} \right)^{3/2} \left(\frac{\mu}{1.22} \right)^{-2} \left(\frac{n_{\rm H}}{10^4\ {\rm cm}^{-3}} \right)^{-1/2} \left(\frac{\gamma}{1.66} \right)^{2}, \tag{2.17}$$

defined as in equation (12) in Hirano et al. (2014). Here, μ is the mean molecular weight and $\gamma = 5/3$ is the adiabatic index. The characteristic radius where we estimate the accretion rate is defined where $M_{\rm enc}(r)/M_{\rm BE}(r)$ reaches its maximum value.

Fig. 2.8 shows various gas properties of Halo 1 when the central density reaches 10^7 H cm^{-3} for simulations with different values of $\rm J_{X0,21}$ (see legend). All the panels show spherically averaged quantities. Panel (a) shows that the gas density profile follows the self-similar solution of Larson (1969) and Penston (1969), as shown also in Omukai and Nishi (1998). In Panel (b) the H_2 fraction profiles are shown. We can see that the H_2 fraction increases with the intensity of the X-ray background. This is due to the enhanced H^- abundance produced by the increased fractional ionization of the gas ($x_{\rm e}$) from direct X-ray ionization and secondary ionization from fast photo-electrons. Panel (c) shows the effective equation of state (T as a function of $n_{\rm H}$ for the collapsing gas obtained by matching the radial density and temperature profiles). As the X-ray intensity increases, the temperature of the gas at each given density decreases. Due to the self-similarity of the collapse, the temperature shown here also represents the temperature evolution of the gas core as a function of time as the core reaches higher densities. The temperature at the lower density is the virial temperature that depends on the halo mass and the redshift. The symbols mark the minimum temperatures ($T_{\rm min}$), roughly reached at the end of the initial free-fall phase when the core gas density is $n_{\rm H} \sim 10^4$ H cm^{-3} (Bromm et al., 2002). The minimum temperature shows a correlation with the X-ray intensity: the stronger the X-ray intensity, the lower the temperature (see also the left panel of Fig. 2.9). This result may appear counterintuitive as X-ray irradiation typically leads to enhanced heating rather than cooling. Instead, we find that, unless the X-ray irradiation is so strong to suppress collapse and Pop III star formation, the enhanced H_2 abundance and cooling rate dominates over the X-ray heating rate. This is the key

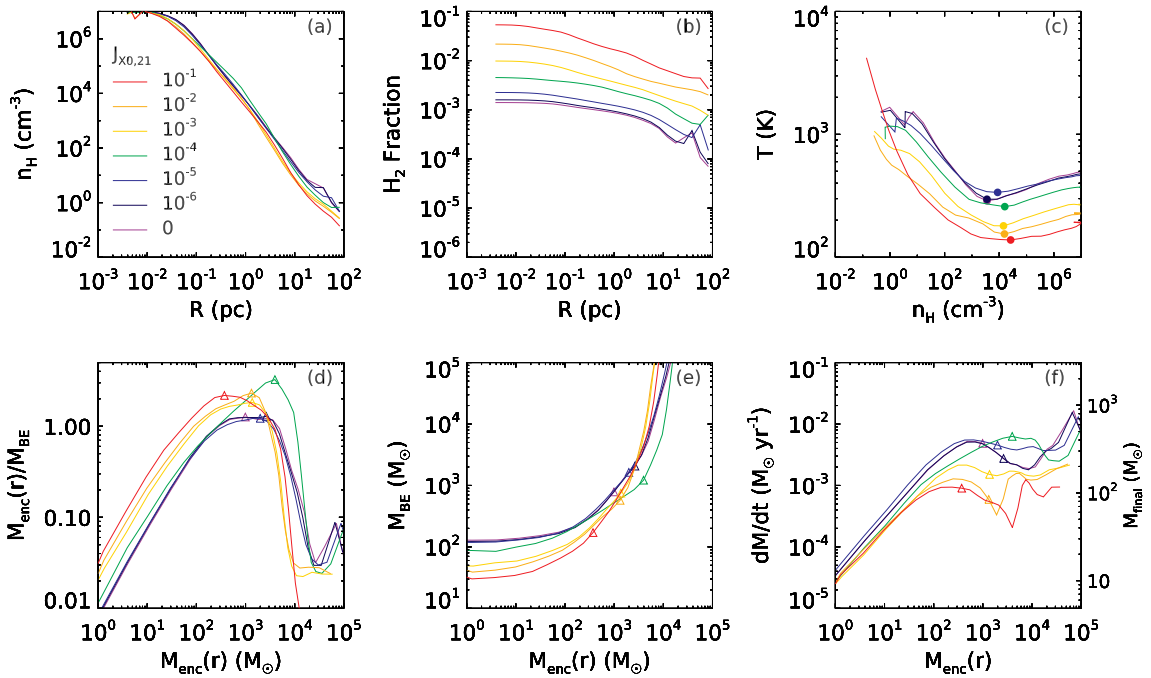

Figure 2.8: Properties of the gas in Halo 1 within 100 pc at the time when the central density reaches 10^7 H cm^{-3}. The solid lines in each panel show simulations with different X-ray intensities $J_{X0,21}$, color-coded as in the legend. The LW intensity in these simulations is zero. Panel (a): The gas density profile, n_H, as a function of the distance from the halo centre, R. The shapes of the profiles are consistent with isothermal sphere profiles, but the density is generally reduced in a strong X-ray background. Panel (b): The H_2 fraction profile as a function of R. X-rays increase the H_2 fraction at all radii. Panel (c): The gas phase diagram constructed from the temperature and density profiles. The circles show density where the gas reaches its minimum temperature. The overall temperature profile and the minimum temperature decrease with increasing X-ray irradiation due to the enhanced cooling rate produced by the increase of the molecular fraction [see panel (b)]. Panel (d): The ratio of the enclosed mass to the Bonnor-Ebert mass as a function of the enclosed mass. Each peak defines the characteristic radius of the quasi-hydrostatic core and it is marked by a triangle. We use the same symbols in Panel (e) and (f) to show the characteristic radii. The enclosed mass within the core (marked by the triangle) is generally lower with increasing X-ray intensity, although for this halo there is an exception (green line). Panel (e): The Bonnor-Ebert mass versus the enclosed mass. Panel (f): The rate of gas accretion (the left axis) and the corresponding final mass (using equation (2.16)). The symbols indicate the accretion rate at the characteristic radii and define the final mass of Pop III stars. The accretion rate and the final mass of Pop III stars are reduced by X-ray radiation.

physical result that will allow us to interpret most aspects of the simulation results.

In Panel (d), we plot the ratio of the enclosed mass to the Bonnor-Ebert mass. At radii where the enclosed mass is greater than $M_{\rm BE}$, we find a collapsing core. Vice versa, at radii larger than the collapsing core, thermal pressure supports the gas against collapse. Following Hirano et al. (2014), we define the peak value of $M(r)/M_{\rm BE}$ as the characteristic core radius in each simulation (marked as triangles). In Panel (e), we plot the Bonnor-Ebert mass as a function of the enclosed mass. In general, for higher X-ray intensity $M_{\rm BE}$ at the characteristic radius is smaller. Hence, X-ray irradiation reduces the mass of the collapsing core and other properties determined by it (such as the accretion rate). Panel (f) shows the gas accretion rate and the final Pop III star mass estimated using equation (2.16). Although we show $\mathrm{d}M/\mathrm{d}t$ at all radii, only the value of $M_{\rm final}$ at the characteristic core radius (marked by a triangle) is meaningful. With increasing X-ray intensity, the accretion rate decreases and the core becomes smaller in mass. The expected final Pop III mass is also lower due to the lower accretion rate. This result is consistent with HM15 in that, in an X-ray background, enhanced H_2 fraction provides efficient cooling and enables smaller gas clouds to collapse.

Although the general trend with X-ray intensity is clear and monotonic, exceptions are observed. In the simulation with $\mathrm{J}_{\mathrm{X0,21}} = 10^{-4}$ (green lines), the gas shows a higher than expected accretion rate. We find that another halo is within the virial radius of Halo 1 (~ 100 pc) when the dense core forms. At this time a strong radial inflow of gas develops within a few parsecs from the halo centre which accounts for the higher accretion rates seen in Fig. 2.8. We speculate that an interaction between two haloes triggers the strong gas inflow but we do not discuss this further as it is beyond the scope of this work.

To summarize, $T_{\rm min}$ in panel (c) is a key property to estimate the characteristic mass of

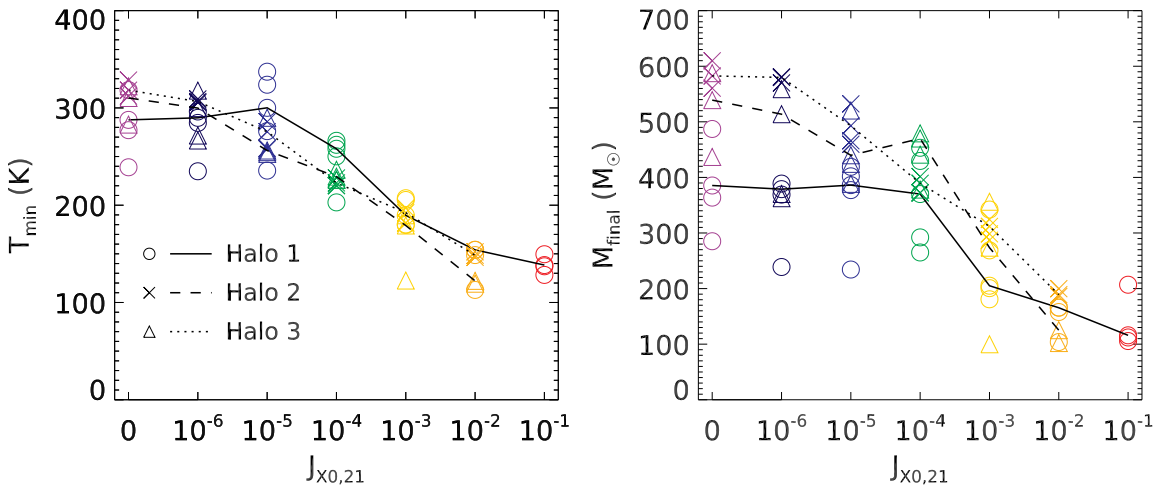

Figure 2.9: Left: Minimum gas temperature, $T_{\rm min}$, as a function of X-ray intensity $\rm J_{X0,21}$. The X-ray intensity is also color-coded as in Fig. 2.8. We distinguish different host haloes with different symbols (see legend). To illustrate the results for different haloes more clearly, we plot trend lines connecting median values for each halo (different line styles as in the legend). Right: Same as the left panel, but showing $M_{\rm final}$ as a function of $\rm J_{X0,21}$. The value of $T_{\rm min}$, that is related to accretion rate on the protostellar core, and the final total mass in Pop III stars decrease with increasing X-ray irradiation.

Pop III star and $T_{\rm min}$ is directly related to the X-ray intensity $\rm J_{X0,21}$. In Fig. 2.9 we provide $T_{\rm min}$ and the final Pop III star mass $M_{\rm final}$, as a function of the X-ray intensity $\rm J_{X0,21}$. Note that the relationship between $T_{\rm min}$ and $\rm J_{X0,21}$ depends on the assumed X-ray spectrum of the sources and the duration of the X-ray irradiation of the halo (hence the time dependence of $\rm J_{X0,21}$ and the growth rate of the minihalo mass). In this paper, we have used a relatively soft power-law spectrum, but if the dominant sources of X-rays are HMXBs the spectrum is expected to be harder. Although the three haloes are different in mass and redshift of Pop III star formation, the figure shows the general trend of a decreasing $T_{\rm min}$ and $M_{\rm final}$ with increasing X-ray intensity. However, Halo 1 (solid lines) deviates from this trend in a weak X-ray background ($\rm J_{X0,21} \lesssim 10^{-5}$), showing a roughly constant $T_{\rm min}$. This is consistent with the discussion in Section 2.3. A bigger halo has higher collisional ionization rate and is irradiated for a shorter period of time

before forming Pop III stars. For these reasons, the threshold of the positive X-ray feedback is higher (dashed lines in Fig. 2.7).

The accretion rate at the critical radius can be estimated analytically (Hirano et al., 2014) assuming spherical symmetry and simple dimensional analysis: $\mathrm{d}M/\mathrm{d}t \sim M_{\rm J}/t_{\rm ff}$, where $M_{\rm J} = (4\pi/3)\rho(c_{\rm s}t_{\rm ff})^3$ is the Jeans mass of the quasi-hydrostatic core at temperature $T_{\rm min}$ and $t_{\rm ff} = 1/\sqrt{G\rho}$ is the free-fall time. Hence,

$$\frac{\mathrm{d}M}{\mathrm{d}t} \sim 3.4 \times 10^{-3}\ \mathrm{M_\odot\ yr^{-1}} \left(\frac{T_{\rm min}}{200\ \mathrm{K}}\right)^{3/2} \left(\frac{\mu}{1.22}\right)^{-3/2}, \tag{2.18}$$

showing that the accretion rate depends only on the gas sound speed or temperature of the collapsing core. Since the gas is nearly neutral ($\mu = 1.22$), using equation (2.16) we obtain the relationship between $T_{\rm min}$ and the final Pop III mass:

$$M_{\rm final} = 287\ \mathrm{M_\odot} \left(\frac{T_{\rm min}}{200\ \mathrm{K}}\right)^{1.05}. \tag{2.19}$$

We found that a strong X-ray radiation background lowers $T_{\rm min}$ and the Jeans mass, reducing the mass of the collapsing core (HM15), thus reducing the accretion rate.

Fig. 2.10 shows the accretion rates at the critical radius and final mass in Pop III stars for all the simulations forming Pop III stars, as a function of the minimum temperature $T_{\rm min}$. The different symbols refer to the three haloes we have simulated and the colors refer to the X-ray background intensity (see legend in the left panel of the figure). As we discuss with Fig. 2.9 they all follow a similar relationship: $T_{\rm min}$ decreases with increasing X-ray intensity and this leads to a slower gas accretion and hence lower mass of the Pop III star. The dashed lines in the left and

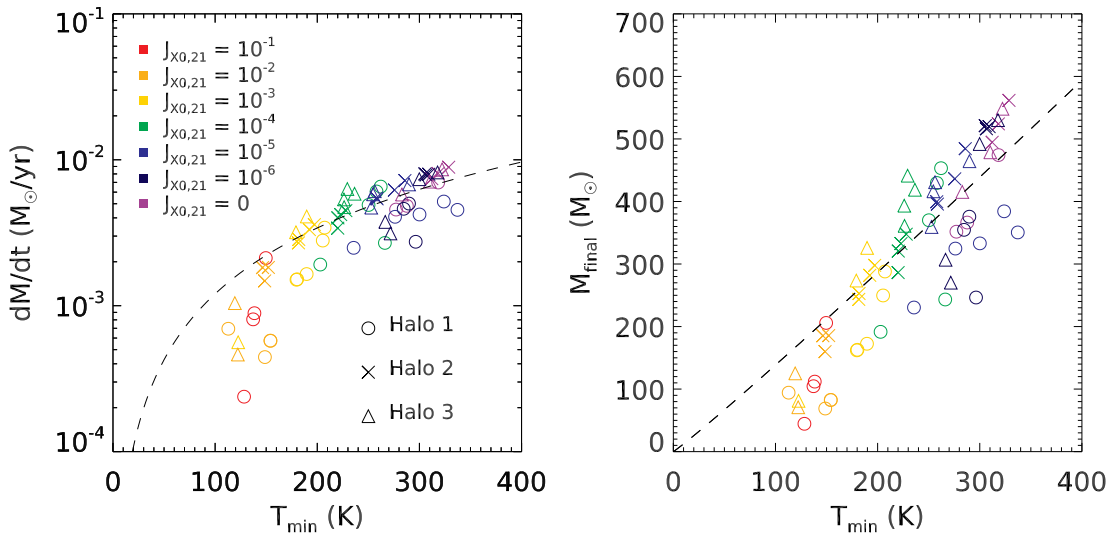

Figure 2.10: The accretion rate on the protostellar core (left panel) and final mass in Pop III stars (right panel) as a function of $T_{\rm min}$. Different symbols indicate different haloes and the X-ray intensity $\rm J_{X0,21}$ is color-coded. Simulations with critical mass $> 10^6$ $\rm M_\odot$ are omitted due to their larger deviations from the trend. In both panels, simple analytic estimates (equation 2.18 and 2.19) are drawn with dashed lines. Although the analytic estimates generally agree with the simulation results for the accretion rates and the Pop III mass, we notice a larger deviation for the strong X-ray irradiation cases. In addition, Halo 2 and Halo 3 show a tighter correlation with the simple analytic expectation than Halo 1.

right panels show the result of the simple analytic model for the accretion rate (equation (2.18)) and Pop III mass (equation (2.19)), respectively. The accretion rates from the simulations are consistent with this simple model, but the uncertainties in determining the location of the characteristic radii (and thus the accretion rates) produce a significant scatter with respect to the analytic calculation, especially for strong X-ray irradiation. The accretion rate $\mathrm{d}M/\mathrm{d}t$ and $M_{\rm final}$ for Halo 2 (crosses) and Halo 3 (triangles) show a much tighter relationship with $T_{\rm min}$, probably because these two haloes grow relatively slowly and do not experience major perturbations. On the other hand, Halo 1 (circles), which grows rapidly and experiences a major merger at some point, shows a larger scatter and $\mathrm{d}M/\mathrm{d}t$ is slightly biased to be lower than the other cases at a given temperature.

Fig. 2.11 shows that the total mass of the protostellar cores grows roughly linearly as a function of time. In other words, the accretion rate is roughly constant as a function of time, and its value decreases with increasing X-ray intensity similarly to $M_{\rm final}$. The trend is quite robust, for instance, when $\rm J_{X0,21} \geq 10^{-2}$ (orange and red lines in the top panels) the protostars grow at a significantly slower rate and the total mass in Pop III stars is lower at any given time. Again, deviations from the general trend are observed (green lines) in Halo 1 and Halo 3. As discussed in earlier in the section, a halo interaction may cause the rapid gas accretion. When Halo 3 is irradiated by X-ray background of $\rm J_{X0,21} = 10^{-1}$ (the orange line in the upper right panel) the growth of the clump stagnates after it reaches ~ 50 $\rm M_{\odot}$. We observe that a bar-like structure develops inside the characteristic radius. Due to the increase in the accretion rate the clump at the centre grows in ~ 10 kyrs but does not grow as most of the disc gas is consumed.

The bottom row in Fig. 2.11 shows the total mass as a function of time for different intensities of the LW backgrounds (see legend) keeping fixed the X-ray intensity ($\rm J_{X0,21} = 10^{-4}$). We do not observe any dependence of the protostellar core growth rate on the LW intensity. Probably this can be explained by H_2 self-shielding (equation (2.4)) that increases rapidly when the gas density exceeds $n_{\rm H} \sim 10^1 - 10^2$ H cm^{-3}. Hence, after the formation of the protostar the LW radiation is shielded and does not play a significant role in determining $T_{\rm min}$ and thus the final Pop III mass. The effect of the LW background is limited to setting the redshift of Pop III star formation. Because the protostar forms and accretes at different redshifts (for the same halo but with different radiation backgrounds), other factors such as the mass of the halo or mergers with other minihaloes are more important in determining the Pop III star mass growth than the gas cooling physics. An extreme example of this is the case of Halo 1 irradiated by a very strong LW background ($\rm J_{LW,21} = 100$, red line in the bottom-left panel). The gas in the halo starts con-

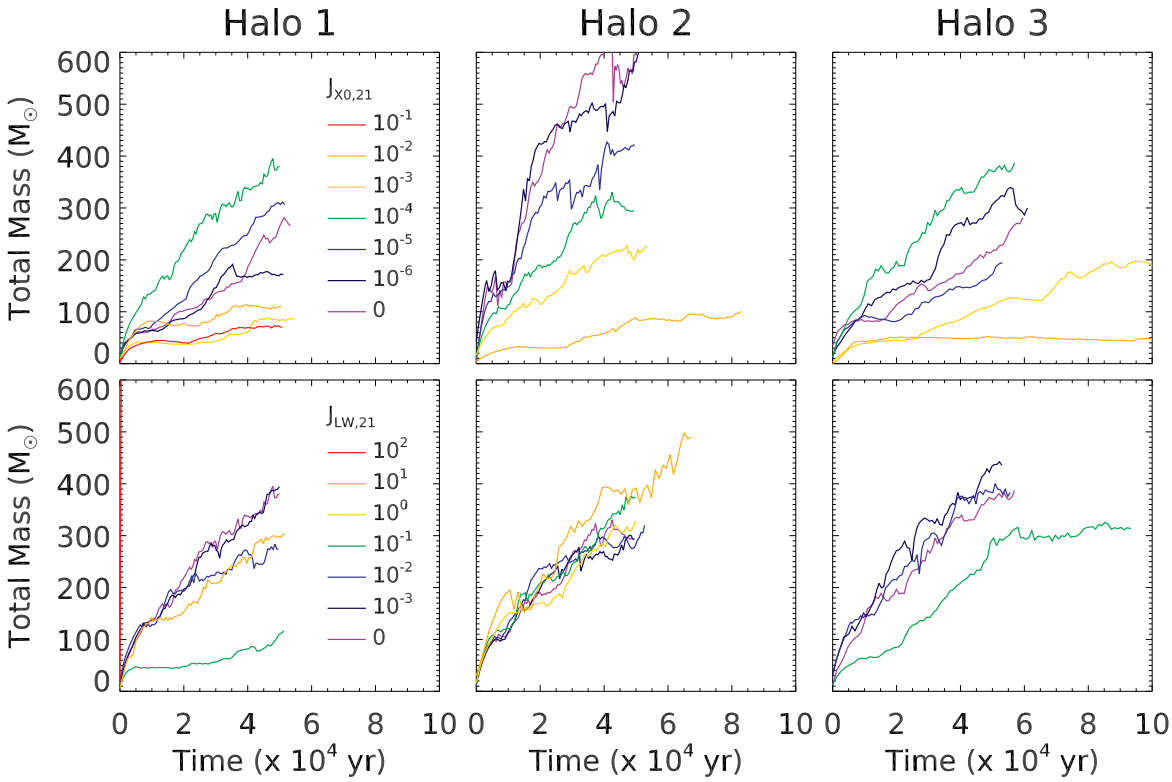

Figure 2.11: Evolution of the total mass of clumps (the protostar) since the formation of the first one in three haloes. Top panels show the total masses in different X-ray backgrounds ($J_{LW,21} = 0$). We clearly observe the general trend of a lower accretion rate and smaller final mass in Pop III stars with increasing X-ray irradiation. The bottom panels show the evolution of the total mass of the protostar changing the LW background keeping the X-ray background constant at $J_{X0,21} = 10^{-4}$. The intensity of the LW background is color-coded as shown in the legend. We do not observe any trend of the protostar growth rate with varying the LW background intensity.

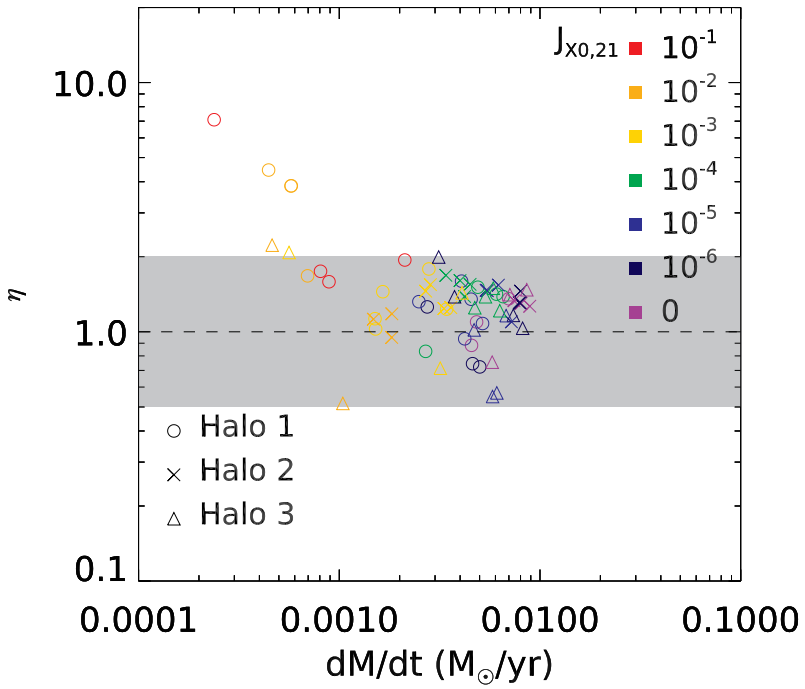

Figure 2.12: The dimensionless ratio η of two accretion rates in equation (2.21), as a function of $\mathrm{d}M/\mathrm{d}t|_{\rm cr}$, defined when the central density is 10^7 H cm^{-3}. The parameter η is the ratio of the average accretion rate on the Pop III star (*i.e.*the total mass at $t_* = 5 \times 10^4$ years, divided by t_*) to $\mathrm{d}M/\mathrm{d}t_{\rm cr}$. Different symbols refer to different host haloes and $\mathrm{J}_{\rm X0,21}$ is color-coded. To guide the eye, the shaded region encompasses a change of a factor of two around unity: $0.5 \leq \eta \leq 2.0$. Simulations with the critical mass of the host haloes larger than 10^6 $\mathrm{M}_\odot$ are omitted. The observation that η is of the order of unity means that the accretion rate at the characteristic radius estimated during the early phases of the collapse (when the central density is 10^7 H cm^{-3}), remains nearly constant as a function of time and at a smaller scales. Hence $\mathrm{d}M/\mathrm{d}t|_{\rm cr}$ is a good predictor of the constant growth rate of the protostars over a relatively long time scale.

densing when the mass of the halo reaches $\sim 2 \times 10^7$ $\mathrm{M}_\odot$ (the virial temperature $\sim 9,000$ K), when Ly α atomic cooling starts to become important. The accretion rate is very rapid and both $M_{\rm final}$ and the core mass exceed 10^4 $\mathrm{M}_\odot$. This is consistent with Regan et al. (2020) in that a LW background allows black hole seeds to form by suppressing the formation of Pop III stars in small mass minihaloes below the atomic cooling limit.

Since the accretion rate onto the protostar is fairly constant, the final mass in Pop III stars increases linearly with time. In order to determine the final mass in Pop III stars we therefore

need to estimate the typical timescale for feedback to halt the accretion. This can be derived from equation (2.16) as long as the accretion rate remains constant and equal to the value $\mathrm{d}M/\mathrm{d}t|_{\rm cr}$ estimated at the critical core radius at $n_{\rm H} = 10^7$ H cm^{-3}:

$$\tau_{\rm SF} = \frac{M_{\rm final}}{\mathrm{d}M/\mathrm{d}t|_{\rm cr}} = 89 \ {\rm kyrs} \left(\frac{\mathrm{d}M/\mathrm{d}t|_{\rm cr}}{2.8 \times 10^{-3} {\rm M}_\odot \ {\rm yr}^{-1}} \right)^{-0.3}, \tag{2.20}$$

In Fig. 2.12 we show the ratio between the average growth rate of the protostar $\langle \mathrm{d}M/\mathrm{d}t \rangle \approx M(t_*)/t_*$, where we use $t_* = 50$ kyrs for this period and the accretion rate $\mathrm{d}M/\mathrm{d}t|_{\rm cr}$ at $n_{\rm H} = 10^7$ H cm^{-3},

$$\eta = \frac{\langle \mathrm{d}M/\mathrm{d}t \rangle}{\mathrm{d}M/\mathrm{d}t|_{\rm cr}} \tag{2.21}$$

as a function of $\mathrm{d}M/\mathrm{d}t|_{\rm cr}$. The ratio η is of the order of unity with a spread within a factor of two (shaded region) in most cases. Since these two accretion rates are nearly the same, the final mass in Pop III stars estimated as $M(\tau_{\rm SF})$ is the same as $M_{\rm final}$ in equation (2.16).

2.5 Summary and Discussion

The first stars have an important effect on the formation of the first galaxies by regulating the formation of metal-enriched stars (Ricotti et al., 2002b, 2008; Wise and Abel, 2008). LW and X-ray photons can travel large distances without being absorbed in the early Universe, building up a radiation background. In addition, X-rays can penetrate deep into star-forming clumps producing both heating and ionization. Each photo-electron has high energy but in a mostly neutral gas fast photo-electrons deposit a large fraction of their kinetic energy into secondary ionizations (Shull and van Steenberg, 1985). Because of these properties, it is thought that early objects (first

stars and their remnants such as SNe, PISNe, HMXBs, and IMBHs) build a LW and X-ray radiation backgrounds that self-regulate their formation Venkatesan et al. 2001; Jeon et al. 2014a; Xu et al. 2016; R16).

In this study, using zoom-in simulations of three minihaloes with different masses and irradiated by different intensities of the LW and X-ray backgrounds, we investigate the effect of X-ray/LW radiation on the formation of the first stars and on their characteristic mass. Below we summarize the key results of the simulations.

1. We confirm the qualitative results of previous analytic models (R16), that an X-ray radiation background promotes the initial gas collapse in small mass minihaloes, while a LW background delays it by regulating the amount of H_2 formation. If the X-ray background is too intense, the feedback effect by gas heating suppresses Pop III star formation in haloes with virial temperature $T_{\rm vir} < T_{\rm gas}$. Below this threshold X-ray intensity, the increase in H_2 formation due to the increased ionization fraction of the gas, reduces the mass above which a minihalo can host a Pop III star (the critical mass) to $\sim 10^5$ $\rm M_\odot$. The positive feedback effect of X-rays is most important when it offsets the negative feedback of an intense H_2-dissociating LW radiation background. For example, X-rays can reduce the critical mass by a factor of ~ 2 in a weak LW intensity ($\rm J_{LW,21} \leq 10^{-3}$), while the reduction is by a factor of ten when $\rm J_{LW,21} = 10^{-1}$. Hence, X-ray radiation can increase the number of Pop III stars forming in the early Universe by about a factor of ten, that is the same factor as the decrease of the critical mass because the number of haloes per unit volume is inversely proportional to the critial mass ($\rm d n_{halo}/d \ln M_{halo} \propto M_{cr}^{-1}$). We provide a quantitative description of the relation between the number of Pop III stars and the critical mass in Appendix A.2.

2. X-ray irradiation produces a net cooling effect on the collapsing protostellar core by increasing the H_2 fraction. Efficient gas cooling reduces the gas sound speed and consequently the accretion rate on collapsing protostellar cores. Therefore the final mass in Pop III stars is lower in X-ray irradiated minihaloes.

The results in this work constitute a first step to understand the self-consistent evolution of the number of Pop III stars forming in the early universe. As shown in R16 using analytic calculations, the critical minihalo mass above which Pop III stars can form and the intensity of the radiation backgrounds are self-regulated by a feedback loop on cosmological scales. While this work considers only a grid of assumed values of the background, the lower value of the critical mass we derive is roughly a factor of 3 higher than the value found in R16 ($\sim 3 \times 10^4$ $M_\odot$). Although cosmological simulations are required to make solid predictions, a simple scaling argument using Press-Schechter formalism (Press and Schechter, 1974; Sheth and Tormen, 1999), suggests that the number of Pop III stars according to our simulation results would be a factor of 3-4 lower than in R16: ~ 100 instead of ~ 400 in 1MPCh estimated by R16.

In addition, following R16, we assume that soft X-ray ($\sim 0.2 - 2.0$ keV) is the dominant source of ionization and our spectra do not cover harder X-ray ($\sim 2.0 - 10$ keV). Whether adding harder photons in this energy bin has positive or negative feedback will be studied in future work.

The model in R16 assumes for simplicity a fixed X-ray and LW luminosity of each DM halo more massive than the critical mass. Therefore the model takes into account the total mass and multiplicity of Pop III stars in haloes, but not their dependence on the halo mass. In this work, we confirm the formation of multiple Pop III stars per halo, as also found in previous studies (Machida et al. 2008; Turk et al. 2009; Clark et al. 2011b; Susa et al. 2014; Stacy et al. 2016;

S20). This implies that the predicted radiation background Pop III stars build-up, depends on the evolution of the IMF of Pop III stars and their total mass. Due to their high masses, typically Pop III stars emit at nearly the Eddington rate 1.25×10^{38} ergs s^{-1} $(M/\mathrm{M}_{\odot})$ (Bromm et al., 2001), so the LW intensity per halo depends on the total mass of the stars. On the contrary, if they explode as PISNe with similar energy ($\sim 10^{52}$ ergs), the X-ray intensity per halo depends on the number of Pop III stars. Furthermore, the fraction of HMXBs ($\sim 35\%$, Stacy and Bromm, 2013) can be affected by the X-ray background. This suggests the number density of Pop III stars or their explosions that JWST (Whalen et al., 2014) will detect may provide constraints of the IMFs and X-ray physics.

HM15 finds that the X-ray radiation background is shielded by the dense central gas and therefore plays a minor role in determining the IMF of Pop III stars. Since self-shielding of the X-ray background is not considered in our simulations, we perform test runs with Halo 1 to investigate whether it has important effects. The results of the simulations suggest that X-ray self-shielding has a negligible effect in most of our simulations and deviations with respect to neglecting it are only evident for very strong values of $\mathrm{J}_{\mathrm{X0,21}} > 10^{-1}$ and, in these simulations, only in high-density gas ($n_{\mathrm{H}} > 10^4$ H cm^{-3}). Details on the method, simulation results, and analysis are presented in Paper II. Here we emphasize that the discussion presented in this paper on the redshift of collapse and total mass of Pop III stars is insensitive to the inclusion of X-ray self-shielding because regulated by gas properties at relatively low densities, where the effect of X-ray self-shielding is always negligible. In particular, X-ray shielding should not affect the final mass in Pop III stars since it is determined by the accretion rate of the quasi-hydrostatic core, related to T_{min} when the gas has density $n_{\mathrm{H}} \sim 10^4$ H cm^{-3}. The collapse to a higher density occurs on a timescale comparable to the ionization/recombination timescales. Hence,

the dense gas retains a memory of the temperature and ionization fraction at lower densities, as shown by panel (c) of Fig. 2.8 up to densities $\sim 10^7$ H cm^{-3}. We confirm that this behaviour continues up to densities $n_{\rm H} \sim 10^{10}$ H cm^{-3}. At densities $n_{\rm H} > 10^4$ H cm^{-3}, the gas temperature rises with increasing density, hence compression heating (or viscous heating in discs at densities $> 10^{10}$ H cm^{-3}, Kimura et al., 2021) dominates over photoionization heating, at least for the range of $\rm J_{X0,21}$ considered in this work. As HM15 has pointed out, however, this result may be sensitive to the column density of the halo and certainly the intensity of the X-ray irradiation. Hence, the growth history of the host halo may be an important factor in determining when X-ray shielding can be neglected.

This work does not include two potentially important physical processes: HD cooling and radiative feedback from protostars. HD provides additional cooling at low temperatures (~ 100 K) and thereby can reduce the characteristic mass of Pop III stars (Yoshida et al., 2007). Its formation rate is proportional to that of H_2 which is regulated by an X-ray background. Furthermore, Fig. 2.8 and 2.9 show the minimum temperature is a function of X-ray. Therefore, X-ray radiation can be crucial to the onset of HD cooling. The role of X-ray radiation in HD formation has been explored by Nakauchi et al. (2014), but not tested yet with hydrodynamics simulation. Finally, a full treatment of radiation feedback from accreting protostars, rather than the semi-empirical approximation used in this work, is important for a more accurate determination of the final masses of Pop III stars (Hosokawa et al. 2011, 2016; S20). Therefore, including the neglected or approximated physical processes mentioned above (X-ray self-shielding, HD cooling, and radiation feedback) will be the focus of future work.

Chapter 3: Population III Star Formation in an X-ray Background - II. Protostellar Discs, Multiplicity, and Mass Function of the Stars

Disc fragmentation plays an important role in determining the number of primordial stars (Pop III stars), their masses, and hence the initial mass function. In this second paper of a series, we explore the effect of uniform FUV H_2-photodissociating and X-ray radiation backgrounds on the formation of Pop III stars using a grid of high-resolution zoom-in simulations. We find that, in an X-ray background, protostellar discs have lower surface density and higher Toomre Q parameter, so they are more stable. For this reason, X-ray irradiated discs undergo fewer fragmentations and typically produce either binary systems or low-multiplicity systems. In contrast, the cases with weak or no X-ray irradiation produce systems with a typical multiplicity of 6 ± 3. In addition, the most massive protostar in each system is smaller by roughly a factor of two when the disc is irradiated by X-rays, due to a lower accretion rate. With these two effects combined, the initial mass function of fragments becomes more top-heavy in a strong X-ray background and is well described by a power-law with slope 1.53 and high-mass cutoff of $61\ \mathrm{M}_\odot$. Without X-rays, we find a slope 0.49 and a cutoff mass of $229\ \mathrm{M}_\odot$. Finally, protostars migrate outward after their formation likely due to the accretion of high-angular momentum gas from outside and the migration is more frequent and significant in the absence of X-ray irradiation.

3.1 Introduction

In the last 20 years, theoretical progress has been made to understand better the formation of the first zero-metallicity stars (Pop III) that formed in the universe (Omukai and Nishi, 1998; Bromm et al., 2001; Abel et al., 2002; Yoshida et al., 2008; Turk et al., 2009; Clark et al., 2011b; Hosokawa et al., 2011; Sugimura et al., 2020). However, predictions on the number and masses of the Pop III stars are still very uncertain. Similarly uncertain are the predictions on the number of pair-instability SNe (PISNe) and hypernovae from Pop III stars and the number of IMBHs they produce. In the era of gravitational wave astronomy (Abbott et al., 2016), the census of intermediate-mass black holes (IMBHs) detected in binary systems is bound to improve, and next-generation optical and IR space telescopes (JWST and Roman space telescope) promise to directly detect the first light from Pop III star clusters, PISNe and hypernovae they may produce (Whalen et al., 2014). It is therefore important to refine our models and predictions for the the rate of formation of the first stars and their remnants.

Part of the difficulty in making these predictions is global feedback processes, in particular the Lyman-Warner (LW) H_2-dissociating background and the X-ray radiation background, regulating their formation in small mass haloes (minihaloes) and their initial mass function (Oh, 2001; Venkatesan et al., 2001; Machacek et al., 2003; Ricotti and Ostriker, 2004; Ricotti et al., 2005; Jeon et al., 2014a; Xu et al., 2016). The LW radiation is emitted directly by Pop III stars and second-generation stars, while high-mass X-ray binaries (HMXBs), accreting IMBHs, and supernova/hypernova explosions are sources of an X-ray radiation background associated with Pop III star formation (Xu et al., 2014; Jeon et al., 2014a, 2015; Ricotti, 2016; Xu et al., 2016). The LW radiation background has always negative feedback on the formation of Pop III stars

as it dissociates H_2, suppressing the cooling of pristine gas. The X-ray background can both suppress Pop III star formation in the smallest minihaloes due to intergalactic medium (IGM) heating (increasing the Jeans mass in the IGM) and promote Pop III star formation by increasing the electron fraction of gas collapsed into minihaloes and thus promoting H_2 formation via the catalyst H^-. The number of Pop III stars depends on the minimum dark matter halo mass in which a zero-metallicity star can form as a function of redshift (the smaller the critical mass the more numerous the minihaloes hosting Pop III stars) and on the multiplicity of stars per minihalo (Hirano et al., 2014; Susa et al., 2014; Stacy et al., 2016). Since both the critical minihalo mass and the multiplicity of stars depend on the radiation backgrounds produced by Pop III stars, a feedback loop is at play. A simple analytic model of this feedback loop was presented in Ricotti (2016), in which the number of Pop III stars in the early universe and the radiation background they produce was estimated self-consistently. He finds that X-rays emitted during the unavoidable death of Pop III stars in cosmic supernova or hypernova explosions can significantly increase the number of Pop III stars forming in the universe with respect to models without X-rays. However, if the X-ray emissivity per minihalo is too large, for instance, because of significant contributions from HMXBs or accreting IMBHs from Pop III stars or miniquasars from direct collapse BHs, X-rays can have a negative feedback effect by heating excessively the IGM.

The buildup and cosmological effects of an X-ray background, including its effect on the formation of the first stars, have been studied by many authors (Oh, 2001; Venkatesan et al., 2001; Machacek et al., 2003; Inayoshi and Omukai, 2011; Jeon et al., 2014a; Xu et al., 2014, 2016). However, its impact on the properties of Pop III stars has received less attention. The pioneering work of Hummel et al. (2015) focused on the initial gas collapse, disc fragmentation, and multiplicity of Pop III stars in the presence of an X-ray background using cosmological

simulations. Evolving their simulations for the first $5,000$ yrs after the formation of the first sink particle, they concluded that the impact of X-rays on Pop III star formation is minimal. However, the process of accretion onto protostellar cores takes typically $\sim 10^4 - 10^5$ yrs (McKee and Tan, 2008; Hosokawa et al., 2011; Sugimura et al., 2020), hence these simulations may have been evolved for an insufficient length of time to fully capture the evolution of Pop III stars and protostellar discs.

In Park, Ricotti, and Sugimura (2021a, hereafter Paper I), we describe a set of zoom cosmological simulations of the formation of Pop III stars in three minihaloes with different masses and growth histories, irradiated by a range of intensities of the LW and X-ray background. The intensity of the background is constant as a function of time in physical units and has a power-law shape with a flat slope for the LW radiation and a slope 1.5 for the X-ray radiation. We explore a grid of $7 \times 7 = 49$ different combinations of LW and X-ray backgrounds: $\mathrm{J_{LW,21}} = 0, 10^{-3}, 0.01, 0.1, 1, 10, 100$, $\mathrm{J_{X0,21}} = 0, 10^{-6}, 10^{-5}, 10^{-4}, 10^{-3}, 0.01, 0.1$, where the intensities are in units of 10^{-21} erg s^{-1} cm^{-2} Hz^{-1} sr^{-1}. We cover wide ranges of intensities by assuming that sources at various distances affect the star formation. In this work, strong X-rays refer to those with ($\mathrm{J_{X0,21}} \geq 10^{-3}$). The X-ray background of Xu et al. (2016) and the fiducial model of Ricotti (2016) correspond to our intermediate X-ray background ($\mathrm{J_{X0,21}} = 10^{-4}$) while the fiducial model of Hummel et al. (2015) and strong X-rays of Ricotti (2016) correspond to our strong backgrounds.

In Paper I, in agreement with Ricotti (2016), we find that the X-ray radiation background generally promotes the initial gas collapse in small mass minihaloes, while the LW background delays it by regulating the amount of H_2 formation. However, if the X-ray background is too intense, gas heating suppresses Pop III star formation in haloes with virial temperature $T_{\rm vir} <$

$T_{\rm gas}$. Below this minihalo mass-dependent threshold, enhancement of the H_2 abundance produced by X-ray ionization of the gas, reduces the critical mass above which a minihalo can host a Pop III star to $\sim 10^5$ $M_\odot$. The positive feedback effect of X-rays is most important when it offsets the negative feedback of an intense H_2-dissociating LW radiation background. In this case, the critical mass can be reduced by a factor of ten. Hence, X-ray radiation can increase the number of minihaloes forming Pop III stars in the early Universe by about the same factor. We also found that the total mass of Pop III stars in each minihalo is lower in a sufficiently intense X-ray background. X-ray irradiation produces a net cooling effect on the collapsing protostellar core by increasing the H_2 fraction. Efficient gas cooling reduces the gas sound speed and consequently the accretion rate on the collapsing protostellar core, and its final mass.

In this work, the second in a series, we investigate how the X-ray and LW radiation backgrounds affect the protostellar disc properties, the binarity/multiplicity of Pop III stars, including their separation and dynamics, and the initial mass function of Pop III stars. The paper is organized as follows. In Section 3.2 we briefly summarize the simulations. We discuss the properties of circumstellar discs in Section 3.3 and the multiplicity of Pop III stars in Section 3.4. In Section 3.5 we provide a summary and discussion.

3.2 Simulation

The simulations and the included physical processes are described in detail in Paper I. Here we summarize the main aspects of the simulations for the sake of completeness. We use the adaptive mesh refinement (AMR) cosmological code RAMSES (Teyssier, 2002), with radiation transfer (Rosdahl et al., 2013). We perform zoom-in cosmological simulations on three haloes:

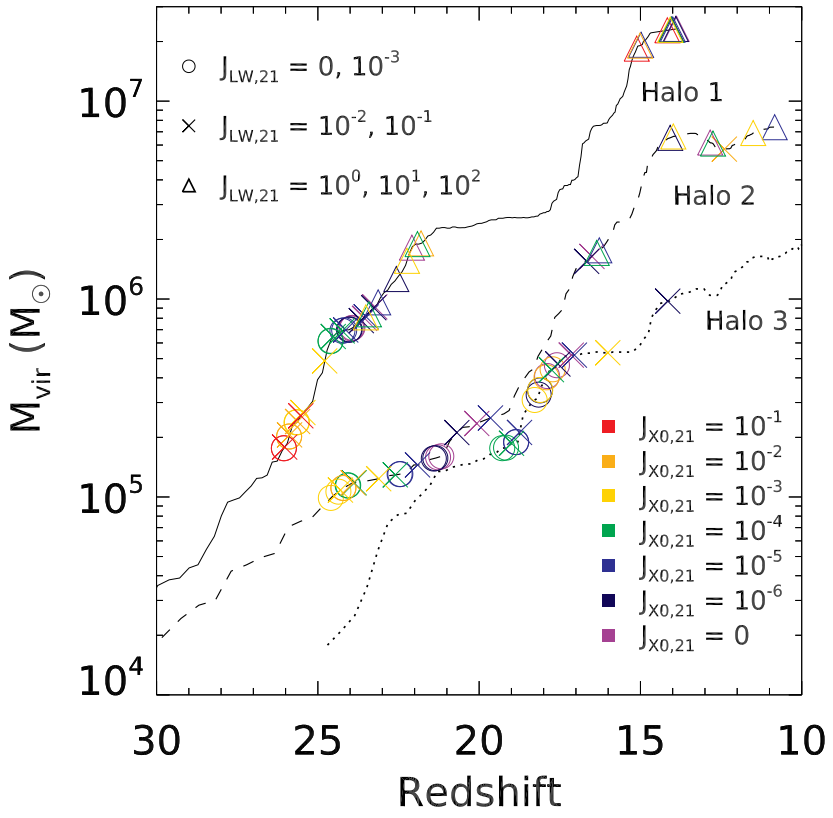

Figure 3.1: Halo mass as a function of redshift. The virial masses of Halo 1, Halo 2 and Halo 3 are shown with different lines. The positions of symbols refer to the redshift of the formation of Pop III stars and the masses of their host minihaloes. Different symbols and colors indicate the intensity of LW and X-ray backgrounds as indicated by the legend.

the mass growth history of these three haloes is shown in Fig. 3.1 along with symbols showing the redshift of formation of the Pop III stars under different intensities of an externally imposed X-ray background.

Inside each zoom-in region, the mass of DM particles is $\sim 800\ \mathrm{M}_\odot$, and the cell refinement criteria are: i) Lagrangian (cells must contain less than 8 DM particles) and, ii) Jeans refinement criteria (Jeans length is resolved with at least N_J cells). For the latter condition, for cell sizes smaller than $\sim$ 1 pc comoving, we adopt $N_\mathrm{J} = 16$ in order to prevent any possible artificial fragmentation and better resolve possible turbulent motions. If the size of a cell is greater than

Table 3.1: Summary of the simulations.

	$M_{\rm vir}$ ($z = 15.7$)	$M_{\rm DM}$ (zoom-in)	Box size	$l_{\rm max}$
Halo 1	7.9×10^6 M$_\odot$	800 M$_\odot$	1 Mpc/h^3	28
Halo 2	4.4×10^6 M$_\odot$	800 M$_\odot$	2 Mpc/h^3	29
Halo 3	7.0×10^5 M$_\odot$	800 M$_\odot$	1 Mpc/h^3	28

~ 30 pc (comoving), we adopt $N_{\rm J} = 4$ to save computational time. Any cells between these two scales are refined with $N_{\rm J} = 8$. The size of the smallest cells is 0.00375 pc/h (comoving). At $z = 20$, this corresponds to a physical size of 2.63×10^{-4} pc (or 54 au). The corresponding AMR levels are shown in Table 3.1. The initial conditions of the DM-only and zoom-in simulations are generated with MUSIC (Hahn and Abel, 2011). The assumed cosmological parameters are $h = 0.674, \Omega_{\rm m} = 0.315, \Omega_\Lambda = 0.685, \Omega_{\rm b} = 0.0493, \sigma_8 = 0.811$ and $n_{\rm s} = 0.965$ (Planck Collaboration et al., 2020).

We consider all important chemical reactions in a gas of primordial composition. We include a network of out-of-equilibrium reactions for the following ions and molecules: HI, HII, HeI, HeII, HeIII, H_2, $H_2{}^+$. The abundance of H^- is approximated assuming the reactions are at equilibrium. The formation of H_2 includes the H^- and the H_2^+ channels as well as 3-body reaction important at densities $> 10^{10}$ H cm^{-3}. We include hydrogen and helium atomic cooling processes and an H_2 cooling function tested to be accurate up to densities $n_{\rm H} \sim 10^{12}$ H cm^{-3}. We also model H_2 self-shielding using fitting functions from Wolcott-Green and Haiman (2019) and the effect of secondary ionizations and heating from fast electrons produced by X-ray photoionizations (Shull and van Steenberg, 1985; Ricotti et al., 2002a). Since we do not use sink particles to create protostellar cores, in order to prevent artificial fragmentation at the maximum refinement level caused by a decreasing Jeans length, we suppress the cooling of cells with the maximum

refinement level following the method in Hosokawa et al. (2016). This is done by multiplying the cooling function by the factor

$$C_{\rm limit} = \exp\left[-\left(\frac{\xi-1}{0.1}\right)^2\right] \quad (\text{if } \xi > 1), \tag{3.1}$$

where $\xi = f_{\rm limit}(\Delta x/\lambda_{\rm J})$ with Δx is the cell size and $\lambda_{\rm J}$ is the Jeans length. We assume $f_{\rm limit} = 12$ as in Hosokawa et al. (2016). The masses of protostellar cores are therefore estimated by flagging cells with $C_{\rm limit} < 10^{-4}$.

X-ray self-shielding is neglected, but we run test simulations showing that it is important only for late stages when the gas reaches densities $> 10^4$ H cm^{-3}, in very strong X-ray background ($\rm J_{X0,21} \geq 10^{-1}$). Hence most of our results in Paper I and here, are insensitive to X-ray self-shielding. In Appendix B.1, we describe how the self-shielding is treated in the test simulations and discuss the results in detail. As Hummel et al. (2015) has pointed out, however, the result depends on the total column density of the halo and the spectrum of the X-ray radiation. In future works, more tests will be necessary to fully assess the importance of X-ray self-shielding in determining the masses and redshift of formation of Pop III stars. We also neglect HD cooling and chemistry. This could be important for strongly irradiated discs in which the H_2 fraction is large and the gas temperature reaches $T_{\rm min} \sim 100 - 200$ K. HD cooling can reduce the characteristic mass of Pop III stars (Yoshida et al., 2007) and its formation in a gas irradiated by X-rays so far has only been explored analytically Nakauchi et al. (2014).

Finally, in this paper, we do not include radiative feedback from the accreting protostar, which is crucial in stopping the accretion onto the protostellar core and therefore in determining the final masses of Pop III stars (Smith et al., 2011; Hosokawa et al., 2011, 2016; Stacy et al.,

2012; Sugimura et al., 2020). We estimate the final masses of Pop III stars using an empirical relationship based on previous work by (Hirano et al., 2015) that includes UV radiation feedback. They provides a relation between the final mass in Pop III stars, $M_{\rm final}$, and the accretion rate onto the protostellar core, $\mathrm{d}M/\mathrm{d}t|_{\rm cr}$, estimated at a characteristic radius:

$$M_{\rm final} = 250\ \mathrm{M}_\odot \left(\frac{\mathrm{d}M/\mathrm{d}t|_{\rm cr}}{2.8 \times 10^{-3}\ \mathrm{M}_\odot\ \mathrm{yr}^{-1}} \right)^{0.7}. \tag{3.2}$$

We define the characteristic radius when the collapsing core density reaches $n_{\rm H} = 10^7$ H cm^{-3} where $M_{\rm enc}(r)/M_{\rm BE}(r)$ reaches its maximum value, consistently with the definition in (Hirano et al., 2015). In Paper I we find that the growth rate of the protostellar core is roughly constant as a function of time and is equal to $\mathrm{d}M/\mathrm{d}t|_{\rm cr}$. Therefore we can also estimate the masses of Pop III stars by calculating their mass directly from the simulation at the characteristic time $\tau_{\rm SF}$ defined as:

$$\tau_{\rm SF} = \frac{M_{\rm final}}{\mathrm{d}M/\mathrm{d}t|_{\rm cr}} = 89\ \mathrm{kyrs} \left(\frac{\mathrm{d}M/\mathrm{d}t|_{\rm cr}}{2.8 \times 10^{-3}\ \mathrm{M}_\odot\ \mathrm{yr}^{-1}} \right)^{-0.3}. \tag{3.3}$$

One of the main results of Paper I is that the accretion rate onto the protostar is $\mathrm{d}M/\mathrm{d}t \sim \mathrm{d}M/\mathrm{d}t|_{\rm cr} \propto c_{\rm s}^3$, where $c_{\rm s}$ is the minimum sound speed of the gas reached when the density is $n_{\rm H} \sim 10^4$ H cm^{-3}. Therefore the timescale for star formation is $\tau_{\rm sf} \propto c_{\rm s}^{-1}$ and $M_{\rm final} \propto c_{\rm s}^2$. In terms of the minimum gas temperature we therefore have: $\mathrm{d}M/\mathrm{d}t \propto T_{\rm min}^{3/2}$, $\tau_{\rm SF} \propto T_{\rm min}^{-1/2}$ and $M_{\rm final} \propto T_{\rm min}$.

3.3 Results: I. Properties of Protostellar Discs

Disc fragmentation is important in determining the number of Pop III stars and their masses. Early cosmological simulations suggested that a single massive star ($\gtrsim 100$ $\mathrm{M}_{\odot}$) forms in each minihalo out of a pristine gas cloud (Abel et al., 2002; Yoshida et al., 2008; Hosokawa et al., 2011), but more recent ones found the formation of multiple stars due to protostellar discs fragmentation (Clark et al., 2011b; Susa et al., 2014; Stacy et al., 2016; Sugimura et al., 2020). In our simulations, gas discs fragment to form multiple clumps once the central density reaches $10^{10} - 10^{11}$ H cm^{-3}. In this section, we discuss the effect of background radiation on disc fragmentation.

The main effect of X-ray irradiation on the properties of the disc is an increased stability to fragmentation. Fragmentation of a thin disc can be characterized by the Toomre Q parameter defined as (Toomre, 1964):

$$Q = \frac{c_{\mathrm{s}}\kappa}{\pi G \Sigma}, \tag{3.4}$$

where κ is the epicyclic frequency and Σ is the disc surface density. If $Q > 1$ the disc is stable to fragmentation. In Fig. 3.2 we show the comparison of the face-on view of two discs in Halo 2 without X-ray background (left column) and with an X-ray background of $\mathrm{J}_{\mathrm{X0,21}} = 10^{-2}$ (right column). The top panels show the surface densities and the bottom panels the Q parameter. It is clear that X-ray irradiated disc has lower surface density and larger Q parameter. We find that the intensity of the X-ray background affects the shape of the disc forming in Halo 2, whose growth is smooth as it does not undergo major mergers while stars are forming. In a strong X-ray background, the shape of a disc tends to be asymmetric as shown in the top right panel of Fig. 3.2.

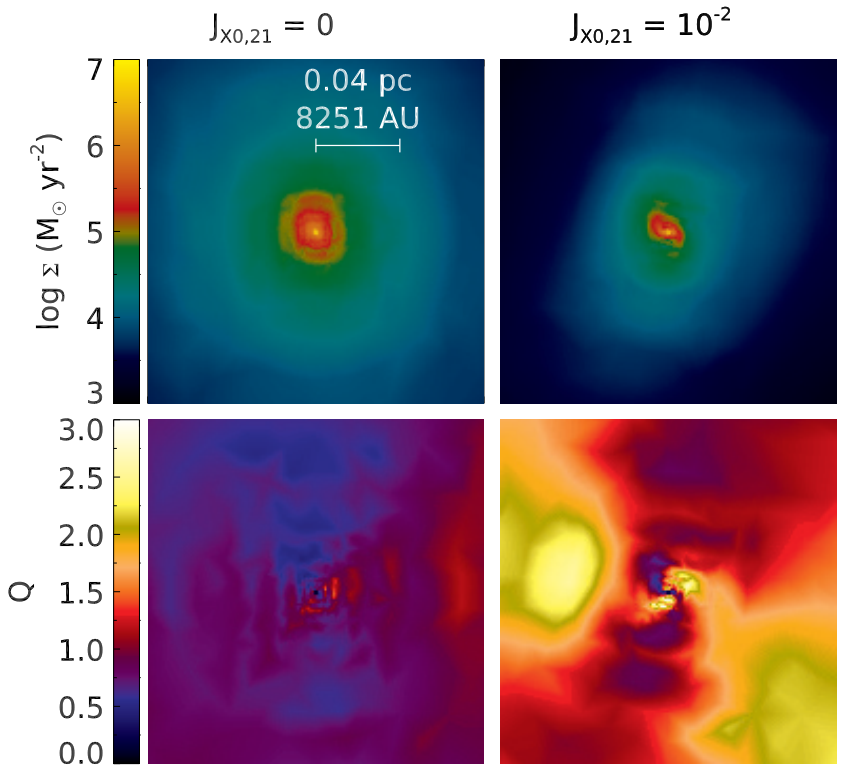

Figure 3.2: Surface density (top panels) and Toomre Q parameter (bottom panels) of the face-on circumstellar disc in Halo 2, at the time when the first protostar forms at the centre. The left panels show the case without X-ray background and the right panels the case with a strong X-ray background with $\mathrm{J_{X0,21}} = 10^{-2}$. In both simulations $\mathrm{J_{LW,21}} = 0$, and the field-of-view is 0.16 pc $\times$ 0.16 pc (33000 au $\times$ 33000 au).

On the other hand, the discs in Halo 1 and Halo 3, which grow quickly and therefore are more easily perturbed by mergers, do not show a clear relationship between the morphology of the disc and the intensity of the X-ray background.

In addition to the parameter Q, another measure the stability of the disc is the fragmentation time t_{frag}, that here we define as the time between the formation of the first clump at the centre of the disc and the second clump. In Fig. 3.3 we plot its dependence on the minimum temperature, T_{min}, of the collapsing core in the phase diagram (see Paper I). The plot shows that the second fragment forms systematically later in discs in a stronger X-ray background. This can

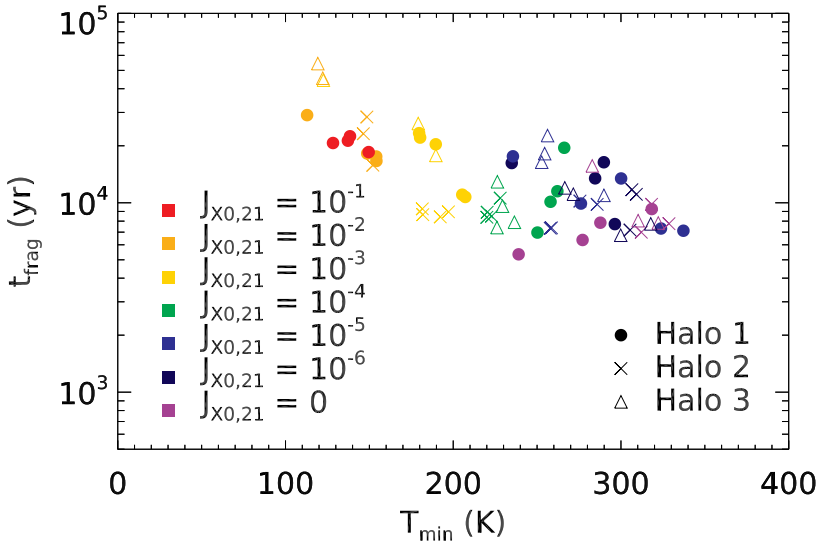

Figure 3.3: Fragmentation time as a function of the minimum gas temperature, $T_{\rm min}$, of the collapsing core in the gas phase diagram. $\rm J_{X0,21}$ is color-coded and the host haloes are shown with different symbols (see legend). Simulations with halo critical mass $> 10^6$ $\rm M_\odot$ are excluded from the analysis.

be interpreted as due to a more stable disc (with larger Q), and/or the lower accretion rate $\mathrm{d}M/\mathrm{d}t$ found in a strong X-ray background.

Two examples of the evolution and fragmentation of discs with and without X-ray irradiation are shown in Fig. 3.4-3.5 for Halo 2. The top panels ((a)-(c)), show snapshots of the projected face-on and edge-on views of the disc at three different times. Panel (d) shows the hydrogen number density at the mid-plane of the disc as a function of r, while Panel (e) to (l) show azimuthally averaged profiles in cylindrical coordinates of various quantities for the same three different snapshots (see legend). Fig. 3.4 shows the disc in the absence of any radiation background. When the first clump forms at the centre of the halo (Panel (a)) the gas has a flat disc-like structure with central density $\sim 10^{10} - 10^{11}$ H cm^{-3}. The disc starts to fragment at $t \sim 14$ kyr after the formation of the first clump (Panel (b)), and at $t \sim 27$ kyr four clumps can be identified (see Panel (c)). As the disc fragments the azimuthally averaged profile of the disc shows fluc-

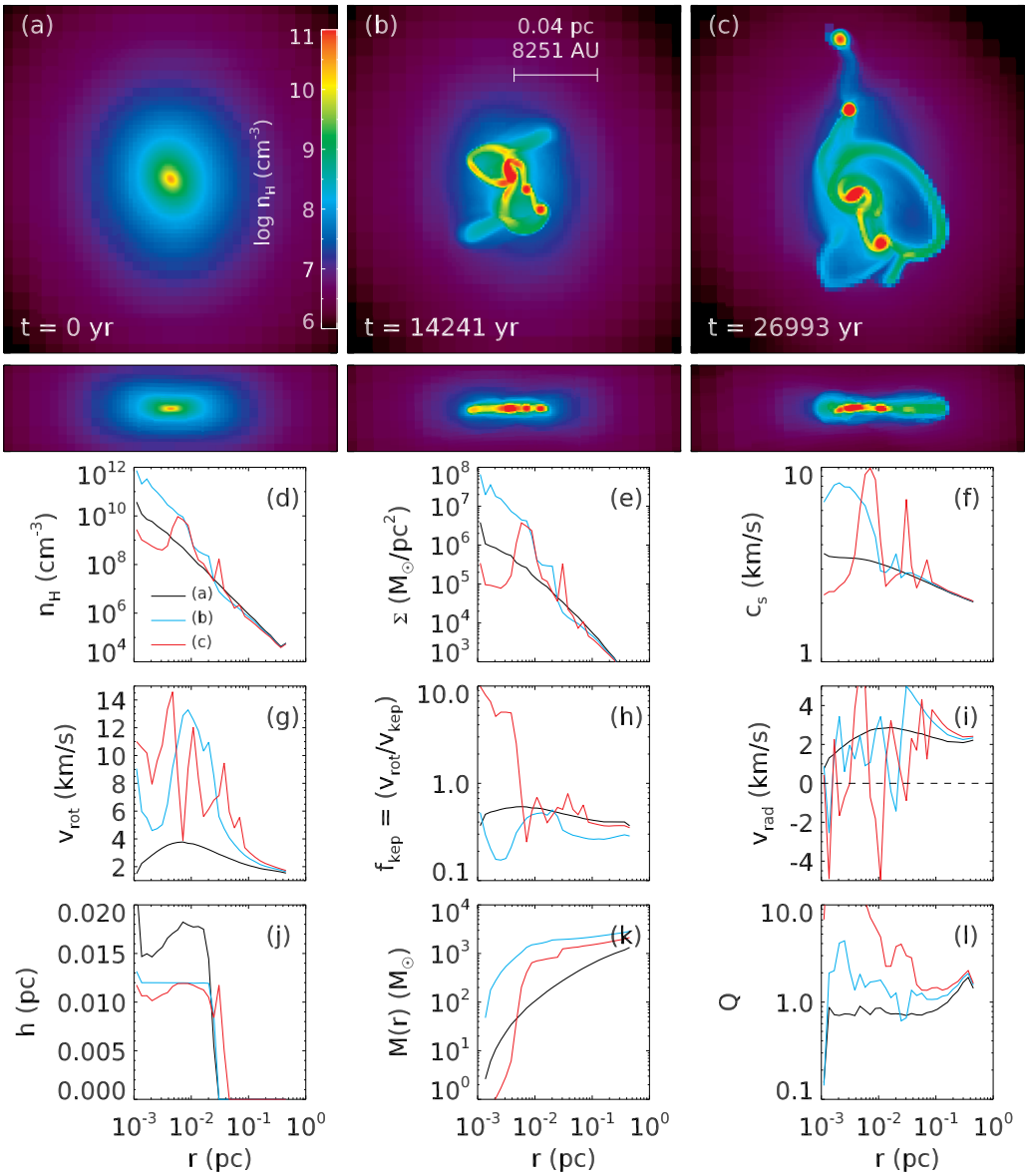

Figure 3.4: Disc of Halo 2 in the absence of a radiation background. Panel (a)-(c): Projected face-on (top) and edge-on (bottom) images of the disc in three snapshots at times $t = 0, 14$ and 27 kyr, where t is defined as the time since the formation of the first protostar. The field-of-view of the face-on images is 0.16 pc $\times$ 0.16 pc (or 33000 au $\times$ 33000 au) and that of the edge-on images is 0.16 pc $\times$ 0.04 pc (or 33000 au $\times$ 8251 au). Panel (d): The radial profile of the hydrogen number density in the disc midplane. We plot the profiles of the three snapshots in Panel (a), (b), and (c) as solid lines with different colors as shown in the legend. Panel (e): The surface density of the gas. Panel (f): The sound speed. Panel (g): The rotational velocity. Panel (h): The ratio of the rotational velocity to the Keplerian velocity. Panel (i): The radial velocity. Panel (j): The thickness of the disc, defined as the value of z where the gas becomes less dense than 5×10^7 H cm^{-3}. Panel (k): The enclosed mass. Panel (l): The Toomre Q parameter.

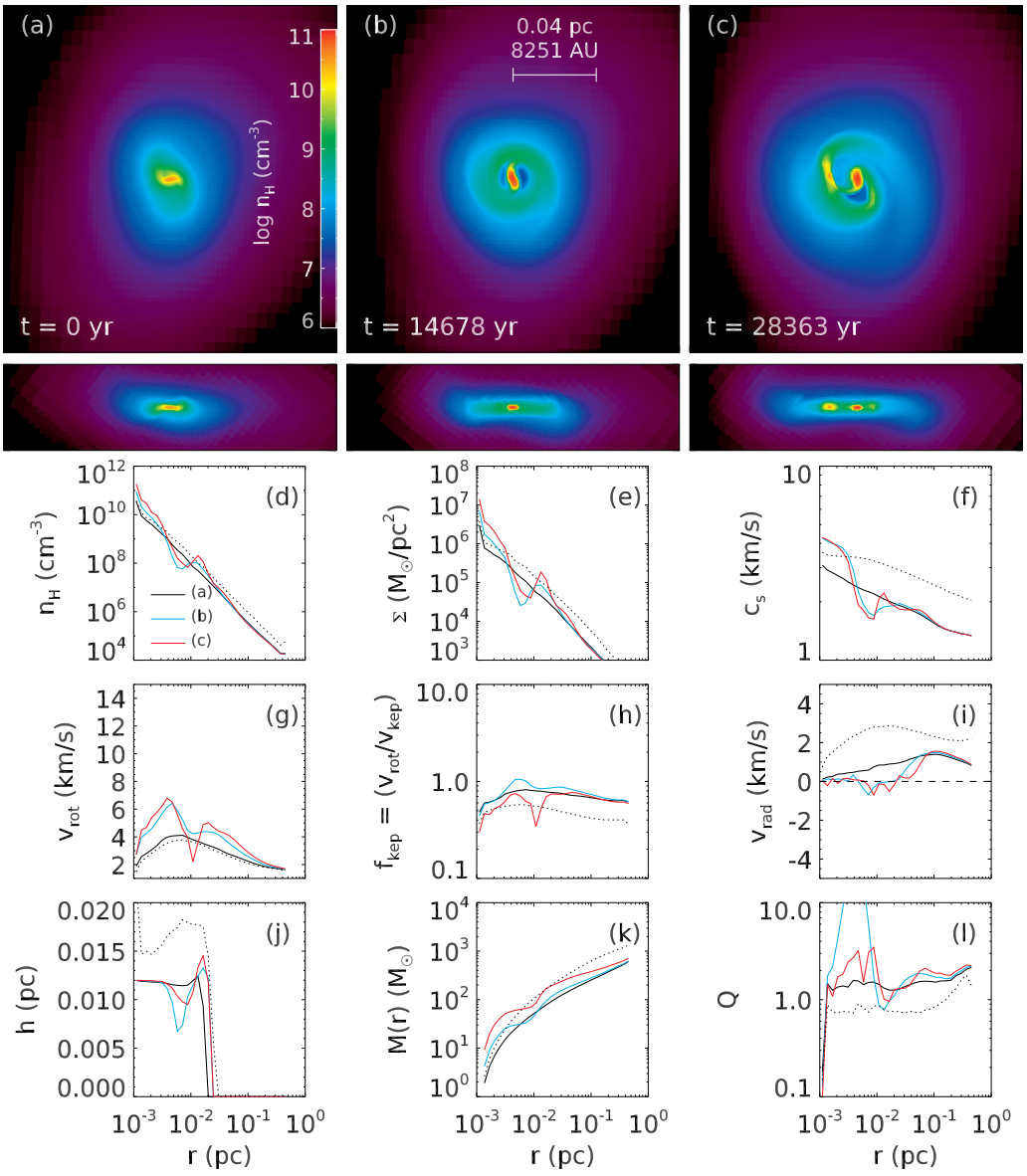

Figure 3.5: Same as Fig. 3.4 but for a disc irradiated by an X-ray background with intensity $J_{X0,21} = 10^{-2}$ and $J_{LW,21} = 0$. For the sake of comparison, the dotted black lines in Panels (d)-(l), show the case without X-ray irradiation at $t = 0$.

tuations in the inner parts (cyan and red lines), hence the averaged profiles are less informative. Fig. 3.5 shows the same halo as Fig. 3.4, but with irradiated by a strong X-ray background with $J_{X0,21} = 10^{-2}$. Fragmentation of the disc is suppressed for a longer time when compared to the case without X-ray irradiation. The disc starts to fragment after $t \sim 28$ kyr (Panel (c)) and the system remains a binary system for more than 30 kyr. In Panel (d) to (l) we plot various properties of the disc and, for comparison, we show the case without X-rays at $t = 0$ as dotted lines. One notable difference is that the surface density of the disc (Panel (e)) and enclosed mass (Panel (k)) become lower if the disc is irradiated by an X-ray background. The disc mass and surface density follow a similar trend as the mass of the collapsing hydrostatic core, which becomes lower in an X-ray background. Other notable difference is seen in the radial (infall) velocity (Panel (i)). This follows from the lower accretion rate in a stronger X-ray background (and lower $T_{\rm min}$). Although the sound speed (Panel (f)) and scale height of the disc decrease with increasing X-ray irradiation, the disc is more stable to fragmentation due to the lower surface density, as shown by the Toomre Q parameter (see Panel (l)). It is worth mentioning that the idealized simulations by Clark et al. (2011a) showed a cloud with initial conditions appropriate for the formation of Pop III.2 stars (*i.e.*, assuming lower initial gas temperature as in our X-ray irradiated discs), is more stable to fragmentation, in qualitative agreement with our findings.

In order to interpret more quantitatively the properties of X-ray irradiated discs, below we derive simple scaling relationships for the main disc parameters as a function of X-ray irradiation. We aim to model the trends for the disc properties at early times when the first protostar forms at the centre of the disc and before the disc fragments. These trends at $t = 0$ can be observed in the bottom nine panels of Fig. 3.5 (from (d) to (l)) as solid black lines for strong X-ray irradiation, and dotted black lines, without X-ray irradiation.

We model the disc properties at $t = 0$ in terms of the sound speed of the gas in the disc, which is related to the X-ray irradiation and $T_{\rm min}$. As mentioned above, the disc fragmentation induces fluctuations of the averaged profiles and therefore we focus on the properties at early times. As shown in Panels (f) of Fig. 3.4-3.5, the gas sound speed in the disc at $t = 0$ increases only by a factor of two with increasing density for densities between 10^4 H cm^{-3} (at $r \sim 0.5$ pc) and 10^{10} H cm^{-3} (at $r \sim 10^{-3}$ pc). Therefore the gas is nearly isothermal with temperature directly proportional to $T_{\rm min}$, defined as the minimum temperature reached by the collapsing gas at density $n_{\rm H} \sim 10^4$ H cm^{-3} (see Section 2.4). Note that Panel (f) shows that, as the density approaches 10^{10} H cm^{-3}, the gas sound speed for the cases without X-ray and strong X-ray irradiation start to converge to a common value ($\sim 3 - 4$ km s^{-1}). This is in agreement with the results obtained in former analytical studies (Matsukoba et al., 2019; Kimura et al., 2021) showing that in the inner and denser regions of the disc, the temperature reaches a thermal balance equilibrium between H_2 cooling and viscous heating. However, because viscous heating increases with increasing accretion rate, hence with decreasing X-ray intensity, the gas temperature in the inner parts of the disc also decreases with increasing X-ray irradiation, although the dependence is weak.

Assuming a thin disc in hydrostatic equilibrium with a central gravitational potential, and supported in the vertical direction by thermal pressure, the disc scale height H is:

$$\frac{H}{R} \sim \frac{c_{\rm s}}{v_{\rm kep}} \sim c_{\rm s}(R/GM)^{1/2} \propto {\rm const}(T_{\rm min}), \tag{3.5}$$

where $v_{\rm kep} = (GM(< R)/R)^{1/2}$ is the Keplerian velocity, and we have assumed that the enclosed mass of the central clump $M(< R) \propto c_{\rm s}^2$, scales as an isothermal sphere and $c_{\rm s} \propto T_{\rm min}^{1/2}$ as

discussed above. Hence, we expect that the disc scale height is roughly independent of the X-ray intensity. Note that here we are only interested in the dependence of H (and other quantities) on the X-ray irradiation and not the radial coordinate of the disc.

We expect that the midplane disc density roughly follows the isothermal cloud solution $n_{\rm H} \propto c_{\rm s}^2$, as suggested by $n_{\rm H} \propto R^{-2}$ power-law of the density profile, that is very close to an isothermal sphere. The surface density profile

$$\Sigma \propto n_{\rm H}(R) H(R) \propto c_{\rm s}^2 \propto T_{\rm min}. \tag{3.6}$$

also scales as $c_{\rm s}^2$ since H is roughly independent of $c_{\rm s}$. In addition, the gas accretion rate in our model (see Paper I) is $\mathrm{d}M/\mathrm{d}t \propto \Sigma(R) v_{\rm infall}(R) \propto c_{\rm s}^3$, hence the gas infall rate should scale as $v_{\rm infall} \propto c_{\rm s}$. The equations above imply that X-ray irradiated discs have a lower surface density (and mid-plane density) and lower infall (radial) velocity than disc without X-ray irradiation. This indeed is what is observed in Panel (d), (e), and (i) in Fig. 3.5 (see black solid and dotted lines).

Using the Toomre Q parameter definition in equation (3.4) we find:

$$Q \approx \frac{c_{\rm s}^2}{\pi G \Sigma H} \frac{v_{\rm rot}}{v_{\rm kep}} \propto \frac{v_{\rm rot}}{v_{\rm kep}} \propto T_{\rm min}^{-1/2}, \tag{3.7}$$

where we assumed $\kappa = \Omega = v_{\rm rot}/R$ and that the rotational velocity of the disc is independent of the X-ray irradiation (as shown in Panel (g) of Fig. 3.5), and used equation (3.5) for the scale height H. Therefore we expect that Q increases and the disc becomes more stable (and with a more Keplerian rotation), with increasing X-ray irradiation (decreasing $T_{\rm min}$). Note that Panel (h)

in Fig. 3.5 supports the assertion that $f_{\rm kep} \equiv v_{\rm rot}/v_{\rm kep}$, similarly to Q, increases with increasing X-ray irradiation. Note that our approach differs slightly from previous modeling work of protostellar accretion discs around Pop III stars. Matsukoba et al. (2019) relate the disc stability to the viscous α parameter in a quasi-Keplerian disc, assuming that $\alpha > 1$ leads to large accretion rates and fragmentation. Kimura et al. (2021) argue that when the disc becomes more massive than the central star, the disc tends to experience fragmentation. Our model instead applies to early times ($t \sim 0$), when the disc may still be slightly contracting, before approaching a quasi-Keplerian rotation curve. However, our conclusions are qualitatively the same as we also find that discs with higher accretion rate (higher $T_{\rm min}$), when the central protostar forms deviate more strongly from Keplerian rotation, and fragment more rapidly. X-ray irradiation leads instead to the rapid formation of a Keplerian accretion disc with a lower accretion rate, and rather stable to fragmentation.

Finally, we can estimate the disc mass as a function of X-ray irradiation. If we define the disc outer radius $R_{\rm disc}$ where the surface density (or gas density) drops below a critical value, using a power-law fit with slope 1.5 (Panel (e) of Fig. 3.4 and 3.5) for the surface density profile ($\Sigma(R_{\rm disc}) \propto c_{\rm s}^2/R_{\rm disc}^{3/2} = \Sigma_{\rm crit}$), we find:

$$R_{\rm disc} \propto c_{\rm s}^{4/3} \propto T_{\rm min}^{2/3}. \tag{3.8}$$

Therefore, using the definition of disc radius above, the size of the disc decreases with increasing X-ray irradiation (decreasing $T_{\rm min}$). The mass of the disc also decreases with increasing X-ray irradiation as:

$$M_{\rm disc} \propto \Sigma(R_{\rm disc}) R_{\rm disc}^2 \propto R_{\rm disc}^2 \propto T_{\rm min}^{4/3}. \tag{3.9}$$

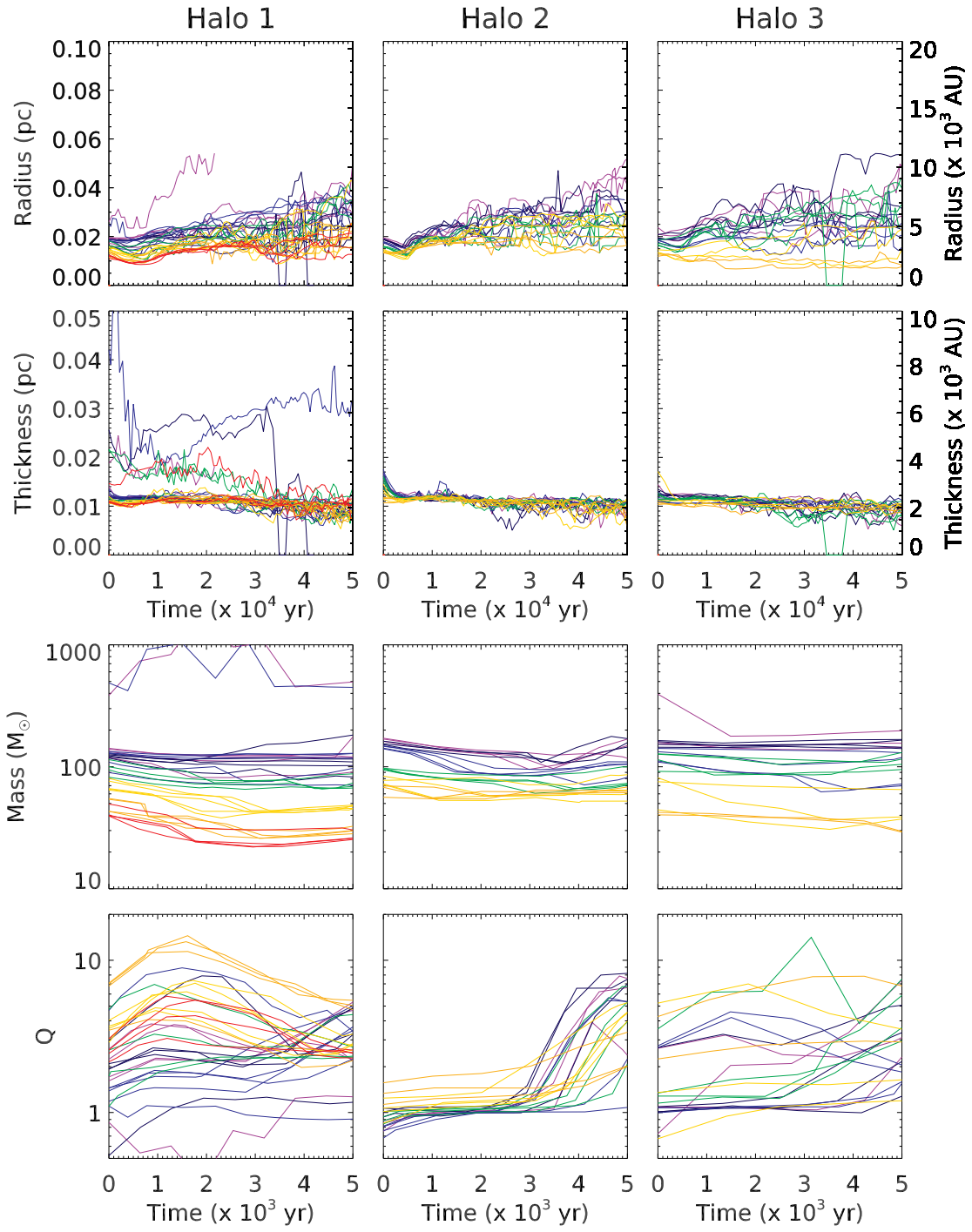

Figure 3.6: The radius, thickness, mass and average Toomre Q parameter of discs as a function of time. Each line shows a simulation with X-ray intensity color-coded as in Fig. 3.3. For the radius and thickness, we plot the results for 50 kyrs, while we only show the first 5 kyrs for the mass and Q due to its large variations at later times due to disc fragmentation. The radius and thickness of the disc are defined as where the gas density drops below 5×10^7 H cm^{-3}.

In order to check whether the simple scaling relationships derived above are consistent with the simulation results, in Fig. 3.6 in each row of panels, from top to bottom, we plot the disc radius, $R_{\rm disc}$, the disc thickness, h, the disc mass, $M_{\rm disc}$, and the average Toomre Q parameter as a function of time. Different columns refer to the three haloes and different $\rm J_{X0,21}$ are shown as lines of different colors (see legend). The X-ray irradiation has an effect on the disc size, with smaller disc sizes in a stronger X-ray radiation background (the top row), in agreement with the analytic estimate in equation (3.8). The disc thickness, $h(R)$, shown in the second row, is defined the same way as in Panel (j) of Fig. 3.5: as the height above the disc midplane where the density drops below 5×10^7 H cm^{-3}. The simulation results show that $h(R)$ is roughly constant as a function of disc radius R, while equation (3.5) shows $H/R \sim {\rm const(R)}$. The disc thickness h is related to H as $h \propto H \times n_{\rm H}(z=0)^{1/\beta}$, where we have approximated the density profile in the z-direction as a power-law: $n_{\rm H}(z) \propto n_{\rm H}(z=0)(1+z/H)^{-\beta}$. Assuming an isothermal profile for $n_{\rm H}(z=0) \propto c_{\rm s}^2/R^2$, and that $h(R)$ is constant as a function of R as shown by the simulations, we find $\beta = 2$ and $h(R) \propto (H/R)c_{\rm s} \propto c_{\rm s}$. This results is in qualitative agreement with Panel (j) of Fig. 3.5 and with the early time evolution ($t \sim 0$) of the disc thickness shown in the second-row panels in Fig. 3.6. However, at later times the mean disc thickness h becomes nearly independent of the X-ray intensity and remains rather constant as a function of time for 50 kyrs. The third row of panels in Fig. 3.6 show the discs masses become smaller with increasing X-ray irradiation, as expected by equation (3.9). In the bottom panels, we plot the average Q parameter as a function of time for the first 5 kyrs of the disc evolution. As from the analytic model, the figure shows that the disc is smaller, has lower surface density, and is more stable (larger Toomre Q parameter) with increasing intensity of the X-ray background. Especially in Halo 2 (and to a lesser extent for Halo 1), which experiences slow growth during star formation, this trend is clear: in a weak X-

ray background $Q < 1$ and increases as the disc is more strongly irradiated by X-rays. In Halo 3 the trend is less clear, probably due to its rapid growth. As Hummel et al. (2015) points out, the growth rate of the minihalo is also an important factor for the fragmentation of the protostellar disc, and can wash out the dependence on the X-ray intensity.

3.4 Multiplicity and Migration of Population III stars

Fig. 3.7 shows the masses (top panels) and the distances from the disc centre (bottom panels) of individual clumps in Halo 2 for different X-ray backgrounds. The mass of the most massive clump (red dots) tends to be smaller in a stronger X-ray background, similarly to the total mass. Disc fragmentation occurs $\sim$ 10 kyrs after the formation of the first clump for the cases with no or weak X-ray background (left and middle panel), while it occurs at $\sim$ 30 kyrs in a strong X-ray background (right panel).

One important aspect of the formation of Pop III star is the survival of the stars after disc fragmentation. Previous simulations showed that while the inward migration of secondary stars leads to the merger with the primary stars, protostars are also observed to migrate outward (see Greif et al., 2012; Stacy and Bromm, 2013; Stacy et al., 2016; Hirano and Bromm, 2017; Susa, 2019; Chon and Hosokawa, 2019; Sugimura et al., 2020). The star migration is affected by gas in the disc through two main processes: i) accretion of gas with higher angular momentum of the protostar produces an outward migration (in a Keplerian disc it is the gas with orbit outward of the protostar orbit); ii) dynamical friction and gravitational torques mediated by resonances, produce a migration inward of the protostars by loss of their angular momentum and energy to the disc (but see, Tiede et al., 2020). Typically the first process is dominant when the disc is thick,

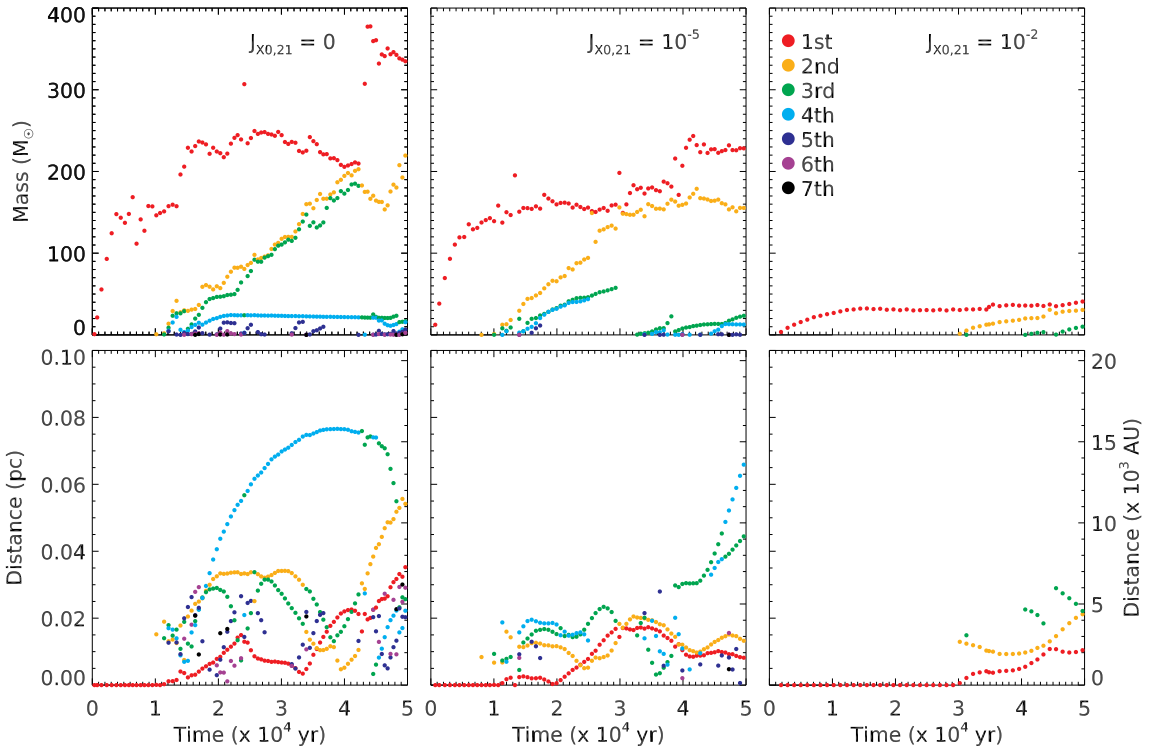

Figure 3.7: Masses (top panels) and distances from the centre (bottom panels) of individual clumps in Halo 2 as a function of time after the formation of the first clump. From left to right, $J_{X0,21}$ is $0, 10^{-5}$ and 10^{-2}. The masses and positions of protostars (disc fragments) are color-coded as shown in the legend, from the most massive to the least massive fragment.

such as the zero-metallicity discs in this study (Heath and Nixon, 2020; Sugimura et al., 2020). In the bottom panels of Fig. 3.7 we plot the distances of individual clumps from the centre-of-mass. In each panel, the most massive clump (red dots) forms first, at the centre of the disc so its initial distance is zero. As the disc fragments and the second clump forms and grows, the primary and secondary protostars both migrate outward from the centre. In zero or weak X-ray backgrounds (left and middle panel), several clumps migrate beyond 10^4 AU while no one migrates to such a large distance for $\sim$ 80 kyr in a strong X-ray background. We speculate this is related to the property of the protostellar disc. The gas accretion of high angular momentum gas onto the protostar is slow and therefore clumps do not migrate rapidly outward. In addition, there are fewer

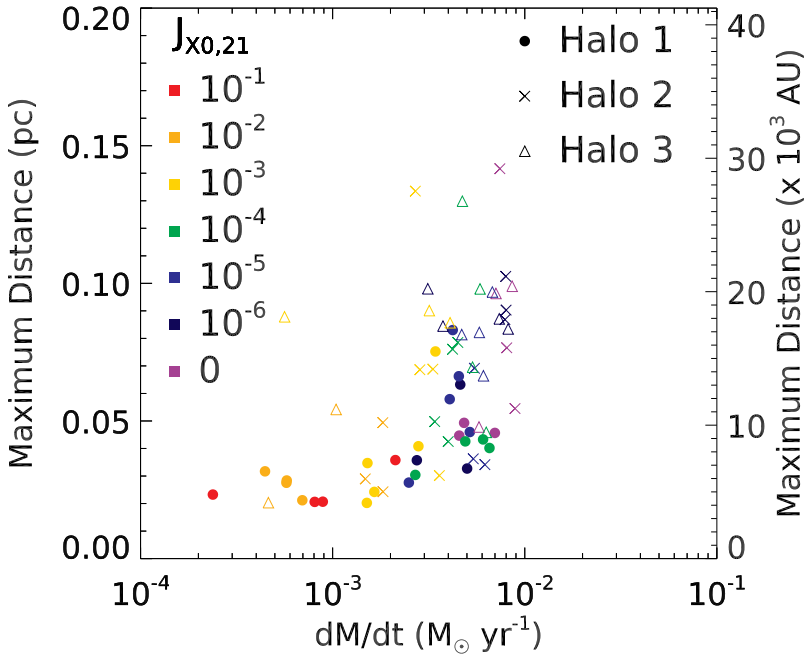

Figure 3.8: Maximum distance of a clump as a function of the gas accretion rate at $n_{\rm H} = 10^7$ H cm^{-3} and $\mathrm{d}M/\mathrm{d}t|_{\rm cr}$. The symbols and color of each point indicate the intensity of the X-ray radiation background and host halo, as in the legend. Only simulations with a critical mass lower than 10^6 M$_\odot$ are shown in the plot.

stars that cause outward migration through angular momentum transfer (see Greif et al., 2012; Stacy and Bromm, 2013). We plot the maximum distance of clumps in each system as a function of the accretion rate at $n_{\rm H} = 10^7$ H cm^{-3} in Fig. 3.8. The large vertical scatter of symbols for $\mathrm{d}M/\mathrm{d}t|_{\rm cr} \sim 2 \times 10^{-3} - 10^{-2}$ M$_\odot$ yr^{-1}, indicates migrations beyond 10^4 AU are common in a weak X-ray background. On the contrary, outward migration is rare in a strong X-ray background and the maximum distances are smaller than 10^4 AU. Fig. 3.9 shows the probability distribution of distances from the disc centre of protostars in a weak ($\mathrm{J}_{\rm X0,21} \leq 10^{-3}$, blue shaded histogram) and strong ($\mathrm{J}_{\rm X0,21} > 10^{-3}$, red shaded histogram) X-ray background. The distances are measured either when the total mass of the stars is equal to $M_{\rm final}$ (equation (3.2)) or at the end of the simulation at $t = 5 \times 10^4$ yrs if the total mass does not reach this limit. Stars in host haloes more massive than 10^6 M$_\odot$ are not taken into account in this analysis. The two distributions are rather

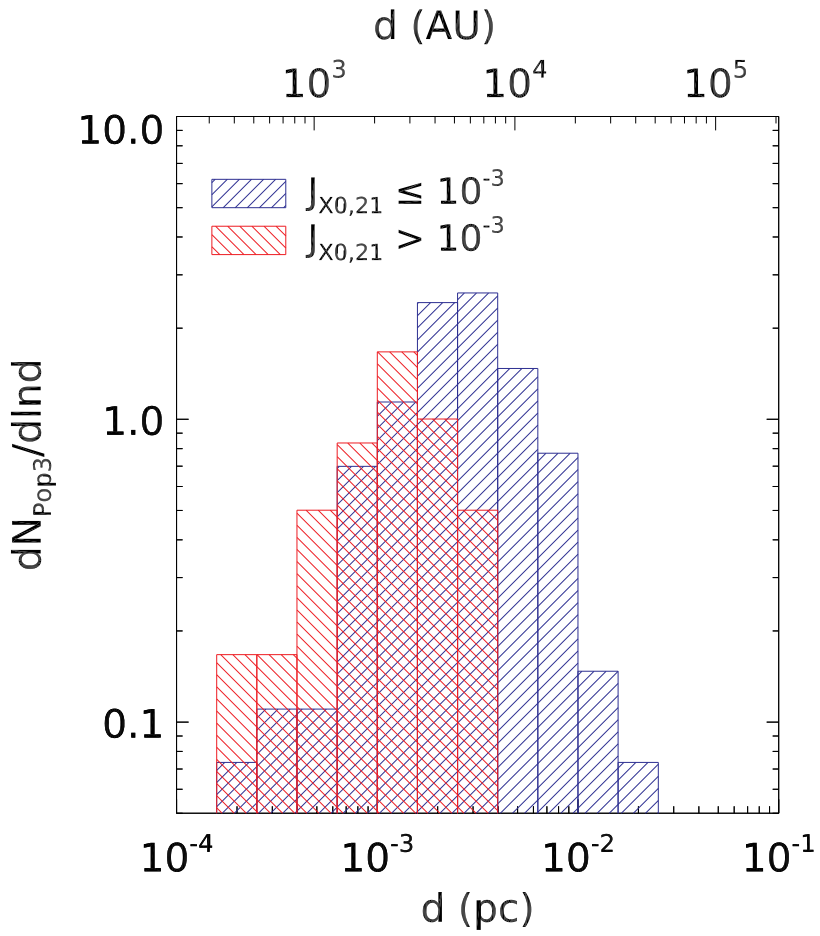

Figure 3.9: Histogram of the distances of Pop III stars from the centre-of-mass in a weak ($J_{X0,21} \leq 10^{-3}$, blue) and strong ($J_{X0,21} > 10^{-3}$, red) X-ray background. The distances are measured either when the total mass of the stars is equal to $M_{\rm final}$ (see equation 3.2) or at $t = 5 \times 10^4$ yrs if the total mass does not reach this limit. Pop III stars forming in host haloes more massive than 10^6 $M_\odot$ are not included in this plot.

similar to each other and symmetric, but the peaks are offset by $\sim$ 3000 AU: at $\sim$ 6000 AU and at $\sim$ 3000 AU in weak and strong X-ray background, respectively. This result also suggests that the accretion rate onto the protostar drives the outward migration.

To study the IMF we need to determine the masses of individual stars. Unlike the total mass, however, individual clumps do not always grow linearly. For this reason, we cannot use the same approach we use in Paper I to estimate the total mass. Instead, define the clump masses

at the time when the total mass reaches $M_{\rm final}$ or, if this condition is not met, at the end of the simulations: ~ 50 kyrs after the formation of the first clump. We define $M_{\rm P}$ as the mass of the most massive star (the primary star) and $M_{\rm S}$ as the mass of the second most massive star (or the secondary star). We also count the total number of clumps that form in the discs. If clumps form and merge to form more massive ones within three snapshot intervals ($\sim 2-3$ kyr), we do not count them as individual clumps. Although this criterion is rather arbitrary, the number and merger history of small mass clumps and/or close binaries is intrinsically uncertain, as it also strongly depends on the initial conditions and the resolution of the simulations.

Panel (a) of Fig. 3.10 shows that the number of clumps decreases with increasing X-ray intensity. The gas disc is more stable in a stronger X-ray background and therefore undergoes fewer fragmentations. In the absence of both X-ray and LW radiation backgrounds, for instance, six clumps form out of the protostellar disc in Halo 2 (one of the clumps merges with a more massive one shortly after its formation). When the total mass reaches $M_{\rm final}$ (~ 33 kyrs after the first clump formation), the system is composed of three massive clumps ($M > 100$ $\rm M_\odot$) and two small ones ($M < 20$ $\rm M_\odot$). On the other hand, in a strong X-ray background, a binary system is formed at ~ 50 kyrs. Two additional smaller mass clumps form in this simulation, but they quickly merge with the other two.

Panel (c) shows the ratio of $M_{\rm P} + M_{\rm S}$ to the total mass. As $\rm J_{X0,21}$ increases, the mass ratio converges to 1. This is consistent with the trend of $\rm N_{star}$ in panel (a), because fewer stars form in a strong X-ray background, and thus the primary plus secondary stars account for most of the mass. The range of the mass ratio gets wider in a weak X-ray background because of the large scatter in the number of stars.

Hence, the multiplicity of stars is related to the intensity of the X-ray background, but what

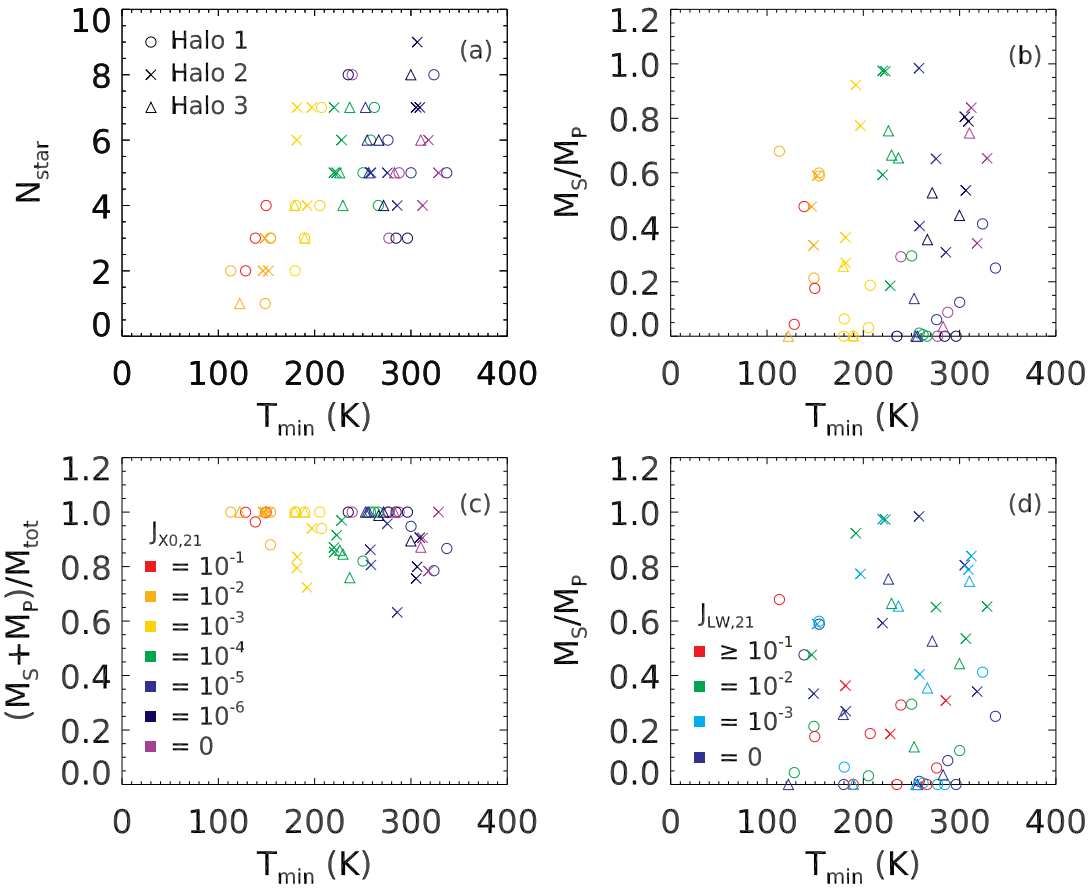

Figure 3.10: Panel (a): Total number of clumps when the total mass exceeds $M_{\rm final}$, including clumps that merged with others. The symbol and color of each point indicates the intensity of the X-ray background, $\rm J_{X0,21}$, and the host halo, as shown in the legend. Results with the critical masses $> 10^6$ $\rm M_\odot$ are omitted. Panel (b): The mass ratio of the two most massive (primary, $M_{\rm P}$, and secondary, $M_{\rm S}$) stars. Panel (c): the ratio of $M_{\rm P} + M_{\rm S}$ to the total mass. Panel (d): Same as Panel (b) but the colors indicates the intensity of the LW background.

is the dependence of the mass function of the clumps on the X-ray background? Panel (b) of Fig. 3.10 shows $M_{\rm S}/M_{\rm P}$ as a function of $T_{\rm min}$. In most simulations, the primary and secondary stars have similar masses ($M_{\rm S}/M_{\rm P} \sim 0.8 - 1$), but the scatter is large, and, considering all the haloes, no clear trend with X-ray intensity is found. However, if we exclude Halo 1 from the analysis (circles), there is a preference for forming equal-mass binary stars in a strong X-ray background. We have seen before that some trends in Halo 1 are less clear due to its rapid accretion rate

and a merger with a satellite clump during Pop III formation. To investigate the role of the LW background on the mass function, we also color-code the symbols according to the LW intensity in Panel (d). With low LW intensity ($J_{LW,21} \leq 10^{-2}$), symbols are widely distributed and show no significant correlation between the backgrounds and the mass ratio. On the other hand, when the LW background is stronger than or equal to 10^{-1}, the two most massive stars tend to be of similar mass.

The trends found so far are quite clear if we bin all the simulation results for the three haloes in two groups: haloes in a strong and weak X-ray background. In the left panel of Fig. 3.11 we show the mass function of the fragments (protostars) in weak ($J_{X0,21} \leq 10^{-3}$, blue shaded histogram) and strong ($J_{X0,21} > 10^{-3}$, red shaded histogram) X-ray background.

Both mass functions are top-heavy and they can be described as a power-law with an exponential cutoff,

$$\frac{dN}{d\ln M} = AM^{\alpha} \exp\left[-\left(\frac{M}{M_{\rm cut}}\right)^2\right]. \tag{3.10}$$

Parameters of each mass function are shown in Table 3.2 with the peak mass ($M_{\rm peak} = M_{\rm cut}\sqrt{\alpha/2}$). They are normalized so that the total mass in each distribution is the mean mass per halo and the total number of stars is the mean multiplicity (*i.e.*, dividing the total mass by the number of runs in each group). The mass function in a strong X-ray background is steeper (higher α) and has a lower peak mass. These differences can be explained by the following two factors. First, the protostellar disc experiences fewer fragmentations and therefore there are fewer low-mass stars in a strong X-ray background. Secondly, in a strong X-ray background, the lower accretion rate leads to a smaller total mass disc stars, $M_{\rm final}$, and a smaller primary star mass ($M_{\rm P}$). Hence both the cutoff mass and the total mass in fragments are lower by about a factor of $2-3$ in a strong

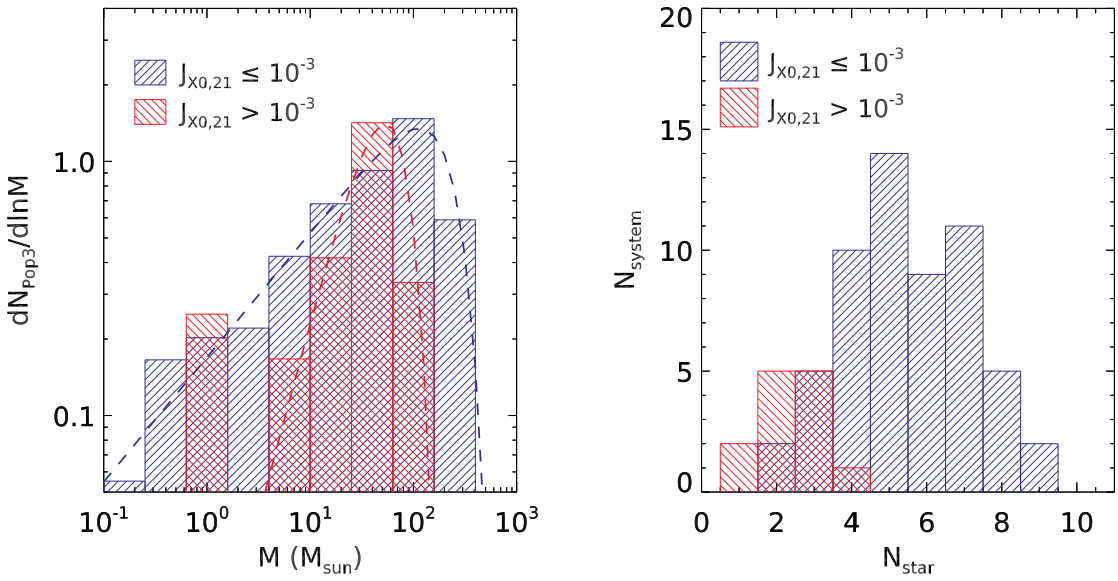

Figure 3.11: Mean mass function per halo (left panel) and distribution of the multiplicity of stars in each halo, $N_{\rm star}$ (right panel) in a weak (blue histograms) and strong (red histogram) X-ray background. The dashed lines in the left panel show the fits to the mass functions with equation (3.10). The parameters of the fit are shown in Table 3.2, including the total mass in Pop III stars, $M_{\rm tot}$, and the average multiplicity per halo $N_{\rm tot} = \int_{\ln 0.1\,{\rm M}_\odot}^{\ln 1000\,M_\odot} ({\rm d}N_{\rm pop3}/{\rm d}\ln {\rm M})\,{\rm d}\ln M$. The values $N_{\rm tot} \sim 2$ and ~ 4 found for the strong and weak X-ray background, respectively, are consistent with the multiplicity distribution shown in the right panel.

X-ray background.

Note that these are mass functions created from multiple stellar systems in only three mini-haloes, but for a large number of simulations with different combinations of the X-ray and LW backgrounds. Hence the variance on the total mass and the mass of the most massive fragment may be not representative of all Pop III stars. Also, we have used a simplistic prescription to take into account the effect of feedback in determining the final masses of the fragments, that may not be accurate. Nevertheless, the distribution should be a rather accurate representation of the initial mass function of the disc fragments, before longer timescale dynamical processes destroy the systems be either ejecting stars or merging them or forming tight binary systems.

The right panel in Fig. 3.11 shows the distribution, $dN_{\rm system}/d\ln N_{\rm star}$, of the stellar mul-

Table 3.2: Parameters of Mass Functions

$J_{X0,21}$	α	M_{cut}	A	M_{peak}	M_{tot}	N_{tot}
$\leq 10^{-3}$	0.490	229 $M_\odot$	0.169	113 $M_\odot$	341 $M_\odot$	4.39
$> 10^{-3}$	1.53	61 $M_\odot$	0.00692	53.4 $M_\odot$	102 $M_\odot$	2.25

tiplicity, N_{star}, of each system (minihaloes). All the systems in a strong X-ray background are either binary or triple/quadruple systems. On the contrary, in a weak X-ray background most of the systems have multiplicity greater than five.

3.5 Discussion

It has been recognized for several years that the first metal-free stars forming in the universe have a top-heavy IMF (Bromm et al., 2001; Abel et al., 2002; Bromm et al., 2002). Hence, the first stars can produce powerful hypernova explosions detectable with JWST and NRST (Whalen et al., 2014), producing a population of IMBHs that may contribute to the gravitational wave detections in LIGO (Abbott et al., 2016). In addition strong or weak feedback from Pop III star explosions and the metal enrichment they produce, may have important effects on the formation of Pop II stars in the first galaxies (Ricotti et al., 2002b, 2008; Wise and Abel, 2008; Greif et al., 2010; Abe et al., 2021).

LW and X-ray photons emitted by Pop III stars and their remnants can travel large distances without being absorbed and build a radiation background. Ionization by the X-ray background produces high-energy photo-electrons and in a mostly neutral gas, a large fraction of their kinetic energy is deposited into secondary ionization (Shull and van Steenberg, 1985). These backgrounds regulate H_2 formation on cosmological scales and thus the formation of early objects (first stars and their remnants such as SNe and HMXBs, Venkatesan et al., 2001; Jeon et al.,

2014a; Ricotti, 2016; Xu et al., 2016). The effects of the LW radiation background on Pop III star formation have been studied rather extensively (Haiman et al., 2000; Omukai, 2001; O'Shea and Norman, 2008; Johnson et al., 2013; Hirano et al., 2015; Regan et al., 2020), instead the role of the X-ray radiation background has received less attention and the impact X-rays have on the formation rate and the IMF of the first stars is still debated (Haiman et al., 2000; Jeon et al., 2014a; Hummel et al., 2015; Ricotti, 2016).

In this study, the second in a series, using zoom-in simulations of three minihaloes with different masses and irradiated by different intensities of the LW and X-ray backgrounds, we investigate the effect of radiation backgrounds on the properties of protostellar discs and their fragmentation, therefore deriving the multiplicity and mass function of the first stars. Below we summarize the key results of the simulations.

1. X-ray radiation affects the properties of protostellar discs and their fragmentation. The discs have lower surface density, they are smaller in size and mass and are more stable to gravitational instabilities (*i.e.*, they have larger Toomre Q parameter).

2. Pop III stars in a weak or absent X-ray background form multiple systems of 6 ± 3 stars, with masses around $100\ \mathrm{M}_{\odot}$ and typical distance from the centre of mass of 2,500-20,000 au.

3. Pop III stars in a strong X-ray background typically form binary systems of nearly equal mass stars with individual masses around $40\ \mathrm{M}_{\odot}$ and distances from the centre of mass of 1,000-5,000 au.

4. Independently of the strength of the X-ray background, protostars form near the centre of the disc (within 5000 au) and migrate outward while growing in mass. The migration is

mainly driven by the accretion of gas with higher specific angular momentum from the outer parts of the nearly Keplerian disc.

5. We find that the mass function of the fragments is well described by a power law with a positive slope and an exponential cutoff. In a strong X-ray background, the mass function of protostars is slightly more top-heavy, with slope $\alpha = 1.53$ and mass cutoff of $61\ \mathrm{M}_\odot$. While for weak or no X-ray background $\alpha = 0.490$ and $M_{\rm cut} = 229\ \mathrm{M}_\odot$.

The final fate of Pop III stars of a given mass is still rather uncertain, but following the work of (Heger and Woosley, 2002; Nomoto et al., 2006) we will assume that Pop III stars with masses in the range $40\ M_\odot < M < 140\ \mathrm{M}_\odot$ and $> 260\ \mathrm{M}_\odot$ collapse directly into BHs without releasing mechanical energy and metals by SN explosions. Instead stars with masses $140\ \mathrm{M}_\odot < M < 260\ \mathrm{M}_\odot$ explode as PISNe without leaving any remnant. Finally stars with masses $11\ \mathrm{M}_\odot < M < 20\ \mathrm{M}_\odot$ explode as normal SNe and stars with masses $20\ \mathrm{M}_\odot < M < 40\ \mathrm{M}_\odot$ as hypernovae.

Given the caveats on the mass function discussed in Section 3.4 and the uncertainties on the final fate of Pop III stars of a given mass, it is nevertheless interesting to estimate the energy in SN explosions and the mass of BH remnants for the strong and weak X-ray irradiation cases. Following Wise et al. (2012) we will assume that

$$\frac{E_{\rm SN}(M)}{10^{51}\ \mathrm{erg}} = \begin{cases} 1 & \text{if } 11\ \mathrm{M}_\odot \leq M < 20\ \mathrm{M}_\odot \\ -13.714 + 1.806M & \text{if } 20\ \mathrm{M}_\odot \leq M < 40\ \mathrm{M}_\odot \\ 5 + 1.304(M_{\rm He} - 64) & \text{if } 140\ \mathrm{M}_\odot \leq M < 260\ \mathrm{M}_\odot \\ 0 & \text{otherwise} \end{cases}, \tag{3.11}$$

where M is the mass of the zero-age main-sequence star and $M_{\rm He} = (13/24)(M - 20)\ {\rm M}_\odot$. The following is the fit to the mass of the remnant (Heger and Woosley, 2002),

$$\frac{M_{\rm rem}(M)}{\rm M_\odot} = \begin{cases} 1.665 & \text{if } 11\ {\rm M}_\odot \leq M < 20\ {\rm M}_\odot \\ -1.032 + 0.1349M & \text{if } 20\ {\rm M}_\odot \leq M < 25\ {\rm M}_\odot \\ \sum_{\rm i=0}^{4} c_{\rm i} M^i & \text{if } 25\ {\rm M}_\odot \leq M < 100\ {\rm M}_\odot \\ 65 & \text{if } 100\ {\rm M}_\odot \leq M < 140\ {\rm M}_\odot \\ 0 & \text{if } 140\ {\rm M}_\odot \leq M < 260\ {\rm M}_\odot \\ -7.761 + 0.8138M & \text{if } 260\ {\rm M}_\odot < M \leq 500\ {\rm M}_\odot \end{cases}, \tag{3.12}$$

where $c_0 = 45.38, c_1 = -4.415, c_2 = 0.1430, c_3 = -0.001559$, and $c_4 = 5.905 \times 10^{-6}$. Note that a black hole forms when the initial mass is greater than $20\ {\rm M}_\odot$. We derive

$$E_{\rm SN}^{\rm tot} = \int E_{\rm SN}(M) \frac{dN_{\rm pop3}}{d\ln M} d\ln M, \tag{3.13}$$

and

$$M_{\rm rem}^{\rm tot} = \int M_{\rm rem}(M) \frac{dN_{\rm pop3}}{d\ln M} d\ln M. \tag{3.14}$$

An important parameter of the radiation background is the ratio of the energies per source $\beta \equiv E_{\rm X-ray}/E_{\rm LW}$ (Ricotti, 2016). We compare the average energies per $100\ {\rm M}_\odot$ in a weak and a strong X-ray background. We find that total supernova explosion and LW energies per $100\ {\rm M}_\odot$ are comparable, although the two IMFs are different in slope and peak mass. The total supernova explosion energies are $E_{\rm SN}^{\rm tot} \sim 1.63 \times 10^{52}$ and 2.13×10^{52} erg. In a weak X-ray background, PISNe are the main energy source while most of the energy comes from hypernovae ($20 < M_* <$

$40\ \mathrm{M}_{\odot}$) in a strong X-ray background. The energy in the LW band is roughly proportional to the total mass in Pop III stars, thus for $100\ \mathrm{M}_{\odot}$ is $E_{\mathrm{LW}} \sim 2.10 \times 10^{53}$ and 1.90×10^{53} erg in both backgrounds. Assuming $E_{\mathrm{X-ray}}/E_{\mathrm{SN}}^{\mathrm{tot}} = 0.006$ (see Ricotti, 2016) the derived values of β are: $\beta \sim 4.64 \times 10^{-4}$ for weak X-ray irradiation and $\beta \sim 6.74 \times 10^{-4}$ for strong X-ray irradiation. Therefore, the IMF of Pop III stars does not have a strong effect on the spectral energy distribution parameter β of the sources. As discussed in Paper I, however, an X-ray background lowers the critical mass for star formation of haloes (hence increasing the total number of haloes forming Pop III stars) and reduces the total mass in Pop III stars per halo. Hence, the X-ray background is nevertheless able to reinforce the feedback loop and promote Pop III star formation.

A result of interest to LIGO science is the mass distribution function of Pop III remnants, shown in Fig. 3.12 for a weak (red histogram) and a strong (blue histogram) X-ray background. The dashed lines show the same distribution function obtained using Monte-Carlo simulations for 10^5 stars. One notable difference between the distribution functions is the lack of IMBHs with mass $> 100\ \mathrm{M}_{\odot}$ and the lack of Pop III stars exploding as PISNe, for the strong X-ray case. This leads to a higher abundance of low-mass BH remnants with $M < 65\ \mathrm{M}_{\odot}$. The Monte-Carlo simulations produce remnants of $158\ \mathrm{M}_{\odot}$ and $63.0\ \mathrm{M}_{\odot}$ out of $341\ \mathrm{M}_{\odot}$ and $102\ \mathrm{M}_{\odot}$ Pop III stars in the two groups. The masses of the remnants per $100\ \mathrm{M}_{\odot}$ are $46.3\ \mathrm{M}_{\odot}$ and $61.1\ \mathrm{M}_{\odot}$, respectively.

In future work, we will improve on these results considering physical processes neglected or treated with simplifying approximations in this work. In particular, we plan to assess the importance of HD molecular cooling in determining the mass function of Pop III stars and further investigate the effect of X-ray self-shielding. Most importantly, rather than using the empirical method adopted in this work to estimate the final masses of Pop III stars, we will use radiative transfer simulations to model the effect of UV radiation feedback from accreting protostar in

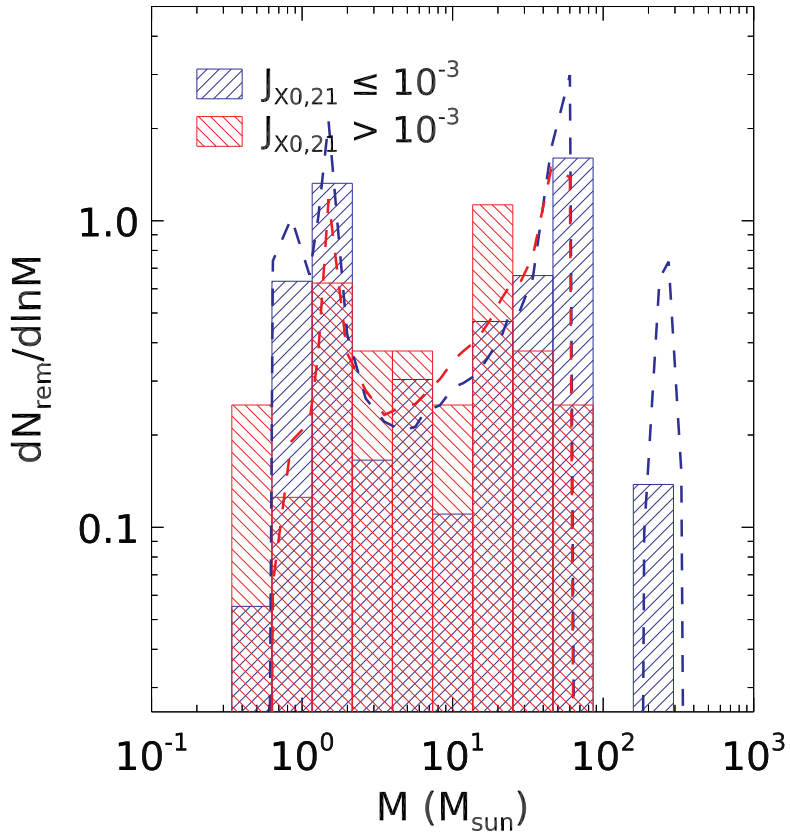

Figure 3.12: The mass functions of compact remnants (NS and BHs) in the two samples corresponding to the mass functions in Fig. 3.11. We converted the masses of stars into those of the remnants using equation (3.12) from results in Heger and Woosley (2002). The dashed lines show the remnant's mass functions obtained using Monte-Carlo simulations with 10^5 stars. The mass functions are normalized consistently with Fig. 3.11, so that the total initial mass in Pop III stars is equal to the mean mass in Pop III star per halo in each group.

reducing the accretion rate and stopping the growth of Pop III stars.

Chapter 4: Population III Star Formation in an X-ray Background - III. Periodic Radiative Feedback and Luminosity Induced by Elliptical Orbits

We model Pop III star formation in different FUV and X-ray backgrounds, including radiation feedback from protostars. We confirm previous results that a moderate X-ray background increases the number of Pop III systems per unit cosmological volume, but the masses and multiplicities of the system are reduced. The stellar mass function also agrees with previous results, and we confirm the outward migration of the stars within the protostellar discs. We find that nearly all Pop III star systems are hierarchical, *i.e.*, binaries of binaries. Typically, two equal-mass stars form near the centre of the protostellar disc and migrate outward. Around these stars, mini-discs fragment forming binaries that also migrate outward. Stars may also form at Lagrange points L4/L5 of the system. Afterward, star formation becomes more stochastic due to the large multiplicity, and zero-metallicity low-mass stars can form when rapidly ejected from the disc. Stars in the disc often have eccentric orbits, leading to a periodic modulation of their accretion rates and luminosities. At the pericenter, due to strong accretion, the star can enter a red-supergiant phase reaching nearly Eddington luminosity in the optical bands ($m_{\rm AB} \sim 34$ for a 100 $M_\odot$ star at z=6). During this phase, the star, rather than its nebular lines, can be observed directly by JWST, if sufficiently magnified by a gravitational lens. The $\sim 10,000$ AU separations and high eccentricities of many Pop III star binaries in our simulations are favorable parameters for IMBH mergers –

and gravitational waves emission – through orbital excitation by field stars.

4.1 Introduction

The James Webb Space Telescope (JWST) and next-generation observatories, such as Nancy Grace Roman Space Telescope (NRST), will enable us to observe and study the properties of high-z galaxies and perhaps discover the first metal-free stars (or Pop III stars). The properties of the first generation of galaxies are sensitive to the poorly constrained models of Pop III star formation because the first stars enrich and spread in the intergalactic medium the first heavy elements (Ricotti, Gnedin, and Shull, 2002a,b; Greif et al., 2010; Wise et al., 2012; Safranek-Shrader, Milosavljević, and Bromm, 2014; Chiaki, Susa, and Hirano, 2018; Abe et al., 2021) that enable and regulate the formation of the second generation stars.

One of the key properties of Pop III stars is their initial mass function (IMF). The mass determines the luminosity of the stars (Schaerer, 2002), therefore the strength of their UV feedback (FB) which blows out the gas in the host halos (Wise and Abel, 2008), but also their metal yield and the SN/hypernova explosion energy (*e.g.*, Nomoto et al., 2006). For instance, Pop III stars are thought to explode as pair-instability supernovae (PISNe) if their masses are $140\ \mathrm{M}_\odot < M < 260\ \mathrm{M}_\odot$ (Heger and Woosley, 2002). The death of these massive stars as hypernovae/PISNe is detectable by JWST or NRST (Whalen et al., 2014), thereby providing constraints on the number and typical masses of Pop III stars.

Another poorly known but important aspect of Pop III stars is their multiplicity. The formation of multiple Pop III protostars systems has been observed in high-resolution simulations (Stacy, Greif, and Bromm, 2010; Clark et al., 2011b; Stacy and Bromm, 2013; Sugimura et al.,

2020), offering a channel of formation of intermediate-mass binary black holes (BBHs). Given the large remnant masses of Pop III stars, the primordial origin of mergers of BBHs detected by VIRGO and LIGO collaboration (Abbott et al., 2016, 2017) is an open possibility, although the expected merger rates are small and uncertain (Hartwig et al., 2016). Pop III binaries can also evolve to high-mass X-ray binaries (HMXBs) which emit X-ray photons. Owing to their long mean free paths, X-rays produce background radiation that can efficiently heat and partially ionize the intergalactic medium and thus have important effects on galaxy formation and reionization (Haiman, Abel, and Rees, 2000; Oh, 2001; Venkatesan et al., 2001; Glover and Brand, 2003; Ricotti and Ostriker, 2004; Ricotti, Ostriker, and Gnedin, 2005; Mirabel et al., 2011; Xu et al., 2014; Jeon et al., 2014a). Whether HMXBs are a dominant source of X-rays in the early universe depends on the number of Pop III binaries (Stacy and Bromm, 2013; Hummel et al., 2015) and therefore the properties of primordial protostellar discs leading to their fragmentation and the formation of multiple Pop III star systems. Prediction of the typical masses and multiplicity of Pop III stars requires modelling several physical processes. One of them is the unknown intensity of the X-ray radiation background that must be present because of the unavoidable emission by Pop III supernovae, but also HMXBs and accreting intermediate-mass black holes (Park and Ricotti, 2011). X-ray photons boost molecular hydrogen (H_2) formation in the gas phase by partially ionizing the intergalactic medium as shown by various authors (Haiman et al., 2000; Ricotti et al., 2001; Venkatesan et al., 2001; Ricotti, 2016). These authors claimed that an X-ray background may compensate the negative FB of H_2-dissociating photons in Lyman-Werner (LW) bands. The impact of X-ray irradiation on the typical masses and multiplicity of Pop III stars was first studied in the seminal work of Hummel et al. (2015). However, their conclusion was that X-rays play a minor role in Pop III star formation. On the other hand, in Park, Ricotti, and

Sugimura (2021a) and Park, Ricotti, and Sugimura (2021b, Paper I and Paper II hereafter), using a set of hydrodynamics simulations we showed that an X-ray background can increase the number of minihalos forming Pop III stars but at the same time it reduces their typical masses and multiplicity.

An important physical process affecting the final masses of Pop III stars is the FUV and EUV radiative feedback (hereafter, RFB[1]) from the stars themselves. Protostars emit FUV photons in the LW bands that can dissociate H_2 in the protostellar disc, and hydrogen ionizing EUV photons that erode and evaporate circumstellar discs, eventually terminating the gas accretion onto them, hence determining their final masses (*e.g.*, McKee and Tan, 2008; Hosokawa et al., 2011). The impact of RFB on Pop III star formation was studied in various minihalos by several authors (McKee and Tan, 2008; Whalen et al., 2008; Stacy et al., 2012; Hirano et al., 2014; Stacy and Bromm, 2014; Hirano et al., 2015; Hosokawa et al., 2016; Sugimura et al., 2020; Latif et al., 2022). In Paper I and II we studied the effect of X-rays on Pop III star formation but we did not directly simulate RFB by UV radiation from protostars, instead, we used an empirical relationship by Hirano et al. (2015, hereafter HR15) to estimate the effect of UV FB and the final masses of Pop III stars. In this work, we build on the results in Paper I and II by simulating the combined effect of RFB and an external X-ray background. This is the first study investigating the masses and multiplicity of Pop III stars regulated by RFB in different X-ray and LW radiation backgrounds.

A physical process that is potentially important in the presence of a strong X-ray background is gas cooling by hydrogen-deuteride (HD) molecules. Thanks to its small dipole moment

[1]Both X-ray/LW background radiation and protostellar radiation effects are called ‘feedback’, but we term only the latter ’RFB’.

HD is an efficient coolant in the early universe (Lipovka, Núñez-López, and Avila-Reese, 2005; Galli and Palla, 2013) and enables the primordial gas to cool down to a few tens of Kelvins. Cooling by HD, therefore, can lower the mass of Pop III stars down to a few $\sim 10\,\mathrm{M}_{\odot}$ (Nagakura and Omukai, 2005). This effect is thought to be important in the formation of second-generation Pop III stars rather than the first-generation.[2] For instance, Pop III stars forming in the gas previously ionized by other Pop III stars (recombining H II regions, see Ricotti et al. (2001)) have lower masses due to the enhanced HD formation and cooling (Yoshida et al., 2007). Cosmic rays (Nakauchi et al., 2014) and/or an X-ray background (Jeon et al., 2014a; Hummel et al., 2015), can also boost the abundance of HD to allow significant cooling to low temperatures.

In this work, we explore the formation and evolution of Pop III protostars in primordial discs regulated by RFB from protostars, also exploring the effects of HD cooling, irradiated by different intensities of an external LW and X-ray backgrounds. This includes their mass growth and motions in the discs. We simulate, with higher resolution with respect to our previous work, a subset of the grid of simulations presented in Paper I and II, either including or excluding RFB from the accreting protostars. We run the simulations for about 100 kyr after the formation of the protostar, a time comparable to the accretion timescale of the protostars (HR15).

The rest of the paper is structured as follows. In Section 4.2 we introduce our simulations and methods with emphasis on the improvements with respect to Paper I and Paper II. In Section 4.3, we present the results of the simulations and discuss the RFB effect in each. In Section 4.4, we discuss the effects of including HD cooling. In Section 4.5, we discuss the implications of our results. In Section 4.6 we summarize the paper and present the key results.

[2]Sometimes they are called Pop III.2 and Pop III.1 in the literature, but we do not make a distinction between them in this work.

4.2 Simulation

The simulations in this paper are run with the adaptive mesh refinement (AMR) radiative hydrodynamics (RHD) code RAMSES-RT (Teyssier, 2002; Rosdahl et al., 2013). RAMSES-RT has been used in RHD simulations of galaxy formation (*e.g.*, Kimm et al., 2017; Katz et al., 2017) and metal-rich star formation (*e.g.*, He, Ricotti, and Geen, 2019, 2020; Commerçon et al., 2022; Han et al., 2022). To our best knowledge, our simulations are the first ones carried out with RAMSES-RT to model RFB from Pop III protostars. For this reason, in this section, we describe in detail the relevant physics modules we added to the code to simulate Pop III star formation.

4.2.1 Grid of Cosmological Initial Conditions and Zoom-in Simulations

Pop III star formation occurs in a protostellar disc and therefore the disc must be resolved with a high spatial resolution ($\sim$ AU) in the simulation. Therefore, to resolve the disc in a cosmological simulation we need to cover a prohibitively large dynamical range (from Mpc to AU). To circumvent this problem we use the same approach taken in several previous studies (Smith et al., 2011; Hirano et al., 2014; HR15; Sugimura et al., 2020). First, we run cosmological zoom-in simulations as in Paper I and Paper II. These include simulations of three haloes of different masses irradiated by various LW and soft X-ray background intensities (see Paper I for details of the setup). We also include some previously neglected physics (HD cooling and X-ray self-shielding) described below. We stop the zoom-in simulations when the central hydrogen number density reaches $n_{\rm H} \sim 10^7$ H cm^{-3} or at $z \sim 10$. Fig. 4.1 shows the redshift when the gas density in the haloes reaches $n_{\rm H} \sim 10^7$ H cm^{-3} for a grid of simulations with different intensities of the LW background (x-axis) and X-ray background (y-axis) for two haloes. Within this set of low-

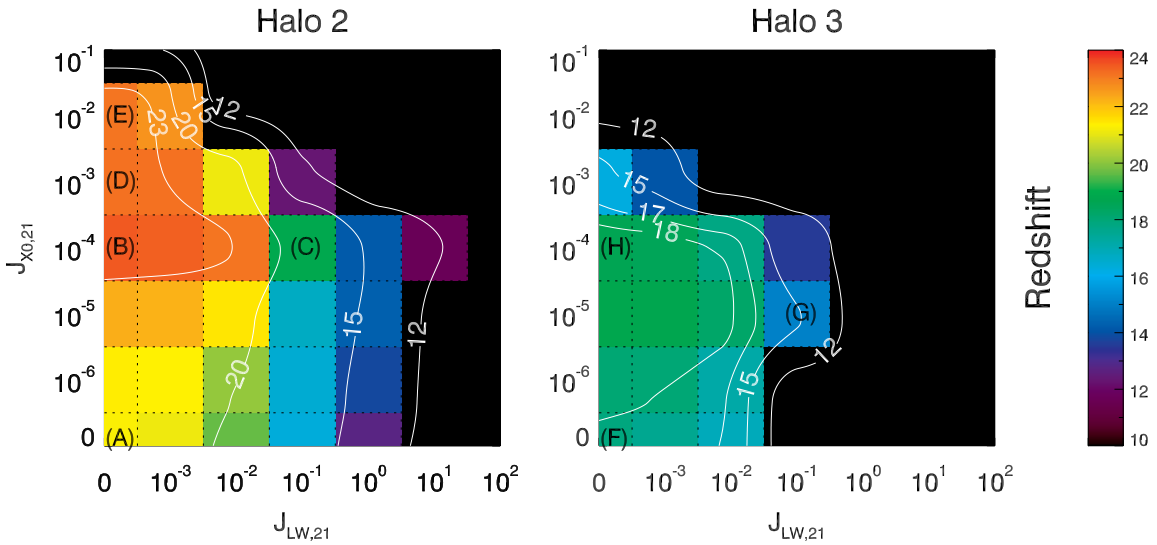

Figure 4.1: Redshift of collapse to a hydrogen number density $n_{\rm H} = 10^7$ H cm^{-3} as a function of LW and X-ray background intensities. The left and right panels are the results of Halo 2 ($M_{\rm dm} \sim 5 \times 10^6$ M$_\odot$ at $z = 15$) and Halo 3 ($M_{\rm dm} \sim 7 \times 10^5$ M$_\odot$ at $z = 15$), respectively. The white lines show the interpolated contour plot of constant redshifts of collapse. The labels (A to H) refer to the simulations in Table 4.1, see the text.

resolution simulations, we pick a few representative cases to continue running further following the formation and growth of the protostars under the effect of RFB. We chose five simulations for Halo 2 (labeled from A to E in the left panel of Fig. 4.1) and three from Halo 3 (F, G, and H, right panel). From A to E have increasing X-ray intensities in general but B and C have the same with different LW intensities. D and E belong to the strong X-ray case ($J_{X0,21} \geq 10^{-3}$) in Paper I and Paper II. F, G and H from Halo 3 have zero and intermediate X-ray intensities ($J_{X0,21} = 0, 10^{-5}$, and 10^{-4}, respectively). We do not show the results for the strong X-ray case in Halo 3 ($J_{X0,21} = 10^{-3}$) because accidentally this halo experienced a recent merger near the time of Pop III stars formation. Therefore, the star formation properties do not follow the expected trends with X-ray intensity. Studying the effects of a major merger is beyond the scope of this paper and will be studied in future work. To see potential LW background effects, we select two simulations with a non-zero LW background (C and G). The name of each selection is shown in

Table 4.1: Summary of simulations.

Label[a]	Halo	RFB	$J_{X0,21}$	$J_{LW,21}$	t_{final} [kyr]	M_{final} [$M_\odot$]	Multiplicity, N_{final}	Group[b]
Run A(_noFB)	Halo 2	Yes (No)	0	0	68 (81)	557 (1086)	4 (7)	Group 1
Run B(_noFB)	Halo 2	Yes (No)	10^{-4}	0	42 (71)	183 (689)	3 (6)	Group 2
Run C(_noFB)	Halo 2	Yes (No)	10^{-4}	10^{-1}	92 (125)	579 (972)	4 (5)	Group 1
Run D(_noFB)	Halo 2	Yes (No)	10^{-3}	0	76 (115)	159 (281)	2 (2)	Group 2
Run E(_noFB)	Halo 2	Yes (No)	10^{-2}	0	115 (185)	105 (433)	2 (5)	Group 2
Run E_noHD	Halo 2	Yes	10^{-2}	0	18	95	2	N/A
Run F(_noFB)	Halo 3	Yes (No)	0	0	108 (87)	338 (470)	7 (5)	Group 1
Run G(_noFB)	Halo 3	Yes (No)	10^{-5}	10^{-1}	142 (148)	539 (801)	10 (10)	Group 1
Run H(_noFB)	Halo 3	Yes (No)	10^{-4}	0	33 (90)	203 (603)	2 (4)	Group 2

[a] Following the labels in Fig. 4.1.

[b] Group 1 includes zero/weak X-rays or a LW background. The X-ray effect is minimal in this case. Group 2 includes moderate/strong X-rays with no LW. The effects of X-rays are important in this group.

Table 4.1. With the same initial condition, we run two sets of simulations: one with RFB and one without RFB. We divide the simulations into two groups: Group 1 and Group 2. In Group 1, the gas clouds are irradiated by zero/weak X-ray background or a moderate LW background, therefore in this group of simulations, the effects of X-rays should be small. Simulations in Group 2, on the other hand, have a zero LW background but a moderate/strong X-ray background. We note that the simulations in Group 2 are typically run for a shorter time than the ones in Group 1 (see Table 4.1), but we expect that this does not affect the results significantly. We found that the gas disc is depleted more rapidly for simulations in Group 2, hence we stop the run when the accretion rate becomes $\dot{M} \lesssim 10^{-4}\,\mathrm{M_\odot\ yr^{-1}}$. For this reason, we expect there is no more fragmentation and, assuming that $\dot{M}$ remains constant at our assumed threshold of $10^{-4}\ \mathrm{M_\odot\ yr^{-1}}$, the mass growth is only $\sim 5\%$ during the next 50 kyr. Note that, for Run E, we evolve the simulation for a longer time (115 kyr) to confirm that indeed stars do not resume growing at later times.

After selecting the simulations we extract the central 2 pc of these runs to generate new initial conditions and perform simulations in non-cosmological settings. Throughout the paper, we call these new simulations "SF (star formation) simulations." We do not include dark matter particles because their density in the halo core is several orders of magnitude lower than the gas density. We confirmed that the SF simulations produce results that agree with simply running the zoom-in cosmological simulations further without extracting a 2 pc box region. Even though the simulations are not identical due to the chaotic nature of the fragmentation process, the results are qualitatively identical and the SF simulations run more efficiently than the zoom-in simulations. In the SF simulations, the base AMR level is 7 and cells are refined with Jeans criterion (Truelove et al., 1997) $N_\mathrm{J} = 16$ up to AMR level 15. The cell size at the maximum AMR level is $\Delta x = 2\ \mathrm{pc}/2^{15} = 6.10 \times 10^{-5}\ \mathrm{pc} = 12.6\ \mathrm{AU}$. Since we aim at running multiple simulations with

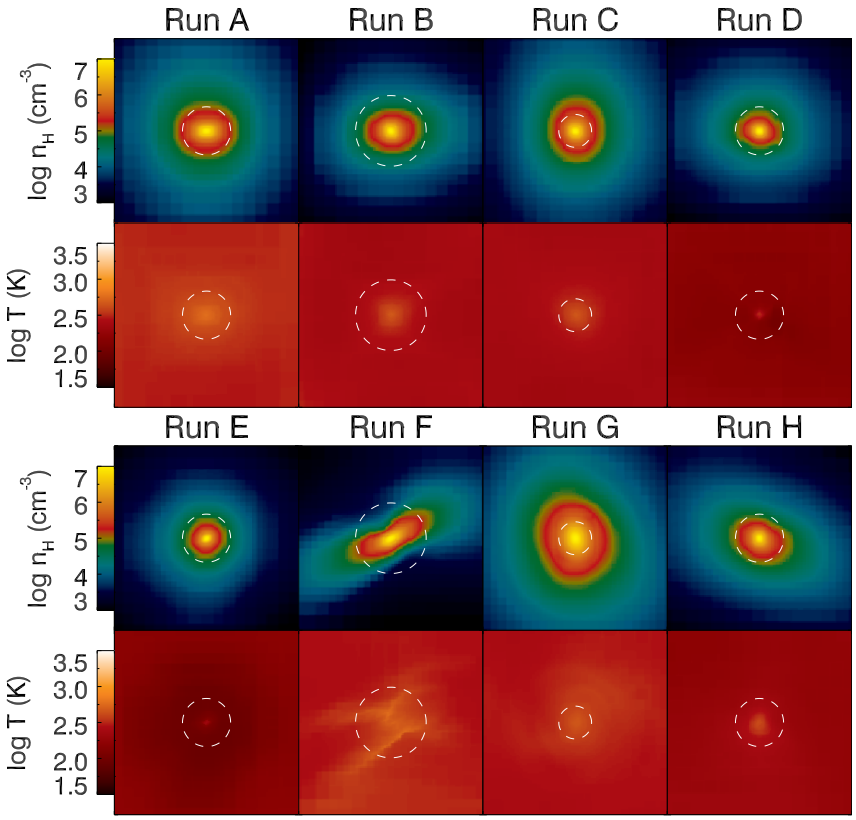

Figure 4.2: Hydrogen number density (top) and temperature (bottom) slices of the initial conditions for the simulations in Table 4.1. White dashed circles indicate the effective radius of the collapsing cloud (Hirano et al., 2014; HR15). The scale of each image is 2 pc on each side.

different radiation backgrounds for about $\sim 50-100$ kyr from the formation of the first protostar, we adopt a spatial resolution a few times lower than other recent simulations of Pop III star formation (~ 3 AU, Hosokawa et al., 2016; Sugimura et al., 2020), but significantly higher than that of our previous works (~ 60 AU, Paper I and Paper II).

The initial conditions are shown in Fig. 4.2. The characteristic radius of the collapsing cloud (Hirano et al., 2014; HR15) does not exceed 1 pc (dashed lines). Initial conditions of Halo 2 display a clear trend with the X-ray intensity with the gas cloud tending to be colder (~ 100 K) and smaller in size in X-rays. When irradiated by LW, on the other hand, the gas cloud becomes larger in size due to the delayed Pop III star formation and therefore a larger halo mass at a lower

redshift.

4.2.2 Primordial H_2 and HD Chemistry and Cooling

We refer to Paper I for a description of the primordial gas chemistry and cooling function of H_2. In this work, we also include the effect of HD cooling that can become important in cases with strong X-ray irradiation due to the significantly increased H_2 molecular fraction and low gas temperature. To consider the HD cooling we implement 6 reactions including D, D^+, and HD following Table 2 of Nakauchi, Omukai, and Susa (2019) and the HD cooling function from Lipovka et al. (2005). The HD cooling is only included in cosmological zoom-in simulations and ignored in SF runs because it is a sub-dominant process at higher densities (Omukai et al., 2005).

4.2.3 Self-shielding of Background Radiation

Although X-ray photons have small ionization cross-sections, they are shielded by the dense central gas in a halo. This X-ray shielding may shut down the additional ionization/heating in the central regions of the protostellar core, weakening the FB effect of X-rays as found in Hummel et al. (2015). In Paper II we also found a weakening effect of self-shielding for strong X-ray irradiation cases, but the self-shielding does not make a meaningful difference in weak or moderate X-ray backgrounds (see Appendix B.1 in Paper II). This is because Pop III properties are determined when the central density reaches moderate densities ($\sim 10^4$ H cm^{-3}), before self-shielding becomes important. However, we include this effect anyway in this work for completeness. For the X-ray shielding, the ionization and heating rate by X-ray background is multiplied

by the self-shielding factor ($0 < f_{\rm shd} < 1$):

$$f_{\rm shd} = \exp(-N_{\rm c}\overline{\sigma}), \tag{4.1}$$

where $N_{\rm c}$ is the column density and $\overline{\sigma}$ is the averaged ionization cross-section in the X-ray range $[200\ {\rm eV}, \infty)$. We assume the halo is spherically symmetric and thus the column density is only a function of the distance, r, from the centre:

$$N_{\rm c}(r) = \int_{\rm R_{vir}}^{r} n(r')|{\rm d}r'| \tag{4.2}$$

where $R_{\rm vir}$ is the virial radius of the halo and $n(r')$ is the number density profile. As a side note, Hummel et al. (2015) considered the geometry of the protostellar disc in the self-shielding factor. We use the above simple approach because the optical depth of soft X-ray becomes ~ 1 when the density reaches $n_{\rm H} \sim 10^4$ H cm^{-3} in our haloes, before the formation of a disc. We expect X-ray FB in high-density gas to be negligible (because self-shielded) in any direction and thus our results are insensitive to this choice. In the SF simulations, the column density is

$$N_{\rm c}(r) = N_{\rm box}(r) + N_{\rm out}. \tag{4.3}$$

Because the virial radius is larger than the size of the box (2 pc), we assume that the column density at $r > 1$ pc ($N_{\rm out}$) is constant in time since $n_{\rm H} = 10^7$ H cm^{-3}. We instead update the column density inside the box ($r \leq 1$ pc, $N_{\rm box}$) at every coarse time-step (~ 13 yr).

We also include shielding of the LW background. The LW shielding includes self-shielding of H_2 and HD and shielding of HD by H_2. For the self-shielding factor of H_2, we use equation (7)

in Wolcott-Green and Haiman (2019). In our work, this factor is denoted by $f_{\rm WGH}(N_{\rm H_2}, T)$ where $N_{\rm H_2} = n_{\rm H_2}\Delta x$ is the H_2 column density and T is the temperature of the cell. We provide a discussion on the column density in Section 4.2.6. We use the same formula for the HD self-shielding but with the column density replaced by that of HD. The shielding of HD by H_2 is computed with equation (12) in Wolcott-Green and Haiman (2011). The total shielding factor of HD is the multiplication of the two factors. We did not implement the shielding of H_2 by HD because the HD density is lower by several orders of magnitude. We study the importance of X-ray self-shielding on the long-term evolution (~ 30 kyr) of the protostars forming in Halo 2, in Appendix C.1.1. Note that Hummel et al. (2015) evolved the simulations for only ~ 5 kyrs, and our test suite in Paper II also covered a shorter time. However, the importance of self-shielding may vary depending on the growth history of the chosen halo as suggested in Hummel et al. (2015).

4.2.4 Sink Formation and Accretion

In hydrodynamics simulations, the Jeans length ($\lambda_{\rm J}$) must be resolved with a minimum number of cells to prevent artificial fragmentation (Truelove et al., 1997) and better resolve turbulent motions. However, as the Jeans length approaches the minimum cell size (Δx) in the simulation, this criterion fails. To circumvent this issue in Paper I and Paper II we artificially reduced the cooling rate of Jeans unstable cells near the resolution limit, as also done in previous works (Hosokawa et al., 2016; Hirano and Bromm, 2017). Because of the nearly adiabatic collapse heating, the gas stops collapsing forming clumps that we regard as Pop III protostars. This method is not ideal to track the evolution of individual clumps and implement RFB from them.

For this reason in this work we utilise sink particles, that we refer to as stars or protostars. However, we point out that a sink particle in our simulations can represent a multiple-star system with a separation that is less than the sink radius. We follow the recipe in the public version of RAMSES (Bleuler and Teyssier, 2014) with minor modifications. The built-in clump finder (Bleuler et al., 2015) identifies gas clumps and we check if each clump satisfies the following,

1. The clump peak density is $n_{\rm H} > n_{\rm sink} = 10^{12}$ cm^{-3}.

2. There is no pre-existing sink within $2r_{\rm sink} = 2 \times N_{\rm Sink}\Delta x$.

3. The flow is converging, $\boldsymbol{\nabla} \cdot \boldsymbol{v} < 0$.

If all conditions are met for a given clump then we create a sink particle at its density peak. When created, the mass of a sink is zero but it gains mass in the next time step (that is roughly 20 days in our simulations) by accreting the surrounding gas as described in the next paragraph. In Appendix C.1.2 we compare the star formation with clumps and sink particles.

In the literature, the sink radius is chosen to be a multiple of the smallest cell size ($N_{\rm Sink}\Delta x$), with values of $N_{\rm S}$ ranging from 4 to 16. We choose $N_{\rm Sink} = 8$ and thus $r_{\rm sink} = 101$ AU. If a gas cell is within the radius of a sink particle and its number density exceeds $n_{\rm sink}$ the excess mass ($(n - n_{\rm sink})\Delta x^3$) is dumped into the sink. We do not check if the gas inside the sink is gravitationally bound because the Bondi radius (Bondi and Hoyle, 1944; Bondi, 1952) of the sink is greater than $r_{\rm sink}$ and therefore the gas is actually bound to the sink. Two sink particles merge if they are closer than $2r_{\rm sink} = 202$ AU. Cells within $1.5r_{\rm sink}$ from the centers of any sink particle are fully refined to guarantee accurate calculation of hydrodynamics and radiative transfer near sinks. In Appendix C.1.3 we validate our choice of $n_{\rm sink}$ and provide test results with different $N_{\rm Sink}$.

4.2.5 Photon Injection

We utilise the model of protostars calculated by Hosokawa and Omukai (2009) and Hosokawa, Yorke, and Omukai (2010) to obtain the number of photons emitted by sink particles. These authors traced the evolution of accreting protostars with a 1-D stellar evolution code and tabulated the radius and luminosity (and thus effective temperature, $T_{\rm eff}$) as a function of stellar mass and gas accretion rate. In our simulations, the luminosity of a sink particle in each frequency bin is,

$$Q = 4\pi R^2 \int_{\nu_1}^{\nu_2} \frac{\pi B_\nu(T_{\rm eff})}{h_{\rm P}\nu} {\rm d}\nu, \tag{4.4}$$

where R is the effective radius of the model star and $T_{\rm eff}$ is its effective temperature, assuming it has a Plank spectrum $B_\nu(T_{\rm eff})$. At each time step of the simulation, the values of R and $T_{\rm eff}$ are interpolated from the table as a function of the mass and accretion rate of the sink particle. The lower and upper bounds of frequency (ν_1 and ν_2) in each bin are given in Table 4.2. We do not include luminosity due to gas accretion. In a time-step Δt, we inject $Q\Delta t$ photons around each sink particle. Throughout the paper, we use the terms LW and FUV (far-ultraviolet) interchangeably for the radiation in the first energy bin. We call the radiation in the other bins either ionizing or EUV (extreme-ultraviolet) radiation.

For a Pop III star to form the core density should exceed 10^{20} cm^{-3} (Omukai, 2001). This density cannot be resolved in our simulations so we need a sub-sink recipe to model photon injection from the sinks. Instead of assuming that all cells within the sink are sources of photons, we distribute photons equally on the sink surface, with fluxes in the outgoing radial direction. The specific intensity of photons launched from the surface in each direction is further reduced

Table 4.2: Energy bins.

bin	$h_{\rm P}\nu_1$ (eV)	$h_{\rm P}\nu_2$ (eV)	Roles
1	11.20	13.60	H_2 dissociation
2	13.60	15.20	H I ionization
3	15.20	24.60	H I, H_2 ionization
4	24.60	54.42	H I, H_2, He I ionization
5	54.42	∞	H I, H_2, He I, He II ionization

by the escape fraction $f_{\rm esc}$:

$$f_{\rm esc} = \begin{cases} 0 & \text{if } n > n_{\rm inj} \\ f_{\rm WGH}(n_{\rm H_2} r_{\rm sink}, T) & \text{if } n \leq n_{\rm inj}\ (\rm FUV) \\ 1 & \text{if } n \leq n_{\rm inj}\ (\rm EUV) \end{cases} , \tag{4.5}$$

where $n_{\rm inj} = 0.1 n_{\rm sink}$ is the photon injection density threshold. We assume $1 - f_{\rm esc}$ photons are absorbed within the sink in the path from the central star to the sink surface. The number of photons injected into a cell on the sink surface is $n_{\rm ph} = f_{\rm esc}(1/N_{\rm surf}) n_{\rm ph,total}$. Here, $N_{\rm surf}$ is the number of cells on the sink surface (hence, the reciprocal is the fraction of the surface in each cell). Here, $n_{\rm ph,total}$ is the total number of photons emitted by the central sink particle. With this recipe, the radiation propagating in directions close to the plane of the disc is efficiently suppressed, while a significant fraction of EUV and LW photons escape in the vertical direction. An accurate calculation of $f_{\rm esc}$ requires the H_2 column density from the central sink to the surface. To save computational time, however, we approximate the column density as the density at the surface multiplied by the sink radius. Cells with injected photons have photon flux $n_{\rm ph} c_{\rm red} \hat{r}$ where $c_{\rm red}$ is the reduced speed of light and $\hat{r}$ is the unit displacement vector from the centre of the sink. Tests leading to the adoption of this recipe and the density threshold for photon injection

($0.1n_{\rm sink}$) are shown in Appendix C.1.4. The results of the simulations can be sensitive to the model of photon injection, especially with respect to the naive assumption that all photons are injected in the centre or are spread within the sink (Jaura et al., 2022).

Finally, we also test for resolution effects in Appendix C.1.5, exploring the range of sink density thresholds between 2×10^{-12} and 3×10^{-11} g cm^{-3}. However, we point out that a recent resolution study of the initial stages of disk fragmentation (Prole et al., 2022) demonstrated that the number and masses of sink particles do not converge for sink creation densities $< 10^{-6}$ g cm^{-3}. This implies the resolution of our simulations is not sufficient to fully resolve fragmentation at small scales. Hence our results on the multiplicity and IMF of surviving fragments require caution. On the other hand, as shown in Appendix C.1.5 and in agreement with the results in Prole et al. (2022), the total mass of the system is less sensitive to the resolution and therefore our results for the total mass in Pop III stars are more reliable.

4.2.6 Radiative Transfer

Radiation transfer in RAMSES-RT is implemented using the M1 closure method (Rosdahl et al., 2013), with photon number density and flux in each cell computed locally. For hydrogen and helium ionizing radiation, we follow the prescriptions in the publicly available version. Unlike the radiative transfer of ionizing UV/X-ray radiation in which the opacities are broad in frequency, opacity in the LW band is produced by absorption by numerous narrow lines with widths and centres that depend on temperature and kinematic of the gas (*e.g.*, see Ricotti et al., 2001), thus its calculation is computationally expensive. A widely used approximation is to assume that the gas is optically thin to LW radiation and correct the H_2 dissociation rate with the

self-shielding factor (Draine and Bertoldi, 1996). For the self-shielding factor we use the up-to-date equations in Wolcott-Green and Haiman (2019),

$$f_{\rm shd} = f_{\rm WGH}(N_{\rm H_2}, T). \tag{4.6}$$

This factor, however, is a function of column density $N_{\rm H_2}$ and its calculation is also cost-prohibitive in a hydrodynamics simulation. For this reason, the column density is often replaced by the local column density computed using the Jeans length, velocity gradient, or density gradient (Wolcott-Green, Haiman, and Bryan, 2011) although their usage still requires cautions (Chiaki and Wise, 2023). We follow a mixed local/global approach to calculate the opacity in the LW bands. We calculate the self-shielding locally for the gas inside each cell using equation (4.6) with $N_{\rm H_2} = n_{\rm H_2}\Delta x$, as in Katz et al. (2017), but we also account for global opacity in the LW frequency bin in the M1 closure method, assuming an effective cross-section $\sigma_{\rm LW} = 2.47 \times 10^{-18}$ cm^2 for H_2 gas (Katz et al., 2017). We also include LW photon absorption by atomic hydrogen with $\sigma_{\rm Lyman} = 5.23 \times 10^{-25}$ cm^2 (Wolcott-Green and Haiman, 2011; Jaura et al., 2022). Using this approximation we are assuming LW radiation transfer in the optically thin regime, therefore we speculate that we are overestimating H_2-photodissociation and the subsequent heating by LW photons. The effect of the shielding by H I is discussed in Appendix C.1.4.

To speed up the calculations, we use the reduced speed of light approximation. One must use this approximation with care in cosmological simulation (Gnedin, 2016) but usage in a high-density regime like in SF simulation is valid. The reduced speed of light is $c_{\rm red} = 10^{-3}c = 300$ km s^{-1} in this work. We validate this choice in Appendix C.1.6. The computation speed does not increase further with a lower value, as the maximum outflow speed is ~ 100 km s^{-1}.

GLF Riemann solver is recommended for cosmological simulation (Rosdahl et al., 2013) but we use HLL Riemann solver (Harten, Lax, and Leer, 1983) motivated by the shadowing effect. However, note that both solvers show a similar degree of diffusivity when radiation is transferred in a diagonal direction and therefore our results are independent of this choice. Finally, we provide test results with FUV- and EUV-only simulations in Appendix C.2 to explore the effect of each radiation.

4.3 Result

4.3.1 Formation of Protostars in Primordial Discs

It has now been shown by several authors that a primordial gas discs fragment to form multiple Pop III protostars (Machida et al., 2008; Stacy et al., 2010; Clark et al., 2011b), but early studies evolved the protostars for short times with respect to the accretion timescale determined by RFB. Later, several studies (Susa, 2013; Susa et al., 2014; Hosokawa et al., 2016; Sugimura et al., 2020) were able to simulate a multiple stellar system until protostellar RFB shuts down accretion on the protostars ($\sim$ 120 kyr). In our simulations we also find that the formation of multiple Pop III stars is ubiquitous, and the growth of protostars is quenched by RFB. Fig. 4.3 shows the 3D rendering of one of our simulations, in which a binary star emitting radiation produce bipolar outflows. Protostars accrete gas from their own circumstellar mini-discs, emitting FUV and EUV photons. These photons create hot bipolar H II regions in the vertical direction, that can be tilted with respect to the main disc and asymmetric as observed for the left star, where the south outflow is weaker than the north one. While the stars orbit each other, their circumstellar discs accrete gas from the main disc and create gaps and extended arms as also seen in idealised

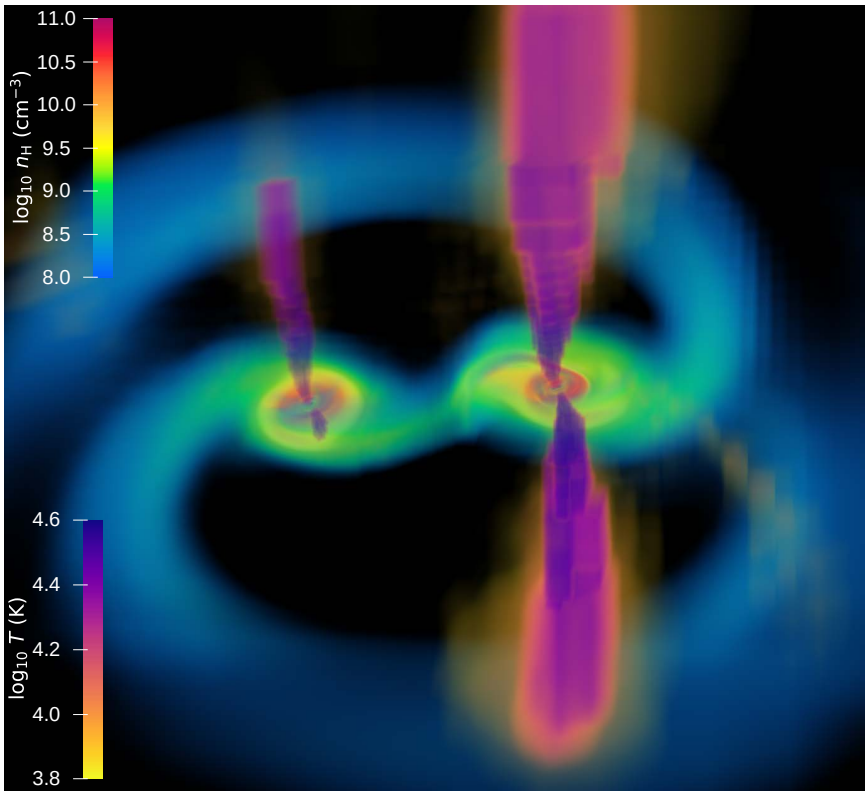

Figure 4.3: Rendered image of a nearly equal mass binary Pop III protostar and disc in Run F. Two stars accrete gas from their own circumstellar mini-discs, and the protostellar UV radiation produces two hot bipolar H II regions and outflows with velocities $\sim$ 100 km/s. The mini-discs orbiting the common CoM sweep and accrete the gas in the main disc. The field of view is $\sim$ 10000 AU $\times$ 10000 AU.

simulations of circumbinary disc (*e.g.*, Tang, MacFadyen, and Haiman, 2017; Moody, Shi, and Stone, 2019; Dittmann and Ryan, 2022). In this section we show the results of simulations of disc fragmentation and Pop III star formation for various radiation backgrounds in two representative dark matter minihaloes. Fig. 4.4 shows the central gas evolution for Run F at different epochs (a movie of the simulation is available in the online version of the paper)[3]. The qualitative evolution is similar across different simulations, even though the masses and multiplicity of the stars show trends with the intensity of the X-ray background.

Typical formation scenario. The gas cloud contracts and flattens to form a disc and proto-

[3]Available at MNRAS or see here

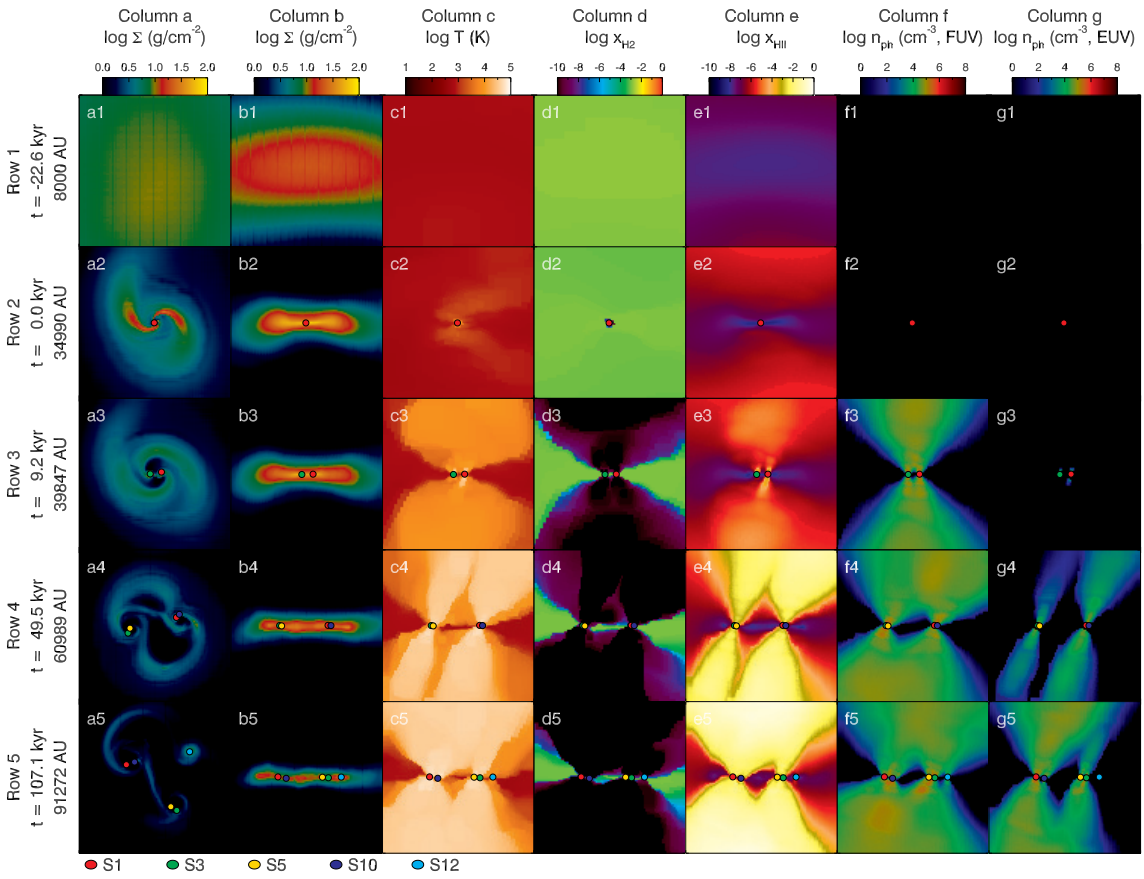

Figure 4.4: Snapshots of Run F at different times (Row 1-5). The scale of each frame, shown on the left, increases as the disc and the protostars' orbits expand. We define $t = 0$ when the first sink particle forms. We also plot protostars as filled circles (see the bottom of the figure for the labels). Column a shows the face-on view while the other columns (Column b to g) show the edge-on view. The label on each panel refers to the column and the row. Column a: Gas surface density. Through the initial fragmentation, the system starts with a binary (a3). The circumstellar discs fragment and a hierarchical binary forms (a4). Column b: Gas column density. The gas flattens (see b1 and b2) and a disc forms. All protostars are in the disc plane. Column c: Slice through the disc center showing the gas temperature. Note that the heated regions are traced by the radiation field. LW radiation heats the gas up to $T \sim 10^3$ K and the heating by ionizing radiation (EUV) results in $T \gtrsim 5 \times 10^4$ K. Column d: Slice of H_2 fraction. LW photons dissociate H_2. The opening angle of the photodissociation region increases with time. Column e: Density weighted H II fraction. The radiation from protostars creates bi-conical H II regions. Column f & g: Projected LW and ionizing UV photon density. Two massive sink particles emit a copious amount of photons. The image shows the precession of mini-discs. A movie version of this figure is available in the supplementary material.

stars (in Fig. 4.4, Panel a1 and a2 show the face-on view and Panel b1 and b2 show the edge-on view). Soon after the first protostar appears ($t = 0$), three stars form near the disc centre at $t \sim 1$ kyr through the initial fragmentation of a prominent barred spiral arm structure developing in the relatively massive disc around the low-mass central protostar (Kimura et al., 2021). Two of them merge with each other and only two nearly equal mass stars (S01) and (S03) are left orbiting the centre-of-mass (CoM) of the system (see Panel a3/b3). Each of these protostars has circumstellar mini-discs which accrete mass from the larger disc. In all the simulations these nearly equal mass binaries (with stars of about 100 $M_\odot$), migrate outward from a few 100 AU separations at formation, to 10,000 AU by the end of the simulation at $t \sim 100$ kyr. At time $t \sim 15$ kyr, the mini-disc around S03 becomes gravitationally unstable through mass accretion and fragments (Sugimura et al., 2020) to form S05. Similarly, at $t \sim 24$ kyr, the fragmentation of the circumstellar disc around S01 forms S10. At this time the system is a hierarchical binary where two binary stars, with nearly equal total mass, orbit each other (Panel a4/b4). The protostars in each binary system have their own circumstellar mini-discs. As discussed in this section and the upcoming paper (in prep) these discs play an important role in the growth and migration of protostars. The stars are getting further from their common CoM with time and the binaries also are getting further as the disc expands. At later times (Panel a5/b5) S12 forms at Lagrange points L4 (or L5) of the main hierarchical binary. Afterward, star formation becomes more stochastic due to the large multiplicity, and zero-metallicity low-mass stars can form when rapidly ejected from the disc.

Fig. 4.4 also shows that the onset of RFB changes the environment around the protostars dramatically. As the protostars grow in mass, they become more luminous and their spectra become harder. In the beginning, LW photons from the stars propagate through the gas and pho-

todissociate H_2 in the vertical direction as shown in Panel (d3), showing the H_2 fraction and (f3), showing the number density of LW photons. For the first $10 - 20$ kyr the ionizing radiation remains trapped by the dense neutral gas in the disc (Panel g3) and the H II region is trapped (Panel e3). Later, ionizing radiation breaks through the gas in the disc forming bi-conical H II regions (see Panel e4/e5 and g4/g5). The radiation field is dominated by the two protostars that form earlier because the ones forming later from the fragmentation of the mini-discs are less massive. Ionization and photodissociation by radiation heat the gas: H_2 dissociation due to LW photons heat the gas above the disc in a broad region to $T \sim 1,000$ K, creating an outflow. Note that the opening angle of the bi-conical regions where the gas is heated to 1,000 K (see panels c3 to c5), is similar to the opening angle of the LW radiation field (panel f3 to f5). As ionizing photons escape the disc they form bi-conical H II regions with a narrower opening angle than the LW counterpart (Column g). Photoionization heating increases the temperature to $T \gtrsim 5 \times 10^4$ K in these narrower conical regions (Column c). The EUV heating enhances the bi-polar outflow velocity as seen in Fig. 4.5, thereby suppressing the growth of the stars.

4.3.2 Roles of FUV and EUV Radiation Feedback

In paper I and II we found that the total mass in Pop III stars depends on the accretion rate as

$$M_{\rm pop3,tot} \propto ({\rm d}M/{\rm d}t)^{0.7}, \tag{4.7}$$

in agreement with HR15. If we define the star formation quenching timescale $\tau_{\rm SF} \equiv M_{\rm pop3,tot}/({\rm d}M/{\rm d}t)$, we expect $\tau_{\rm SF} \propto M_{\rm pop3,tot}^{-0.3}$: *i.e.*, higher mass protostars have a stronger feedback effect than lower mass stars.

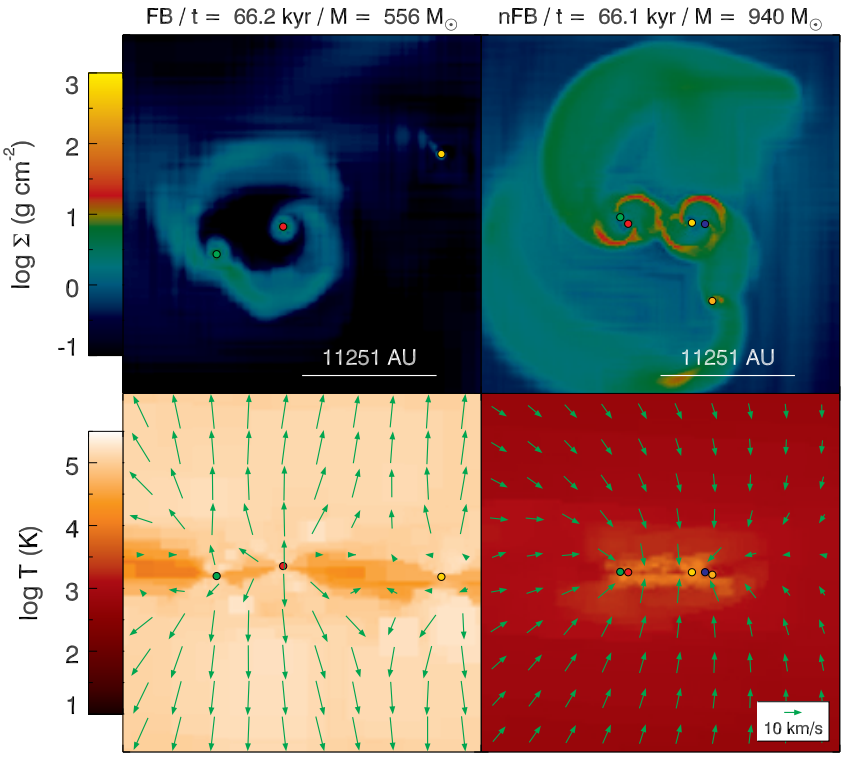

Figure 4.5: Face-on gas surface density (top) and edge-on temperature (projected, bottom) in Run A. We present FB (left) and noFB (right) for comparison. The time and total mass are shown above each density plot. The time is nearly at the end of the FB run. The field-of-view is 30000 AU $\times$ 30000 AU. On top of the temperature plots, we plot the velocity field (green arrows). The size of an arrow scales with the speed logarithmically and the maximum speed is $\sim$ 100 km s^{-1}. Protostars are shown by the filled circle.

Without X-ray irradiation the accretion rate is highest (because X-rays cool the primordial cloud core by enhancing H_2 and HD formation), thus stars grow rapidly and are more massive than in cases with X-ray irradiation. Hence, we expect a faster suppression of the mass growth of Pop III stars due to RFB in runs without X-rays. To test this model, we explore the evolution of protostars including and excluding RFB effects in Halo 2, when irradiated by different intensities of the radiation background.[4] In Appendix C.2 we test the relative importance of EUV and FUV feedback by running the same simulation with both EUV + FUV feedback, only EUV, only FUV, and noFB. We find that FUV and EUV feedback have comparable effects on the suppression of

[4]In Paper I we found that Halo 2, because of its regular accretion history, shows the clearest trend with varying the intensity of the X-ray background.

the accretion rate onto Pop III stars.

Fig. 4.5 shows the gas surface density (face-on) and temperature (edge-on) of the FB (left) and noFB (right) Run A ($J_{X0,21} = 0$) at $t \sim 66$ kyr. The overall gas density is lower in the FB run because RFB suppresses the gas supply and available gas is already consumed by the existing stars. The protostars in this simulation are more massive ($M \sim 100 - 200$ $M_\odot$) than those in Run D ($M < 100$ $M_\odot$) seen in Fig. 4.4, hence the bipolar H II regions reach temperatures of nearly 10^5 K. As seen in the temperature plots an outflow with velocity ~ 100 km s^{-1} in the vertical direction develops and reverses the gas motion (arrows in the bottom left panel), that would otherwise be accreting onto the disc and stars (bottom right). Generally, we find across all simulations that FB reduces the total mass in stars both at intermediate times and even more at late times, since the total mass in stars continues to increase with time at a nearly constant rate in the noFB cases. The multiplicities in the last snapshot ($N_{\rm final}$) are 4 and 7 showing fewer stars in the FB run. Again, at an earlier time ($t \sim 68$ kyr), the number of stars is 4 and 5 in both runs, hence the difference is smaller.

4.3.3 Modulation of the Accretion Rate and Feedback due to Eccentricity of the Orbits

In Fig. 4.6 we plot the masses, accretion rates and distances from the CoM as a function of the time of the stars forming in Halo 2 for the case without X-ray and LW backgrounds (Run A). Single stars are shown by colored lines for the fiducial simulation, while the total mass for the noFB simulation (black dashed lines) is compared to the fiducial case (black solid lines). The bottom panel shows that the two most massive stars are in a binary with a rather eccentric orbit

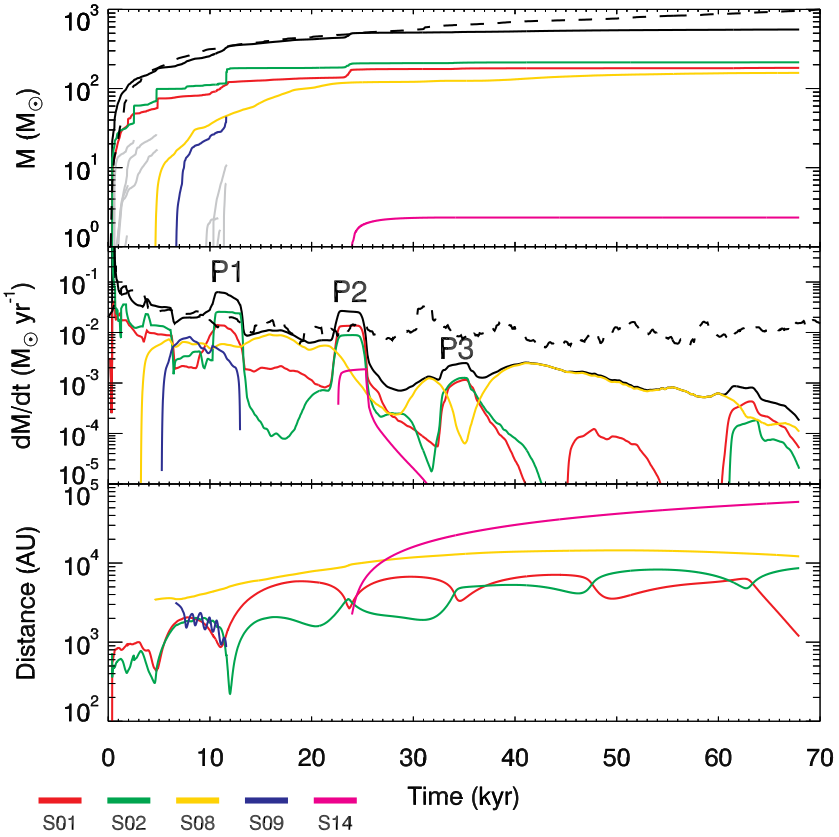

Figure 4.6: Top: Mass in protostars with time for Halo2 with $J_{X0,21} = 0$ (Run A). Solid lines are in the fiducial case and the dashed line is in noFB case. The total mass is shown in black and individual stars are shown in different colors and grey with long-lived ones highlighted (see bottom). Note that the mass of low mass S14 (magenta) remains constant without merging with other stars. Middle: Accretion rates in $\mathrm{M}_\odot\ \mathrm{yr}^{-1}$. Similar to the top panel but we plot only the long-lived ones. We mark accretion rate peaks with P1, P2 and P3. Bottom: Distance from CoM. The final distance of S14 is $\sim 6 \times 10^4$ AU.

($e \approx 0.8$) as shown by the bottom panel. This is somewhat surprising given that the stars are still deeply embedded in a gas-rich quasi-Keplerian disc. However, the disc is highly inhomogeneous due to the presence of prominent arms and bar features. We will see in a follow-up paper that these non-axisymmetric features are responsible for the outward migration of the stars and allow initially eccentric orbits to avoid circularizing.

Eccentricity-induced periodic growth. RFB suppresses the growth of protostars as suggested in previous studies (Hosokawa et al., 2011). The accretion rate in the noFB run is almost constant

for at least 100-200 kyrs, while the accretion rate slows down in the run with RFB (fiducial run). However, in the fiducial run there are times when $\mathrm{d}M/\mathrm{d}t$ suddenly increases and sometimes the accretion rate exceeds that in the noFB case. We mark these episodes with the labels P1, P2 and P3 in the middle panel of Fig. 4.6. At each peak, the S01-S02 pair (red and green) grows rapidly and this occurs at the minimum separation of the two stars (*i.e.*, at pericenter distance). As shown in the bottom panel, the binary has an eccentric orbit, and the distance between S01 and S02 has a minimum at P1, P2 and P3. The periodic increase of the accretion rate is likely produced by the tidal interaction of the circumstellar mini-discs, funneling the gas to the stars and thus boosting the growth of the protostars. The accretion rates at these peaks decrease with time due to the gas depletion and the third peak is lower than the noFB case. Unlike the case of AGN feedback in galaxy merger simulations (Park, Smith, and Yi, 2017), tidal interaction does not always lead to stronger feedback. At P1 and P2 the tidal interaction reduces the ionizing luminosities of S01 and S02 by several orders of magnitude, weakening RFB. This is because protostars are modeled to enter a supergiant phase (and therefore their effective temperature drops) when they have high accretion rates: $\mathrm{d}M/\mathrm{d}t \gtrsim 10^{-2}\ \mathrm{M}_{\odot}\ \mathrm{yr}^{-1}$ (Hosokawa and Omukai, 2009; Hosokawa et al., 2010, 2016). As seen in the figure, the accretion rates of these two stars are similar to this critical value at P1 and P2. At P3, however, the stars do not enter the giant phase and their luminosities increase for a short period of time. While RFB from stars S01 and S02 are shut down during the close encounters, the ejected star S08 keeps radiating and produces an outflow.

In Paper I and Paper II we used the empirical relationship from Hirano et al. (2014) and HR15 to determine the final masses of Pop III stars (RFB was not included in those simulations). In this work we simply define the mass in stars as the one in the final snapshot of the simulation, denoted M_{final}. The total mass in stars in Run A is $557\ \mathrm{M}_{\odot}$ as seen in Table 4.1 and is clearly lower

than the noFB case at the same time ($1086\ \mathrm{M}_\odot$). However, even at the end of our simulations, RFB has not fully evaporated the gas disc, especially the gas in the circumstellar mini-discs, and therefore the stars keep growing at a very slow rate. For this reason, $M_{\rm final}$ provides only a lower limit to the mass of the stars, even though we do not expect that their masses would increase significantly even if we evolved Run A further. As seen in Fig. 4.4, little dense gas is left due to the strong RFB and the total accretion rate in the last snapshot is $\sim 10^{-1}\ \mathrm{M}_\odot\ \mathrm{kyr}^{-1} = 10^{-4}\ \mathrm{M}_\odot\ \mathrm{yr}^{-1}$ (Fig. 4.6): if stars accrete the gas at the same rate for the next 100 kyr, the mass increase would only be $10\ \mathrm{M}_\odot$ and the total mass growth less than 10 percent. On the other hand, in the noFB simulations, the accretion rate would remain constant at about 100 times higher rate, and the total mass would roughly double reaching 2000 $\mathrm{M}_\odot$.

Hierarchical binaries and outward migration. The bottom panel of Fig. 4.6 shows the distances from the CoM of long-lived stars. Eight protostars form initially in the inner disc, but they merge with each other producing a triple system of stars: S01, S02 and S08. Star S08 (in yellow) is ejected via gravitational interaction and only S01 and S02 orbit each other in the end. The orbits of these stars initially migrate outward, but at later times they reach a constant radius. The orbit of the S01-S02 binary is highly eccentric with the pericenter distance ~ 1000 AU and the apocenter distance ~ 8000 AU. Although new protostars form while S01 and S02 orbit each other, they all merge with S01 and S02. At each pericenter, tidal interaction between the two mini-discs increases and tidal tails and a gas bridge/bar become more prominent, somewhat reminiscent of features observed in galaxy merger simulations (Toomre and Toomre, 1972; Cox et al., 2008).

At $t \sim 24$ kyr, S14 (magenta in Fig. 4.6) forms out of a tidal tail and is ejected from the system (see the bottom panel). At the time of its formation, the gas is significantly depleted, so it does not have enough gas to accrete and thus remains with a relatively small mass ($M \approx 2\ \mathrm{M}_\odot$).

Although its mass is greater than $1\ \mathrm{M}_\odot$ this supports the possibility that low-mass Pop III stars can be observed today (Clark et al., 2011b; Greif et al., 2011; Stacy and Bromm, 2013). While previous works simulated the protostellar disc for a relatively short time (a few kyr), our simulation follows the orbit of unbound low-mass protostars for about 100 kyr, as in Susa, Hasegawa, and Tominaga (2014). Two protostars are also ejected in the noFB case, but they are more massive (10 and $4\ \mathrm{M}_\odot$).

4.3.4 Pop III Masses and Multiplicity in Different X-ray Backgrounds

Multiplicity. We confirm the results in Paper II that in an X-ray background the disc is more gravitationally stable and the multiplicity of stars is reduced. Results on the multiplicity are sensitive to the resolution of the simulation because fragmentations within the sink radius cannot be resolved in our simulations, hence a sink may represent a multiple star system (see, Prole et al., 2022, for a convergence study). Nevertheless, for a given resolution, the X-ray background systematically reduces the multiplicity by stabilizing the disc and reducing the mass of the initial gas cloud. For $\mathrm{J}_{\mathrm{X0,21}} = 10^{-4}$ (Run C), the mini-discs do not fragment for ~ 29 kyr since the initial formation of a central binary as seen in the top panel of Fig. 4.7 (left). At $t \sim 29$ and 52 kyr, S06 and S12 form in the circumstellar mini-discs of S01 and S02, respectively, forming a hierarchical quadruple system. The final multiplicity is equal to that found for $\mathrm{J}_{\mathrm{X0,21}} = 0$, mostly because in the latter several sinks merge with each other (see Table 4.1). For stronger X-ray irradiation, $\mathrm{J}_{\mathrm{X0,21}} = 10^{-2}$, the second fragmentation occurs similarly at $t \sim 25$ kyr but the new sink quickly merges with the existing star. No further fragmentation occurs for the next ~ 90 kyr (see the top right panel of Fig. 4.7) and the system ends up being a binary. Other simulations

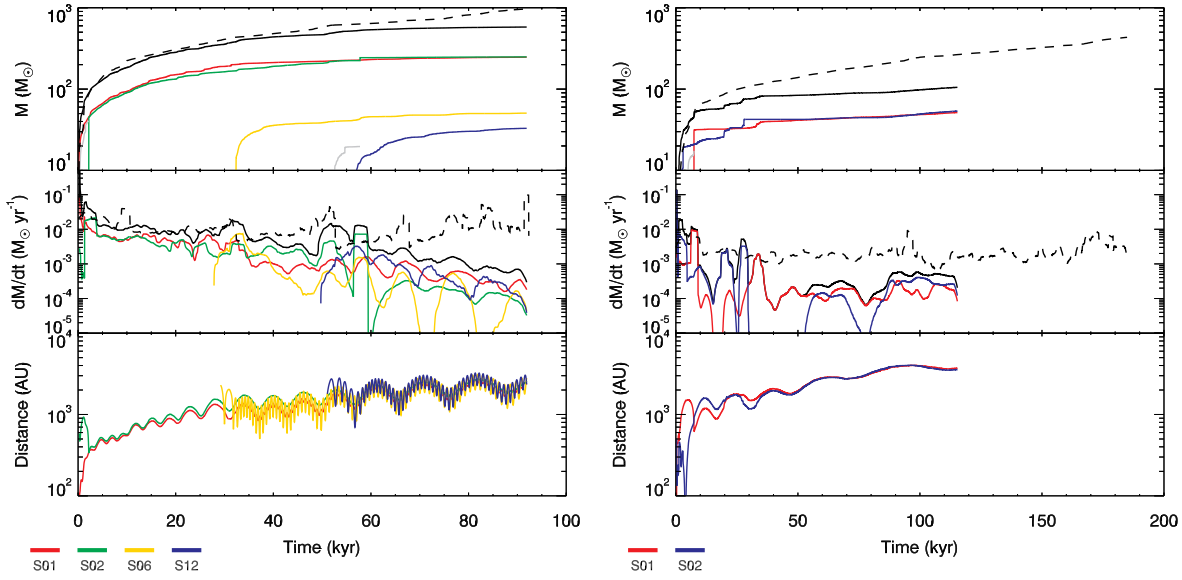

Figure 4.7: Left: Same as Fig. 4.6 but for $\mathrm{J}_{\mathrm{X0,21}} = 10^{-4}$ (Run C). Note that the middle and bottom panels shows only long-lived stars. Right: Same as the left panel but for $\mathrm{J}_{\mathrm{X0,21}} = 10^{-2}$ (Run E). Four protostars form in total but only two of them do not merge with each other for $\gtrsim 100$ kyr.

with non-zero X-ray backgrounds (Run B and Run D) have multiplicity 3 and 2, respectively. Although Run C seems to deviate from the general trend (we attribute it partially to the larger halo/disc mass produced by the delayed collapse in a non-zero LW background), the other runs agree with the expectation from Paper II: X-rays make the disc more Toomre-stable, reducing the multiplicity.

Total mass in stars. The masses of Pop III stars are reduced by X-ray irradiation (see Paper I). The physics is simple: in an X-ray background, the molecular fraction is higher and the gas temperature lower; this reduces the accretion rate ($\mathrm{d}M/\mathrm{d}t \propto M_{\mathrm{J}}/t_{\mathrm{ff}} \propto c_{\mathrm{s}}^3$) onto the protostar and its final mass. As seen in the middle panels of Fig. 4.7, the initial accretion rates ($\sim 10^{-1}$ and 10^{-2} $\mathrm{M}_{\odot}$ yr^{-1}) are lower than that in Fig. 4.6 ($\gtrsim 10^{-1}$ $\mathrm{M}_{\odot}$ yr^{-1}). The total mass in Pop III stars in three X-ray simulations without LW background (Run B, Run D, and Run E) decreases with increasing X-ray intensity ($183, 156$, and 105 $\mathrm{M}_{\odot}$, see Table 4.1). We also confirm the H II and photodissociation regions are narrower and the outflows are slower with increasing X-ray

irradiations due to the lower masses of the stars (*e.g.*, $\sim 70\ \mathrm{km\ s^{-1}}$ in Run E). The total final mass in Run C, on the other hand, is slightly greater than that of Run A due to the delayed collapse induced by the LW background ($579\ \mathrm{M_\odot}$). All simulations end with $\dot{M} \lesssim 10^{-4}\ \mathrm{M_\odot\ yr^{-1}}$ and thus we expect M_{final} does not change significantly after that.

Accretion peaks exist in Run C as in the previous case (see Fig. 4.6). From $t \sim 20$ kyr to 40 kyr, the accretion rate of S02 increases periodically (see middle panel of Fig. 4.7) with the peaks coincident with the minimum separations in the binary. These peaks, however, are less pronounced than in Run A due to the less eccentric orbit and the larger average separation (~ 2000 AU). Periodic accretion is less pronounced in the other three simulations with X-ray irradiation because the gas discs are smaller in mass.

Outward migration. The stars migrate outward in all simulations, and we show examples in the bottom panels of Fig. 4.7. S01 and S02 in Run C orbit each other with an initial separation of ~ 500 AU. The distances from CoM increase up to ~ 2000 AU by $t \sim 90$ kyr. Due to the formation of the hierarchical binary, two young stars (yellow and blue) are orbiting their companions with short periods in relatively close orbits (separations ~ 500 AU). Due to the low multiplicity, the orbits in Run E are simple. The stars' orbits expand with time as in Run C; they are born on an eccentric orbit, but they eventually circularise.

In Paper II we found that outward migration tends to be slower and to lower distances in simulation with increasing X-ray irradiation. This trend is not observed in this work: the maximum separation in Run E ($\mathrm{J_{X0,21}} = 10^{-2}$) is larger than in Run C ($\mathrm{J_{X0,21}} = 10^{-4}$). We simulated the system for a relatively short time for Run B and Run D (since accretion is suppressed early), but we find their orbits also expand with time. We will further explore the physical explanation for this ubiquitous outward migration in an upcoming paper.

4.3.5 Results for a Smaller Mass Halo

Halo 3 has a lower mass than Halo 2 at all redshifts (see Paper I), hence Pop III star formation in this halo is sensitive to lower values of the X-ray background, as shown by Fig. 4.1.

Multiplicity. Without an X-ray background, Halo 2 (Run A) is dominated by three massive stars ($M \sim 200, 200$ and 100 $\mathrm{M}_{\odot}$) while Halo 3 (Run F) has a less massive hierarchical quadruple system with masses between $M \sim 50$ $\mathrm{M}_{\odot}$ and 70 $\mathrm{M}_{\odot}$. However, at a late time, Halo 3 becomes a more complex system as several smaller mass protostars form through late-time fragmentation ($N_{\mathrm{final}} = 7$, see Table 4.1). Similarly to the case of Halo 2, the run with $\mathrm{J}_{\mathrm{X0,21}} = 10^{-5}$ in a LW background for Halo 3 (Run G), has the largest multiplicity ($N_{\mathrm{final}} = 10$) among the runs with RFB (see Fig. 4.8). This is probably due to the delayed redshift of formation of the Pop III stars and therefore a higher mass halo when irradiated by a strong LW background. However, the trend of decreasing multiplicity with increasing X-ray background is also found in Halo 3: for $\mathrm{J}_{\mathrm{X0,21}} = 10^{-4}$ (Run H) only two stars form in an eccentric orbit ($e \approx 0.5$).

Total mass in stars. The protostars in Halo 3 (Run F) are less massive than in Halo 2, producing weaker RFB. This creates narrower bipolar H II and photodissociation regions, thus suppression of the accretion rate is less significant. As it can be observed in the middle panels of Fig. 4.8, the total accretion rate remains nearly constant as a function of time, although at a lower level than in the case without feedback (Run F/noFB). The accretion rates of individual stars are very low ($\sim 10^{-4}$ $\mathrm{M}_{\odot}$ yr^{-1}) but the total accretion rate is about one order of magnitude higher as the multiplicity becomes larger at late times. In addition to the slow gas accretion, mergers between stars also contribute to the mass growth of individual stars. The mass of S10 after the merger is greater than the sum of the two masses because of the enhanced gas accretion triggered by tidal

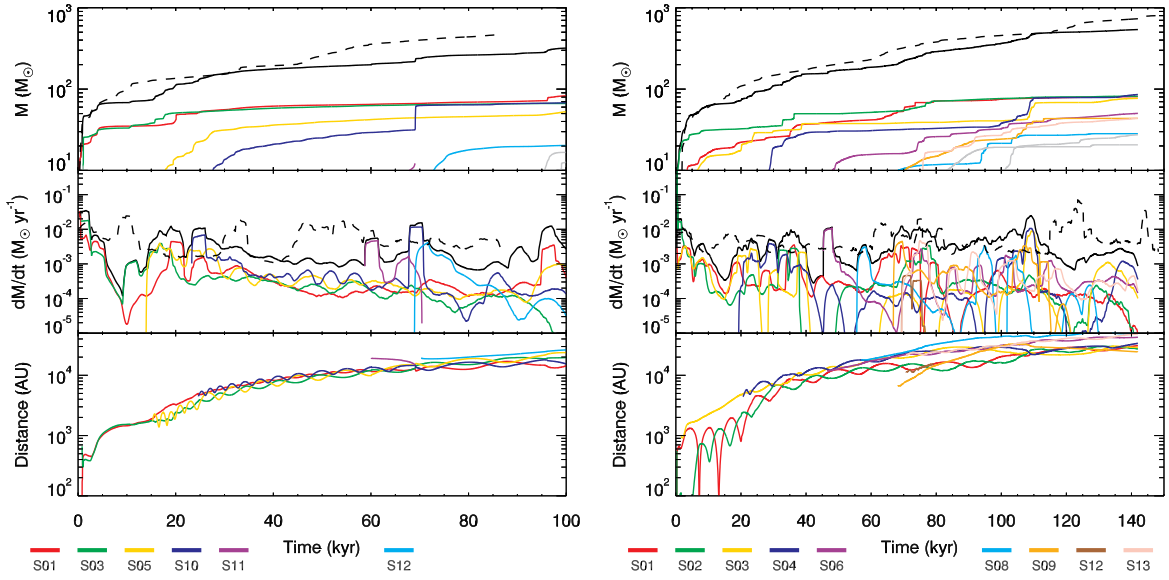

Figure 4.8: Left: Same as Fig. 4.6 but for Halo3 with $J_{X0,21} = 0$ (Run F). Right: Same as the left panel but for $J_{X0,21} = 10^{-5}$ (Run G).

effects on the mini-discs.

The trend with X-ray intensity is the same as for Halo 2: without X-ray irradiation (Run F) the total mass is 338 $M_\odot$, while for $J_{X,21} = 10^{-4}$ (Run H) the total mass is 203 $M_\odot$. As in Halo 2, the case with LW irradiation and weak X-ray background (Run G) has a greater total mass (539 $M_\odot$) due to the delay formation.

The protostars in Halo 3 also grow periodically as in Run A. To better demonstrate the physical mechanism, in Fig. 4.9 we plot the accretion rates and separations of selected binaries in Run F and Run G. For Run F, the accretion rate of S10 (blue) shows multiple peaks with the clearest ones between $t \sim 40$ kyr and 60 kyr. We marked them with P1, P2 and P3 in the top left panel. They have the same period and are in phase as the orbital separation: the peak accretion happens at the minimum separations in an eccentric orbit (bottom left). We thus conclude that the accretion is modulated by the tidal interaction of the mini-discs as discussed in Section 4.3.2. This periodic behaviour, however, is less pronounced for S01 (red) because the companion (S10)

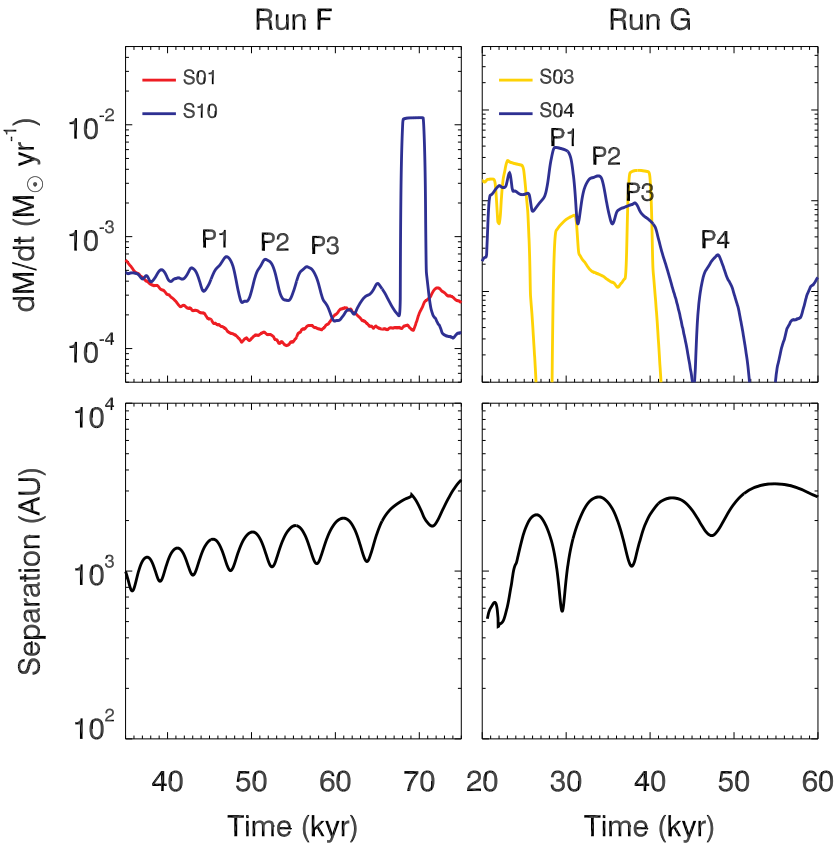

Figure 4.9: Top left: Accretion rates of S01-S10 binary in Run F. We highlight prominent peaks with P1, P2 and P3. Bottom left: Separation between the same two stars. Top right: Accretion rates of S03-S04 binary in Run G. Clear accretion peaks of S04 are marked with P1, P2, P3 and P4. Bottom right: The peaks except P2 coincide with the minimum separation and thus have a gravitational origin. P2 takes place at the apocenter and this is due to the accretion of the gas in a spiral arm.

and its circumstellar disc are smaller in mass and therefore the tidal force on the S01 disc is weaker. The other binary (S03-S05) in the same simulation evolves similarly. Binary stars in Run G behave similarly and an example is shown in the right panels. Three peaks (P1, P3 and P4) take place at the minimum separations meaning the sink growth is driven by the interaction between discs. Interestingly, P2 happens at an apocenter of the orbit. At this time S04 passes through a spiral arm feature and therefore accretes the gas in it. As aforementioned, a boost of the accretion onto the bigger star (S03) is not clear because of the low mass of the companion (S04). Also in Run H, the interaction in an eccentric binary boosts the gas accretion periodically,

however, the periodic accretion does not last long as the accretion rate drops to $\sim 10^{-6}$ $\mathrm{M_\odot\ yr^{-1}}$ in ~ 40 kyr.

Outward migration. As in Halo 2, most of the stars migrate outward in Halo 3. One exception is S11 in Run D (magenta, the bottom panel of Fig. 4.8). Forming at 2×10^4 AU, it migrates inward and finally merges with S10 after 10 kyr from its formation. Another distinct feature of Halo 3 is star formation in the proximity of Lagrange points L4 and L5 around the main binary. Using hydrodynamics simulations, several authors (Lyra et al., 2009; Montesinos et al., 2020) showed that gas and dust in protoplanetary discs accumulate at L4 and L5.

4.4 Effect of HD Cooling

The effect of HD cooling kicks in at about $T \sim 150$ K. The temperature of primordial gas may not reach this threshold with H_2 cooling alone (Paper I). However, additional ionization by cosmic rays (Nakauchi et al., 2014), X-rays (Jeon et al., 2014a; Hummel et al., 2015; Paper I), or star formation in relic H II regions (Ricotti et al., 2001), may enhance H_2 abundance and reduce the gas temperature enough to trigger HD cooling and thereby reduce the typical Pop III mass scale. As in this work, previous simulations with X-ray irradiation have taken into account HD formation and cooling (Jeon et al., 2014a; Hummel et al., 2015). However, in this section we quantify its importance with respect to the case in which HD is neglected.

In Fig. 4.10 we compare two simulations with strong X-ray irradiation in Halo 2 (Run E), including (solid lines) and excluding (dashed lines) HD chemistry/cooling. The phase diagrams (n vs T, the top left panel) show that the minimum gas temperature, $T_{\rm min}$, at $n \sim 10^4$ $\mathrm{cm^{-3}}$ is reduced by the HD cooling from $T_{\rm min} = 161$ K to 92 K. Because of the lower gas temperature,

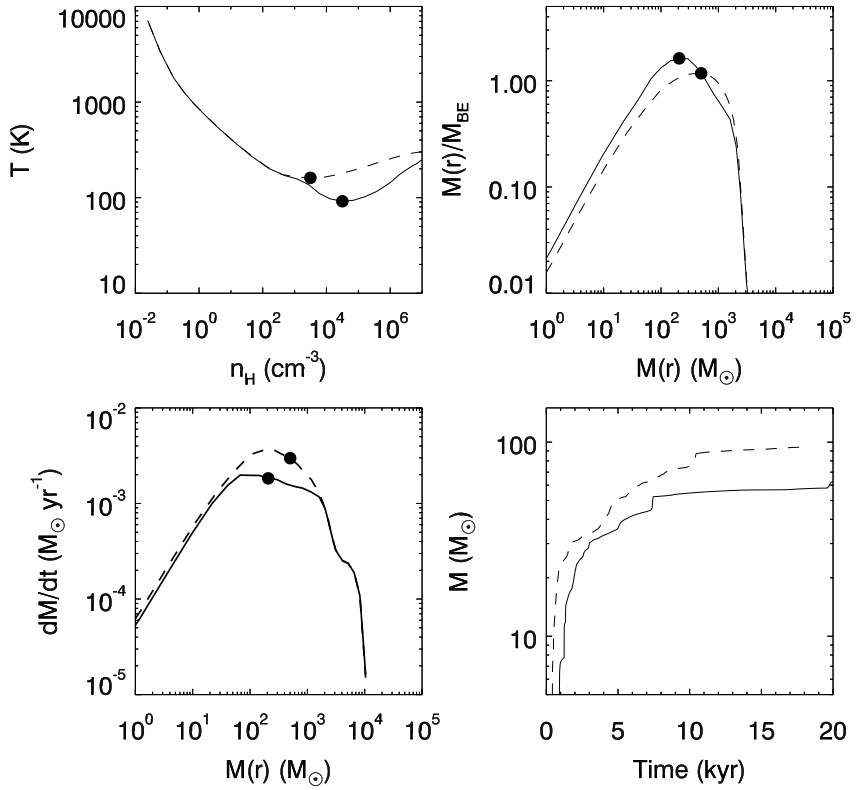

Figure 4.10: Top left: Phase diagram of Run E (solid line) and Run E˙noHD (dashed line). In the former, the temperature drops to 92 K thanks to HD cooling. Top right: The ratio of the enclosed mass ($M(r)$) to Bonner-Ebert mass ($M_{\rm BE}$, Ebert, 1955; Bonnor, 1956). The peak radius is defined as the characteristic radius of the cloud. Due to the additional cooling in Run E the cloud is smaller in size. Bottom left: Accretion rate. The smaller size results in a lower accretion rate. Bottom right: Total mass in sinks. Due to the reduced cloud size the sinks in Run E are smaller in mass.

HD cooling reduces the size and mass of the collapsing core (top right panel) and reduces the gas accretion rate (bottom left). The bottom right panel compares the total mass in Pop III stars in the simulations with and without HD. Since we run the case without HD cooling (Run E_noHD) for a relatively short time (~ 18 kyrs), we only compare the masses at early times. The figure shows a reduction of $\sim 50\%$ of the total mass in Pop III stars, from 95 $\rm M_\odot$ to 57 $\rm M_\odot$ at 18 kyr.

HD cooling has a small effect also in simulations of Halo 3, however, the decrease of $T_{\rm min}$ and therefore the decrease of the total mass in stars is weak for $\rm J_{X0,21} < 10^{-3}$. Note that $T_{\rm min}$ may be as low as $\sim$ 100 K and trigger HD cooling also in the absence of X-ray irradiation,

depending on the collapse history of the halo (*e.g.* Hirano et al., 2014; HR15). However, an X-ray background has a systematic effect in reducing $T_{\rm min}$ below 100 K, making HD cooling important in further reducing the temperature and therefore the masses of Pop III stars.

4.5 Discussion

Accretion timescale in X-ray background. To quantify the efficiency of RFB, we can estimate the star formation timescale, $\tau_{\rm SF} \equiv M_{\rm pop3,tot}/({\rm d}M/{\rm d}t)$, defined as the final mass of Pop III stars over the mass accretion rate. According to equation (4.7), $\tau_{\rm SF}$ is shorter for a higher accretion rate, making the final mass of Pop III stars less sensitive to the accretion rate (*i.e.*, $M_{\rm final} \propto ({\rm d}M/{\rm d}t)^{\alpha}$ with $\alpha < 1$). In other words, Pop III protostars are more massive in a rapidly accreting cloud, but their stronger RFB shuts down accretion more rapidly. In our simulations we include RFB, hence we can directly derive $\tau_{\rm SF}$ and compare our results to HR15.

In Fig. 4.11 we show the total mass in Pop III stars including and excluding RFB for Halo 2 and Halo 3 in different X-rays and LW backgrounds. Because ${\rm d}M/{\rm d}t$ and the masses of Pop III stars decrease when increasing the X-ray background, following the aforementioned logic, we also expect a monotonic increase of $\tau_{\rm SF}$. However, this is not observed in all our simulations, suggesting that $\tau_{\rm SF}$ may be determined by another physical parameter in addition to the strength of RFB.

To be more quantitative in Fig. 4.12 we plot $M_{\rm final}$ and $\tau_{\rm SF} \equiv M_{\rm final}/({\rm d}M/{\rm d}t)$ as a function of ${\rm d}M/{\rm d}t$ estimated from the last snapshot for the noFB simulations: *i.e.*, ${\rm d}M/{\rm d}t \equiv M_{\rm final}/t_{\rm final}$. We find that ${\rm d}M/{\rm d}t$ estimated from the noFB simulations agrees within a small scatter with the accretion rate at the characteristic radius (${\rm d}M/{\rm d}t|_{\rm cr}$) as defined in HR15. The figure shows that

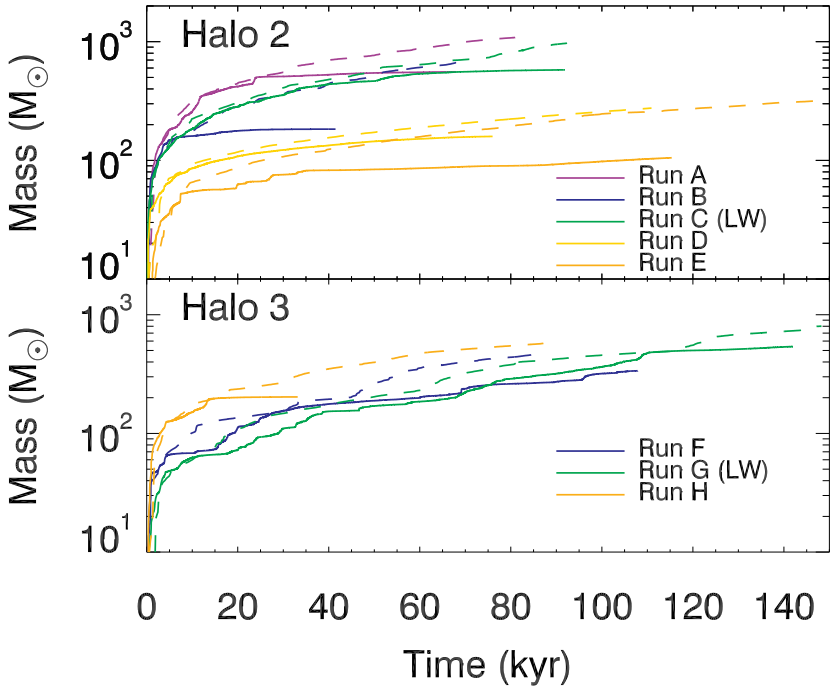

Figure 4.11: Total mass of protostars. Top and bottom panels show the results for Halo 2 and Halo 3, respectively. The simulations with RFB are shown with solid lines and those without RFB are shown with dashed lines. "LW" indicates the disc is irradiated by a strong LW background.

$M_{\rm final}$ and $\tau_{\rm SF}$ in the X-ray-only (without LW background) simulations are systematically lower with respect to the empirical relationships in HR15, shown by the solid blue lines. For this reason, we categorize the simulations into two groups. Group 1 (Run A, Run C, Run F and Run G) consists of zero/weak X-rays and the two simulations including the LW background, which follow the relationship in HR15 (blue line). Group 2 (Run B, Run D, Run E and Run H) consisting of simulations with moderate to high X-ray irradiation ($\rm J_{X0,21} \geq 10^{-4}$), showing significant discrepancy from the HR15 relationships. The solid red lines are power-law fits to the data points in Group 2:

$$M_{\rm final} = 126\ {\rm M}_\odot \left(\frac{{\rm d}M/{\rm d}t}{2.8 \times 10^{-3}\ {\rm M}_\odot\ {\rm yr}^{-1}} \right)^{0.4}, \tag{4.8}$$

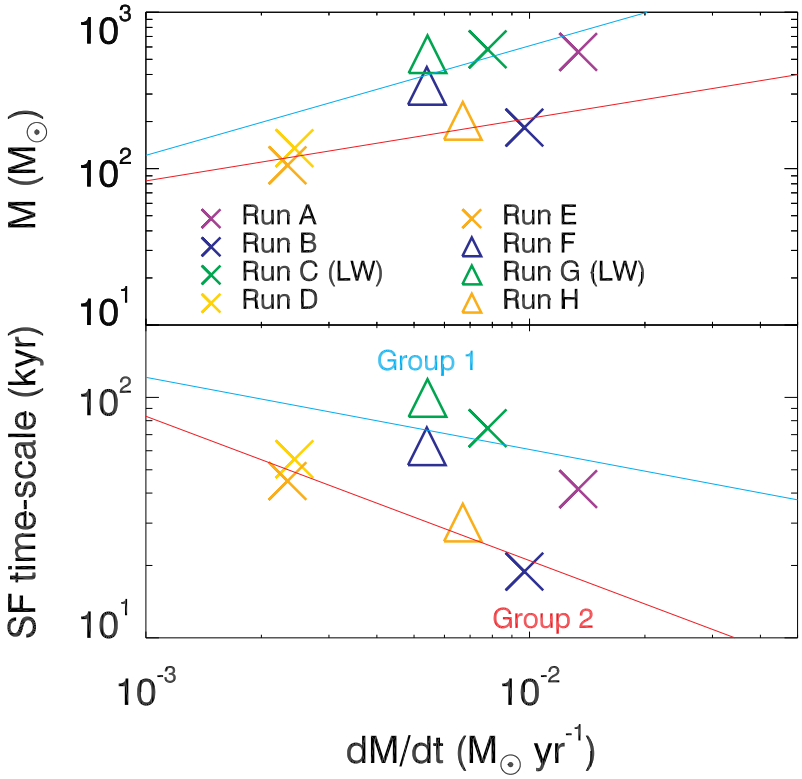

Figure 4.12: The final mass (top) and star formation timescale (bottom) in the fiducial simulations as a function of accretion rate. We categorize the simulations into two groups: Group 1 and Group 2. Group 1 (cyan) includes runs with no X-ray background and runs with non-zero LW background and weak X-rays: Run A, Run C, Run F, and Run G. On the other hand, Group 2 (red) consists of X-ray-only cases. The cyan line is the empirical relationship in HR15 and Group 1 follows this trend well. The red line is the fit to Group 2. SF timescale is defined as $M_{\rm final}/({\rm d}M/{\rm d}t)$ with ${\rm d}M/{\rm d}t$ is defined by $M_{\rm final}/t_{\rm final}$ derived in the noFB counterpart of each simulation (see the text for detail). As in Fig. 4.11, simulations with LW backgrounds are shown with label "LW".

and

$$\tau_{\rm SF} = 45 \ {\rm kyrs} \left(\frac{{\rm d}M/{\rm d}t}{2.8 \times 10^{-3} \ {\rm M}_\odot \ {\rm yr}^{-1}} \right)^{-0.6}. \tag{4.9}$$

We interpret the lower Pop III masses and shorter star formation timescales found for Group 2, as due to the effect of X-rays in reducing the typical masses of protostellar discs (see Paper I). X-rays increase H_2 formation and cooling at high densities, reducing the accretion rate of the collapsing core, but also heats the IGM and the low-density gas at the outskirt of the halo, thereby somewhat decreasing the baryon fraction ($f_{\rm b}$) in the minihalo. For example, when the central density is

10^7 H cm^{-3} (Fig. 4.1), $f_{\rm b}$ is close to the cosmic average ($\Omega_{\rm b}/\Omega_{\rm DM} \sim 0.2$) if $\rm J_{X0,21} \lesssim 10^{-4}$ but it is a factor of 2 to 4 smaller in simulations with $\rm J_{X0,21} \gtrsim 10^{-2}$, depending on the halo mass. Indeed in our simulations we observe smaller and less massive discs/cores with strong X-ray irradiation (see also Fig. 6 in Paper II), even when keeping constant $\mathrm{d}M/\mathrm{d}t|_{\rm cr}$ at the critical radius and therefore the total mass in Pop III stars (see Fig. 4.2 and Paper I). The smaller discs are more fragile to RFB, therefore the mass growth is suppressed more rapidly even in the presence of a weak RFB from lower-mass protostars.

Initial mass function of Pop III stars. In Paper II we found that the IMF of Pop III stars can be described as a power-law with an exponential cutoff at high mass:

$$\frac{\mathrm{d}N}{\mathrm{d}\ln M} = AM^{\alpha} \exp\left[-\left(\frac{M}{M_{\rm cut}}\right)^2\right], \tag{4.10}$$

where we find $\alpha = 0.49, 1.53$ and $M_{\rm cut} = 229, 61$ M$_\odot$ for weak and strong X-ray irradiation, respectively. In strong X-rays, the IMF has a lower cutoff mass $M_{\rm cut}$ and steeper power-law slope α because the gas cloud becomes less massive and fragmentation is suppressed. In this work we find results roughly in agreement with Paper II as shown in Fig. 4.13 with fitting parameters given in Table 4.3. For comparison, in their galaxy formation simulation Wise et al. (2012) assumed a Pop III MF with the peak at ~ 100 M$_\odot$, while Susa et al. (2014) found an MF with a peak at a lower mass (a few $\times$ 10 M$_\odot$). The MF in Stacy and Bromm (2013), on the other hand, is flat without a peak.

Caveats. The IMF and multiplicity of Pop III stars is sensitive to the assumed resolution. The results of Prole et al. (2022) imply that disc fragmentation is not fully resolved in our simulations, meaning that each sink may represent multiple stars. Therefore, if these smaller mass

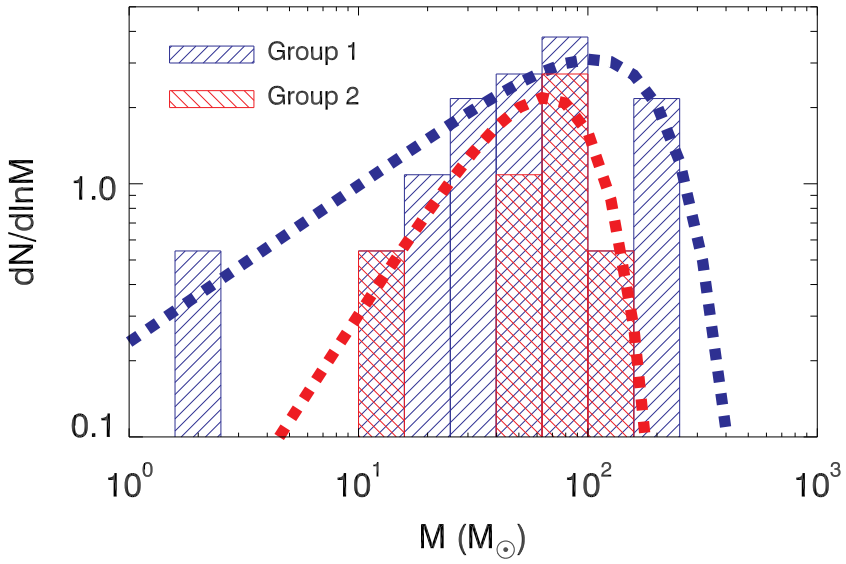

Figure 4.13: The IMFs for the runs in Group 1 with weak or no X-ray background (shaded blue histogram) and Group 2 with stronger X-ray irradiation (red shaded histogram). We count only Pop III stars that survive without merging in the last snapshots. We also show the best fits (dashed lines) using equation (4.10).

Table 4.3: Parameters of equation (4.10).

Paper II				
X-ray	α	$M_{\rm cut}$	A	$M_{\rm peak}$[a]
Weak	0.490	229 $M_\odot$	0.169	113 $M_\odot$
Strong[b]	1.53	61 $M_\odot$	0.00692	53.4 $M_\odot$
This work				
FB	α	$M_{\rm cut}$	A	$M_{\rm peak}$
Group 1	0.620	188 $M_\odot$	0.237	105 $M_\odot$
Group 2[c]	1.41	79 $M_\odot$	0.012	66 $M_\odot$

[a] $M_{\rm peak} = M_{\rm cut}\sqrt{\alpha/2}$.
[b] $J_{\rm X0,21} \geq 10^{-3}$.
[c] $J_{\rm X0,21} \geq 10^{-4}$ and include no LW simulations.

fragments do not merge with each other, the single-star IMF might be bottom-heavier and/or with a lower cutoff mass in higher-resolution simulations. However, an X-ray background should still produce a systematic change of the IMF as the mass of the gas cloud plays a significant role for the stability of the disc.

Although our results show a clear trend with the intensity of radiation backgrounds, our statistical sample is small: we only have eight simulations in two different mini-halos. As previous studies showed, Pop III properties are also sensitive to other factors such as the mass and accretion history of their host haloes (Greif et al., 2011; Stacy and Bromm, 2013; Hirano et al., 2014, 2015) or different initialization (Wollenberg et al., 2020). Hence, many more simulations are necessary for statistically robust results. For a discussion of halo-to-halo variation, we refer the readers to Paper I and Paper II in which a large parameter space of LW and X-ray backgrounds was covered for three different halos. These backgrounds regulate H_2 cooling and therefore Pop III formation precedes or is delayed with respect to the zero background case. As each of the three host halos has different growth histories (see Fig. 2 of Paper I), Pop III star formation occurs in different environments. For example, we found that some simulations do not follow the general trend due to a recent merger between mini-haloes (see Fig. 11 in Paper I). Even with these more stochastic effects, the general trend from Paper I was clear: reduced Pop III mass and multiplicity in a stronger X-ray background. Although in this work with RFB the sample is smaller due to the computational cost of the simulations, we observe that our simulations follow the same trend. We conclude that variations due to host halo effects can be important and add noise to the results, but statistically, on a sufficiently large sample, the intensity of the radiation backgrounds produces the physically motivated systematic trends discussed in this and previous papers.

Protostellar variability. As discussed in Section 4.3.3, Pop III protostars grow periodically via

enhanced gas accretion in an eccentric orbit. As the luminosity is a function of mass and accretion rate, Pop III protostars may display variability of their luminosity and effective temperature potentially on interestingly short timescales, perhaps observable by JWST or NRST. We expect when strongly lensed, the detection of this system is probable like Pop III stars (Diego, 2019) and recent studies of "Earendel" support this idea (Welch et al., 2022a,b).

As shown in Fig. 4.14, individual protostars of about 100 $M_\odot$ cannot be directly detected by JWST, unless their luminosity is magnified by a factor $\sim$ 100 by a gravitational lens. For instance, in the rest-frame optical filter $m_{\rm F322W2}$ in Run A (bottom left panel) the peak magnitude is $\sim 34-35$, below JWST detection limit ($\sim 30-31$). The periodic increase in accretion can bring the star from being bright in the UV band (effective temperatures $T_{\rm eff} \sim 10^5$ K) to a red-supergiant phase with peak brightness in the optical bands and faint in the UV (Hosokawa and Omukai, 2009; Hosokawa et al., 2010, 2016). Due to the short mean free path of UV photons, typically Pop III stars can be identified at high-z by nebular line emission: He II recombination lines and the large equivalent width of the Ly α line (Oh et al., 2001). However, during the strong accretion phase, Pop III stars shine in the rest-frame visible at nearly the Eddington luminosity and in principle the light of the star can be observed directly. As a reference, a Pop III protostar of mass M at $z = 6$ has magnitude $m_{\rm AB} \sim 34 - 2.5\log_{10}(M/100\ M_\odot)$ in the rest frame visible when the accretion rate is above the critical threshold of 10^{-2} $M_\odot$ yr^{-1}. However, the strongly accreting phases are shorter than the lifetime of the star, hence these objects are relatively rare.

During the bloated phase, the star becomes brighter in red but fainter in blue due to the low $T_{\rm eff}$, therefore the magnitude reaches $m_{\rm F322W2} \sim 34$ in the rest frame optical. When observed with a narrower band filter in the rest frame UV (F140M, top left panel) the apparent magnitude actually increases (*i.e.*, the star becomes fainter) during the strongly accreting phase. In Run F

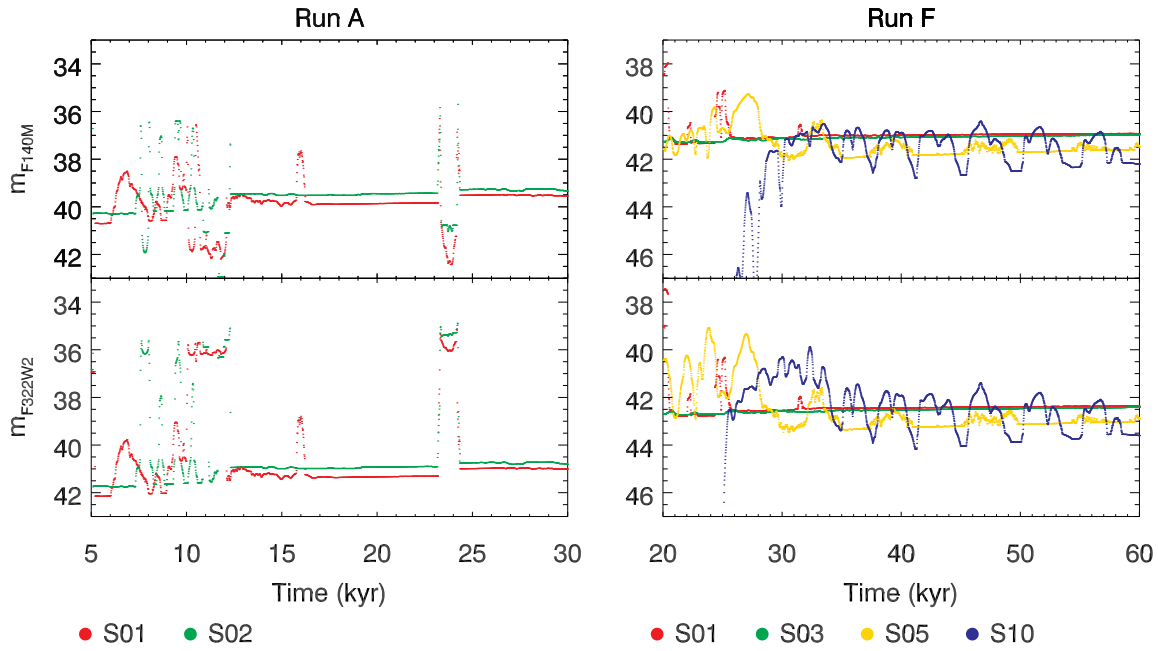

Figure 4.14: Apparent magnitudes of protostars in two JWST NIRCam bands: F140M and F322W2. We assume the protostars emit like a perfect blackbody and they are at $z = 6$. With this redshift, the centres of the bands trace the rest-frame non-ionizing UV ($\sim$ 2000 Å) and visible light ($\sim$ 4600 Å). The left panels show S01-S02 binary in Run A and the right panels show the stars in the hierarchical binary in Run F. In the latter, S01 and S10 are in a close binary and S03-S05 are in the other close binary.

(right panels) a low-mass star (S10) orbits its massive companion (S01) and shows a clear variability. In general, S10 is fainter than S01 in rest frame UV due to the lower mass (it has a lower effective temperature and size), but becomes brighter periodically when is rapidly accreting (top right, Fig. 4.14). On the contrary, S10 is brighter than the companion in the rest-frame optical bands most of the time but still shows periodicity on relatively short timescales (bottom right).

The periodic modulation of the luminosity due to pericenter passages depends on the total mass of the binary and separation: in our simulations, it varies on timescales between several tens of kyr to a few 100 years. However this is simply because close binaries with separation < 200 AU are not resolved in our simulations, but we expect that harder Pop III binaries are common as we find several protostars that artificially merge with each other due to our sink

prescription (see Section C.3). In addition, as it can be observed in Fig. 4.14 (left), the magnitude of the star, as it transitions to the supergiant phase, can decrease by 7 magnitudes (about a factor of 600 increase in luminosity) in a few tens of years. Even considering time dilation at $z = 6$, such a rapid increase can be observed with a short time baseline. Note that the star may become bloated on a very short timescale but return to its normal size on a longer timescale (comparable to the Kelvin-Helmholtz timescale), not modeled here.

Possible channels for GW sources. Close Pop III binaries, given their large masses, are likely to produce IMBH binaries that may be sources of gravitational waves detectable by LIGO/VIRGO. Unfortunately, due to resolution limitations in our simulations, we cannot directly resolve the orbits of binary stars with separations < 200 AU, even though the resolution of the simulations is about 13 AU. This is because, stars are represented by sink particles that have radii of 8 cells (about 101 AU), and we assumed that any two sinks with separation < 202 AU merge into one. To understand the behaviour of two stars closer than this threshold, we performed a test simulation dropping this assumption (see Appendix C.3). In this test simulation, the stars form close binaries with separations of ~ 30 AU and 80 AU. Hence, we expect that such binaries are a common occurrence in Pop III star systems and once they evolve to binary black holes (BBHs) with a smaller separation, they can possibly merge and emit detectable GWs (Liu and Bromm, 2020). It is beyond the scope of this paper to make predictions on the GW emission rate from such systems.

Wide Pop III star binaries, that are very common in our simulations, can also be potential GW sources. The physical mechanism allowing this channel of GW emission is dynamical hardening by other stars (Liu and Bromm, 2020) and BBH mergers in wide eccentric orbits triggered by orbital excitation by field stars (Michaely and Perets, 2019, 2020). When a wide eccentric

orbit becomes more eccentric due to an encounter with a field star, the orbit may shrink due to the GW emission at each pericenter, allowing the BBHs to merge within a Hubble time. Several of the binaries in our simulations have rather circular orbits with eccentricities $e \lesssim 0.2 - 0.3$. But in our small sample of simulations we found some binaries with large eccentricities, hence such cases are not rare. For instance, the S01-S02 binary in Run A starts with a large eccentricity ($e \sim 0.8$) as shown in Fig. 4.15, and later e slightly decreases to ~ 0.7 but we expect it does not decrease further because there is no gas disc or Pop III stars to circularise the orbit. Although its eccentricity and semi-major axis ($a \sim 5000$ AU) are lower than the values for the maximum merger probability of e approaching unity and $a \sim 10,000$ AU found by Michaely and Perets (2019) (see their Fig. 1 and Table 1), the probability of merger is only a factor of 2 lower than the maximum value reported by Michaely and Perets (2019) in terms of the semi-major axis. However, the merger rate increases significantly for values of e closer to unity than $e = 0.9$. Nevertheless, we point out that this channel of GW emission can be important for Pop III star systems given the ubiquitous outward migration and large eccentricities of the hierarchical binaries found in our simulations. Clearly, more work is needed to estimate IMBH merger rates at $z = 0$ through this channel and compare it to hard-binary merger rates.

4.6 Summary

Using radiative hydrodynamics simulations we explore the evolution of Pop III protostars regulated by protostellar radiative feedback. The initial conditions for star formation are extracted from cosmological zoom-in simulations of two minihaloes in different X-ray and LW radiation backgrounds. In this paper, the third in a series, we implement sink particles, gas accretion and

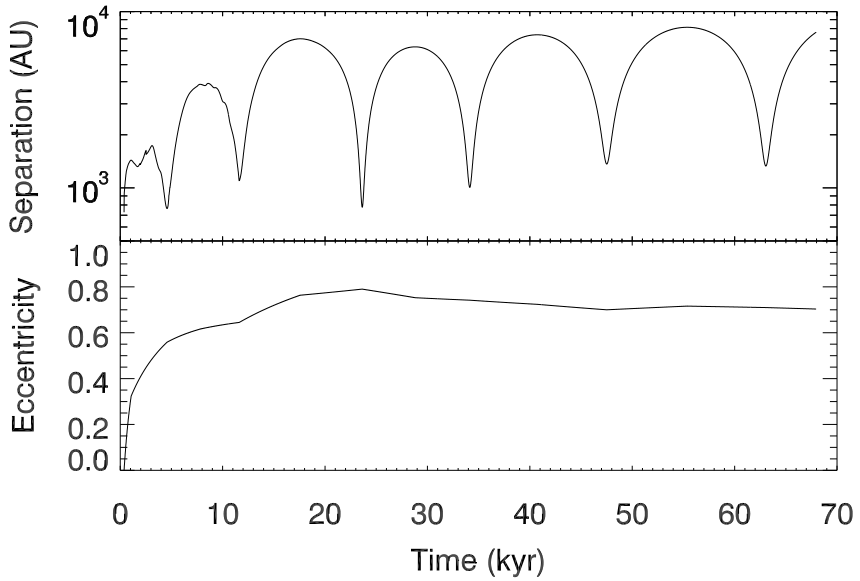

Figure 4.15: Top: Separation between S01 and S02 in Run A. The minimum and maximum separations are ~ 1000 AU and 8000 AU. Bottom: Eccentricity of the orbit.

photon injection to model radiative feedback from protostars. Below we list the key findings and implications of this study.

1. Protostellar feedback suppresses the growth of protostars as in earlier works (Hosokawa et al., 2011). LW photons photodissociate H_2 and increase the gas temperature to a few 10^3 K in broad bipolar regions above and below the disc. Ionizing photons are initially trapped in the vicinity of the stars but eventually also produce narrower bipolar regions where the ionized gas reaches temperatures between $\sim 10^4 - 10^5$ K. Hot gases create an outflow and suppress the growth of protostars by reversing the gas flow. Feedback has instead negligible effect on stellar multiplicity during the first 100 kyrs.

2. Nearly all Pop III star systems are hierarchical, *i.e.*, binaries of binaries. Most commonly two equal-mass stars form near the centre of the protostellar disc and migrate outward. Around these stars, two mini-discs become Toomre unstable and fragment forming binaries

that also migrate outward. Later on, stars may form at the Lagrange points L4 and L5 of the system. Afterward, star formation becomes more stochastic due to the large multiplicity.

3. We show that low-mass Pop III protostars can form when rapidly ejected from the disc. Although this star has mass $\sim 2\ \mathrm{M}_{\odot}$ this result suggests low-mass Pop III star might exist and be detected in the local universe.

4. Another notable result is that often the stars in the disc have eccentric orbits, leading to a periodic modulation of their accretion rates and their luminosities (on time scales that vary between a few tens of years and several tens of kyr).

5. Pop III protostars can enter a supergiant phase being bright in the rest-frame optical bands but faint in the UV due to the periodic increase in accretion. During this phase, they can be observed with the JWST directly rather than by nebular line emission. At $z = 6$, $100\ \mathrm{M}_{\odot}$ star has $m_{\mathrm{AB}} \sim 34$ and this can be above the detection limit of the JWST if magnified by gravitational lensing.

6. We confirm previous results that a moderate X-ray background reduces the minihalo mass threshold for star formation, thus increasing the number of minihalos forming Pop III stars per unit volume, but this increase is mitigated by a reduction of the typical masses and multiplicities of the stars. The stellar mass function also agrees with previous results (Park et al., 2021b) and we confirm the outward migration of the stars within the protostellar disc for nearly all the stars.

7. We confirm that HD cooling is important in reducing Pop III star masses in a strong X-ray background.

8. From our small set of simulations we derive a relationship for the typical duration of the accretion phase of protostars due to their radiative feedback. We find that this timescale depends not only on the gas accretion rate (and therefore total mass in Pop III stars), but also on the protostellar disc mass, that is systematically smaller for strong X-ray irradiation.

9. The common occurrence of eccentric Pop III binaries with large separation ($e \approx 0.8$ and $a \sim 5000$ AU) observed in our simulations, implies that a new channel for GW emission – binary black hole mergers through orbital excitation (Michaely and Perets, 2019, 2020) – is likely for Pop III systems. Therefore, Pop III stars may contribute more than previously thought to gravitational wave signals detected by LIGO/VIRGO observatory. Calculation of detection rates through this channel is a topic of future work.

Chapter 5: On the Origin of Outward Migration of Population III Stars

Outward migration of massive binary stars or black holes in their circumbinary disc is often observed in simulations and it is key to the formation of wide black hole binaries. Using numerical simulations of Population III (Pop III) star formation, we study the angular momentum of Pop III binaries and the torques between stars and gas discs to understand the origin of outward migration and high ellipticity. The outward migration of protostars is produced by gravitational torques exerted on them by their circumstellar minidiscs. The minidiscs, on the other hand, migrate outward mainly by gaining angular momentum by accreting gas from the circumbinary disc. The angular momentum transfer is most efficient for rapidly accreting equal-mass binaries, and weaker when the secondary mass is small or the massive companion evaporates the gas disc via radiative feedback. We conclude that outward migration and the formation of wide equal-mass massive binaries is common in metal-free/metal-poor star formation, mainly driven by their large accretion rates. We expect that the lower gas temperature and accretion rates in metal-enriched circumstellar discs would lead more often to inward migration and closer binary separations. We also observe inward migration for smaller mass Pop III protostars/fragments, leading to the rapid merging of sink particles and likely the formation of close binary black holes that, however, reach separations below the resolution of our simulations. We discuss the implications that Pop III separations and ellipticity may have on the interpretation that gravitational wave signals

from merging intermediate-mass black holes come from Pop III remnants.

5.1 Introduction

In recent years understanding the formation and properties of metal-free first stars (Population III or Pop III stars) has gained renewed impetus thanks to the discovery of gravitational wave (GW) emission from merging intermediate-mass black holes (IMBHs) and the successful launch of the *James Webb Space Telescope* (JWST). The detection by VIRGO and LIGO of signals from merging black hole binaries (BHBs) with individual masses ~ 30 $\mathrm{M}_{\odot}$ (Abbott et al., 2016, 2017) indicate that they might be the remnants of metal-poor or metal-free star formation (Hartwig et al., 2016; Liu and Bromm, 2020). The *Hubble Space Telescope* and the JWST have detected a few high-z lensed stellar objects at $z \sim 5-6$ (*e.g.*, Welch et al., 2022a,b), thereby suggesting detection of Pop III stars is possible at high magnification. The search of Pop III stars with JWST is actively ongoing and strongly-lensed extremely metal-poor small mass star clusters (10^4 $\mathrm{M}_{\odot}$ with $Z \sim 10^{-3}$ $\mathrm{Z}_{\odot}$, possibly with a top-heavy IMF) at $z \sim 6$ have already been observed (Vanzella et al., 2023). Remarkably, compact objects with similar properties have been predicted to exist in simulations of the first galaxies (Garcia et al., 2023). Finally, massive Pop III stars may explode as pair-instability supernovae (Heger and Woosley, 2002), and these extreme events may be detected by the *JWST* and in the near future by the *Nancy Grace Roman Space Telescope* (Whalen et al., 2014). Given this context, understanding the formation and properties of Pop III stars and more generally the fragmentation and evolution of metal-poor gas clouds and circumstellar discs is especially timely and well-motivated.

Among the many properties of Pop III stars, their multiplicity is still poorly understood,

despite its importance. There is a general consensus that the fragmentation of a metal-free gas disc and the subsequent formation of Pop III binaries is a common occurrence (Machida et al., 2008; Stacy, Greif, and Bromm, 2010; Clark et al., 2011b; Susa, 2013; Susa, Hasegawa, and Tominaga, 2014; Hosokawa et al., 2016; Sugimura et al., 2020). Once they form, these binaries can migrate either inward or outward. Inward migration may lead to the formation of close BHBs or to mergers between Pop III protostars. In the latter case, this enhances the growth of the primary star (Greif et al., 2012; Hosokawa et al., 2016) and reduces the multiplicity of the Pop III star system, thereby reshaping the Pop III initial mass function (IMF). Inward migrations appear commonly in several numerical simulations (Greif et al., 2012; Stacy and Bromm, 2013; Hirano and Bromm, 2017; Chon and Hosokawa, 2019) but outward migrations have also been observed (Greif et al., 2011, 2012; Stacy and Bromm, 2013; Chon and Hosokawa, 2019; Sugimura et al., 2020).

A series of papers (Park et al., 2021a,b, 2023, hereafter, Papar I, II, and III, respectively) found that the formation of wide hierarchical binaries via outward migration, often with relatively large eccentricities, is the most typical outcome for massive Pop III stars (semimajor axis, $a_{\rm b} \sim$ a few 1,000 AU to 10,000 AU). This is the fourth paper in the series focusing on understanding the physical mechanisms driving outward migration and exploring the origin of high eccentricities. In Paper III, we underscored their importance in forming wide Pop III BHBs because even these may lead to BH mergers and GW emission through two different dynamical channels: dynamical hardening (Liu and Bromm, 2020) or orbital excitation (Michaely and Perets, 2019, 2020).

Due to its ubiquity and importance, there have been several previous studies aimed at understanding the origin of outward migration in circumbinary discs. Several authors studied ejections via N-body processes (Greif et al., 2011, 2012; Stacy and Bromm, 2013) or gas accretion (Chon

and Hosokawa, 2019, CH19 hereafter). This latter study focused on the evolution at small scales (tens of AUs) while Pop III binaries typically reach separations up to 10,000 AU over a timescale of 50-100 kyr (Sugimura et al., 2020; Paper II; Paper III). These previous works suggested the accretion of high angular momentum gas as the dominant mechanism for outward migration. In Paper II, although we lacked a quantitative analysis, we discussed the possible connection between outward migration and gas accretion. The migration rate and separation of wide binaries were found to depend on the intensity of an external X-ray background in the following way. An X-ray background enhances the H_2 cooling and thus lowers the gas temperature. The reduced sound speed $c_{\rm s}$ leads to a lower accretion rate due to its $c_{\rm s}^3$ dependence. In an X-ray, therefore, protostars grow more slowly and accrete less high-angular momentum gas, and thus stars have lower masses and the extent of their outward migration is reduced. For this reason, the maximum separation of wide binaries tends to be smaller in an intense X-ray radiation background (see Fig. 8 of Paper II). This correlation, however, was less evident in Paper III which differs from our previous work in that it included a full treatment of radiative feedback from accreting protostars.

In this work, we analyse the simulations presented in Paper III to study in detail the physical mechanism that induces outward migrations and ultimately produces the large separations of hierarchical Pop III binaries. As discussed above, previous works on stars and black hole binaries had some disagreement on whether the main mechanism for migration is gravitational torques or the accretion of high angular momentum gas. We aim at clarifying this issue and analyse the role of radiative feedback that is likely responsible for the somewhat different results between Paper II and Paper III regarding migration. The ultimate goal is to determine what are the unique conditions in Pop III protostellar discs that lead to migration and eccentric orbits, and why this behaviour is not observed in simulations of binaries formed in protostellar discs with solar metal-

licity (He and Ricotti, 2023).

Finally, a methodology note: There is a large body of work focusing on understanding the physics of star and black hole binaries migration in gas discs (*e.g.*, Tang, MacFadyen, and Haiman, 2017; Muñoz, Miranda, and Lai, 2019; Muñoz et al., 2020; Dempsey, Muñoz, and Lithwick, 2020; Dempsey, Muñoz, and Lithwick, 2021; Dittmann and Ryan, 2021, 2022). This field of research typically adopts idealised initial and boundary conditions and neglects radiative feedback effects. For these reasons, these works can typically achieve higher resolution, evolve the systems for hundreds of orbits, and perform a systematic exploration of disc parameters and numerical experiments. This paper is instead a follow-up in a series of papers on Pop III stars formation from cosmological initial and boundary conditions (see Paper I, II, and III). We present one of the most detailed and in-depth analysis of the physics of Pop III binary migration when compared to previous Pop III literature but the present paper has a different focus and it is hard to compare to the results from idealised discs simulations, even though it has a strong cross-section with these papers. Nevertheless, given the caveat mentioned above, when possible we will highlight and discuss the connections between our results on Pop III stars and the rich literature on binary migration in idealised gas discs.

This paper is organised as follows. In Section 5.2 we summarise the method and simulation focusing on the features relevant to this work. In Section 5.3, we explore the origin of outward migration. In Section 5.4, we discuss binaries without outward migration to better understand the outward cases. In Section 5.5 and 5.6, we discuss the implication of our findings and summarise the main conclusions.

5.2 Method

5.2.1 Simulations

5.2.1.1 Overview

We make use of Adaptive Mesh Refinement (AMR) code RAMSES-RT (Teyssier, 2002; Rosdahl et al., 2013) to simulate the formation of Pop III stars in metal-free gas discs extracted from minihaloes in cosmological simulations. The non-viscous gas motion is described by solving the Euler equations using a second-order Godunov method and an approximate solution of the radiative transfer equations for UV radiation emitted from massive protostars is included and coupled to primordial chemistry (Rosdahl et al., 2013; Paper I; Paper III). Motivated by early analytic results presented in Ricotti (2016), in addition to radiative feedback from protostars, we include external radiation backgrounds in the Lyman-Werner (LW) bands and X-rays. Time-dependent primordial gas chemistry and relevant cooling/heating processes for gas densities up to 10^{14} cm^{-3} are included. In this paper we analysed the same simulations run in Paper III, hence we refer to that paper for details on the simulation methods and convergence tests (see Appendix in Paper III). Here, for completeness, we only summarise some basic information on the simulations and the parameters of different runs.

We extract the central regions (2 pc) at the centre of two minihaloes in cosmological zoom-in simulations (see Fig. 2 of Paper III) to create the initial conditions. These initial conditions include a metal-free gas cloud that has been irradiated by various X-ray and LW backgrounds. We performed 8 simulations and identified 14 binaries in them. Table 5.1 summarises the set of simulations and some properties of the binaries. Once a simulation begins, the gas cloud with

Table 5.1: Summary of simulations. From left to light, we show 1) binary name, 2) formation time, 3) final time, 4) separation at formation, 5) final separation, 6) eccentricity, 7) mass ratio, 8-9) mass of individual stars, and 10) type of migration.

Label[a,b]	$t_{\rm form}$ [kyr]	$t_{\rm final}$ [c] [kyr]	$d_{\rm form}$ [AU]	$d_{\rm final}$ [AU]	e[d]	q[e]	$M_1(\mathrm{M}_\odot)$[f]	$M_2(\mathrm{M}_\odot)$[f]	Migration[g]
Run A									
S01-S02*	0.38	68	727	7637	0.79	0.847	183	215	neutral
Run B									
S01-S04	0.30	42	1528	1594	0.46	0.971	88	85	neutral
Run C									
S01-S02	0.22	92	584	4927	0.22	0.943	247	249	outward
- S01-S06	29	92	1544	705	0.63	0.205	247	51	inward
- S02-S12†	51	92	1149	484	0.33	0.132	249	33	inward
Run D									
S01-S02	0.31	67	492	2910	0.19	0.901	74	82	outward
Run E									
S01-S02	0.30	103	498	7623	0.28	0.971	49	51	outward
Run F									
S01-S03	0.83	108	664	40982	0.16	0.800	83	67	outward
- S01-S10*	25	108	519	5244	0.34	0.870	83	71	outward
- S03-S05	15	108	426	4240	0.32	0.840	67	56	outward
Run G									
S01-S03	1.6	95	1537	43310	0.27	0.505	73	41	outward
- S01-S02	0.31	95	558	4846	0.40	0.971	73	75	outward
- S03-S04	21	95	520	6711	0.61	0.833	41	34	outward
Run H									
S01-S03	0.33	33	1799	4405	0.53	0.775	89	114	outward

[a] Following the labels in Fig. 1 in Paper III.
[b] A hyphen before the name indicates the binary belongs to a hierarchical binary.
[c] Final time of the simulation.
[d] Maximum eccentricity.
[e] $q = M_2/M_1$ if $M_1 \geq M_2$; $q = M_1/M_2$ if $M_1 < M_2$.
[f] At $t_{\rm final}$.
[g] Outward if $d_{\rm form} < d_{\rm final}$; inward if $d_{\rm form} > d_{\rm final}$; neutral if $d_{\rm form} \sim d_{\rm final}$. An exception is Run A where the orbit is kept highly eccentric.
* Representative case of non-migration binaries. Throughout the paper, it is referred to as "Fiducial-Neutral".
† Representative case of inward migration binaries. Throughout the paper, it is referred to as "Fiducial-Inward".
* Representative case of outward migration binaries. Throughout the paper, it is referred to as "Fiducial-Outward".

peak hydrogen number density $n_{\rm H} \sim 10^7$ H cm^{-3} contracts and flattens out to form a disc. As the cloud contracts and the central density increases, cells are refined from AMR level 7 to 15 with the Jeans refinement criterion $\lambda_j < N_j \Delta x$. Here, λ_j is the local Jeans length in each gas cell, Δx is the cell size, and $N_j = 16$ is the number of cells into which we resolve the Jeans length. The smallest cell size or the maximum spatial resolution is $\Delta x_{\rm min} = 2\ {\rm pc}/2^{15} = 12.6$ AU.

5.2.1.2 Sink prescription

The flattened disc fragments and multiple blobs form in the disc or spiral structures. Using the built-in halo finder (Bleuler et al., 2015) we identify these dense blobs at every coarse timestep (~ 13 yr) and assign a sink particle at the density peak of each blob if,

1. $n_{\rm H}$ at the peak exceeds $n_{\rm sink} = 10^{12}$ H cm^{-3},
2. there is no other sink particle within $2r_{\rm sink}$,
3. the velocity field in the blob has a net negative divergence.

A sink particle has the radius of $r_{\rm sink} = 8\Delta x_{\rm min} = 101$ AU. This resolution of sink is insufficient to resolve a close binary and therefore a single sink particle may represent multiple Pop III stars. In this work, however, we assume that each sink particle describes a Pop III star and use the terms 'sink particle' and 'star' interchangeably. If a sink particle mass exceeds $1\ {\rm M}_\odot$, it emits UV radiation. The luminosity is determined by the sink mass and accretion rate and is computed by interpolating the tabulated model of massive protostar by Hosokawa and Omukai (2009) and Hosokawa, Yorke, and Omukai (2010). We record the masses, positions, and velocities of the existing sink particles at every coarse timestep (~ 13 yr).

If two sink particles are closer than $2r_{\rm sink} = 202$ AU, they merge into one. The new sink particle is positioned at the centre-of-mass (CoM) of the two and momentum is conserved. We explored the impact of varying the sink radius in Appendix D.1.1. The acceleration of a sink particle by the gas or other sinks is softened assuming a smoothing-length $\varepsilon = 4\Delta x_{\rm min} = 50.4$ AU. A difference of this study with respect to the more common approach of running idealised circumbinary disk (CBD) simulations is the adoption of softening the gravitational force between sink particles. Although typical CBD simulations ignore this modification, we keep this term in the force calculation for consistency with our previous cosmological simulations (Paper I, II, and III). In Appendix D.1.2, we show that the impact of force softening on our conclusions is negligible. The accretion of gas onto the sinks is performed by checking the gas density of each cell within $r_{\rm sink}$. If a hydrogen number density $n_{\rm H}$ exceeds the threshold value, the excess mass $(n - n_{\rm sink})\Delta x^3$ is added to the sink and subtracted from the cell. The position and velocity of the centre-of-mass are conserved before and after the accretion. Recent numerical studies (Dempsey et al., 2020; Dittmann and Ryan, 2021) suggested that the sink particle methods of removing mass within a boundary may change the density profile unphysically and introduce an artificial (numerical) torque. We argue that this effect is negligible in our simulations because the time scales of our simulation differ from those of the above papers and strong radiative feedback by Pop III stars is the dominant physical process shaping the gas density profile rather than gas removal within the sink. We discuss this topic in-depth in Appendix D.1.3. Sink particle motions are calculated using a second-order mid-point scheme which reduces to the leapfrog method with constant time step (Bleuler and Teyssier, 2014). The tests performed by Bleuler and Teyssier (2014) showed that the energy and angular momentum are conserved in a Keplerian orbit. Note that, however, this test was performed to explore the impact of different force calculation methods, not N-body

integrators. It is well known that the leapfrog method, although it is a symplectic integrator and conserves energy, may introduce numerical precession of the orbit, especially if the timestep is large (Springel, 2005). In our applications, our choice of a 2nd order N-body integrator should be sufficiently accurate and not change the result substantially. The first reason is the long orbital periods of the binaries: our wide binaries make fewer orbits ($<< 200$ orbits as in Springel (2005)) from formation to the end of the simulation. There is a possibility that the orbits may be affected by the type of integrator when there are multiple sink particles. However, this usually happens when a gas disc fragments and this phase lasts only a few kyrs. Hence, we expect that the orbits after the initial fragmentation phase should be insensitive to the integration scheme given the short integration time steps determined by the radiation/chemical time scales and the wide separations of the stars. In addition, the initial phase is highly unpredictable and complex because other factors such as feedback, sink formation criterion, and mergers play a significant role. Therefore, we are confident that our integration method is sufficiently robust and convergent when compared to other uncertainties introduced by the complex physics adopted in the realistic simulation of Pop III star formation.

5.2.2 Torque

To study the migration of stars we estimate their orbital angular momentum. The torques are measured in the reference frame where the angular momentum vector is aligned with the $z-$axis. The CoM of the binary is at the origin of the frame and the frame is not accelerated. In Appendix D.3, we show that the torques on the binary measured in accelerated and non-

accelerated frames are equal. The total orbital angular momentum of a binary is,

$$\boldsymbol{J} = \sum_{i=1}^{2} \boldsymbol{J}_i = \sum_{i=1}^{2} m_i \boldsymbol{r}_i \times \boldsymbol{v}_i, \tag{5.1}$$

where the subscript i indicates the index of a sink in the binary, $\boldsymbol{J}_i$ is each angular momentum, m_i is the mass, $\boldsymbol{r}_i$ is its position from the CoM of the binary, and $\boldsymbol{v}_i$ is the velocity relative to the CoM. The rate of change of $\boldsymbol{J}$ is,

$$\frac{\mathrm{d}\boldsymbol{J}}{\mathrm{d}t} = \sum_{i=1}^{2} \left(\frac{\mathrm{d}m_i}{\mathrm{d}t} \boldsymbol{r}_i \times \boldsymbol{v}_i + m_i \frac{\mathrm{d}\boldsymbol{r}_i}{\mathrm{d}t} \times \boldsymbol{v}_i + m_i \boldsymbol{r}_i \times \frac{\mathrm{d}\boldsymbol{v}_i}{\mathrm{d}t} \right). \tag{5.2}$$

The first term on the right-hand side of the equation describes the change in the angular momentum due to the mass growth of the binary. The change of J caused by the third term is due to external torques exerted on the binary. When gas is accreted smoothly, the second term is zero since $d\boldsymbol{r}_i/dt \times \boldsymbol{v}_i = \boldsymbol{v}_i \times \boldsymbol{v}_i = 0$. This does not hold, however, when a merger with a third body offsets the position of Sink i. In this case, the second term is treated as a merger torque (see equation (5.6)). We can arrange the various terms contributing to the angular momentum change as follows:

$$\frac{\mathrm{d}\boldsymbol{J}}{\mathrm{d}t} - \left(\sum_{i=1}^{2} \frac{\mathrm{d}m_i}{\mathrm{d}t} \boldsymbol{r}_i \times \boldsymbol{v}_i \right) = \boldsymbol{\tau}_{\mathrm{total}} = \boldsymbol{\tau}_{\mathrm{gas}} + \boldsymbol{\tau}_{\mathrm{sink}} + \boldsymbol{\tau}_{\mathrm{merge}} + \boldsymbol{\tau}_{\mathrm{acc}}. \tag{5.3}$$

Here, $\boldsymbol{\tau}_{\rm gas}$ is the gravitational torque exerted by the gas,

$$\begin{aligned}\boldsymbol{\tau}_{\rm gas} &= \sum_{i=1}^{2} \boldsymbol{r}_i \times \boldsymbol{F}_{\rm gas} \\ &= \sum_{i=1}^{2} \boldsymbol{r}_i \times \left(\sum_{j={\rm cell}} \frac{G m_i m_j}{(s^2+\varepsilon^2)^{3/2}} \boldsymbol{s}_j \right),\end{aligned} \tag{5.4}$$

where $\boldsymbol{F}$ is the gravitational force on Sink i, G is the gravitational constant, m_j is the mass of gas cell j, $\boldsymbol{s}_j$ is the displacement vector from the sink to the cell, and $s = ||\boldsymbol{s}_j||$ is the distance between them. The gravitational torque exerted by other sinks is calculated similarly,

$$\begin{aligned}\boldsymbol{\tau}_{\rm sink} &= \sum_{i=1}^{2} \boldsymbol{r}_i \times \boldsymbol{F}_{\rm sink} \\ &= \sum_{i=1}^{2} \boldsymbol{r}_i \times \left(\sum_{\substack{j={\rm sink} \\ j\neq i}} \frac{G m_i m_j}{(s^2+\varepsilon^2)^{3/2}} \boldsymbol{s}_j \right),\end{aligned} \tag{5.5}$$

where we sum the gravitational torques exerted on Sink i from all the other sinks in the simulation. Note that the torque from the companion star that makes up the binary is zero. For this reason, if a third sink particle does not exist or is far away, this term does not contribute to the evolution of the orbit. $\boldsymbol{\tau}_{\rm merge}$ is the change in angular momentum due to mergers. If a third body merges with Sink i, then it has a new position and velocity. The rate of change is,

$$\boldsymbol{\tau}_{\rm merge} = \frac{1}{\Delta t} \sum_{i=1}^{2} m_{i,{\rm old}} \left(\boldsymbol{r}_{i,{\rm new}} \times \boldsymbol{v}_{i,{\rm new}} - \boldsymbol{r}_{i,{\rm old}} \times \boldsymbol{v}_{i,{\rm old}} \right), \tag{5.6}$$

where the subscripts "new" and "old" refer to the position and velocity vectors with respect to the CoM of Sink i after and before the merger with a third body, respectively. Finally, we calculate

the torque due to the accretion of gas onto the stars following Tang et al. (2017).

$$\boldsymbol{\tau}_{\rm acc} = \sum_{i=1}^{2} \sum_{\substack{j=\rm cell \\ s\leq r_{\rm sink} \\ \Delta m_j>0}} \frac{\Delta m_j}{\Delta t} \boldsymbol{r}_i \times (\boldsymbol{v}_j - \boldsymbol{v}_i). \tag{5.7}$$

Note that this term plus $(\mathrm{d}m_i/\mathrm{d}t)\boldsymbol{r}_i \times \boldsymbol{v}_i$ (left-hand side of equation (5.3)) is equal, neglecting numerical errors, to the rate of angular momentum accretion onto the sinks. The latter, however, does not directly contribute to the change in the orbit, and thus only the former is treated as torque in equation (5.7). When a gas cell inside the sink radius and its number density exceeds the sink density threshold ($n \geq 10^{12}$ cm^{-3}), the linear momentum of the extra mass $\left[\frac{\Delta m_j}{\Delta t}(\boldsymbol{v}_j - \boldsymbol{v}_i)\right]$ is dumped to the central sink particle where Δt is the time-step. The time evolution of the angular momentum due to each of the torques is calculated by integrating in time each torque,

$$\boldsymbol{J}_i = \int \boldsymbol{\tau}_i \mathrm{d}t \approx \sum \boldsymbol{\tau}_i \mathrm{d}t, \tag{5.8}$$

where the subscript i denotes tot, acc, merge, sink, or gas. We also consider the specific angular momentum of the binary,

$$\boldsymbol{j} = \sum_{i=1}^{2} \frac{\boldsymbol{J}_i}{m_i} = \sum_{i=1}^{2} \boldsymbol{j}_i = \sum_{i=1}^{2} \boldsymbol{r}_i \times \boldsymbol{v}_i. \tag{5.9}$$

Note that $\boldsymbol{J}/M_{\rm b} = (m_1\boldsymbol{j}_1 + m_1\boldsymbol{j}_2)/M \neq \boldsymbol{j}$, where we have defined the total mass $M_{\rm b} \equiv m_1 + m_2$.

5.2.3 Orbital Energy

In order to quantify how the orbits of stars in a binary respond to torques, we estimate the orbital parameters and their changes following the notation in Muñoz et al. (2019, hereafter, M19). The orbital energy is

$$\begin{aligned}\mathcal{E}_{\rm b} &= \frac{1}{2}v_{\rm b}^2 - \frac{GM_{\rm tot}}{r_{\rm b}} \\ &= -\frac{GM_{\rm tot}}{2a_{\rm b}},\end{aligned} \tag{5.10}$$

where $r_{\rm b} = |\boldsymbol{r}_{\rm b}| = |\boldsymbol{r}_2 - \boldsymbol{r}_1|$ and $v_{\rm b} = |\boldsymbol{v}_{\rm b}| = |\boldsymbol{v}_2 - \boldsymbol{v}_1|$. $M_{\rm tot}$ is the enclosed total mass including the stars and the gas mass within r_2 (when $r_1 \leq r_2$). We calculate the orbital energy at every coarse time step of the simulations (~ 13 yr). From the orbital energy and $M_{\rm tot}$ we can get the semimajor axis of the orbit, $a_{\rm b}$. Unlike in M19, the mass of the gas disc is not always negligible in some binaries and therefore we include the enclosed gas mass. Note that the time steps between outputs of hydrodynamics information are limited to $\sim 1-2$ kyr (due to the large size of the files). For this reason, the gas mass between two snapshots is interpolated. Hence, especially for the cases when the gas mass is a non-negligible fraction of the total mass, the estimates of $M_{\rm tot}$ and $\mathcal{E}_{\rm b}$ may become less accurate due to sparse sampling. The orbital eccentricity is,

$$e_{\rm b} = \sqrt{1 + \frac{2l_{\rm b}^2\mathcal{E}_{\rm b}}{(GM_{\rm tot})^2}}. \tag{5.11}$$

In this equation, $l_{\rm b} = |\boldsymbol{l}_{\rm b}| = |\boldsymbol{r}_{\rm b} \times \boldsymbol{v}_{\rm b}|$. This is equal to J divided by the reduced mass (see Equation (5.1)) but differs from the specific angular momentum defined in Equation (5.9). The

rate of energy change as a function of time is,

$$\frac{\mathrm{d}\mathcal{E}_\mathrm{b}}{\mathrm{d}t} = -\frac{G\dot{M}_\mathrm{tot}}{r_\mathrm{b}} + \dot{\boldsymbol{r}}_\mathrm{b} \cdot \boldsymbol{f}_\mathrm{ext}. \tag{5.12}$$

In this work, however, when we plot the rate of orbital energy change we show the left-hand side of the equation, approximating the derivative as it finite time difference ($\Delta\mathcal{E}_\mathrm{b}/\Delta t$). We leave studying the contribution of different external forces to the orbital energy evolution as future work.

5.3 Origin of Outward Migration

5.3.1 Typical Formation Scenario

In this subsection, we briefly summarise the general scenario of Pop III star formation in a primordial disc according to the results of our previous papers in the series. For a more detailed picture, see Section 3.1 and Fig. 4 of Paper III. A gas cloud with a nearly isothermal profile and peak density $n_\mathrm{H} \sim 10^7$ H cm^{-3} contracts and flattens out to form a protostellar disc due to the angular momentum conservation. This gas disc becomes gravitationally unstable and fragments (Kimura, Hosokawa, and Sugimura, 2021), and multiple sink particles form. Some of the sinks migrate inward in a few kyr and merge with others while the others survive and migrate outward. The survivors possess a circumstellar minidisc and these minidiscs may fragment to form multiple stars. Some stars migrate inward while others migrate outward repeating the initial fragmentation time evolution but on the smaller scale of the circumstellar disc (rather than the larger circumbinary disc). In this scenario, the most common outcome is a hierarchical binary (a

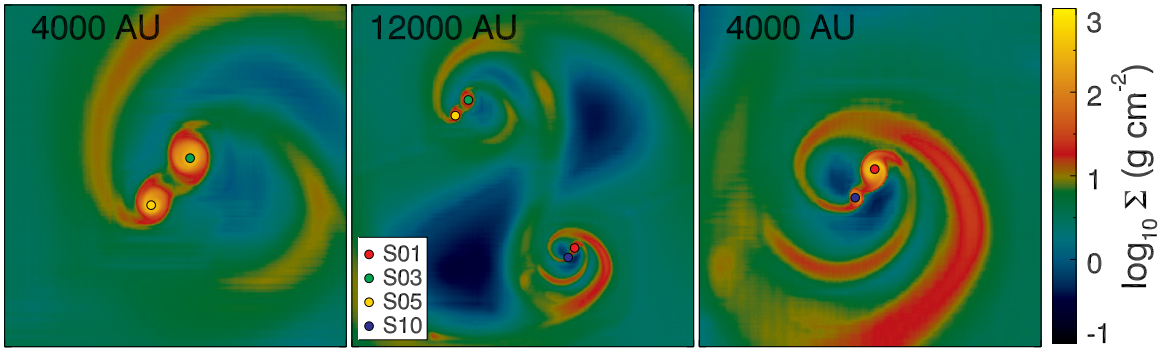

Figure 5.1: Snapshot of the case Fiducial-Outward. The colour map represents the gas surface density. Sink particles are shown in coloured circles. The hierarchical binary (middle panel) consists of two binaries (left and right panels). The centre of each plot is the CoM of the binary. The FoVs are $(4{,}000\ \mathrm{AU})^2$, $(12{,}000\ \mathrm{AU})^2$, and $(4{,}000\ \mathrm{AU})^2$, respectively.

binary of binaries, Fig. 5.1), but dynamically unstable systems (*e.g.*, single-triple pair, Sugimura et al., 2020) may appear. Each of the binaries generally also migrates outward, but there are a few exceptions (Section 5.4). At late times, in some systems stars can form at Lagrange points L4/L5 of the main binary. This scenario, however, depends on the intensity of the X-ray background that regulates the gas accretion rate onto the disc and stars via enhanced cooling. Strong X-ray irradiation typically lowers the multiplicity and masses of Pop III stars (see Paper II and Paper III).

In Fig. 5.2 we plot the trajectories of long-lived sink particles (shown as coloured circles at the time of formation and crosses when they merge) for the three runs in which our fiducial binary cases are found. The top panels show the star orbits in a system of reference centred on the CoM, while in the bottom panels the system of reference is centred on one of the binary stars. Sinks that are short-lived are not shown here: they migrate inward on a timescale of a few kyr before merging with other sinks. In general, the orbits of long-lived sinks are eccentric and expand with time. This can be clearly seen in the orbit of the Fiducial-Outward case (red and blue symbols in the bottom left panel). The top left panel also shows the outward migration of the individual

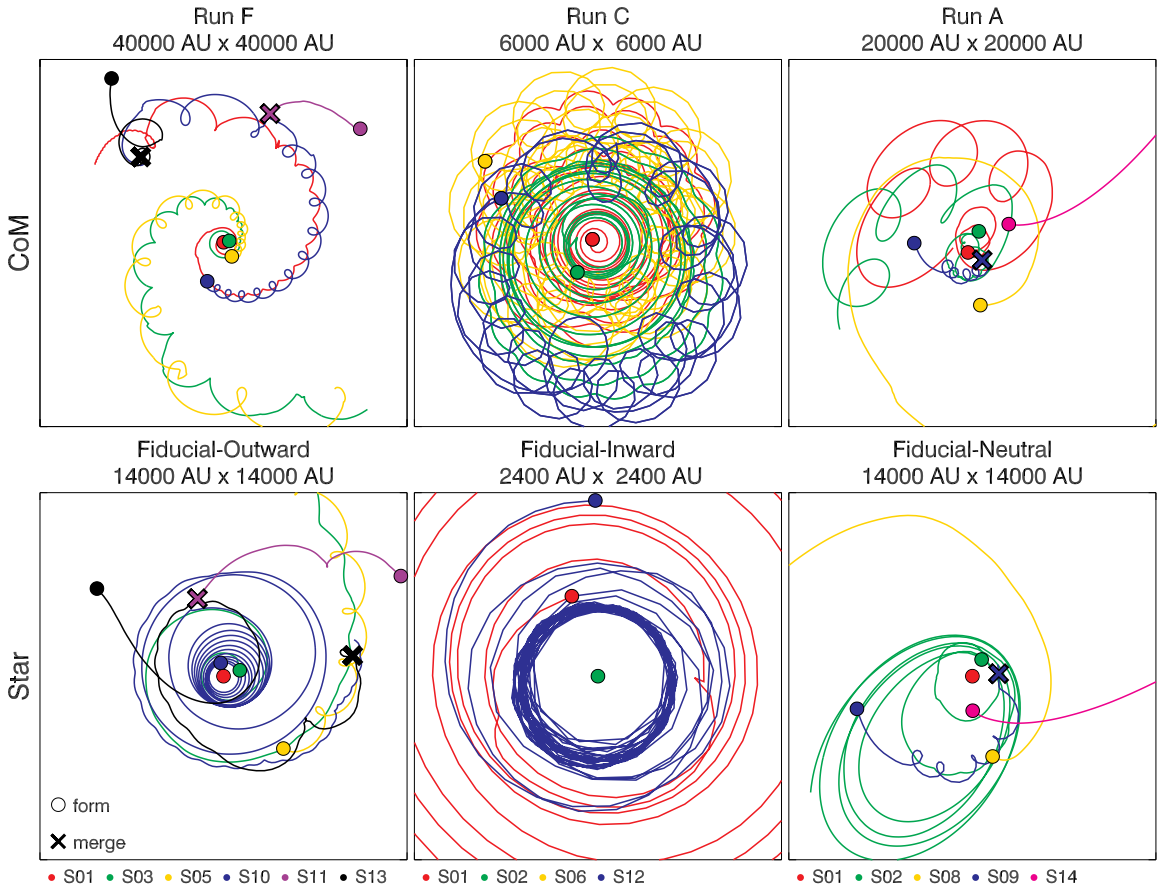

Figure 5.2: Trajectories of sinks around three representative binaries. Long-lived sinks (more than 10 kyr) are colour-coded and short-lived ones are not shown here. The FoV of each panel is shown at the top. Circles and crosses indicate the locations of sink formation and mergers, respectively. Top panels: Trajectories in the CoM frame of reference. Bottom panels: Trajectories in the frame of reference centred on one of the binary star. Left panels: Fiducial-Outward binary. S01 (red) is at the centre of the plot. Most long-lived stars migrate outward and have eccentric orbits but an exception is S11 (purple) merging to S10 in Run F. Middle panels: Fiducial-Inward binary. S02 (green) is at the centre. S01 (red) migrates outwards but S12 (blue) migrates inward. Right panels: Fiducial-Neutral binary. The orbit of S02 becomes highly eccentric ($e \sim 0.8$) in $2-3$ orbits.

binaries. The orbit of this binary expands faster at a later time due to the gravitational torque by S11 (purple) and the merger with it (purple cross).

In the middle panels, we plot the trajectories of the stars in Run C (top) and the Fiducial-Inward binary (bottom). With S02 (green) fixed at the centre of the frame of reference (bottom middle panel), its companion (S12, blue) forms at a distance of ~ 1200 AU and it migrates inward

down to ~ 400 AU. Later, the size of the orbit remains nearly constant without further migrating or merging with S02. In the right panels, we show a case (Fiducial-Neutral: red and green) in which the orbit does not expand significantly but it is highly eccentric ($e \sim 0.8$). In this run at later times S09 (blue) merges with S02 while other stars (S08 and S14) are ejected via three-body interactions.

5.3.2 Source of Angular Momentum of Sinks

Conservation of angular momentum imposes that, in the absence of external torques and gas accretion from outside the system, the binary orbital parameters remain constant. The migration of the stars, therefore, is caused by the transfer of angular momentum between the binary and other parts of the system via torques and/or gas accretion (Tang et al., 2017; M19; Moody et al., 2019; CH19; Tiede et al., 2020; Dittmann and Ryan, 2022). The first step to understanding the dominant physical mechanism causing migration, therefore, is to estimate the torques existing in the system. Note that we often loosely refer to the accretion of angular momentum as a torque, $\tau_{\rm acc}$, as defined in equation (5.7).

Fig. 5.3 shows an example of such calculation for our prototype binary system showing outward migration (Fiducial-Outward). This system is the binary S01-S10 in the minidisc around star S01 in Run F (see also top left panel of Fig. 5.2). S10 forms at $t \sim 25$ kyr from the fragmentation of the circumstellar disc around S01 ($M \sim 50$ M$_\odot$). It has an initial separation from S01 of ~ 500 AU and a mass $q \sim 0.1$ times that of S01. While the binary is accreting gas, the mass ratio q increases and reaches $q \sim 0.5$ before the merger of S10 and S11 (Panel b). This can also be interpreted as a preferential accretion onto the secondary star, also pointed out in previous works

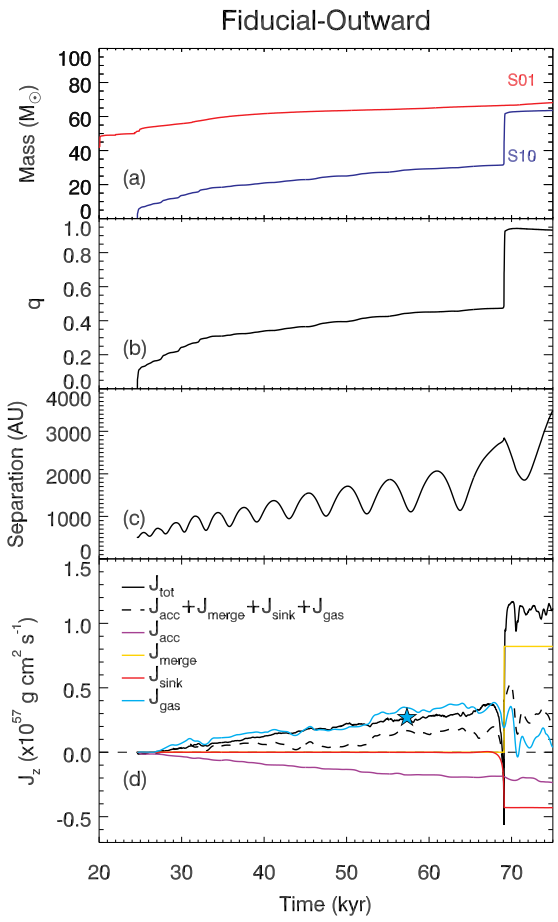

Figure 5.3: Panel a: The masses of the individual stars in Fiducial-Outward binary. Panel b: The mass ratio between the stars. Panel c: The separation between the stars. Panel d: Predicted and measured (solid line) time evolution of the angular momentum due to the effect of different torques (from equation (5.3) to (5.8)). Only the z-components of the vectors are shown in the figure. We distinguish the sum of the angular momentum from individual torques (dashed line) from the actual angular momentum of the binary measured directly (black solid line). As a sanity check, the light blue star indicates the contribution to the angular momentum from the gas disc calculated with the method discussed later and shown in Fig. 5.6.

(Bate, 2000; Farris et al., 2014; Muñoz et al., 2020). In addition, the separation increases by a factor of 4 ($\sim$ 2,000 AU, Panel c). After the merger, this initially unequal mass binary becomes of nearly equal mass (top panel) and the separation increases by a factor of two. Here, however, we focus on understanding the effect of other torques (*i.e.*, accretion and gravitational) before the merger.

Before exploring the main mechanism for the outward migration, we try to understand the outward migration by looking at the changes in the parameters related to the binary. Following M19, we plot the evolution of $\dot{M}_{\rm b}/M_{\rm b}$, $\dot{l}_{\rm b}/l_{\rm b}$, $\dot{\mathcal{E}}_{\rm b}/\mathcal{E}_{\rm b}$, $\dot{a}_{\rm b}/a_{\rm b}$, and $\dot{e}_{\rm b}$ for the Fiducial-Outward binary in Fig. 5.4. As the original plot is noisy, we smoothed each plot by averaging the values for every $\Delta t \approx 0.4$ kyr (30 data points). In M19, these values are shown as a fraction of the prescribed constant gas inflow rate ($\dot{M}_0/M_{\rm b}$) but this quantity is unavailable in our non-idealised simulation. For this reason, we normalise those rates with the average accretion rate $< \dot{M}_{\rm b}/M_{\rm b} > \approx 1/t_{\rm acc}$ in Panel a. The accretion time scale $t_{\rm acc}$ of Fiducial-Outward is ~ 81 kyr. The net force exerts a torque on the binary and delivers energy to it (Panel b and c) causing the binary to migrate outward (Panel d). The initial eccentricity of the binary is 0.14 and increases with time (Panel e). It is unlikely, however, that the gas disc drives this evolution toward the eccentricity attractor ~ 0.4 (Zrake et al., 2021; M19; D'Orazio and Duffell, 2021; Lai and Muñoz, 2023) because other sink particles and mergers appear to be the main factors responsible for a substantial increase of the eccentricity (see discussed in Section 5.3.5).

To understand the main mechanism for the outward migration we compare the increase of angular momentum by separating the effect of various torques as a function of time (see bottom panel). Before the merger, the gravitational torque from the disc (light blue line) and accretion of angular momentum (purple line) are the two dominant sources of angular momentum (see bottom panel). However, they work in opposite directions: the gas accretion torque is negative, hence reducing the binary angular momentum and acting as a viscous or drag term. The gravitational torque is instead positive (producing outward migration) and it dominates over the negative torque. The net change in $J_{\rm z}$ from the sum of all torques (dashed line) is positive. When compared to the actual orbital angular momentum of the binary (black solid line) the agreement is not

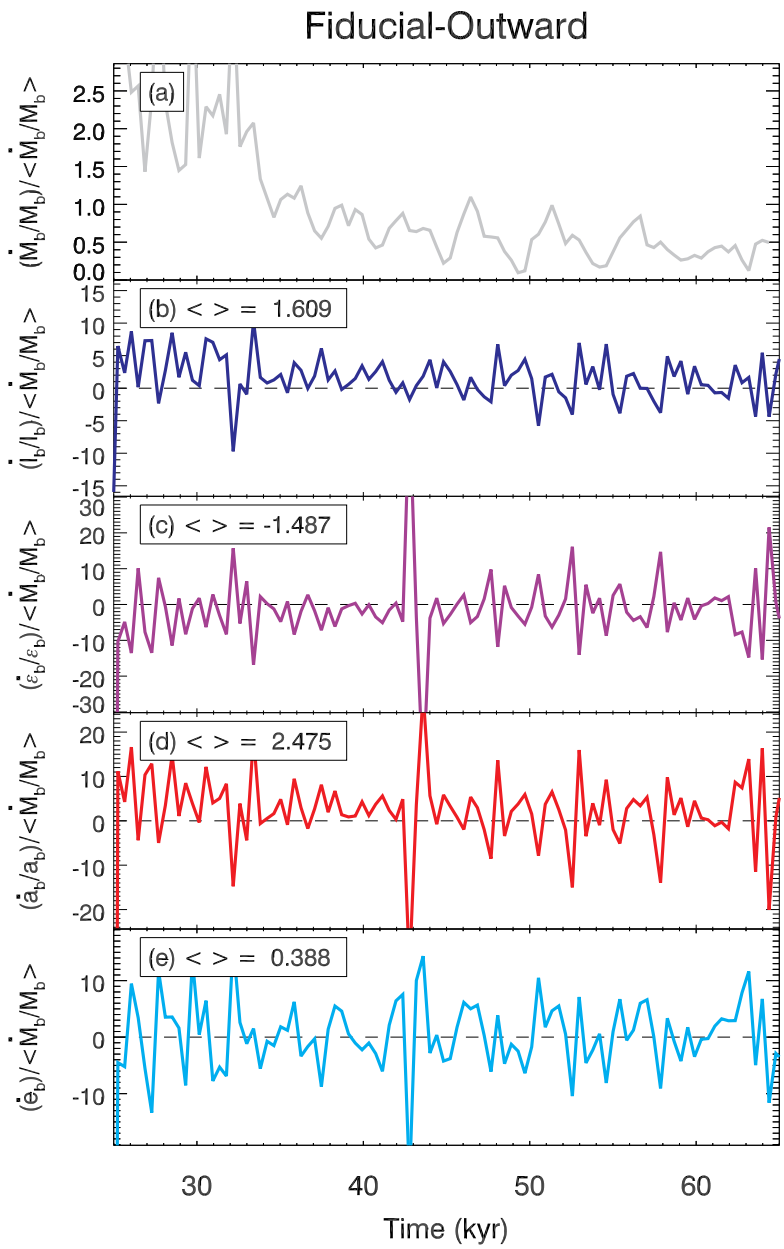

Figure 5.4: The evolution of $\dot{M}_{\rm b}/M_{\rm b}$ (Panel a), $\dot{l}_{\rm b}/l_{\rm b}$ (Panel b), $\dot{\mathcal{E}}_{\rm b}/\mathcal{E}_{\rm b}$ (Panel c), $\dot{a}_{\rm b}/a_{\rm b}$ (Panel d), and $\dot{e}_{\rm b}$ (Panel e) in the Fiducial-Outward binary. The rates in Panel a to e are normalised by $< \dot{M}_{\rm b}/M_{\rm b} >$ (Panel a). We show the first ~ 40 kyr before a merger. At the top left corner of each panel, we show the average value (except Panel a, the average is unity). Each plot is smoothed over 30 points to show the general trend better. In Panel b and c, we found that external forces lead to an increase in angular momentum and orbital energy. The orbit expands as shown in Panel d. $< \dot{e}_{\rm b} >$ is positive meaning the orbit becomes more eccentric (Panel e).

perfect because the calculations are somewhat uncertain due to the finite time steps of our outputs ($\sim 1 - 2$ kyr). The result shown in Fig. 5.3 is representative of most simulations in that the

gravitational torque is the dominant term and the accretion torques have a negative sign, somewhat reducing the outward migration effect. When stars are observed to migrate outward, both the solid and dashed lines are increasing nearly in all binaries we analysed, meaning the gas disc plays the dominant role in producing the binary migration via gravitational torque.

We established that the outward migration of stars is caused by the gravitational torque by the gas disc. Now we need to understand why the sign is positive (*i.e.*, the star is accelerated in the direction of its rotation by some gas overdensity in front of it) and which part of the gas disc contributes most to the torque (outer disc, the spiral structure or the minidisc). There is a general agreement that the outer gas disc exerts negative torque on the binary (Gould and Rix, 2000; Armitage and Natarajan, 2002; Chang et al., 2010; M19; Dittmann and Ryan, 2022) thereby shrinking it. In the context of Pop III binaries, CH19 also demonstrated that disc spiral structures extract the angular momentum from the binaries. Hence, the question becomes whether other components in the system provide positive torque to overcome the effect of the outer disc. Tang et al. (2017) argued that the gravitational torque by the minidiscs around sink particles (SMBHs in this case) drives inward migration. On the other hand, M19 demonstrated the torque from the inner circumstellar discs is dominant over the outer torques and is responsible for the outward migration. In our simulations, as observed in CH19, a spiral structure often appears when newly formed sinks migrate inward to merge with the central one. Once this initial merger phase is over, the remaining stars have circumstellar minidiscs and spiral arms extending outward and connecting the minidiscs (see Fig 5.1). For this reason, we hypothesise these non-axis-symmetric structures are the dominant contribution to the torque and outward migration of the binary. To test this hypothesis, we construct maps showing the contribution to the gravitational torque on the binary from each gas cell on the disc (shown face-on). To visualise these maps we choose a

Table 5.2: Parameters of the logarithmic polar grid.

Parameter	Value	Description
$r_{\rm min}$	10 AU	inner boundary
$r_{\rm max}$	7071 AU	outer boundary
$N_{\rm r}$	100	number of grids in the radial direction
N_θ	60	number of grids in the azimuthal direction
$\mathrm{d}\ln r$	0.0656	radial resolution
$\mathrm{d}\theta$	0.105π	azimuthal resolution

2-dimensional logarithmic polar grid (r and θ) around each sink particle and calculate the total torque on the binary contributed by each cell on this grid. These grids are on the orbital plane of the binary and are perpendicular to the binary angular momentum vector. This approach imposes the cell size $r^2\mathrm{d}\theta\mathrm{d}\ln r$ and thus eliminates r^{-2} dependence of gravity which might lead to visually underestimating the effect of outer spiral arms despite their large extent and mass. The parameters of the logarithmic grid are provided in Table 5.2. Note that the colour maps show the total torque in each cell, not torque density like in previous works (*e.g.*, Tang et al., 2017; M19; Dittmann and Ryan, 2021, 2022): in this work the torque density would also lead to visually underestimating the role of the outer structures because of the increasing cell size with radial distance.

The contribution to the torque from different parts of the gas disc is visualised in the left panel of Fig. 5.5 for Fiducial-Outward binary. Although the torque by the minidiscs is large, spiral arms also exert significant torques on the binary, although the sign of the torque varies between positive and negative values making it difficult to determine if the net torque is positive or negative. For quantitative analysis, we fold the torque map twice along the x-axis and vertical line crossing the midpoint of two sinks (dotted-dashed lines). This approach is novel and we found only one other study folding torque maps similarly to here (Li et al., 2022). Unlike in Li et al. (2022), however, our binaries are unequal mass, hence the torque maps on each side are

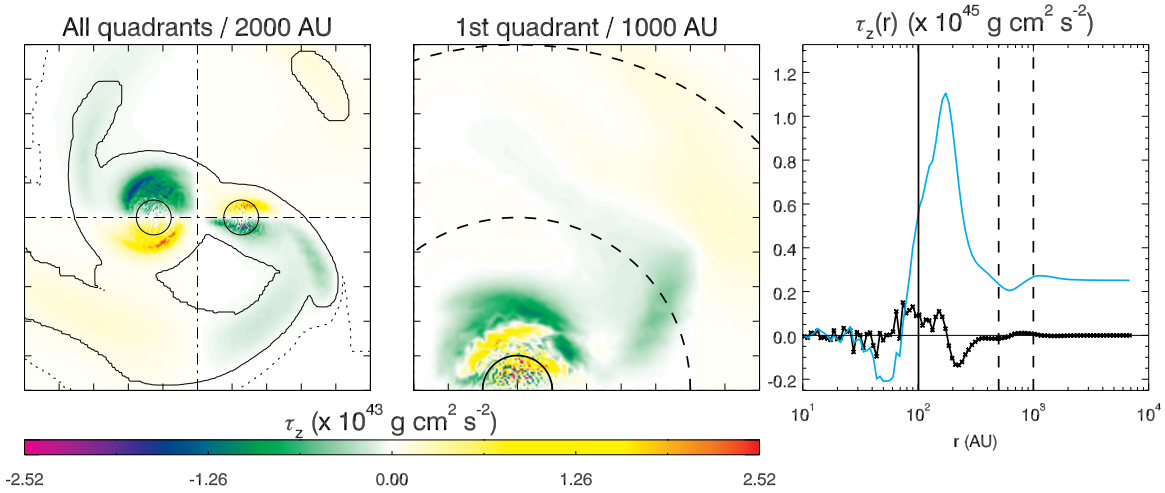

Figure 5.5: Left: Gravitational torque map right after the formation of the binary in the Fiducial-Outward binary ($t \sim 25$ kyr). We calculate the gravitational torque exerted on the binary from gas cells. The torques are projected onto the logarithmic polar grid (r and θ) around each star. The angular momentum vector of the binary is perpendicular to each plane. The density on the left half of the figure is projected onto the polar grid around S01 (left circle) and the density on the other side is projected onto the grid around S10 (right circle). In addition, we cover the gas cells with height $\lesssim 41000$ AU along the line-of-sight and, therefore no torque is effectively missing. Circles are sink particles with radii to scale. The centre of the plot is the midpoint between two stars. The midpoint is chosen as the centre so that two sinks are overlapped when the map is folded (see the description of the middle panel). The iso-density contours indicate $n_{\rm H} = 10^9$ cm^{-3} and 10^{10} cm^{-3} (dotted and solid lines, respectively). The binary is orbiting in the counterclockwise direction. The FoV is 2,000 AU $\times$ 2,000 AU. Middle: Net torques folded and added to the first quadrant. The torque map in the left panel is folded twice along the dotted-dashed lines so that the two sinks overlap. The FoV is 1,000 AU $\times$ 1,000 AU. Dashed lines are two concentric circles with radii 500 and 1,000 AU. Right: The torque as a function of distance. We measure the torque in the middle panel and r indicates the distance from the sink particles (centre of the semicircle) in the disc plane. We do not show the torques with $r < 10$ AU because this scale is smaller than the spatial resolution of the simulation (12.6 AU). The black line is the torque at r and the blue line is the cumulative torque. The vertical lines show the locations of the sink radius (solid line) and 500 AU and 1,000 AU (dashed lines).

not symmetric. We highlight, however, that our approach distinguishes the torque by the two circumstellar minidiscs from that by the outer gas disc and shows that they play a major role in producing outward migration (as discussed in the next paragraph). In this way, torques in the entire domain are added to the 1st quadrant and it is easier to determine the relative importance of the positive and negative regions of the torque and their location. As can be seen in the middle

panel, the torque is positive near the sink radius (solid line) and outside ($\sim$ 200 pc, top left of the solid line). This region corresponds to the front side of the minidiscs and therefore this result implies that the sinks are accelerated in the directions of the binary orbital velocity. The azimuthally averaged radial profile, shown in the right panel, also shows that the gas just outside the sinks dominates the contribution to the net positive torques and therefore is the cause of the outward migration.

Fig. 5.5 illustrates the importance of the minidiscs in driving the outward migration of the binary at a specific time. However, it does not show the overall effect integrated over time. As seen in Fig. 5.2 and Fig. 5.3 the stars in the binary migrate continuously. This means that the net positive torque has to be kept during this period. This is visualised in Fig. 5.6, showing the same torque map integrated over time (*i.e.*, showing the angular momentum, equation (5.8)). In the figure, the bright yellow feature (top panel) and the cumulative torque (blue line, bottom panel) indicate the gas near the sink (minidiscs) exert net positive torque consistently. This result, therefore, implies the minidiscs play the most significant roles in producing the migration of the stars as found in Tang et al. (2017), although contrary to the BH binary case in their work, in our case the sign of the torque is positive and the migration is outward.

5.3.3 Source of Angular Momentum of Disc

As mentioned in the previous subsection, the minidiscs are the dominant source of the gravitational torque on the stars. This means that they inevitably lose some of their angular momentum by dragging their central stars with them. For the circumstellar minidiscs and their central stars to keep migrating outward, therefore, there must be an external source of angular momentum acting

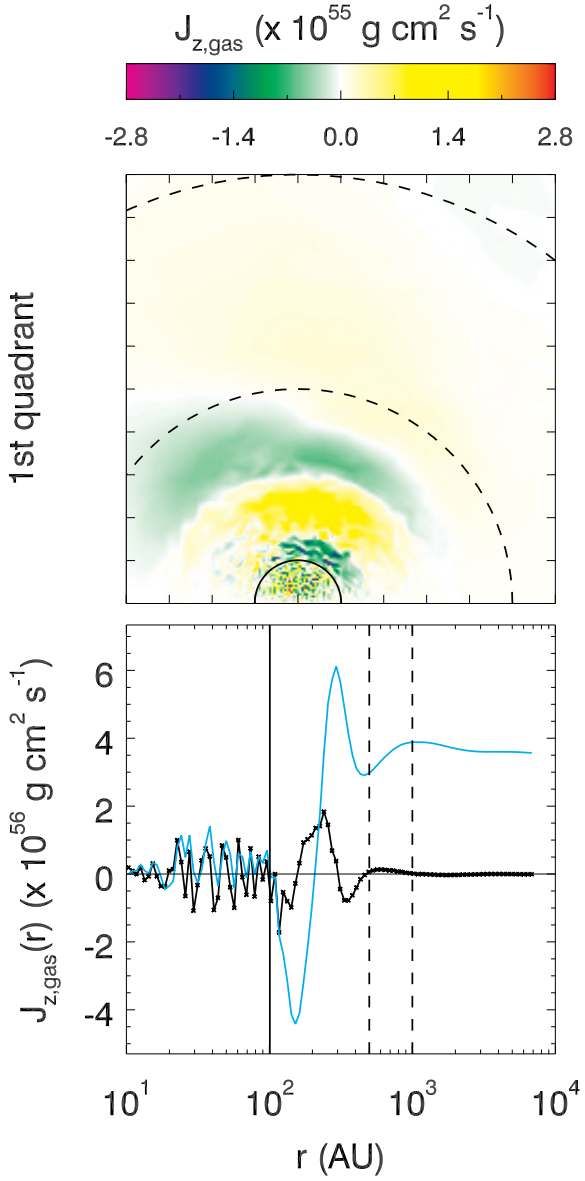

Figure 5.6: Top: Folded torque map (see caption for the middle panel of Fig. 5.5) integrated over time. Therefore, the colour map represents the contribution to the change in angular momentum of the binary from different regions of the gas disc. The sinks are dragged in the direction of the motion by the gas in front of them (yellow region). Bottom: Radial profile of torque. The format of this panel is the same as that in the right panel of Fig. 5.5. The figure shows the values at $t \sim 57$ kyr. As a sanity check, we plot the total torque in Panel d of Fig. 5.3 with a light blue star.

on the minidiscs. An obvious candidate is the accretion of high angular momentum gas from the circumbinary envelope. This idea was first suggested in Sugimura et al. (2020) and in Paper II, without a quantitative analysis of this effect. However, Paper II provided several hints that out-

ward migration is connected to the gas accretion rate. The global rate of gas accretion from larger scales to the disc center ($\dot{M}$) is proportional to $c_{\rm s}^3$, where $c_{\rm s}$ is the gas sound speed. Even though it seems counter-intuitive, the sound speed is reduced if the gas is irradiated by a strong/moderate X-ray background because of the enhanced formation and cooling by H_2. The reduction in $\dot{M}$ slows down the accretion of high angular momentum gas onto the circumstellar discs and stars. We therefore found that, when irradiated by an X-ray background, Pop III protostars tend to have smaller masses and the rate of outward migration is reduced, producing binaries with smaller separations (Fig. 8 of Paper II). We concluded that the rate of gas accretion plays an important role in the angular momentum supply and outward migration of Pop III binary stars.

To test the idea that minidiscs gain angular momentum by accreting high angular momentum gas from the outer parts of the disc, we estimate the external gas gravitational torque and angular momentum accretion rate of the discs. To carry out this calculation, we first define a cylinder with a radius $r_{\rm cyl} = 300$ AU and height of $h_{\rm cyl} = 600$ AU around each sink particle. We assume that this cylindrical boundary contains the minidiscs around each sink particle. The gravitational torque is calculated as explained in Section 5.3.2 for the case of the sinks, using equation (5.4). In the equation, however, the subscript i runs over all gas cells within the cylinder and j runs over gas cells outside the cylinder. The change in angular momentum over time due to this effect is shown in light blue in Fig. 5.7. To calculate the accretion rate of angular momentum, we identify the cells near the cylinder walls ($r_{\rm cyl} - \Delta x_{\rm min}/2 \leq r < r_{\rm cyl} + \Delta x_{\rm min}/2$), where r is the radial distance in the cylindrical coordinates. The radius of the cylinders is kept fixed for

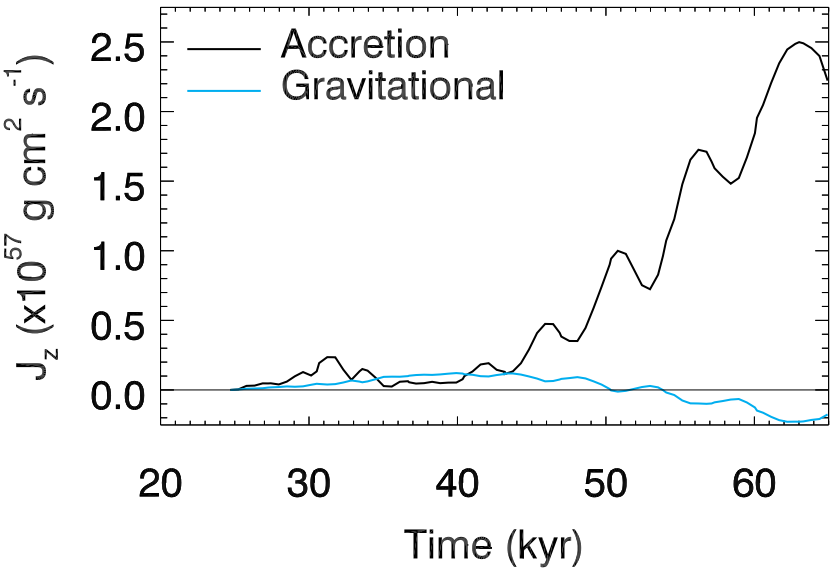

Figure 5.7: Angular momentum of the minidiscs as a function of time for the Fiducial-Outward binary due to the gas accretion torque (black line) and external gravitational torque (cyan line). Only the z-component of the angular momentum is considered.

simplicity. The total accretion rate through the walls is calculated as follows:

$$\frac{\mathrm{d}J_z}{\mathrm{d}t} = \sum_{i=1}^{2} \sum_{j=\mathrm{cell}} \frac{J_{j,z}}{V_j} v_{j,r} \Delta x_j^2. \tag{5.13}$$

The subscripts i and j indicate the sinks and gas cells, respectively. V_j is the volume of cell j and therefore $(J_{j,z}/V)$ is its angular momentum density. $v_{j,r}$ is the radial velocity in the cylindrical coordinate. As seen in Fig. 5.7, the change in angular momentum due to gas accretion (black) is dominant over the gravitational torque (light blue) on the disc. Other binaries with outward migration follow a similar trend with a more pronounced difference. Another result that can be noticed inspecting the accretion of angular momentum as a function of time in Fig. 5.7, is that the angular momentum accretion has periodic oscillations with peaks happening just after the stars reach the apocentre of the elliptical orbit. This aspect is more clearly seen in Fig. 5.8, showing that the disc angular momentum (red lines in panel a) peaks near the maximum binary separation

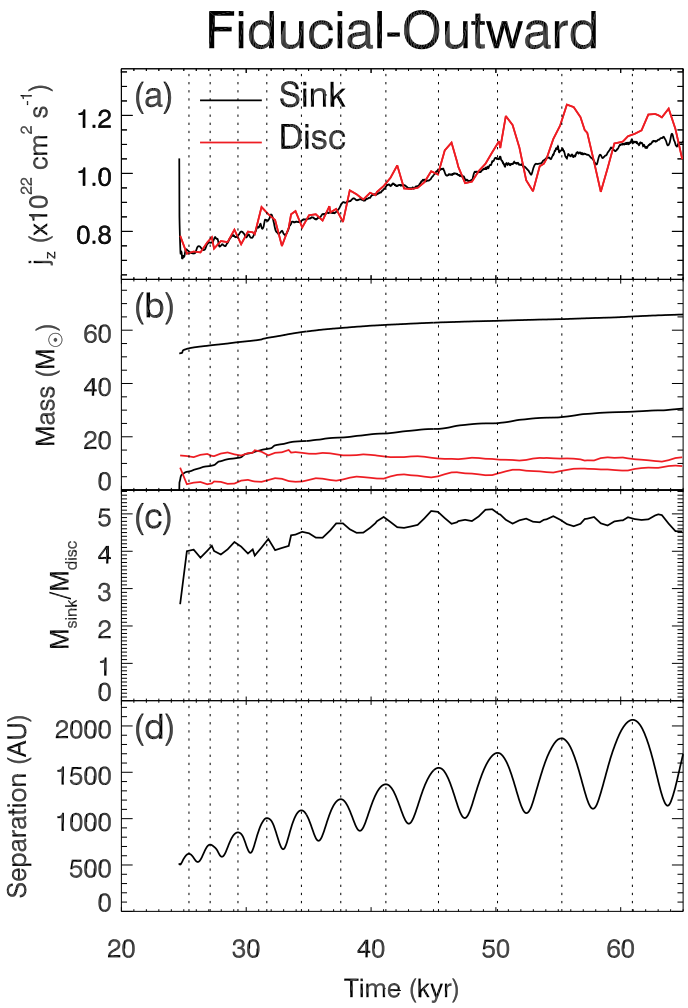

Figure 5.8: Properties of the Fiducial-Outward binary. Vertical dashed lines indicate maximum separations between two stars. Black lines in Panels a and b refer to stars (sinks) properties while the red lines refer to the same quantities for the gas discs. The discs are defined as gas within a cylinder with a diameter of 600 AU and height of 600 AU. Panel a: Specific angular momentum of the stars and minidiscs (equation (5.9)). Overall, both the stars and discs angular momenta increase with time but that of the discs shows larger fluctuations as a function of time with peaks near the apocentres. Panel b: Time evolution of the masses of individual stars and discs. Panel c: Ratio of the mass in sinks to the mass in the minidiscs as a function of time. The system mass is dominated by the stars and therefore the disc rotation outsided of the stars' outer orbit is nearly Keplerian. The oscillation of the ratio is due to the mass increase of the discs at apocentres. Panel d: Separation between the two stars as a function of time.

(vertical dotted lines). This is because stars are further from the CoM and therefore they can accrete high angular momentum gas more easily. These accretion peaks are pronounced when the secondary star passes the outer spiral arm. At pericentres, on the other hand, the discs lose

angular momentum to the sinks, but the net effect integrated over time is toward an increase of the angular momentum.

5.3.4 Efficiency of Angular Momentum Accretion

For binaries to gain angular momentum and migrate outward by gas accretion, the specific angular momentum of the accreted gas must be higher than that of the stars. The difference between these two values, in addition to the mass accretion rate, may explain why some stars migrate outward efficiently while others do not. The answer to this question requires an understanding of the distribution of the angular momentum of gas and stars. The specific angular momentum of the stars in a binary is,

$$\begin{aligned} j_{\rm star} &= j_{\rm star,1} + j_{\rm star,2} = r_1^2\omega_{\rm kep} + r_2^2\omega_{\rm kep} \\ &= r_1^2\sqrt{GM/r^3} + r_2^2\sqrt{GM/r^3} \\ &= \left(\frac{m_2}{M}\right)^2 r^2\omega_{\rm kep} + \left(\frac{m_1}{M}\right)^2 r^2\omega_{\rm kep}, \end{aligned} \tag{5.14}$$

where $\omega_{\rm kep} = 2\pi/P = \sqrt{GM/r^3}$ is the angular velocity of the binary, with $r = r_1 + r_2$, $r_1/r = m_2/M$ and $r_2/r = m_1/M$. Without loss of generality, we assume that $m_2 \leq m_1$ (or $q \equiv m_2/m_1 \leq 1$), hence the orbit of (Star 2) is further from the CoM of the system. The radial profile of the specific angular momentum of the disc beyond the secondary minidisc is approximately Keplerian as seen in Fig. 5.9 (solid and dashed lines). The discs are $\sim 4-5$ times less massive than the Pop III stars (Panel c of Fig. 5.8), which is a non-negligible fraction in terms of mass. Due to its $\sqrt{M}$ dependence, however, this translates into a ~ 10 % deviation of the rotational velocity with respect to perfect Keplerian case. The profile inside the orbit deviates

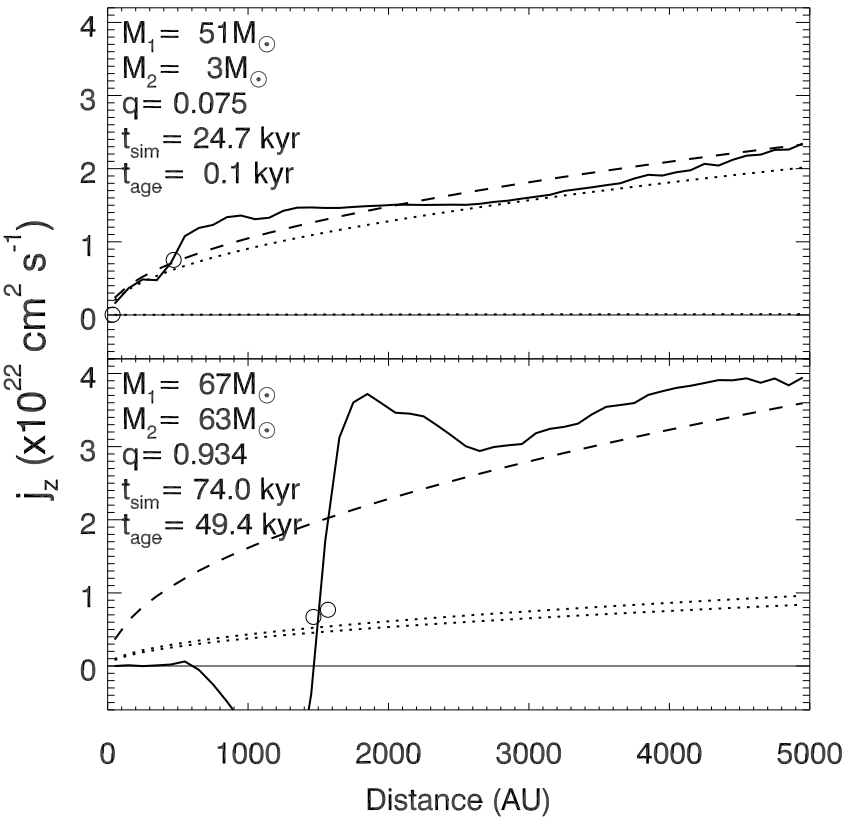

Figure 5.9: Specific angular momentum of various components in the Fiducial-Outward binary as a function of distance from the CoM (*i.e.*, the centre of the frame of reference). The solid line shows the specific angular momentum of the gas measured at distance r. Circles indicate the position and specific angular momenta of the stars. The two dotted lines show the Keplerian specific angular momentum of the individual stars ($j_{\rm star,1}$, $j_{\rm star,2}$), and the dashed line the Keplerian specific angular momentum $j_{\rm gas,kep}$ (see equation (5.15)). The top and bottom panels refer to two different epochs in binary evolution. The individual masses, the mass ratio (q), simulation time ($t_{\rm sim}$), and binary age ($t_{\rm age}$) are shown in the legend. Top panel: Binary soon after its formation ($t_{\rm age} \sim 0.1$ kyr). Note that j of the primary is an order of magnitude smaller than that of the secondary. At large radii, the gas angular momentum is close to that of the secondary star (M_2) although it deviates near the secondary due to the presence of a minidisc. Bottom panel: Binary at $t_{\rm age} \sim 39$ kyr since its formation. Since the two stars have comparable masses, their velocities and thus specific angular momenta are significantly lower than the measured gas specific angular momentum at their distance (solid line) that is approximated by the Keplerian specific angular momentum dominated by the star masses (dashed line).

from Keplerian. However, this is irrelevant to the analysis because we focus on the accretion of angular momentum from the outer disc. The profile near each sink particle also deviates from the Keplerian value because of the gas motion around the sink. This deviation is especially evident

in the bottom panel of Fig. 5.9 (between $\sim$ 500 and $\sim$ 2000 AU). However, the main takeaway of this plot is that the binary's angular momentum (dotted lines and circles) is significantly lower than the Keplerian rotation value of the gas disc (dashed line) and thus the binary (or more precisely the minidiscs) gain angular momentum from accreting gas from the outer disc. We approximate the specific angular momentum of the gas beyond the outer star orbit (*i.e.*, at a distance r_2 from the CoM) to the Keplerian value as follows,

$$j_{\rm gas,kep}(r_2) \approx r_2 v_{\rm kep}(r_2) = \sqrt{GMr_2}, \tag{5.15}$$

where $v_{\rm kep} = \sqrt{GM/r_2}$ is the Keplerian velocity. If we compare the specific angular momentum of the gas at the same distance of the outer star orbit (r_2) we have:

$$j_{\rm gas,kep}(r_2)/j_{\rm star,2} \approx (r/r_2)^{3/2} = (M/m_1)^{3/2} = (1+q)^{3/2} \geq 1. \tag{5.16}$$

This ratio approaches unity when the mass ratio of the binary is $q = m_2/m_1 \ll 1$ and reaches a maximum of $2^{3/2}$ for equal mass binaries (*i.e.*, $q = 1$). In this latter case, both stars in the binary contribute equally to the accretion of higher angular momentum gas. We point out that Sugimura et al. (2023) has interpreted the cause of outward migration similarly. We assume the angular momentum vectors are perpendicular to the orbital plane and thus the quantities in the equations above are scalars. The actual distribution of angular momentum is shown in Fig. 5.9. The solid line, two dotted lines, and a dashed line in each panel indicate $j_{\rm gas}$ (measured), $j_{\rm star,1\ or\ 2}$, and $j_{\rm gas,kep} = \sqrt{GMr}$, respectively. As can be seen in the figure, the actual measured values for the sinks (circles) agree with having Keplerian orbits (dotted lines). The figure illustrates how the

specific angular momentum distribution varies with the mass ratio. When q is small (top panel), the difference between $j_{\rm gas}$ (solid line) and $j_{\rm star,2}$ (dotted line) is relatively small. When the two stars have comparable masses (bottom panel), on the other hand, individual stars have smaller angular momentum (dotted lines below dashed and solid lines) and thus have a greater difference. Consequently, a binary obtains angular momentum more easily in an equal-mass binary.

The gas motion deviates from the perfect Keplerian motion due to the presence of gas. This deviation is greatest right after the initial fragmentation and the formation of the first binary as shown in Fig. 5.10 (Run F at $t = 1.3$ kyr). Since a larger amount of gas is available in the beginning, the gas angular momentum scales linearly rather than with $\sqrt{r}$ (Keplerian). Because the infalling gas has a higher specific angular momentum than the sinks, the stars that survive mergers migrate outward efficiently.

This mechanism also explains why the mass ratio of the binaries often approaches $q = 1$ for several of the binaries in this work (see Panel b of Fig. 5.3) and in previously published works (Bate, 2000; Muñoz et al., 2020). When q is low, the outer star intercepts most of the gas from the circumbinary disc and it grows faster than the primary star. By doing so, q approaches unity and the binary can migrate outward more rapidly.

Finally, we measured the Toomre-Q parameter to figure out the main driving mechanism of the gas accretion. In this subsection, we explain the efficiency of the accretion assuming the gas disc is Keplerian. If the gas disc is gravitationally unstable, the instability-driven spiral arms may exert torques and affect the angular momentum transfer within the Keplerian disc. In Fig. 5.11, we plot Q of the gas disc for the Fiducial-Outward binary at $t = 57.1$ kyr. We find that at this time the CBD around the binary is Toomre-stable ($Q > 1$), unlike the marginally unable CBD found by Sugimura et al. (2023). Therefore, we speculate spiral arms are not produced by

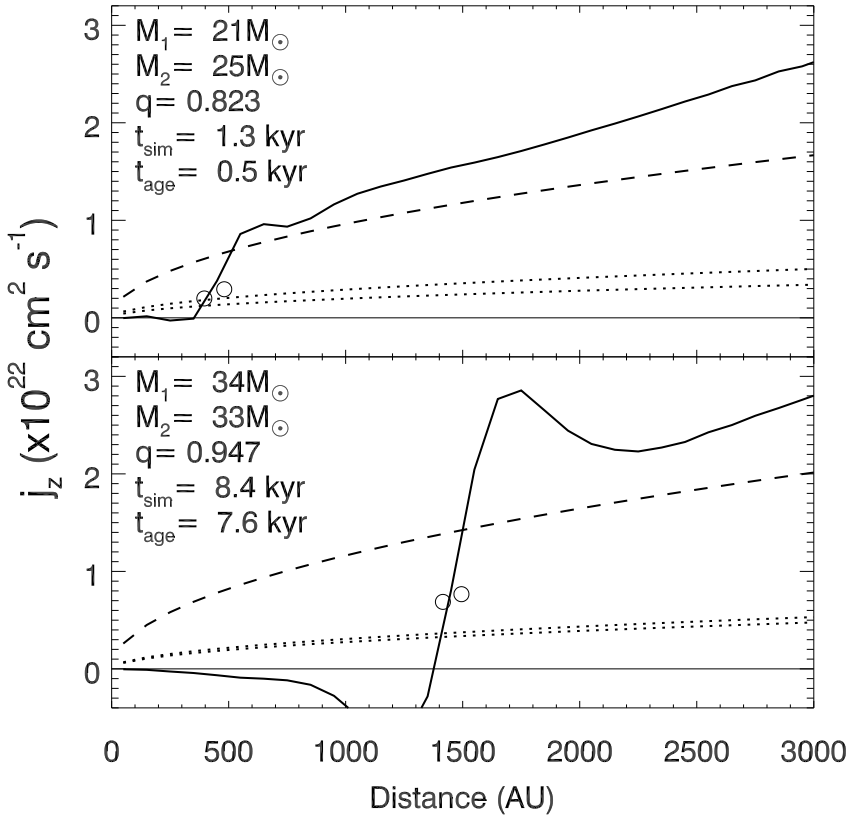

Figure 5.10: Same as Fig. 5.9 but showing the specific angular momentum of the S01-S03 binary in Run F right after the formation of S03 ($t = 1.3$ kyr).

fragmentation/gravitational instability in this phase. The difference seen in the circumbinary disc stability in this work and in Sugimura et al. (2023) is beyond the scope of this paper, so we leave it as future work.

To summarise, in this section, we explore the origin of the outward migration of binary stars. The outward migration takes place in a two-step process. First, the minidiscs around stars gain angular momentum by accreting high angular momentum gas. Then the stars embedded in the circumstellar minidiscs gain angular momentum from them via gravitational torque and migrate outward.

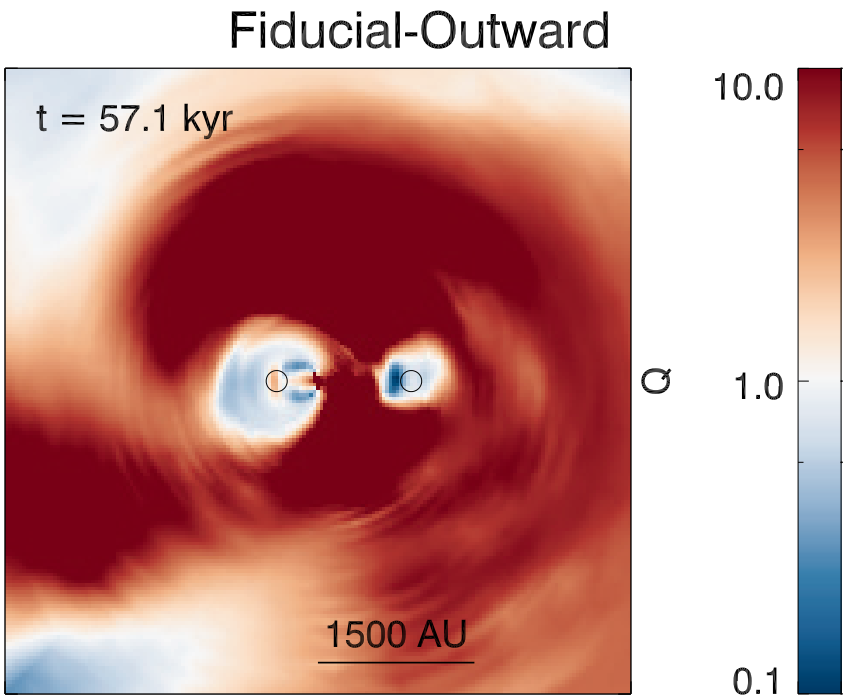

Figure 5.11: Snapshot of the toomre-Q parameter for the Fiducial-Outward binary at $t = 57.1$ kyr. The regions with low Q around the sink particles (circles) indicate the circumstellar discs are toomre unstable and hence subject to fragmentation The circumbinary disc has $Q > 1$, hence it is gravitationally stable at this time during its evolution.

5.3.5 Origin of Eccentric Orbits

Many Pop III binaries have eccentric orbits. This is interesting because the eccentricity often gives rise to a periodic variability of Pop III stars' luminosity and spectral type as discussed in Paper III. In addition, the existence of highly eccentric orbits (*e.g.*, Fiducial-Neutral with $e = 0.8$) suggests the possible relevance of a new channel for GW emission: binary black hole mergers via dynamical excitation (Michaely and Perets, 2019, 2020). These reasons motivate us to further explore the origin of eccentricity. Fig. 5.12 shows the orbital eccentricity since the formation of each binary in the three migration groups (from top to bottom). We highlight the fiducial cases with thick solid lines. The binaries are generally born eccentric through 3-body or N-body inter-

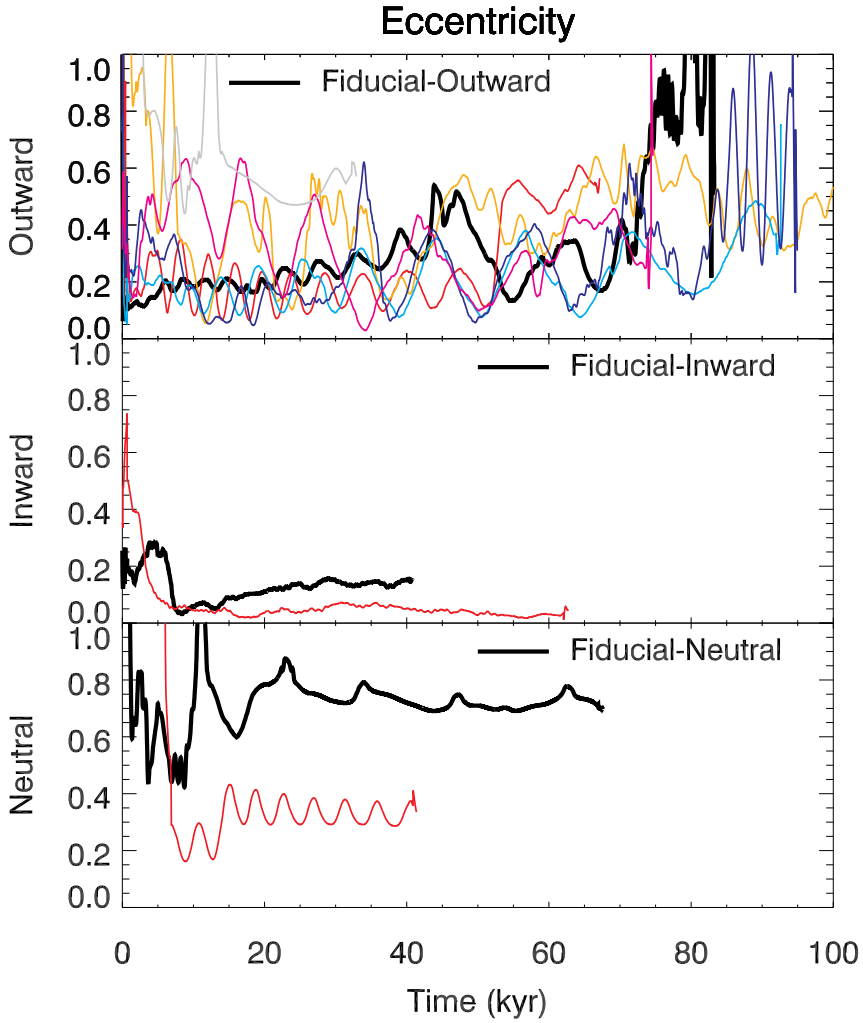

Figure 5.12: Time evolution of the orbital eccentricities (equation 5.11) for the three migration groups (from top to bottom). All the simulations are colour-coded and the fiducial systems are highlighted with thick solid lines. The x-axis indicates the time since the formation of the binary.

actions/mergers with other sink particles or gravitational torque by non-axisymmetric structures. In general, the eccentricity oscillates due to the influence of the gas disc and other sink particles. For the cases with outward migration or no migration, the eccentricities oscillate around a nearly constant value (between $e \sim 0.2$ and 0.4). If we take a look at the Fiducial-Outward binary, its initial eccentricity is $e \sim 0.14$, it increases to ~ 0.2 within a few kyr. This value remains nearly constant for a prolonged time and only starts increasing again at $t \sim 35$ kyr when another sink particle (S11) forms nearby. The eccentricity is affected by the external gravitational force un-

til this new sink merges with one of the binary constituents at $t \sim 55$ kyr. Note that outward migration happens continuously over a long period of time (see Fig. 5.3). This implies that the relationship between torques (except merger-induced torque) or the resulting outward migration and orbital (de-)excitation is insignificant. Interestingly, the periodic forcing from the accretion of gas of high-angular momentum at the apocentre (driving the outward migration) should circularise the orbit. However, we speculate that this does not happen because the periodic forcing happens only on the minidiscs while the forcing on the sinks by the gravitational torque is rather continuous over time (see Fig. 5.8).

Finally, the inward-migrating binaries (middle panels) show a behaviour more in line with what is observed in normal protostellar discs and/or protoplanetary discs: the orbits that are initially eccentric circularise while the stars migrate inward, due to the loss of angular momentum.

5.4 Cases without Outward Migration

Most binaries migrate outward in our simulations but there are a few exceptions (see runs labeled as "neutral" or "inward" in Table 5.1). To better understand the conditions necessary for outward migration, we select some cases in which it does not happen and we make a comparative analysis. Fig. 5.13 shows the time evolution of the mass, mass ratio, separation, and angular momentum and torques for the case Fiducial-Inward, and can be compared directly, having the same format, to Fig. 5.3 for our Fiducial-Outward case. The simulation ends at $t \sim 92$ kyr but we show only the first 10 kyr to focus on the initial inward migration. In this binary, similarly to the Fiducial-Outward case, the minidisc of the primary (S02) fragments to form the secondary star (S12). However, for this binary, the initial separation between the stars is initially about 2-3 times

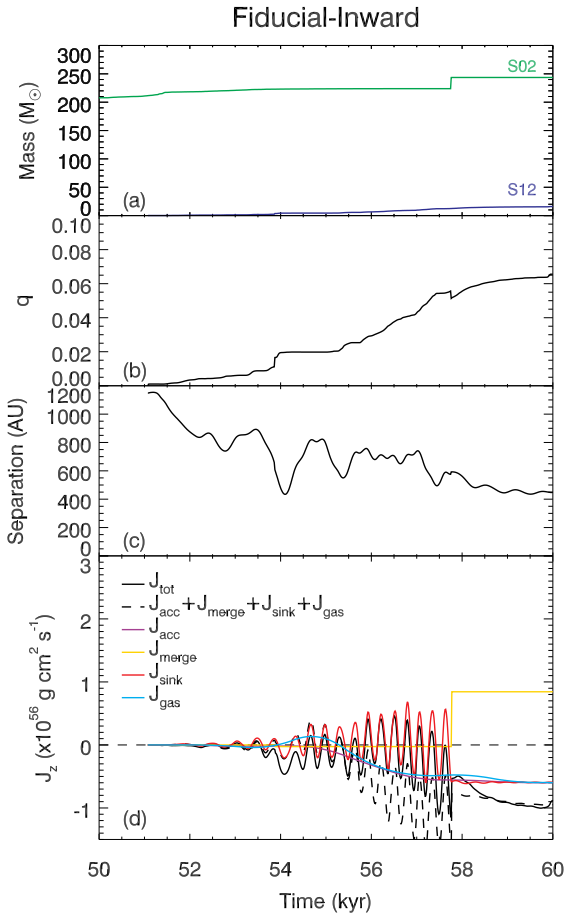

Figure 5.13: Same as Fig. 5.3 but for the Fiducial-Inward binary. The stars migrate inward (Panel c). Notable differences with respect to the Fiducial-Outward binary case are the small mass ratio (Panel a and b) and the negative gravitational torque from the gas disc (light blue, Panel d).

than for the Fiducial-Outward case (1200 AU) but decreases down to 400 AU during the first $\sim$ 10 kyr as S12 migrates inward (third panel). This inward migration is caused by the accretion (purple), gravitational torque from the gas disc (light blue line), and other stars in the system (red line, Panel d). Similarly to the Fiducial-Outward case, the accretion torque is negative but, unlike in the outward case, the gravitational torque is also negative. The angular momentum evolution due to the gravitational force from sink particles (red line) oscillates because other sink particles formed together in the minidisc of S02. Before they merge ($t \lesssim 58$ kyr), however, the average value is much smaller than the other contributions to the angular momentum evolution, therefore

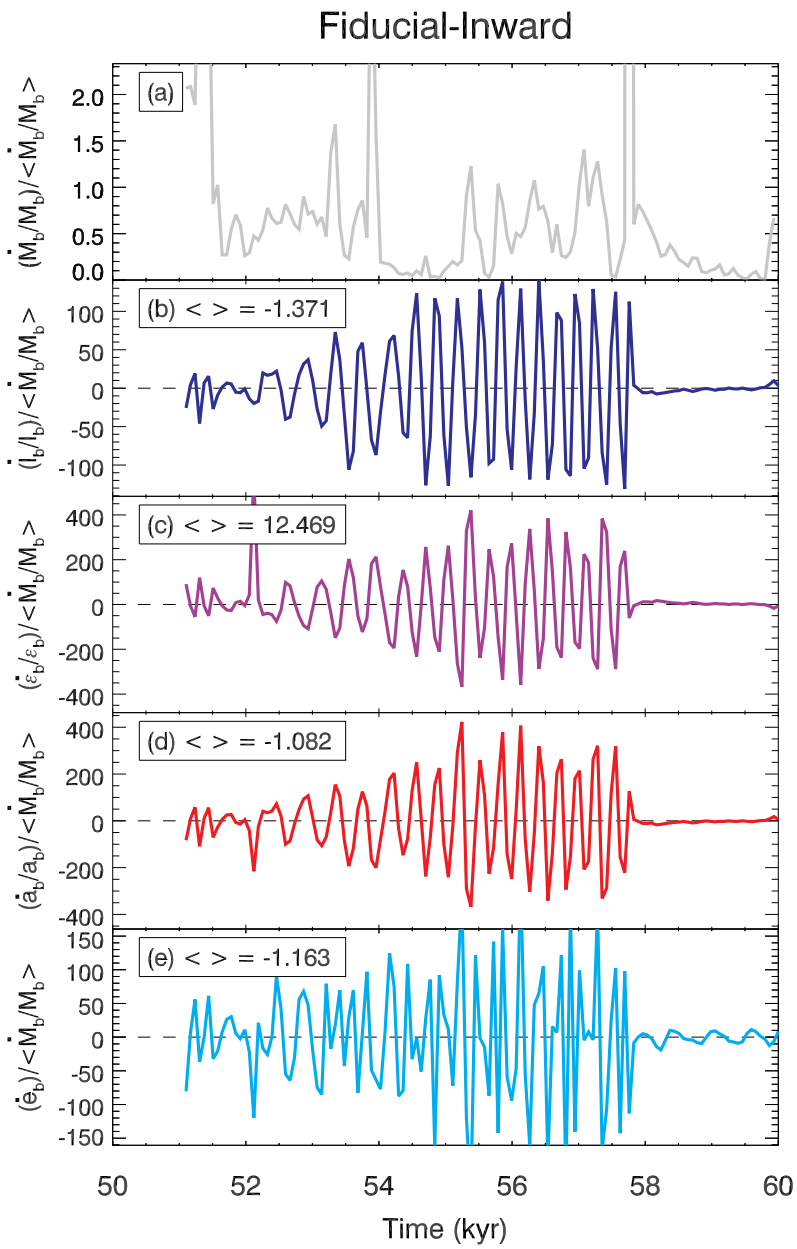

Figure 5.14: The time evolution of $\dot{M}_{\rm b}/M_{\rm b}$, $\dot{l}_{\rm b}/l_{\rm b}$, $\dot{\mathcal{E}}_{\rm b}/\mathcal{E}_{\rm b}$, $\dot{a}_{\rm b}/a_{\rm b}$, and $\dot{e}_{\rm b}$ for the Fiducial-Inward system. We show only the first ~ 10 kyr during which the binary migrates inward. The format is the same as in Fig. 5.4. The rates are normalised by $1/t_{\rm acc} \approx 43$ kyr. The data is smoothed over 5 points (≈ 0.07 kyr). Contrary to the outward case, the angular momentum and semimajor axis (Panels b and d) decrease meaning the orbit shrinks.

forcing from other sink particles does not contribute to the inward migration substantially for the first several kyrs. At $t \gtrsim 58$ kyr, this term remains negative because sinks disappear through mergers and this angular momentum offset is compensated by the angular momentum term due

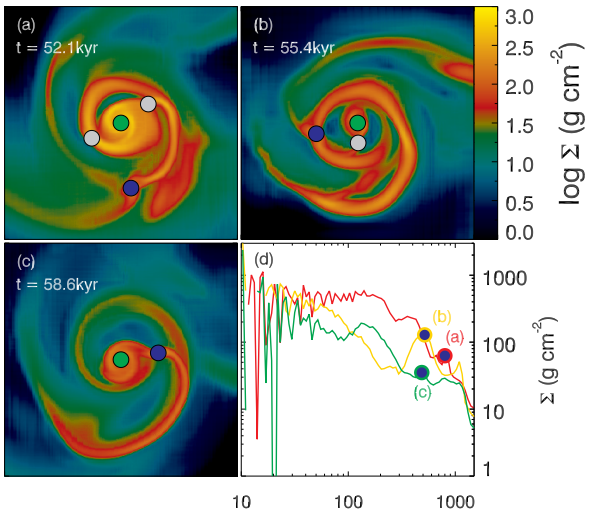

Figure 5.15: Panels (a) to (c): Snapshots of the gas surface density of the Fiducial-Inward binary system at different times. Each image is centered on the primary star (S02, green circle). The secondary S12 is shown as a blue filled circle and the other short-lived sinks are shown as grey circles. S12 forms in a spiral arm of the minidisc (a). As S12 migrates inward, it grows in mass and opens a gap (b). Once the inward migration stalls, the spiral structures exerting a negative torque disappear (c). Panel (d): Gas surface density profile in the three panels are shown with lines of different colors. The secondary star opens a gap at $t \sim 55$ kyr (yellow line).

to the mergers that becomes positive (yellow line). In Fig. 5.14 we show $\dot{M}_{\rm b}$, $\dot{l}_{\rm b}$, $\dot{\mathcal{E}}_{\rm b}$, $\dot{a}_{\rm b}$, and $\dot{e}_{\rm b}$ as a function of time for the Fiducial-Inward binary. The figure confirms that, contrary to the Fiducial-Outward case, external forces extract orbital angular momentum and energy (Panel b and c) causing the inward migration (Panel d). During the inward migration, we notice that a prominent spiral structure develops and it disappears nearly when the migration stops. We speculate, therefore, that this spiral structure drives the inward migration as found in CH19. We present gas density maps for the Fiducial-Inward binary in Fig. 5.15. Non-axisymmetric spiral structures developed within the orbit of the secondary star (S12, blue circle) in the early stage (Panel a) but this feature becomes less clear at a later stage (Panel c) when the secondary opens a gap. In Section 5.3.3, on the other hand, we argued that the fundamental reason for the outward migration is the accretion of high angular momentum gas by the circumstellar discs that migrate outward and

drag the stars with them by gravitational torques. This implies that this latter process is weakened or suppressed in this binary. A possible explanation for this difference is the small mass ratio of the binary stars (Fig. 5.13, Panel b). The mass ratio for this binary remains small ($q \lesssim 0.01$) for the first $\sim$ 10 kyr when the inward migration takes place, also implying a lower gas accretion rate with respect to the Fiducial-Outward case. On the other hand, in the outward migration case in Fig. 5.3, the secondary star grows quickly and retains mass comparable to the primary. This difference in mass ratio and accretion rate is critical to the direction of migration for the following reasons. First, as discussed in Section 5.3.4 and Fig. 5.9, the mass ratio of the stars determines the efficiency of the accretion of high angular momentum gas for a fixed mass accretion rate. With a small mass ratio, the secondary, which accretes a gas at the outer orbit, has nearly Keplerian angular momentum. In this case, the change in angular momentum through accretion is reduced and the binary cannot overcome the torque from the spiral structure. Second, if the mass ratio is large enough, the binary opens a gap more easily then the migration can turn into an outward one by accreting gas (CH19). The dependence of the gap opening on the binary mass ratio has been reported also in earlier studies (Escala et al., 2005; Crida et al., 2006). On the other hand, if the secondary star fails to gain a large mass and the mass ratio remains small, it cannot open a gap to halt the inward migration. In conclusion, the mass ratio of binary plays a crucial role in the direction of migration because it affects the efficiency of angular momentum accretion and gap opening. Note that the binaries with inward migration have large initial separations and small mass ratios (Table 5.1). The secondary star cannot open a gap and does not migrate outward and grow in mass. If a binary, on the other hand, forms at the centre of a barred spiral structure, stars have a small initial separation and typically mass ratios closer to unity, thereby they can more easily start the outward migration that is self-sustained by continuously accreting higher angu-

lar momentum gas from the circumbinary disc. Our interpretation of mass ratio as the reason for inward migration is consistent with previous works. The binary shrinks for the first few kyrs when the mass ratio remains small and stops shrinking when $q \sim 0.05$. The orbit slowly expands later on as in CH19 while the binary keeps the mass ratio greater than this. This critical value of the mass ratio q is consistent with the one suggested in the literature. For instance, Muñoz et al. (2020) and Duffell et al. (2020) predicted that inward migration happens when $q \lesssim 0.2$ and 0.05, respectively. In Dempsey et al. (2021), on the other hand, binaries migrate inward when the value is even lower ($q \lesssim 0.01$).

Finally, we discuss another consequence of the mass ratio that is likely relevant: radiative feedback from the central massive stars. To motivate this effect, we briefly introduce one of the main results of Paper II, which did not include radiative feedback from the protostars. According to simulation results in that paper, there is a correlation between the accretion rate, that is proportional to the gas temperature of the disc and regulated by the external irradiation from X-rays, and the maximum distance of the stars from the centre. This result suggests the high accretion rate causes the outward migration of the stars. In Paper III, however, this trend was less clear. For instance, some binary stars in a strong X-ray background were found to expand with time to large distances ($d_{\rm max} \sim$ 8,000 AU, Run E in Table 5.1) while binaries in a moderate X-ray background (*e.g.*, Run B and Run D) have smaller separations ($d \sim$ 2,000 AU), even though the global accretion rate is lower in the former. Our interpretation is that this discrepancy between the results in Paper II and Paper III occurs because the radiative feedback from massive stars weakens the correlation between the accretion rate and outward migration found in Paper II. In the feedback model used in Paper III (Hosokawa and Omukai, 2009; Hosokawa et al., 2010), the luminosity of a star is not a linear function of the mass and accretion rate. For this reason, the local accretion

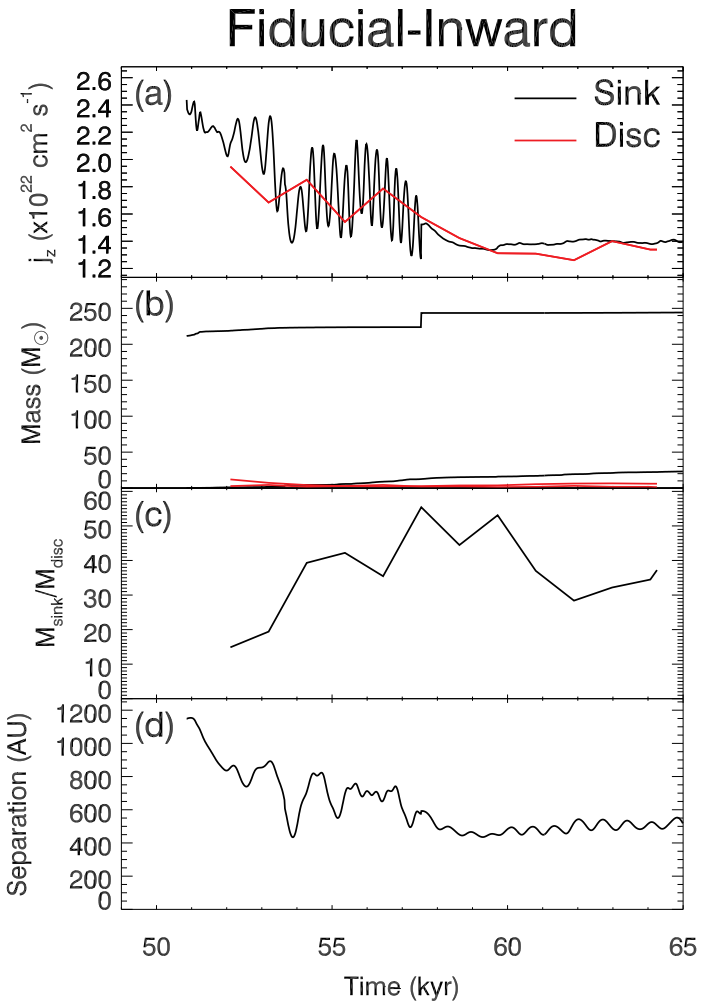

Figure 5.16: Same as Fig. 5.8 but for the Fiducial-Inward binary case. The orbit initially shrinks and later the separation remains nearly constant. Note the disc mass is always negligible in this case and the secondary star forms at a wide separation from the primary.

rate of the stars deviates from the global accretion trend regulated by an X-ray background. In addition, under strong protostellar feedback, the gas disc is evaporated and remains small compared to the stars (compare Panel c of Fig. 5.8 and Fig. 5.16). The result is that the secondary star lacks a significant circumstellar minidisc which accretes high angular momentum gas and drags the star in the direction of the motion. With the lack of a minidisc, stars may not overcome the angular momentum loss by the inner spiral arms (CH19). The process is also visualised in Fig. 5.17. In Fiducial-Inward case, the primary star (green circle) creates an intense UV radiation

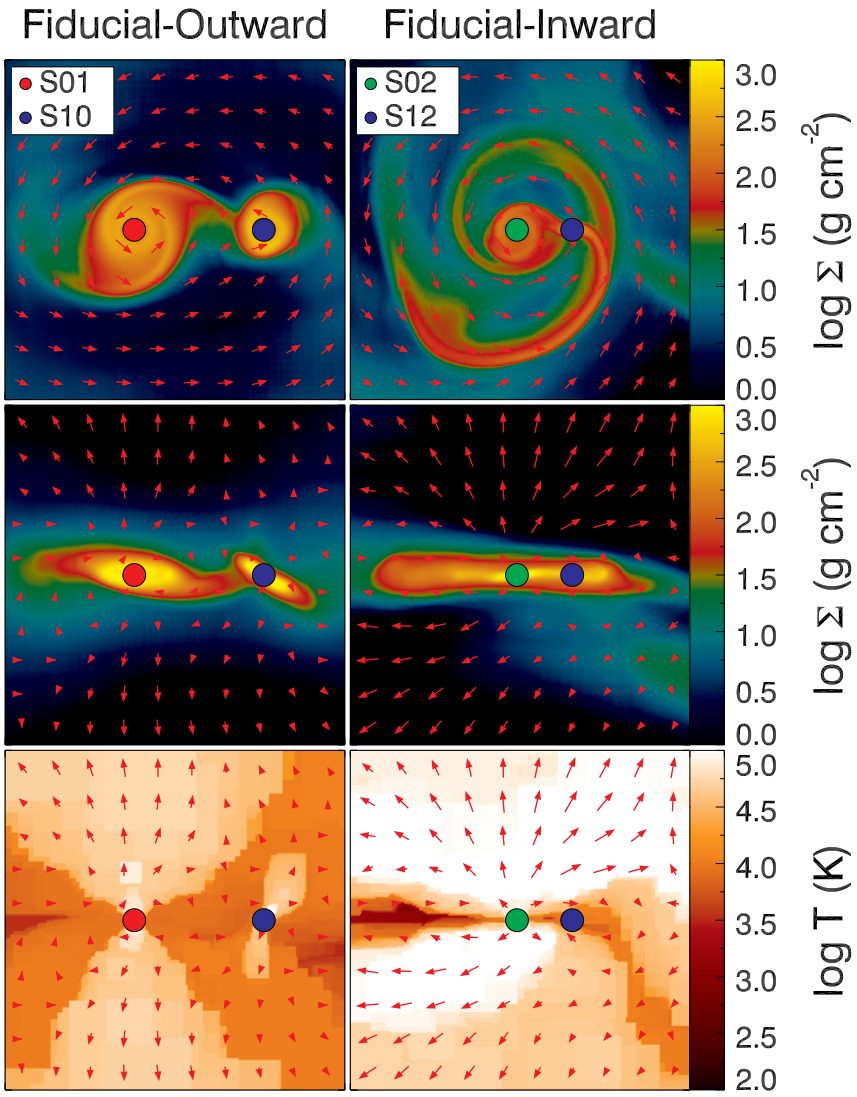

Figure 5.17: Snapshots of outward (left) and inward(right) migration binaries. The top two panels show the face-on and edge-on gas densities. The bottom panels show the gas temperature (edge-on). Sink particles are shown as circles and red arrows represent the velocity fields. Compared to Fiducial-Outward, Fiducial-Inward binary lacks a circumstellar disc of the secondary star (blue circle) due to the strong radiative feedback (bottom panels).

field (bottom panel) and the secondary (blue circle) lacks a prominent circumstellar minidisc.

As seen in Table 5.1 we have four binaries without outward migration (inward and non-migrating). In these binaries, the primary stars are either born massive (Fiducial-Neutral) or the secondary star forms so late that the primary has enough time to grow in mass by accretion (Fiducial-Inward). Then the massive stars evaporate the gas discs and suppress gas accretion

from the envelope. In this condition, it becomes harder for the small secondary to halt the inward migration and initiate the outward migration by accreting high angular momentum gas. A caveat of this work is that a small minidisc may be present even with strong radiative feedback but it may not be resolved in our simulations due to the insufficient sink resolution. Since the minidisc is poorly resolved or unresolved in cases with small mass ratios we cannot rule out that the inward migration is due to resolution effects and outward migration is possible in better-resolved simulations. Although the resolution effect cannot be completely ruled out, we speculate the mechanism for inward migration is still valid because the efficiency of angular momentum accretion (Section 5.3.4) is not sensitive to the resolution.

5.5 Discussion

We find that most massive Pop III binary stars form at relatively close separations (~ 500 AU) but migrate outward to form wide Pop III binaries (5,000$-$10,000 AU). If these binaries survive with such orbits for the next ~ 2 Myr, when the stars explode, they become wide black hole binaries. Thanks to their wide separation, they have greater opportunities of being perturbed by field stars than close binaries. When perturbed, the orbits of the wide binaries are dynamically hardened (Liu and Bromm, 2020). Furthermore, if the orbits are eccentric (*e.g.*, Fiducial-Neutral), the orbits may get excited and become more eccentric reducing their pericentre distance. If the distance at pericentre becomes sufficiently small, the emission of gravitational waves becomes important in removing angular momentum eventually leading to BHB merger and the emission of a strong GW signal within a Hubble time (Michaely and Perets, 2019, 2020).

The role of radiative feedback in migration has been discussed by many authors. This

has been considered insignificant when stars migrate inward because the migration time scale is shorter than the Kelvin-Helmholtz time scale after which stars become luminous in the UV (Stacy et al., 2010; Inayoshi and Haiman, 2014; Latif and Schleicher, 2015; Hirano and Bromm, 2017). In addition, by modifying the gas profile around sink particles, Li et al. (2022) reported heating of the minidiscs may change the direction of the migration suggesting radiative feedback may play a dominant role. del Valle and Volonteri (2018), on the other hand, implemented AGN wind and mechanical feedback to idealised CBD simulations and found that AGN feedback is important in the fast migration case. In this work, we did not perform a systematic numerical study focusing on the responses of the minidiscs to thermal/mechanical feedback and their impacts on migration as in previous works (del Valle and Volonteri, 2018; Li et al., 2022). We found, however, that radiative feedback may contribute to migration in particular situations as discussed in Section 5.4. The main difference between this work and others is the fact that binaries can form at late times. If the UV photons from the primary star are blocked in the disc plane, the minidisc of the primary is not fully evaporated and the secondary can form. At the same time, the radiative feedback from the primary is strong enough to prevent the secondary from growing. If the secondary is kept small in size, the gap opening is delayed and the star is found in a smaller orbit. Furthermore, the secondary competing with the massive companion cannot accrete high angular momentum gas and thus fails to migrate outward. We note, however, that the result is sensitive to the feedback prescription (Jaura et al., 2022). We artificially reduce the amount of radiation in the disc plane (See Section 2 of Paper III). If the feedback is strong enough to evaporate the disc quickly ($\sim$ 10 kyr), outward migration would occur less frequently due to the lack of high angular momentum gas. We leave numerical experiments on the effects of changing the radiative feedback recipes on the binary migration in an idealised setup as future work.

In this paper, we do not analyse in depth the role of alignment/misalignment between the minidiscs and the CBD, but this may be potentially important for migration as pointed out by other authors before (Miranda and Lai, 2015; Moody et al., 2019; Tiede and D'Orazio, 2024). As seen in the middle left panel of Fig. 5.17, the minidiscs of Fiducial-Outward are tilted with respect to the orbital plane (as well as the CBD). The fact that this binary with the misaligned discs migrates outward is consistent with the results in Moody et al. (2019) but it is opposite to the main result in Miranda and Lai (2015). We found that minidiscs are slightly tilted ($\lesssim 20°$) in binaries migrating outward. However, studying the relation between tilt and migration is beyond the scope of this paper, and this topic should be revisited with a more systematic approach in future work.

An interesting discussion is a trend in migration across different metalicities. He and Ricotti (2023) reported that metal-rich stars preferentially migrate inward. The difference from our work is that these systems are dominated by the central stars while the other stars have relatively low masses (that is, low mass ratio q). In this case, as mentioned in Section 5.3.4, the angular momentum difference between the secondary star and the gas is reduced. Since the star accretes less angular momentum, the outward migration becomes less efficient. In our simulations, on the other hand, stars survive if they have masses comparable to the primary and migrate outward efficiently.

Differences in gas metallicities may result in different behaviour of migration in the two populations of stars. A primordial gas cloud has a high temperature due to inefficient H_2 cooling. Since the accretion rate is proportional to c_s^3, Pop III star formation happens in a gas cloud with a high accretion rate. As seen in Paper II, however, a disc in this environment is more Toomre-unstable and thus fragmentation is more active. Stars forming in this disc are likely to have similar

masses and migrate outward in the end. On the contrary, the opposite happens in a metal-rich gas cloud. The accretion onto each prestellar core remains low and thus the disc is Toomre-stable and smooth as seen in He and Ricotti (2023). Once stars form, however, the evolution of the system is dominated by the massive central star and smaller secondary easily migrate inward as discussed in Section 5.4. An interesting question is whether there is a critical metallicity above which stellar migration transitions from outward to inward migration. Since it is the accretion rate determining this transition, and the accretion rate is also responsible for the typical high-masses of Pop III stars and their top-heavy IMF, it is likely that the critical metallicity is the same determining the transition from top-heavy to Salpeter IMF (*e.g.*, Chon et al., 2021).

5.6 Summary

We exploit radiative hydrodynamics simulations of star formation at the centre of metal-free minihaloes to explore the mechanisms leading to the outward migration of Pop III protostar binaries. The initial conditions are created by extracting the central regions of two minihaloes irradiated by LW/X-ray backgrounds of various intensities as described in Paper III. In each simulation, the typical outcome is the formation of hierarchical binaries or more generally multiple-star systems with a top-heavy IMF. The orbits of the binaries are typically elliptical and have a wide separation that increases with time, *i.e.*, outward migration is a common occurrence. We investigate the time variation of the orbital angular momentum of the stars and the different torques and/or accretion of angular momentum leading to its increase. Below we summarise the key findings:

1. Multiple stars form out of disc fragmentation. Some of them migrate inward and merge

with the primary star on relatively short timescales, often producing an initial ellipticity significantly larger than zero of the stellar orbits of surviving stars. Of the stars that survive without merging for a longer time, however, most of them form binaries that migrate outward (for 10 out of 14 binary systems) producing wide binaries with separations up to 5,000−10,000 AU and elliptical orbits. The circumstellar minidiscs around each of the stars in this wide binary often fragment forming a quadruple hierarchical system in which even the binary stars in the minidiscs migrate outward. We conclude that outward migration and the formation of wide Pop III binaries with elliptical orbits is the most common outcome for Pop III stars.

2. Pop III protostars obtain orbital angular momentum from the gravitational torque of their circumstellar minidiscs. These minidiscs, lose angular momentum to the stars but gain angular momentum by accreting high angular momentum gas from the circumbinary envelope. The accretion of angular momentum per unit mass is most effective in an equal-mass binary because their orbital velocity is significantly lower than that of the Keplerian disc at the same radial distance from the CoM. Then the angular momentum in the minidisc is transferred to the stars by gravitational torque and therefore the binary expands with time. On the other hand, inward migration happens in a binary that forms with a wider separation and with a small mass ratio ($q = m_2/m_1 \lesssim 0.1$), because in this case, the angular momentum accretion is less effective.

3. Outward migration happens with the following periodic cycle. At the apocentre, the minidiscs grow in mass and migrate outward by accreting high angular momentum gas from the circumbinary disc. At pericentre, the accreted gas stored in the minidisc is accreted

onto the stars. This cycle repeats until the density of the circumstellar minidiscs are low and the accretion rate of high angular momentum gas becomes negligible (at separations of 5,000−10,000 AU).

4. Unlike previous studies, we find radiative feedback from protostars may affect the migration of stars in certain conditions. When a binary forms via late-time fragmentation, the massive primary star blows out the gas in the disc, suppressing the accretion rate on the secondary star and preventing it from gaining angular momentum by gas accretion. In these cases, the gravitational torque from spiral structures produces a net negative torque and therefore the binary star spirals inward.

5. The lack of efficient cooling in a gas of primordial composition is the ultimate reason for the top-heavy IMF of Pop III stars and their outward migration, which is not observed as frequently in Pop II star formation He and Ricotti (2023). As the accretion rate is proportional to $c_{\rm s}^3$, metal-free discs are relatively massive and Toomre-unstable, fragmenting rapidly. In these discs nearly equal-mass Pop III binaries easily form in barred spiral structures at the centre of the disc, producing a configuration where disc gas with higher angular momentum than the stars is accreted most effectively. Pop II star formation, on the other hand, is dominated by the central massive star and a disc with significantly less mass and Toomre-stable. According to He and Ricotti (2023) the fragments in the disc are pre-existing and simply accreted into the disc from outside. In this case, the angular momentum accretion is less effective and therefore Pop II stars tend to migrate inward and often get ejected by 3-body interactions.

6. Binaries are typically born eccentric through 3-body encounters/mergers or non-axisymmetric

potential. For outward migrating or non-migrating binaries the orbital eccentricity remains constant unless perturbed by mergers, while the orbits circularize for the fewer inward migrating cases. This implies that the periodic forcing at apocentre from torques producing outward migration do not excite or circularise the orbit. We speculate this is because the periodic force is applied onto the circumstellar discs while gravitational torque from the mini-disc to the star remains relatively constant over an orbital period.

Chapter 6: Population III Star Formation in an X-ray Background: IV. On-the-fly Calculation of an X-ray Radiation Background and the X-ray Effects on the Critical Mass for Star Formation

The presence of an X-ray background plays a crucial role in ionizing the intergalactic medium and promoting the formation of molecular hydrogen, which is essential for the formation of Population III stars. Therefore, understanding the role of the X-ray background is vital for studying the formation of the first galaxies. In this study, we conduct cosmological zoom-in simulations to explore the formation of Pop III stars and their potential impacts on the formation of Pop II stars and the first galaxies. To realistically calculate the intensity of the background radiation, we implement on-the-fly cosmological radiative transfer calculation. In this approach, the intensity of the radiation background reflects the star formation history in the simulation. Therefore, we realize the interaction between star formation and the radiation background, a feedback loop within the simulation. We found that a weak X-ray background with $\mathrm{J_X} \sim 10^{-5}$ (in $\mathrm{J_{21}}$ unit) is established, which significantly alters the properties of the intergalactic medium through heating and ionization. Furthermore, the presence of an X-ray background leads to a doubling in the number of Pop III stars formed. However, the feedback from these Pop III stars results in a delay and suppression of Pop II star formation in the X-ray background. Additionally, we discuss the potential impact of environmental factors, such as halo number density, on the effects of the

X-ray background.

6.1 Introduction

Metal-free Population III stars (or Pop III stars) are responsible for the production of metals (Greif et al., 2011; Wise et al., 2012; Safranek-Shrader et al., 2014; Chiaki et al., 2018; Abe et al., 2021) and play a crucial role in regulating the formation of metal-enriched second-generation stars (or Pop II stars) and the first galaxies through radiative and supernova (SN) feedback (Ricotti et al., 2002b; Wise and Abel, 2008; Jeon et al., 2014b). Therefore, understanding the formation and characteristics of Pop III stars is essential for comprehending recent observations of the first galaxies (Bouwens et al., 2019; Finkelstein et al., 2022, 2023; Curtis-Lake et al., 2023). However, the properties of Pop III stars remain poorly understood due to uncertainties in the intensities of the radiation backgrounds in the early universe.

These background radiations, can either enhance or suppress Pop III star formation by regulating the fraction of molecular hydrogen (H_2), which serves as the primary coolant in the primordial gas. For example, a Lyman-Werner (LW) background dissociates H_2 (Haiman, Abel, and Rees, 2000; Regan et al., 2020) while X-ray photons ionize the medium and promote H_2 formation through the H^- channel (Haiman et al., 2000; Ricotti, 2016). LW and X-ray photons are of particular importance in the early universe as they can penetrate the nearly neutral intergalactic medium (IGM) and establish a radiation background (Ricotti, 2016, hereafter R16). Therefore, it is crucial to investigate the roles of LW and X-ray background radiation in the formation of Pop III stars and the first galaxies.

In a series of papers on the formation of Pop III stars (Park et al., 2021a,b, 2023, hereafter,

Paper I, II, and III), we explored the impact of X-rays on the properties of Pop III stars. When X-ray backgrounds are present, both the mass and multiplicity of Pop III stars are reduced (Paper I and II). This decline stems from the fact that the accretion rate is proportional to $c_{\rm s}^3$ and the sound speed $c_{\rm s}$ decreases in the X-ray thanks to the enhanced H_2 cooling. This results in slower protostar growth and the formation of stable disks (Paper I, II, and III). Furthermore, the rate of outward migration is also reduced by the X-ray background (*i.e.*, protostars migrate slowly, Paper II), although association weakens when considering radiative feedback from protostars (Paper III). These findings underscore the significant impact of X-ray backgrounds on shaping the characteristics of Pop III stars.

Additionally, X-ray backgrounds affect the conditions conducive to star formation. R16 analytically calculated the intensities of both LW and X-ray radiation backgrounds, suggesting that a moderate X-ray background enhances H_2 formation and compensates for the negative feedback of a LW background. Consequently, this allows for the formation of Pop III stars in low-mass halos, thereby reducing the critical halo mass (the threshold mass above which Pop III stars can form within the halo). According to R16's calculation, ~ 10 Pop III stars form per $1\ {\rm Mpc}/h^3$[1] volume when X-ray radiation is negligible but this number may increase to ~ 400 when accounting for the X-ray effect. Through hydrodynamics simulations, we confirmed that X-rays may reduce the critical mass by a factor of ~ 10, thereby enhancing the number of Pop III stars per unit comoving volume by a similar factor (Paper I).

In this paper, we revisit the concept of critical mass using cosmological simulations to refine our understanding of the X-ray impact on it. In prior research (Paper I, II, and III), we employed a simple approach to account for the effects of X-ray radiation backgrounds. We assumed

[1] Any length scale divided by h indicates the comoving length unless specified otherwise.

that the halos are isolated, implying that they are not subject to irradiation from neighboring halos' Pop III stars; hence only the global feedback was considered while local feedback was ignored. In addition, we assumed a constant radiation background in time. As highlighted by R16, however, an X-ray background initiates a feedback loop that strengthens itself. Consequently, understanding the X-ray effects and the formation of Pop III stars necessitates a cosmological perspective.

While many pioneering studies have explored an X-ray radiation background in the early universe, we propose that a more comprehensive understanding can be achieved by considering the following aspects in the calculation of an X-ray background. Firstly, the calculation should encompass star formation at high redshifts ($z \gtrsim 15$), when Pop III star formation is active. Although Haardt and Madau (2012) computed the UV and X-ray background and provided their results in tabular form for numerical simulations, they did not include the contribution of Pop III stars and their remnants. Secondly, it is essential to account for the feedback loop. As highlighted by R16, an X-ray background enhances the formation of Pop III stars which subsequently evolve into SNe or black holes (BHs) and emit X-ray radiation. Several researchers have calculated the intensity of an X-ray background and investigated its effects on the IGM, reionization, 21 cm signatures, etc (Xu et al., 2014; Ahn et al., 2015; Xu et al., 2016). However, these studies post-processed the results of *Renaissance Simulations* (Xu et al., 2013), and thus, the interaction between the X-ray background and Pop III star formation was not considered in the calculation. Finally, it is crucial to consider the contribution of distant sources. X-ray photons have mean free paths ($\gtrsim 10\,\mathrm{Mpc}/h$) much larger than the typical size of simulation boxes ($\sim 1\,\mathrm{Mpc}/h$). While some studies (Jeon et al., 2012, 2014a) have explored the effect of X-ray photons emitted and transferred within the simulation boxes ($< 1\,\mathrm{Mpc}/h$), they may not fully capture the contribution of distance sources.

In this work, we propose a method for calculating an X-ray background that incorporates both the feedback loop and the contribution of distance Pop III stars. With this approach, our aim is to investigate the impact of an X-ray background on the IGM and the formation of Pop III stars.

The organization of this paper is outlined as follows. Section 6.2 elucidates our cosmological simulations and the on-the-fly calculation of radiation background. The findings from these simulations are detailed in Section 6.3. Section 6.4 is dedicated to discussions and summarizing the results obtained.

6.2 Simulation

In this work, we employ RAMSES-RT (Teyssier, 2002; Rosdahl et al., 2013), a radiative hydrodynamics (RHD) code with adaptive mesh refinement (AMR) to perform cosmological zoom-in simulations. Initially, we generate a cosmological initial condition of an $L_{\rm box} = 8\,{\rm Mpc}/h^3$ box using MUSIC (Hahn and Abel, 2011) and perform a DM-only simulation. The simulation is conducted with assumed cosmological parameters: $h = 0.674, \Omega_{\rm m} = 0.315, \Omega_\Lambda = 0.685, \Omega_{\rm b} = 0.0493, \sigma_8 = 0.811$, and $n_{\rm s} = 0.965$ (Planck Collaboration et al., 2020). The base grid comprises 512 units on each side, with each dark matter (DM) particle having a mass of $2.8 \times 10^5\ {\rm M}_\odot/h$. We identify DM halos at $z = 9$ and determine their positions and masses using ROCKSTAR halo finder (Behroozi et al., 2013). We then construct the halo mass functions within arbitrary boxes of $(1\ {\rm Mpc}/h)^3$ and compare them with the halo mass function of the entire box. Three distinct subvolumes are selected based on different halo number densities. An illustration depicting the entire volume and these subvolumes is presented in Fig. 6.1. Notably, Region 1 (hereafter, R1) encompasses a higher concentration of DM halos compared to the average, with the most massive

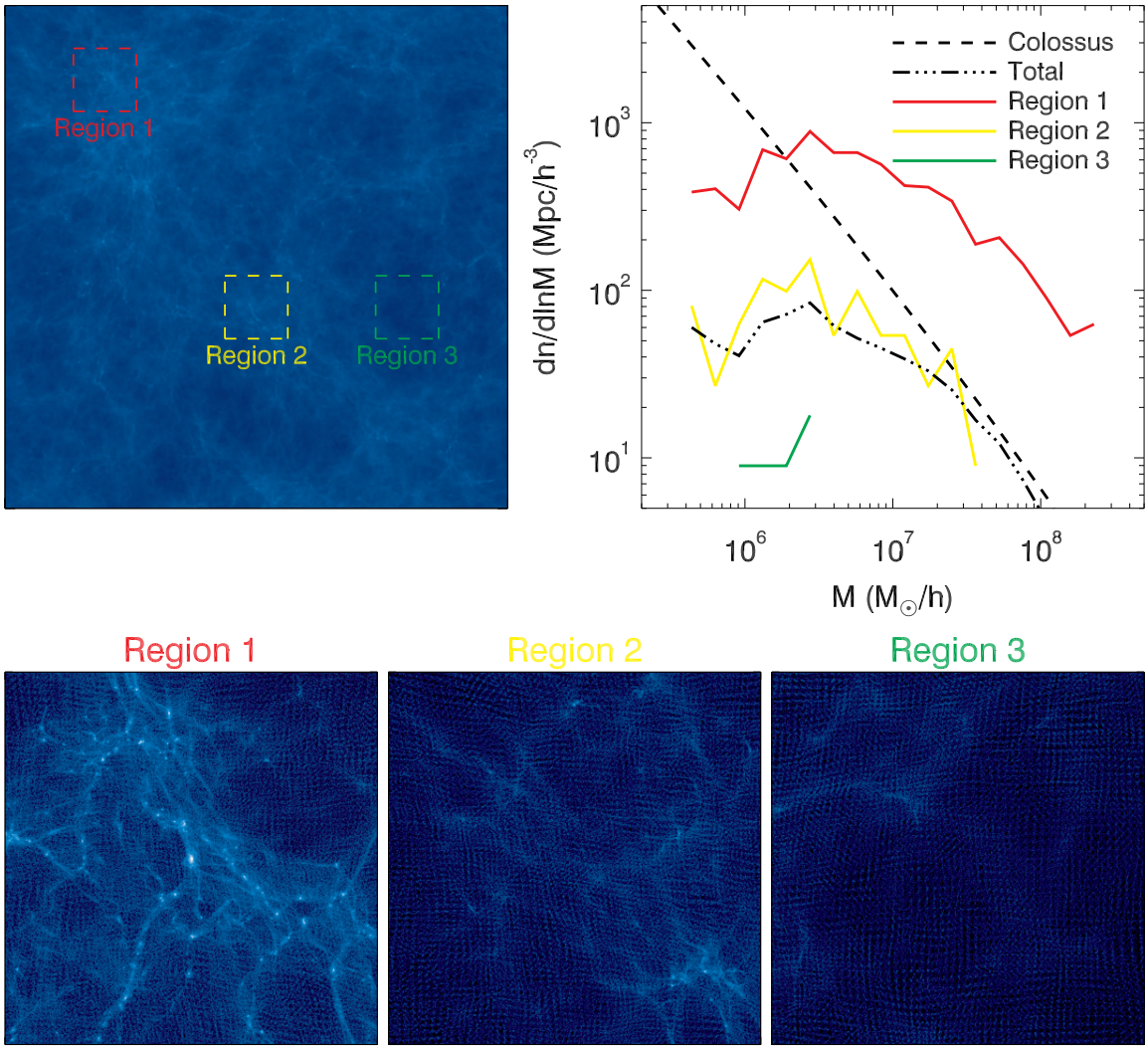

Figure 6.1: Top left: The density map derived from a DM-only simulation at $z = 9$, depicting an $8\ \mathrm{Mpc}/h$ box. Colored boxes denote the three selected regions designated for zoom-in simulations. Top right: Halo mass functions, with the entire box represented by a dotted dashed line. The mass functions of the zoom-in regions are indicated by different colors (consistent with those in the left panel). For reference, the mass function computed by COLOSSUS is illustrated by a dashed line (Diemer, 2018). Bottom: Enlarged views of the three regions.

halo within the volume. The mass function of R1 (red line, top right panel) exceeds that calculated by COLOSSUS (Diemer, 2018) using the Press-Schechter (PS) formalism (dashed line, Press and Schechter, 1974; Sheth and Tormen, 1999) and that of the entire volume (dotted dashed line). In contrast, Region 2 (R2, yellow) exhibits a mass function similar to that of the entire volume. R2 is specifically utilized for calculating the radiation background (Section 6.2.3). Region 3 (R3) rep-

Table 6.1: Parameters of the cosmological simulations

Title	$L_{\rm box}$[a]	$L_{\rm zoom}$[b]	$L_{\rm fid}$[c]	$l_{\rm min}$[d]	$l_{\rm max}$[e]	$\Delta x_{\rm com}$[f]	$\Delta x_{\rm phy}$[g]	$m_{\rm DM}$[h]	Radiation[i]
DM-only	8			9	14	488.3	72.4	2.813×10^5	
R1LW	8	1.2	1	8	21	3.81	0.57	4395	LW
R1X	8	1.2	1	8	21	3.81	0.57	4395	LW + X-ray
R2LW	8	1.2	1	8	21	3.81	0.57	4395	LW
R2X	8	1.2	1	8	21	3.81	0.57	4395	LW + X-ray
R3LW	8	1.2	1	8	21	3.81	0.57	4395	LW
R3X	8	1.2	1	8	21	3.81	0.57	4395	LW + X-ray

[a] Side of the entire box (Mpc/h).
[b] Side of the zoom-in box (Mpc/h). This includes the fiducial box and zoom-in region.
[c] Side of the zoom-in box (Mpc/h).
[d] Minimum AMR level.
[e] Maximum AMR level.
[f] Smallest cell size (pc/h).
[f] Smallest cell size at $z = 9$ (pc).
[h] Mass of a DM particle ($\mathrm{M}_\odot/h$). For the zoom-in simulations, we show the effective mass resolution (mass within the zoom-in region).
[i] Types of the global radiation background and radiation from the stellar particles in the simulation. Note that simulations titled 'X' include 'both' LW and X-ray effects.

resents a sparser region with only a few DM halos. While we conducted the zoom-in simulations of R2, plans are in place to simulate the other two regions as well. For the scope of this thesis, we concentrate on the radiation background calculation using R2 and subsequent simulation analysis. The parameters of the simulations are summarized in Table 6.1.

To perform zoom-in simulations, we relocate each of these subvolumes (R1, R2, and R3) to the center of the box. The minimum AMR level of the zoom-in simulations is 8, encompassing $2^8 = 256$ base grids on each side. Within the base grid, we establish three levels of nested grids using MUSIC. The central grid's dimensions measure $1.2\ \mathrm{Mpc}/h$ on each side, with DM particles inside this area having a mass of $4395\ \mathrm{M}_\odot/h$, serving as the effective DM mass resolution of the zoom-in simulations. Gas cells within this region are refined under the following conditions.

1. The cell contains 8 DM particles.

2. The local Jeans length of the cell exceeds $N_{\rm J}$ times the cell size, with $N_{\rm J} = 4$ (Truelove et al., 1997).

These criteria confine structure formation exclusively within the zoom-in region. As stars cannot form beyond this area and DM particles possess different masses, numerical artifacts may impact the outcomes at the boundary. Hence we designate this area as the "padding" and exclude any data from it during analysis. We consider the box measuring $L = 1\ {\rm Mpc}/h$ inside the padding to be physically significant, utilizing the gas and particles within this area to derive the primary findings. This central $1\ {\rm Mpc}/h$ region is referred to as the "fiducial" region/box. The encompassing area, including both the fiducial box and padding, is termed the "zoom-in" region/box. An illustration of the zoom-in region is presented in Fig. 6.2. The maximum AMR level reaches 21, with the smallest cell size measuring $\Delta x = 3.81\ {\rm pc}/h$ (comoving) or ≈ 0.57 pc at $z = 9$ (physical). Finally, we employ the primordial chemical network. Further technical details are available in Paper I for interested readers.

6.2.1 Pop III Star Formation

Star formation: Due to the limited resolution of cosmological simulations, accurately modeling the gas accretion onto protostars and intricate radiative feedback processes at small scales is unfeasible. Therefore, we adopt a simplified approach to simulate star formation. At each coarse time step, we identify gas clumps using the built-in halo finder (Bleuler et al., 2015). We then place a single Pop III star particle with a mass of $M = 100\ {\rm M}_\odot$ at the density peaks of these clumps if they meet the following criteria,

1. The hydrogen number density at the peak ($n_{\rm H}$) exceeds 10^4 H cm^{-3}.

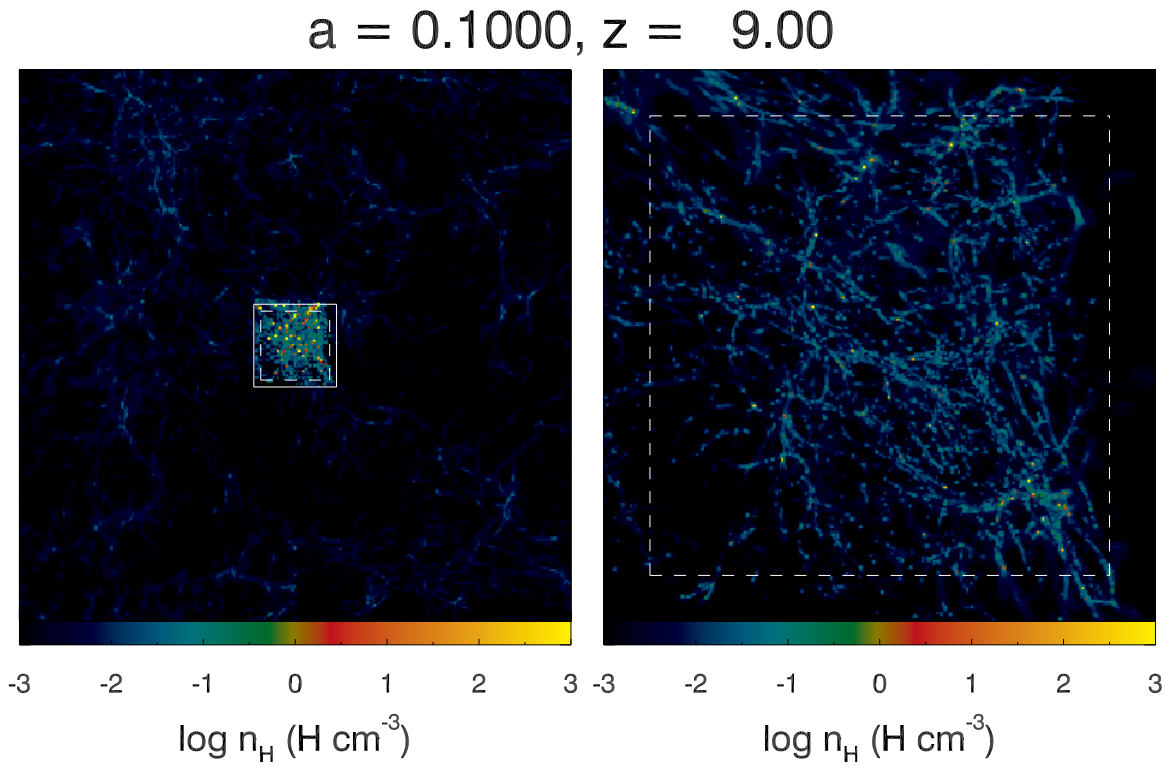

Figure 6.2: Snapshot of zoom-in simulation R2X (see Table 6.1) at $z = 9$. In the left panel, the gas density map of the entire $8\ \mathrm{Mpc}/h$ box is depicted. Only the gas cells within the central $1.2\ \mathrm{Mpc}/h$ zoom-in region, outlined by a solid white square, are eligible for refinement and exhibit high gas densities. The right panel provides a detailed view of the zoom-in region. A dashed line separates the fiducial box (inner region) from the padding (outer region). The analysis presented in Section 6.3 is based on the stars and gas located within the fiducial box.

2. The metallicity at the peak is below $10^{-4}\ Z_{\odot}$.

3. No other Pop III stars are present within a radius of $100\ \mathrm{pc}$.

Condition 3 ensures that only one Pop III star forms per halo. Once a Pop III particle is placed, we subtract $100\ \mathrm{M}_{\odot}$ equally from all cells with $n_{\mathrm{H}} > 10^3\ \mathrm{H\ cm}^{-3}$ in the clump.

Radiative feedback: We inject UV photons into the 27 cells surrounding each Pop III star particle. The luminosity of each photon group (see Table 6.2) is computed based on the results of Schaerer (2002). Notably, even massive Pop III stars emit faintly at $E > 54.42$ eV. The injected photons are propagated using the M1-closure method (Rosdahl et al., 2013) and

Table 6.2: Energy bins.

bin	$h_{\rm P}\nu_1$ (eV)	$h_{\rm P}\nu_2$ (eV)	Roles
1	11.20	13.60	H_2 dissociation (LW)
2	13.60	15.20	H I ionization
3	15.20	24.60	H I, H_2 ionization
4	24.60	54.42	H I, H_2, He I ionization
5	54.42	200	H I, H_2, He I, He II ionization
6	200	∞	H I, H_2, He I, He II ionization, X-ray radiation (Pop III SN)

chemically interact with gas cells (Rosdahl et al., 2013; Katz et al., 2017).

Pop III Supernova: We assume that a Pop III star explodes as an energetic hypernova or pair-instability supernova (PISN) following its main-sequence lifetime ($t_{\rm pop3} = 2.77$ Myr, Schaerer, 2002). We consider its explosion to be $\alpha_{\rm HN} = 100$ times more powerful than a standard supernova ($E_{\rm SN} = 10^{51}$ erg), resulting in $E_{\rm HN} = \alpha_{\rm HN} E_{\rm SN} = 10^{53}$ erg. This energy is uniformly distributed among the 27 neighboring cells. The star does not leave a compact remnant (black hole) and returns the entire mass ($100\ {\rm M}_\odot$) to the same cells, with $20\ {\rm M}_\odot$ as a form of metal. It is worth noting that some studies (*e.g.*, Wise et al., 2012; Kimm et al., 2017) introduce Pop III stars with random masses based on a top-heavy initial mass function and consider the mass-dependent evolution of the stars. For instance, following the result of Heger and Woosley (2002), Pop III stars in the above simulations implode without returning any material when their masses are $40\ {\rm M}_\odot < M < 140\ {\rm M}_\odot$. However, in our work, we opt for a fixed Pop III mass ($100\ {\rm M}_\odot$) and metal yield ($20\ {\rm M}_\odot$) for simplicity. The metal yield in this work is lower than the interpolated value from the yields of $40\ {\rm M}_\odot$ and $140\ {\rm M}_\odot$ supernovae given by Wise et al. (2012) ($M_Z \sim 40\ {\rm M}_\odot$, see their equation (2) and the text).

After the SN explosion, the Pop III star particle transforms into a supernova remnant particle, which persists for 10^4 years and emits X-ray photons (energy bin 6, Table 6.2) akin to

main-sequence Pop III stars (see **Radiative feedback**). The X-ray energy from this Pop III supernova remnant is $E_{\rm HN,X} = \alpha_{\rm HN} E_{\rm SN,X} = 6 \times 10^{50}$ erg with the normal supernova X-ray energy $E_{\rm SN,X} = 6 \times 10^{48}$ erg (see Lopez et al., 2011 and R16).

6.2.2 Pop II Star Formation

When a metal-enriched gas undergoes cooling and collapses within an adequate timeframe, it leads to the formation of Pop II stars. We place a Pop II particle in a gas cell if it meets the following criteria.

1. The hydrogen number density ($n_{\rm H}$) exceeds 10^4 H cm^{-3}.

2. The metallicity is greater than the critical value 10^{-4} $Z_\odot$.

In contrast to Pop III star formation (Section 6.2.1), Pop II star formation can occur at a fine time step since we avoid the computationally expensive clump-finding process. Each Pop II star particle represents a star cluster and has a mass of $M_{\rm pop2} \sim 5 \times 10^4$ M$_\odot$. The luminosity of the particle is determined using the stellar population synthesis model developed by Bruzual and Charlot (2003). After 10 Myr, 10 % of the particle's mass undergoes SN explosions, further heating and enriching the surrounding medium. The time-dependent spectrum utilized for Pop II star particles is depicted in Fig. 6.3.

6.2.3 Effect of Background Radiation

Ionizing UV and X-ray radiation ionize the medium and enhance H_2 formation. While previous studies (from Paper I to Paper III) only considered the global background radiation,

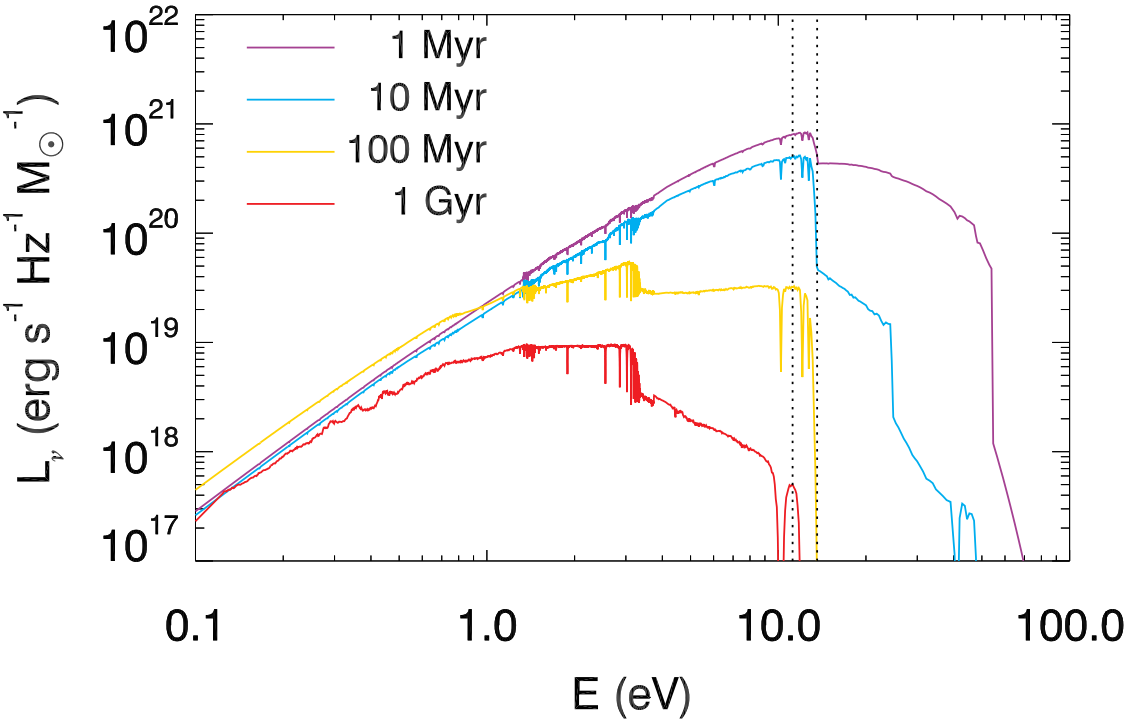

Figure 6.3: Time-dependent spectrum of a Pop II star particle, synthesized using the model of Bruzual and Charlot (2003), is depicted at different ages: 1 Myr, 10 Myr, 100 Myr, and 1 Gyr (shown in different colors). The assumed metallicity is $Z/Z_\odot = 5 \times 10^{-3}$. The LW band is indicated by dotted dashed lines. It is important to note that the population synthesis model offers luminosity per unit mass, thus multiplying the particle's mass yields its luminosity.

neglecting any radiative feedback from neighboring Pop III stars, this work addresses the combined influence of local and global radiation backgrounds, as multiple Pop III stars emit radiation within the same box. The ionization rate of chemical species i of a gas cell is,

$$-\frac{\mathrm{d}x_\mathrm{i}}{\mathrm{d}t} = (1 + f_{\mathrm{ion,i}})\zeta^\mathrm{i}, \tag{6.1}$$

and the heating rate due to species i is,

$$\frac{\mathrm{d}e_\mathrm{i}}{\mathrm{d}t} = f_{\mathrm{heat,i}}\Gamma^\mathrm{i}. \tag{6.2}$$

Here, i represents H I, He I, and He II. $x_{\rm i}$ denotes its fraction, and e is the internal energy. The terms $\zeta^{\rm i}$ and Γ^{i} denote the photoionization and photoheating rates, respectively, while $f_{\rm ion,i}$ and $f_{\rm heat,i}$ represent the secondary ionization and heating fraction, accounting for the effect of the photoelectrons. Further details on these secondary effects can be found in works by Shull and van Steenberg (1985), Ricotti et al. (2002a), and Paper I.

The photoionization rate is split into two components based on the sources of the radiation background,

$$\zeta^{\rm i} = \zeta^{\rm i}_{\rm loc} + \zeta^{\rm i}_{\rm glo}. \tag{6.3}$$

The local photoionization rate due to stellar particles in the simulation box is computed as follows.

$$\zeta^{\rm i}_{\rm loc} = \sum_{\rm j=2}^{6} \sigma^{\rm j}_{\rm i} c_{\rm red} n_{\rm j}, \tag{6.4}$$

where j represents an energy bin from Table 6.2. j $= 1$ is omitted because this corresponds to the LW band. $\sigma^{\rm j}_{\rm i}$ is the average ionization cross-section of chemical species i by photons in group j, weighted by the number of all photons in the simulation. $n_{\rm j}$ is the number density of photons in the cell. $c_{\rm red} = f_{\rm red} c$ is the reduced speed of light with $f_{\rm red} = 10^{-3}$.

The global photoionization rate due to the global radiation background is,

$$\zeta^{\rm i}_{\rm glo} = 4\pi \int_{I_{\rm i}/h_{\rm P}}^{\infty} \frac{{\rm J}_{\nu}}{h_{\rm P}\nu} \sigma_{\rm i}(\nu) {\rm d}\nu, \tag{6.5}$$

where $h_{\rm P}$ is the Planck constant, $I_{\rm i}$ is the ionization potential (*e.g.*, $I_{\rm H\,I} = 13.6$ eV), and $\sigma_{\rm i}(\nu)$ is the ionization cross-section of species i at frequency ν taken from Verner et al. (1996). The difference between the local and global effects is that the local effect is treated with the photon

groups (Table 6.2) while the global one is estimated with the full spectrum of the background radiation. J_ν represents the specific intensity of the radiation background, and its calculation is outlined in Section 6.2.4. The heating rates due to the local and global background radiation are calculated similarly. The dissociation rate of H_2 by LW photons follows the methodology described in previous papers in the series (see Paper I and Paper III).

6.2.4 On-the-fly Calculation of Radiative Background

Photons emitted by stellar particles within the zoom-in region, comprising the fiducial box and padding, contribute to the formation of the local radiation background influencing ζ^{i}_{loc} and Γ^{i}_{loc}. In addition, we assume that sources beyond this region contribute to the build-up of the global background radiation and affect the star formation in the box. To calculate this, we need to estimate the star formation history (SFH) outside the zoom-in region, reflecting the impact of the radiation background. Hence, we implement the on-the-fly calculation of the radiative background, guided by the following assumptions.

1. The global radiation background within the zoom-in region is uniform, implying that the intensities at the center and boundaries of the box are identical.

2. The SFH of the fiducial region is representative of the entire universe.

The first assumption simplifies the calculation, although in reality, the background at the box's center experiences more absorption. The second assumption allows us to estimate the star formation rate (SFR) of the entire universe. For this reason, we select R2 to compute the radiation background. The halo density in R2 closely mirrors the cosmic average (see Fig. 6.1). We capture the spectrum of the background derived from R2 and employ it to simulate R1 and R3, enabling

an investigation of the X-ray effect in these regions. Using either R1 or R3 to calculate the radiation background would result in an overestimation or underestimation of the X-ray effect, respectively.

Now we explain how the background is calculated. See also the schematic diagram (Fig. 6.4). To compute the background, we utilize equation (2) of Haardt and Madau (2012), with the intensity of the background at the observed frequency $\nu_{\rm o}$ when the simulation box's redshift is $z_{\rm o}$. The equation is as follows,

$$\mathrm{J}_{\nu_{\rm o}}(z_{\rm o}) = \frac{c}{4\pi}\int_{\rm z_{box}}^{z_{\rm start}} \left|\frac{\mathrm{d}t}{\mathrm{d}z}\right| \mathrm{d}z \frac{(1+z_{\rm o})^3}{(1+z)^3}\epsilon_\nu(z)e^{-\tau_\nu(z)} \quad [\mathrm{erg\ s^{-1}\ cm^{-2}\ Hz^{-1}\ Sr^{-1}}] \tag{6.6}$$

where $\nu = \nu_{\rm o}(1+z)/(1+z_{\rm o})$. We consider sources between $z_{\rm start} = 40$ and $z_{\rm box}$. $z_{\rm box}$ corresponds to half the size of the zoom-in region ($0.6\,\mathrm{Mpc}/h$). We exclude radiative transfer within this scale ($z_{\rm o} \leq z \leq z_{\rm box}$) because radiation from the stellar particles in the box contributes to local effects and affects $\zeta_{\rm loc}$ and $\Gamma^{\rm loc}$. At each coarse time step, we numerically integrate equation (6.6) to calculate the background radiation, assuming that the background remains constant between two coarse time steps.

The optical depth $\tau_\nu(z)$ contributes to radiation absorption and is determined as follows,

$$\tau_\nu(z) = \begin{cases} \mathrm{d}s/\ell_{\rm mean} & (\mathrm{LW}) \\ \alpha_\nu(z)\mathrm{d}s & (\mathrm{X-ray}) \end{cases}, \tag{6.7}$$

where $\mathrm{d}s = c\mathrm{d}t$ represents the length of the subinterval at z for the numerical integration of equation 6.6. $\ell_{\rm mean}$ denotes the effective mean free path of LW radiation, assumed to be 150th of

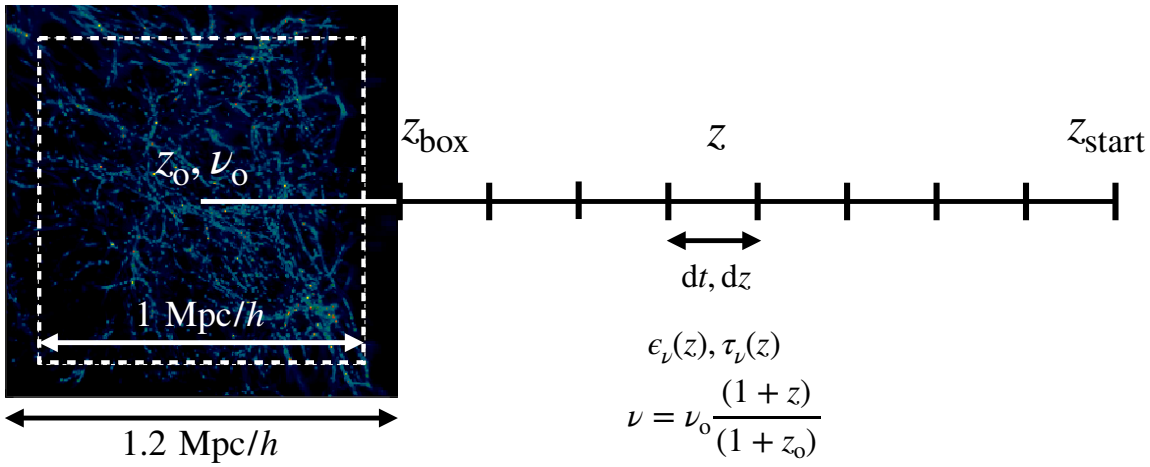

Figure 6.4: Schematic diagram of the on-the-fly background calculation. The x-axis indicates both the distance and time (redshift). We calculate the specific intensity at the observed frequency $\nu_{\rm o}$ in the refined region at $z_{\rm o}$ ($\mathrm{J}_{\nu_{\rm o}}(z_{\rm o})$) by numerically integrating equation (6.6). The left snapshot indicates the padding with the fiducial box (white dashed square). We assume that sources that existed between $z_{\rm box}$ and $z_{\rm start}$ contribute to the radiation background. Photons with frequency $\nu = \nu_{\rm o}(1+z)/(1+z_{\rm o})$ are redshifted and contribute to the intensity at the observed frequency $\nu_{\rm o}$ at the current redshift $z_{\rm o}$.

the particle horizon following R16,

$$\ell_{\rm mean} = \frac{t_{\rm univ} c}{150}, \tag{6.8}$$

where the $t_{\rm univ}$ is the age of the universe at z, and c is the speed of light. For X-ray radiation, the opacity is,

$$\begin{aligned}\alpha_\nu(z) &= n_{\rm H\ I}(z)\sigma_{\rm H\ I}(\nu) + n_{\rm He\ I}(z)\sigma_{\rm He\ I}(\nu) \\ &= n_{\rm H}(z)x_{\rm H\ I}(z)\sigma_{\rm H\ I}(\nu) + n_{\rm He}(z)x_{\rm He\ I}(z)\sigma_{\rm He\ I}(\nu) \quad [\mathrm{cm}^{-1}],\end{aligned} \tag{6.9}$$

where $n_{\rm i}(z)$ represents the number density of particles, and He II is disregarded. The hydrogen density at z is

$$n_{\rm H}(z) = h^2(1+z)^3\rho_{\rm crit}\Omega_{\rm b}\frac{X}{m_{\rm H}}, \tag{6.10}$$

where $\rho_{\rm crit} = 1.88 \times 10^{-29}$ g cm^{-3} is the critical density of the universe, $X = 0.76$, and $m_{\rm H}$ is

the mass of a hydrogen atom. The helium number density is,

$$n_{\rm He}(z) = n_{\rm H}(z)\frac{Y}{X}\frac{1}{4}, \tag{6.11}$$

where $Y = 0.24$. The neutral fractions at z ($x_{\rm H\ I}(z)$ and $x_{\rm He\ I}(z)$) are approximated by the values at $z_{\rm o}$ for simplicity. At $z = 9$, the neutral fraction is $\sim 0.8-0.9$ (or ionization fraction $\sim 0.1-0.2$). This approximation may result in an underestimation of the optical depth at a high redshift z by $\sim$ 20 %, consequently leading to a similar overestimation of the X-ray radiation background intensity.

The emissivity at frequency ν is given by

$$\epsilon_\nu(z) = j_\nu n_{\rm pop3}(z) \quad [{\rm erg\ s^{-1}\ cm^{-3}\ Hz^{-1}}], \tag{6.12}$$

where j_ν is the specific luminosity (${\rm erg\ s^{-1}\ Hz^{-1}}$) of a single Pop III star and its supernova, and $n_{\rm pop3}(z)$ is the number density of Pop III stars at z. The spectrum consists of two parts: LW and X-ray. The X-ray spectrum is generated with a thermal bremsstrahlung radiation formula (Rybicki and Lightman, 1986)

$$\epsilon_\nu^{\rm ff} = 6.8\times10^{-38} Z_{\rm ch} n_{\rm e} n_{\rm i} T^{-1/2} e^{-h_{\rm P}\nu/k_{\rm B}T} \bar{g_{\rm ff}} e^{-\tau_{\rm SN}}, \tag{6.13}$$

where $g_{\rm ff} = \left(\frac{3}{\pi}\frac{k_{\rm B}T}{h_{\rm P}\nu}\right)^{1/2}$ is the averaged Gaunt factor (see Rybicki and Lightman, 1986). The temperature of the supernova remnant is $T = 10^6$ K. The term $e^{-\tau_{\rm SN}}$ accounts for absorption in the remnant, with $\tau_{\rm SN}$ defined as $N_{\rm col,H}\sigma_{\rm HI}(\nu)$, where $N_{\rm col,H} = 10^{21}\ {\rm cm^{-2}}$ is the hydrogen column

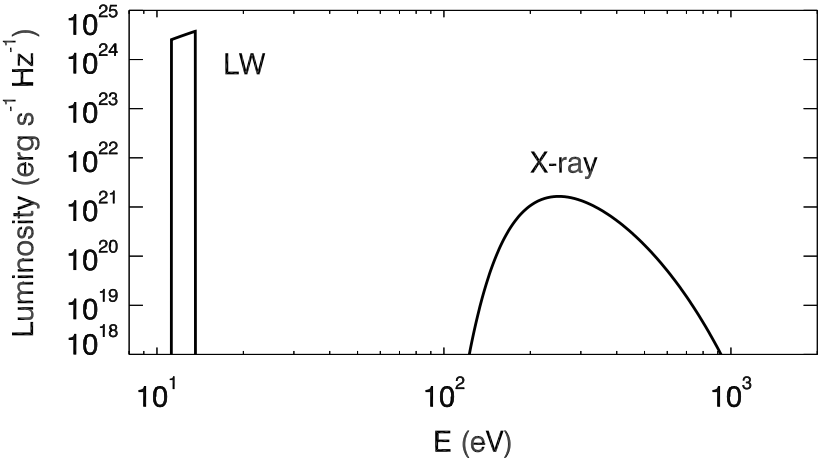

Figure 6.5: Spectrum of a single Pop III star.

density of the supernova remnant[2]. We take this value from observations of Lopez et al. (2011). In addition, $Z_{\rm ch} = 1, n_{\rm e} = 1$, and $n_{\rm i} = 1$ are assumed. However, these parameters are not critical as the spectrum is normalized to satisfy,

$$\begin{aligned} \int_{0.2\ \mathrm{keV/h_P}}^{2.0\ \mathrm{keV}/h_{\rm P}} j_\nu \mathrm{d}\nu &= \frac{E_{\rm HN,X}}{t_{\rm pop3}} \\ &= \frac{\alpha_{\rm HN} E_{\rm SN,X}}{t_{\rm pop3}}, \end{aligned} \tag{6.14}$$

where $\alpha_{\rm HN}$ is the boost factor of the X-ray energy of a HN. For the local background calculation (Section 6.2.1), $\alpha_{\rm HN} = 100$, but a higher value, 1000, is adopted for the global background to ensure strong X-ray effects. The LW spectrum is obtained from the results of Schaerer (2002). The spectrum of a single Pop III star is illustrated in Fig. 6.5. Lastly, the number density of Pop III stars is

$$n_{\rm pop3}(z) = \begin{cases} N_{\rm pop3}(z)/L_{\rm fid}^3 & (z < z_{\rm ana}) \\ f_{\rm duty} \int_{M_{\rm crit,1}}^{\infty} \left(\frac{\mathrm{d}n}{\mathrm{d}\ln M}\right) \frac{1}{M} \mathrm{d}M & (z > z_{\rm ana}) \end{cases}. \tag{6.15}$$

$N_{\rm pop3}(z)$ is the number of Pop III stars in the fiducial box. This equation implies that $n_{\rm pop3}(z)$ is

[2]We also use N for the number of Pop III stars in equation (6.15). To indicate column density, we attach 'col' in the subscript.

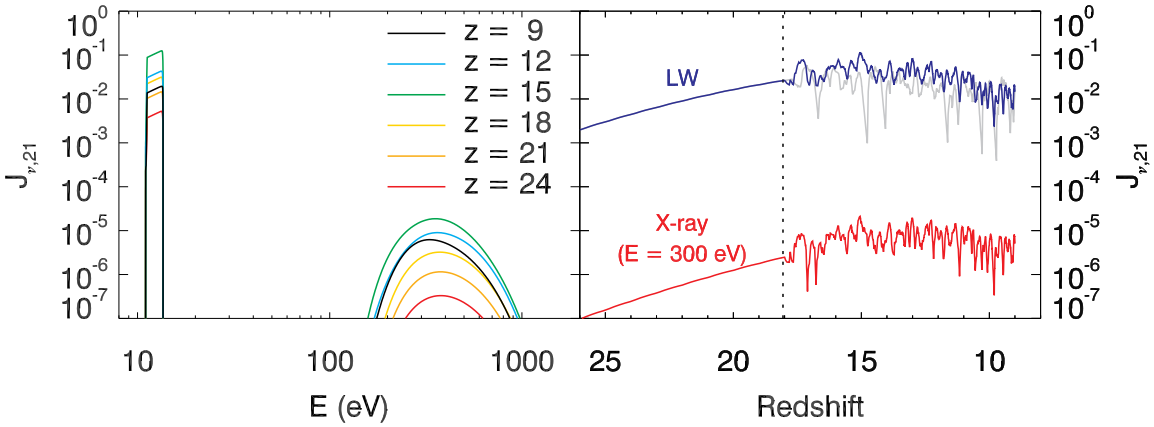

Figure 6.6: The intensity of the radiation background in J_{21} unit. The left panel showcases the spectra at several selected redshifts. Notably, the LW intensity ranges from $\sim 10^{-2}$ to $\sim 10^{-1}$, while the peak X-ray intensity exceeds 10^{-5} at $z = 15$. In the right panel, the intensity is plotted against redshift. The blue and red lines represent the mean LW intensity and X-ray intensity at $E = 300$ eV in R2X, respectively. The vertical dotted line denotes $z_{\rm ana}$ in that simulation. Additionally, the grey line denotes the intensity of the LW radiation in the LW simulation (R2LW).

regulated by the background and again affects the intensity of the background, demonstrating the development of a feedback loop. At high redshifts, however, there are only a few or no Pop III stars in the simulation, and therefore the emissivity is uncertain. Thus, $n_{\rm pop3}(z)$ is estimated analytically for $z > z_{\rm ana}$ (second line). To calculate $n_{\rm pop3}(z)$ analytically, we determine the number of DM halos more massive than the critical mass $M_{\rm crit,1} = 2 \times 10^6$ M$_\odot$ by integrating the halo mass function (Diemer, 2018, indicated by $(\frac{{\rm d}n}{{\rm d}\ln M})$ in equation 6.15). We then multiply this by the duty cycle $f_{\rm duty} = t_{\rm pop3}/t_{\rm univ}$ to obtain the number density of Pop III stars, as done in the previous research of R16. When the total number of Pop III stars in the simulation is greater than 10 ($z < z_{\rm ana}$), $n_{\rm pop3}(z)$ is simply the number of Pop III stars ($N_{\rm pop3}(z)$) divided by the volume of the fiducial box. In Fig. 6.6, we present the spectrum of the global radiation background over time. Note that the calculation method for the emissivity (equation (6.12) and (6.15)) switches at $z_{\rm ana} \approx 18$ (vertical dotted line, the right panel) in both simulations. While the intensities fluctuate because stars form and die, the general trends remain consistent before and after $z_{\rm ana}$.

6.3 Results

6.3.1 X-ray Background, Heating, and Ionization

From Paper I to III, we extensively studied the formation of Pop III stars in X-ray backgrounds with different intensities, spanning from negligible ($J_{21} \sim 10^{-6}$) to substantial ones ($J_{21} \sim 10^{-2} - 10^{-1}$). To better understand the impact of an X-ray background on Pop III star formation, we must estimate its intensity. This intensity is influenced by emission from local X-ray sources, typically stronger around black holes or HNe. However, our focus here lies on the global radiation background originating from distance X-ray sources, which is uniform throughout the volume.

The left panel of Fig. 6.6 illustrates the spectra at several redshifts. At around $z \sim 15$, the peak intensities for LW and X-ray radiation reach $\sim 10^{-1}$ and 10^{-5} in terms of J_{21} units, respectively. This places the X-ray background in a weak X-ray regime of our previous works (from Paper I to III). The right panel displays the LW and X-ray ($E = 300$ eV) intensities as a function of redshift. Both intensities steadily rise until $z \approx 15$. While the X-ray intensity remains relatively constant below $z \sim 15$ due to the longer mean free path for X-rays, the LW intensity decreases later on (see R16).

The global X-ray radiation background significantly impacts star formation by influencing the properties of the gas. Fig. 6.7 and 6.8 provide insights into these effects, comparing gas properties with (left) and without (right) the X-ray effects. In Fig. 6.7, the top panels display the overall gas density, where the presence of X-ray effects (left) appears to result in slightly thinner filaments compared to the absence of X-ray radiation (right). This suggests that X-ray heating

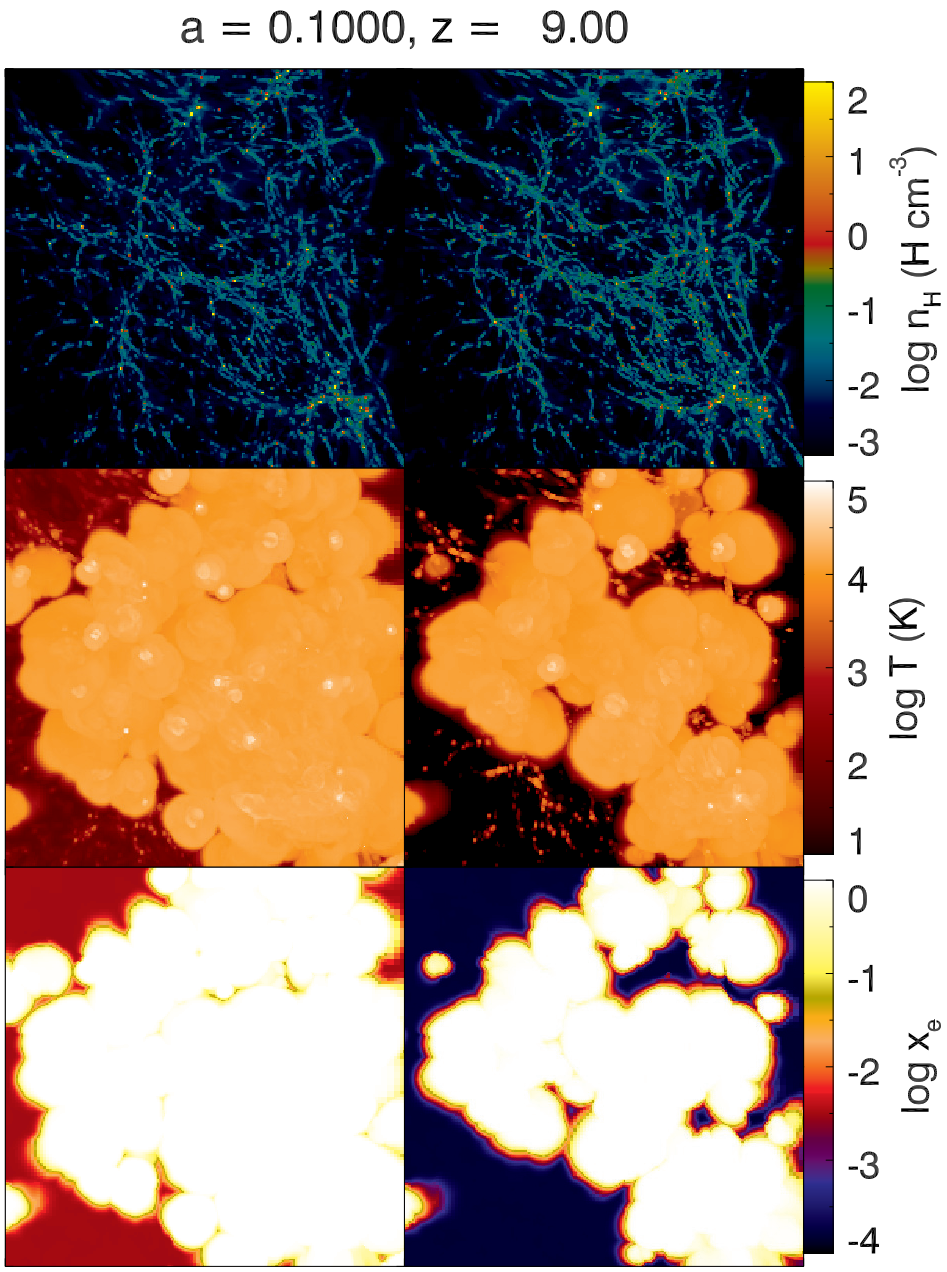

Figure 6.7: Snapshots of R2 at $z = 9$. From top to bottom, we demonstrate the hydrogen number density, gas temperature, and electron fraction. Each panel shows the maximum value along the line of sight. The field-of-view is $1\ \mathrm{Mpc}/h \times 1\ \mathrm{Mpc}/h$. The left column is the result of the X-ray simulation (R2X) and the right column is that of the LW simulation (R2LW).

suppresses gas collapse in low-mass structures. The middle and bottom panels illustrate two key effects of X-ray radiation. Firstly, hot ionized H II regions occupy a larger volume in the X-ray background, implying enhanced Pop III star formation due to X-ray ionization. Secondly, X-rays

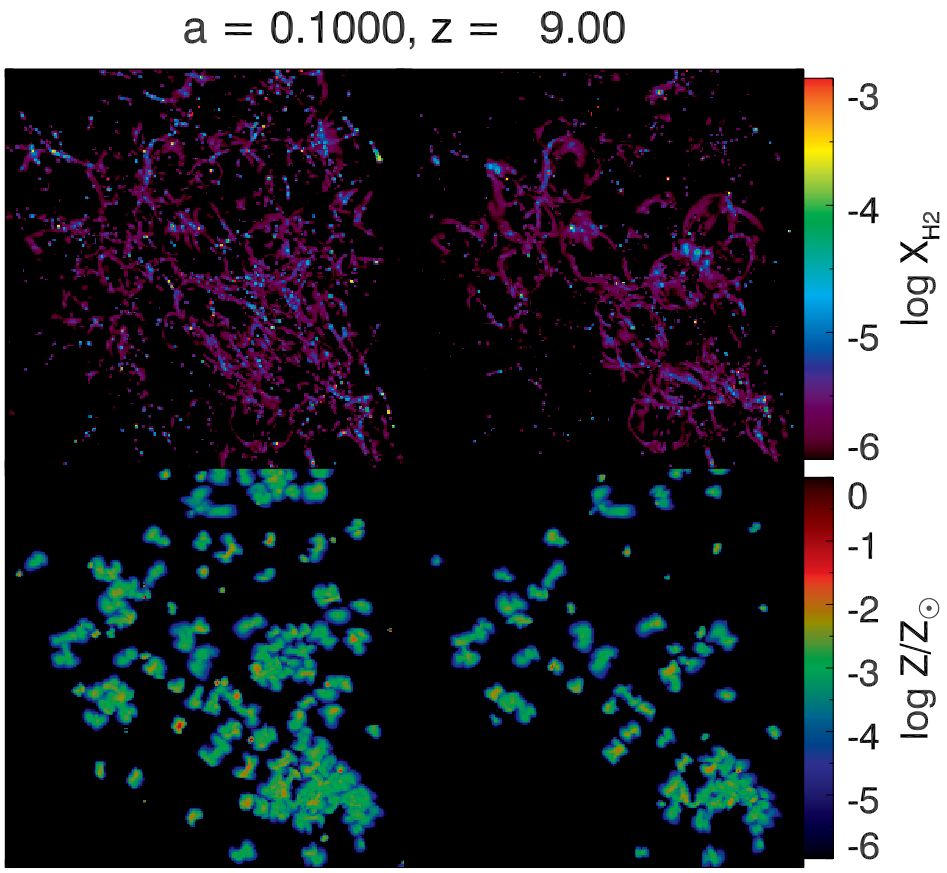

Figure 6.8: Same as Fig. 6.7 but for the H_2 fraction (top) and metallicity (bottom).

heat the IGM (*e.g.*, top left and bottom left corners of each panel), manifesting as mild heating ($T \sim 100$ K) and ionization ($x_e \sim 10^{-2}$) of the IGM. The top panels of Fig. 6.8 highlight the positive feedback of the X-ray background. Despite the LW background dissociating H_2, the X-ray background compensates for the negative LW feedback and increases the H_2 fraction, as evident from the filaments in the top panels. In addition, the presence of X-ray radiation promotes Pop III star formation, indicated by the distribution of H_2 in DM halos (small colored dots). Moreover, metals (bottom panels) are more widely spread in the X-ray background due to enhanced Pop III star formation.

To approach these X-ray effects more quantitatively, we present the average temperature,

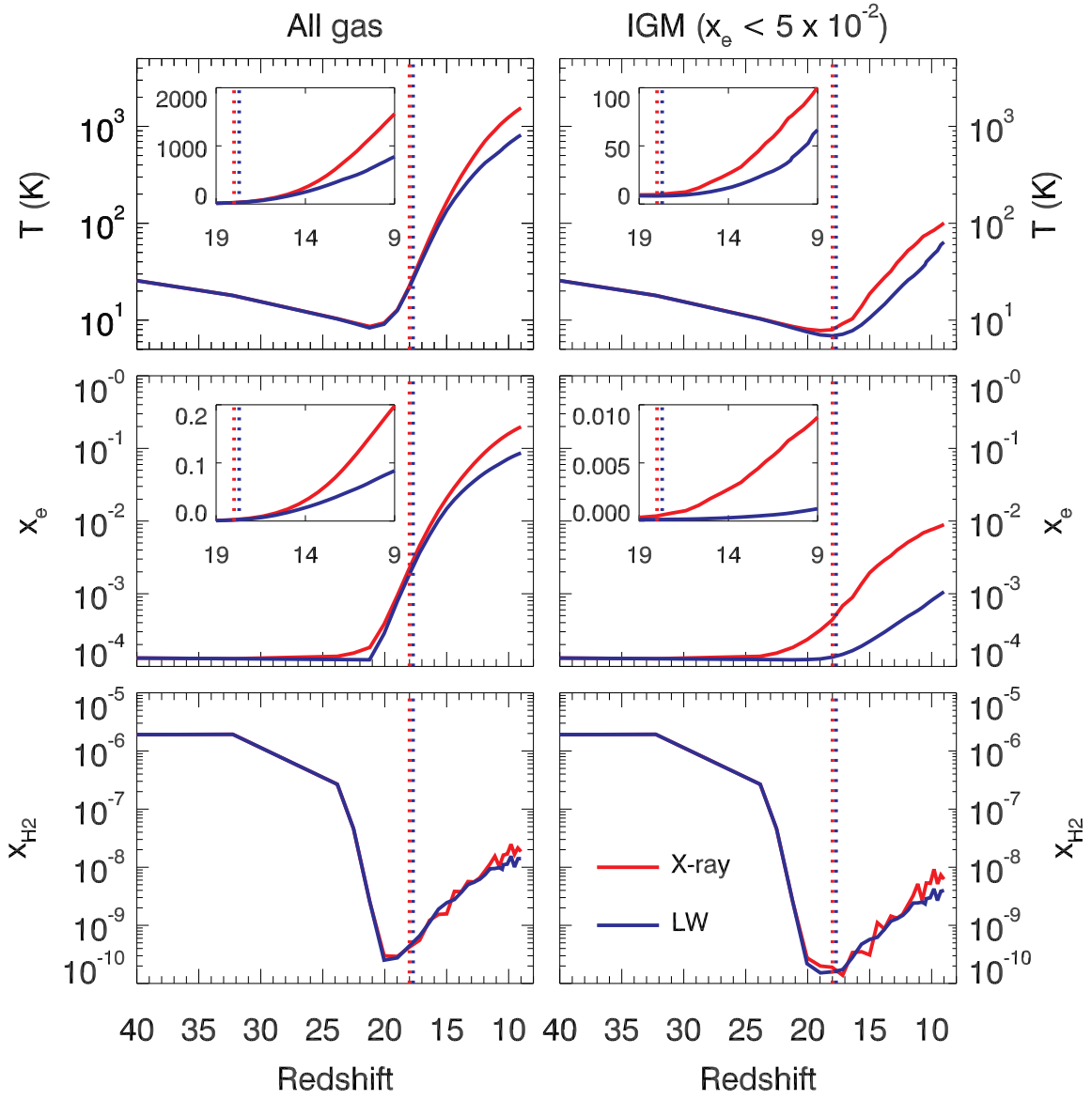

Figure 6.9: Volume-weighted mean temperature, electron fraction, and H_2 fraction of R2 (from top to bottom). In the left column, we average all gas cells in the fiducial box. In the right column, on the other hand, gas cells with $x_e > 5 \times 10^{-2}$ are excluded to distinguish the IGM from the H II bubbles. The primary result remains robust regardless of the threshold chosen. In each panel, the results of R2X are plotted in red, while those of R2LW are shown in blue. Additionally, sub-panels are provided in the top and middle panels to better visualize the differences between the two simulations on a linear scale. Although the differences in the temperature and H_2 fraction are within a factor of ~ 2, the IGM electron fraction (middle right panel) exhibits a larger discrepancy (factor of ~ 10).

electron fraction, and H_2 fraction of the gas as a function of redshift in Fig. 6.9. The volume-weighted mean values are plotted to illustrate the overall evolution. Furthermore, average values

of all gas cells (left column) and those with $x_{\rm e} < 5 \times 10^{-2}$ (right column) are shown to distinguish the contribution of the global X-ray background from that of local UV feedback. Hence, the right panels show the response of the IGM to the global radiation background. We assume that the gas with $x_{\rm e} > 5 \times 10^{-2}$ is in the H II regions. The choice of the threshold ($x_{\rm e} = 5 \times 10^{-2}$) is somewhat arbitrary. We tested other thresholds (0.02 and 0.1) and found that while the average values change within a factor of two, the general trend remains consistent. It is important to note, however, that there is no clear boundary around an H II region, and therefore gases in the H II regions are not completely excluded when calculating the IGM properties.

Fig. 6.9 illustrates that the X-ray background leads to an increase in the average temperature and electron fraction. While the H_2 fraction remains higher in the presence of X-rays, the difference between the two simulations is less significant. This observation aligns with the top panels of Fig. 6.8. In the fields, the H_2 fraction is notably low due to dissociation by the LW background, while the X-ray background primarily enhances the H_2 fraction in filaments and DM halos. Low-density gas cells in the field have large sizes while high-density cells have small sizes. Therefore, the volume-weighted average H_2 fractions in the two simulations do not exhibit a pronounced difference. However, the number of colored dots, which trace the gases in DM halos with high H_2 fractions, demonstrates the effect of the X-ray background on Pop III star formation (top panels of Fig. 6.8).

The top panels of Fig. 6.9 reveal that the gas temperature in the X-ray simulations is higher. This is attributed to both stellar feedback and the global X-ray background, as depicted in the left and right panels, respectively. In the absence of X-rays, the mean gas temperature of the fiducial box at $z = 9$ is $T \sim 800$ K. However, In the X-ray background, the temperature at the same redshift rises ~ 1600 K, indicating a twofold increase. The number of Pop III stars in

R2X is twice that of R2LW, resulting in a larger volume covered by hot gas. This underscores the significant role played by local UV stellar feedback, which was not considered in R16, in enhancing Pop III star formation.

In the right panel, it is evident that the X-ray background directly heats the IGM. At $z = 9$, the temperatures in R2X and R2LW are ~ 100 K and ~ 60 K, respectively, showing a smaller difference. The X-ray-induced heating of the IGM is not as dramatic for two reasons. Firstly, most of the energy from photoelectrons is deposited into ionization, particularly in a neutral medium, where the secondary heating factor $f_{\rm heat}$ (equation 6.2) has a low value (~ 0.1 when $x_{\rm e} \sim 10^{-4}$, Paper I). Despite X-ray ionization, the IGM remains nearly neutral ($x_{\rm e} \lesssim 10^{-2}$), limiting the effectiveness of X-ray heating. Secondly, the X-ray background in this study is not as strong as in previous works (Paper I and II). In a stronger X-ray background, the difference in temperature between the two simulations would likely be more significant, as the photoionization heating rate increases with X-ray intensity and $f_{\rm heat}$ approaches 1 as $x_{\rm e}$ increases.

The evolution of the electron fraction can be similarly understood. The average of all gas cells also exhibits a moderate increase (by a factor of ~ 2) in the electron fraction (middle left) due to the presence of H II bubbles. However, in the X-ray background, the IGM electron fraction increases by a factor of ~ 10. In a neutral gas, X-ray ionization is highly effective due to the secondary ionization ($f_{\rm ion} \sim 10$), leading to a more pronounced increase in the electron fraction.

6.3.2 Pop III Star Density and Critical Mass

The X-ray background enhances the H_2 fraction in DM halos through ionization, which in turn affects the formation of Pop III stars. This influence extends to properties such as the charac-

teristic mass and multiplicity (Paper I, II, and III). In this work, our focus lies on a fundamental condition for Pop III star formation: the critical mass of halos required to initiate star formation. The increase in the H_2 fraction facilitates the formation of metal-free Pop III stars in low-mass DM halos by reducing the critical mass. Consequently, this results in an increase in the number density of Pop III stars. R16 and Paper I predicted a substantial increase in the number density by more than a factor of 10. However, neither of these studies considered the X-ray effect in cosmological simulation. In this section, we aim to address this gap by comparing the number of Pop III stars in simulations with and without an X-ray background (R2X and R2LW). By doing so, we can elucidate the impact of the X-ray background on Pop III star formation.

In Fig. 6.10, we present the numbers of Pop III stars in R2X and R2LW as a function of redshift (time). Initially, the numbers are quite similar, but the disparity between them grows over time. At $z = 9$, 274 Pop III stars form in the X-ray background (R2X), whereas only 165 stars form in its absence (R2LW), indicating a factor of ~ 2 difference. However, this difference is not as significant as initially predicted by R16 and Paper I, where a factor of ~ 10 was anticipated. To understand this discrepancy, we delve into the LW-only simulation. R16 predicted the number density of Pop III stars in a weak X-ray background to be ~ 10 per $(1\ \mathrm{Mpc}/h)^3$. Interestingly, in our LW-only simulation (R2LW), the number of Pop III stars in the same volume is 165. This discrepancy can be attributed to the effect of stellar UV feedback from Pop III stars, which creates an H_2 shell (Ricotti et al., 2002a,b). This shell triggers the formation of other Pop III stars, a phenomenon not considered in R16 and Paper I. Consequently, this mechanism plays a crucial role in enhancing Pop III star formation.

The increase in the number of Pop III stars is linked to the X-ray effect on the critical mass. However, defining the critical mass in cosmological simulations poses a challenge. In R16, it was

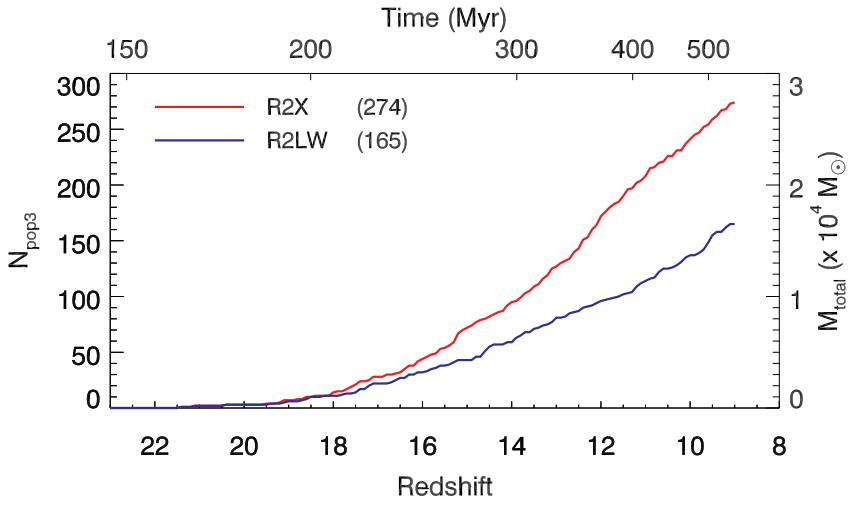

Figure 6.10: The number of Pop III stars in R2X (red) and R2LW (blue). The bottom axis is labeled with the redshift, while the top axis corresponds to the age of the universe. The left axis represents the number of Pop III stars ($N_{\rm pop3}$) in the fiducial box. However, since the size of the fiducial box is $1\ {\rm Mpc}/h$ on each side, this value is equivalent to the Pop III number density ($n_{\rm pop3}$). Additionally, the total mass of Pop III stars ($N_{\rm pop3} \times 100\ {\rm M}_\odot$) is labeled on the right axis. At $z = 9$, there are 274 and 165 Pop III stars in R2X and R2LW, respectively.

defined as the mass above which all halos could potentially host Pop III stars. Yet, in cosmological simulations, there is no clear threshold for Pop III star formation. For this reason, in this work, we define the critical mass differently, integrating the halo mass function.

Before newly defining the critical mass, the halo mass function needs to be understood. In Fig. 6.11, we display the halo mass functions at $z = 9$ of R2X and R2LW. The dashed lines represent the mass functions of all DM halos in R2X and R2LW. The mass functions in both simulations appear nearly identical. We also present the PS fit, calculated with COLOSSUS (Diemer, 2018), in a dotted dashed line. Note that in the DM-only simulation, the DM mass function and PS fit align well (Fig. 6.1). However, in the high-resolution simulation of R2 (R2X and R2LW), the DM mass function (dashed line) surpasses the PS function (dotted dashed line). Furthermore, we plot the mass functions of halos hosting Pop III stars in solid lines. Notably, in the X-ray background, more halos with masses $\lesssim 10^7\ {\rm M}_\odot/h$ host Pop III stars, evident from the red line

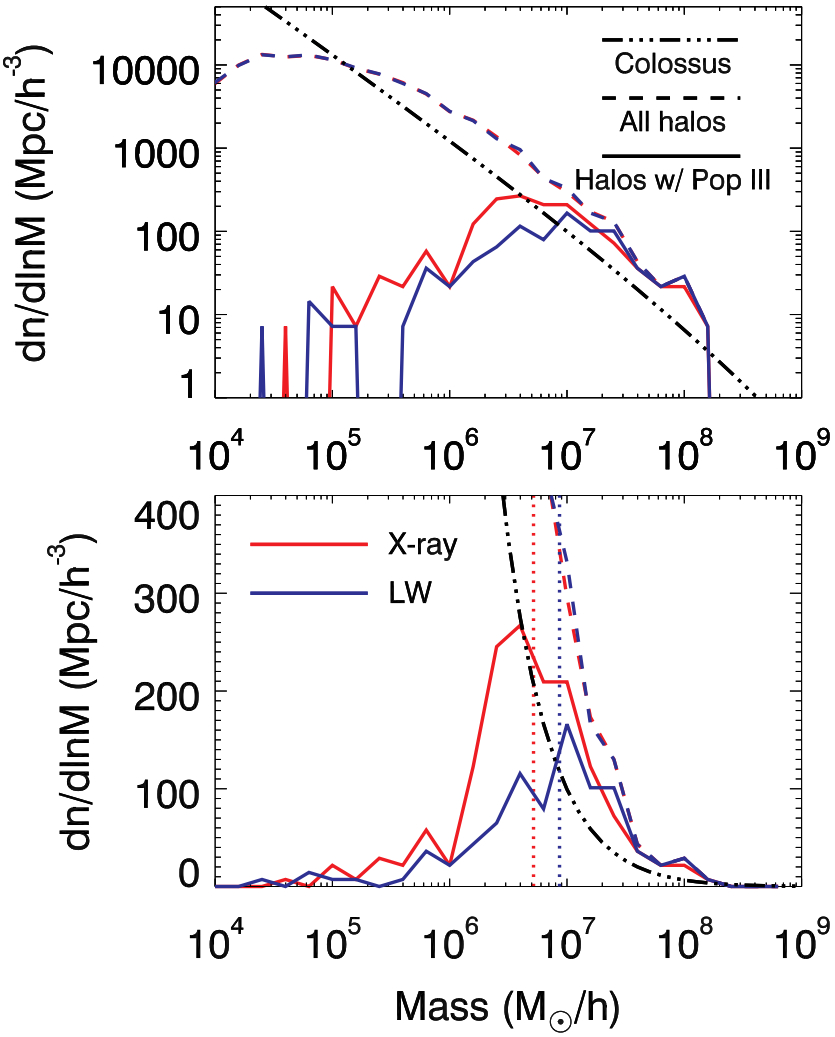

Figure 6.11: Mass functions at $z = 9$. In the top panel, dashed lines represent the mass functions of all halos in Region 2 (dashed lines), while solid lines indicate halos hosting Pop III stars. Additionally, the mass function obtained from COLOSSUS (Diemer, 2018) is plotted for comparison with a dotted dashed line. Colors indicate the existence of an X-ray background (see the legend in the bottom panel). It is evident that more DM halos host Pop III stars in an X-ray (red), indicating that the critical mass is lower in the X-ray simulation. The bottom panel depicts the same mass functions but on a linear scale, focusing on the halos hosting Pop III stars. The critical mass ($M_{\rm crit,2}$) is indicated with dotted vertical lines. For its definition, see the text.

positioned above the blue line. This observation suggests that the presence of X-rays promotes the formation of Pop III stars in lower-mass halos.

In the bottom panel Fig. 6.11, we depict the mass functions on a linear scale, focusing on those hosting Pop III stars. To define the critical mass, we first integrate the mass functions of

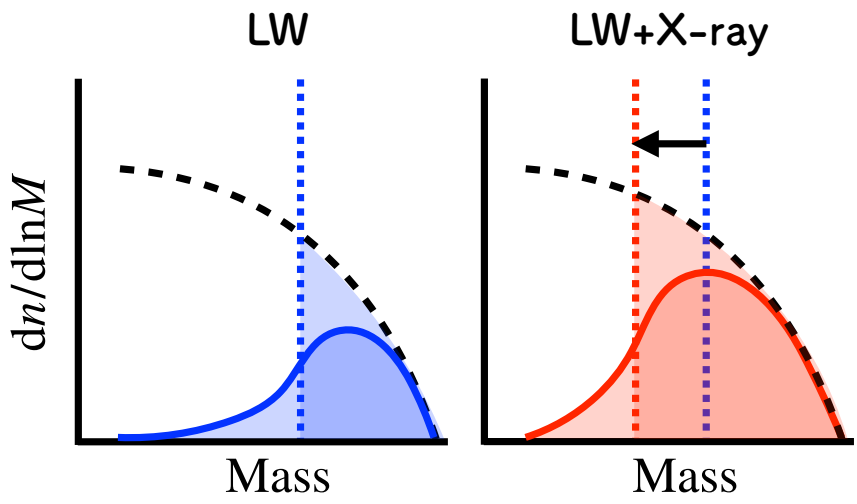

Figure 6.12: Schematic diagram illustrating the definition of the critical. The format is the same as that of Fig. 6.11. We show the mass functions of the LW-only simulation in the left panel and the X-ray simulation in the right panel. The shaded regions represent the areas under the curves. The arrow in the right panel indicates that the critical mass is reduced in the X-ray background.

halos hosting Pop III stars (solid lines) to obtain the number density of Pop III stars. Then we integrate the mass function of all halos (dashed lines) using the following equation,

$$\int_{\mathrm{M_{crit,2}}}^{\infty} \left(\frac{\mathrm{d}n}{\mathrm{d}\ln M} \right) \frac{1}{M} \mathrm{d}M. \tag{6.16}$$

We determine $M_{\mathrm{crit,2}}$ such that the areas under those two curves become equal. For instance, in an X-ray background, more DM halos host Pop III stars and the area under the solid line becomes larger. For the area under the dashed line to be equal to this, $M_{\mathrm{crit,2}}$ becomes smaller and therefore the critical mass is reduced in the X-ray background. We present schematically this effect of the X-ray background lowering the critical in Fig. 6.12. Note that we define the two critical masses: $M_{\mathrm{crit,1}}$ and $M_{\mathrm{crit,2}}$. The former (equation 6.15) represents the critical mass for the analytic background estimate and is fixed at 2×10^6 $\mathrm{M_\odot}$. The latter reflects the X-ray effects that enhance Pop III star formation. In Fig. 6.13, we present the mass functions in R2X

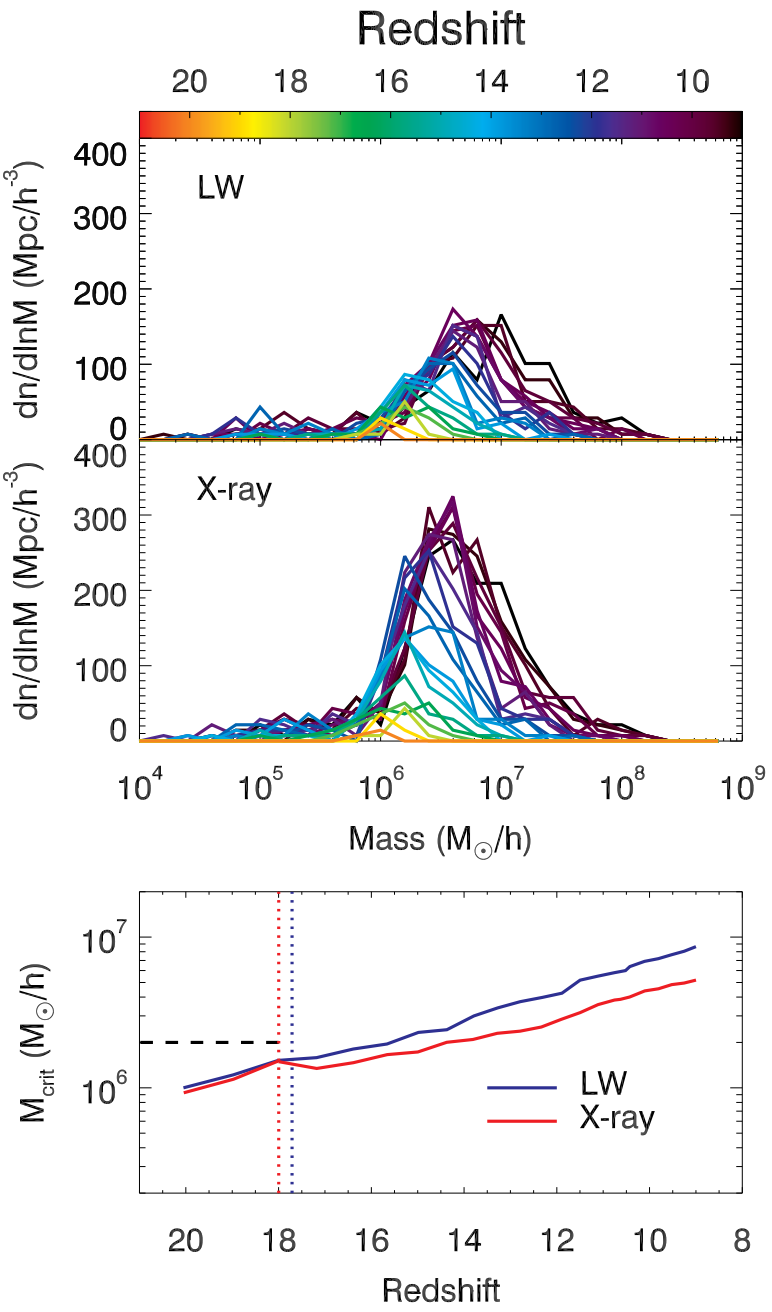

Figure 6.13: Mass functions of halos hosting Pop III stars (top) and the critical mass (bottom) at different redshifts. In the bottom panel, the solid lines represent the critical mass measured with equation (6.16). The vertical dotted lines indicate $z_{\rm ana}$, and the dashed line at higher z represents the analytic critical mass $M_{\rm crit,1} = 2 \times 10^6$ M$_\odot$. Below $z \sim 18$, the critical mass in the X-ray simulation is smaller than the LW-only counterpart by a factor of 2.

and R2LW at all redshifts in the top two panels. The bottom panel shows $M_{\rm crit,2}$ as a function of redshift for both simulations. Despite both simulations starting with the same analytic critical

mass ($M_{\rm crit,1} = 2 \times 10^6$ M$_\odot$), the critical mass diverges after the transition of the background calculation ($z_{\rm ana} \sim 18$), showing a factor of two difference at $z = 9$. In the X-ray background, the critical mass is reduced by a factor of two. Specifically, at $z = 9$, the critical mass is 10^7 M$_\odot$ in R2LW and 5×10^6 M$_\odot$ in R2X.

6.3.3 X-ray Effects on the Formation of the Second-generation Stars

The enhanced Pop III star formation in the X-ray background affects the formation of the second-generation stars and the first galaxies. As shown in Fig. 6.14, the star formation rate density (SFRD) of Pop III is higher in R2X (solid lines) due to the positive feedback of X-rays. As Pop II stars start forming around $z \sim 12$, their SFRD becomes significantly higher than that of Pop III, reaching ~ 3 orders of magnitude greater. Interestingly, the SFRD of Pop II stars (dotted dashed lines) is lower in the X-ray background (R2X, red) compared to the LW-only case (R2LW, blue), particularly between redshift 12 and 11, by a factor of ~ 10. This suggests that the enhanced Pop III star formation suppresses the Pop II star formation through feedback mechanisms.

Fig. 6.15 illustrates the volume-filling factors of ionized regions and metal pollution. The volume represented by $x_{\rm e} > 0.5$ corresponds to the H II regions created by stars, which remains greater in the X-ray background (red solid and dashed lines) due to the higher formation rate of Pop III stars and the subsequent emission of UV photons from the stars. Interestingly, the contribution of Pop II stars to these ionized regions is negligible, despite their larger total masses. To interpret this, we focus on the environments in which Pop II stars form. Pop III stars explode with substantial energies as PISNe, resulting in a significant delay in the formation of the second-

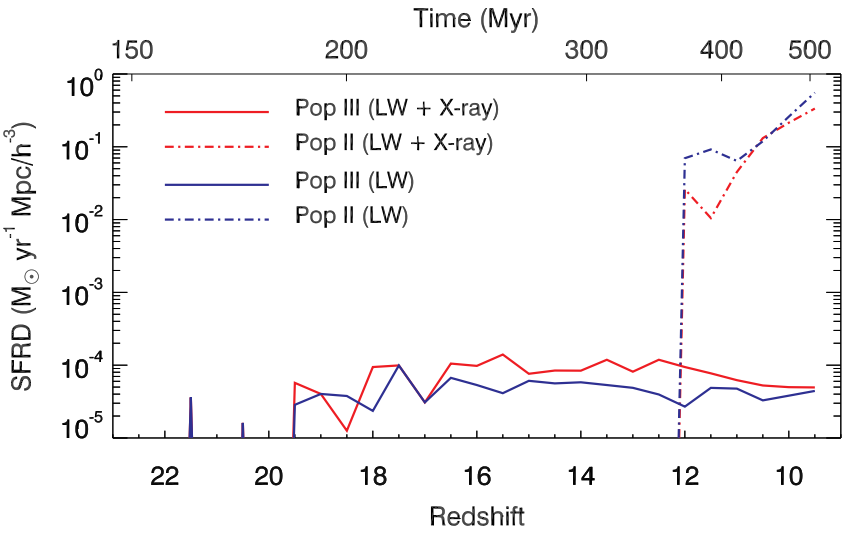

Figure 6.14: Star formation rate density of Pop III (solid lines) and Pop II stars (dotted dashed lines) in X-ray (red) and LW (blue) radiation backgrounds. Pop III star formation rate density is a factor of two higher in the X-ray background. On the other hand, Pop II star formation rate is higher in the LW background at $z \sim 12$.

generation Pop II stars. Consequently, only the most massive halos in the simulation can host Pop II stars by $z = 9$, and these halos tend to be located near the center of the galaxy groups with dense gases. This leads to a relatively low escape fraction. However, if these halos evolve further or if Pop II stars form in filaments, we might observe larger H II regions and a more significant contribution to the volume-filling factor from Pop II stars. The volume-filling factor of $x_{\rm e} > 10^{-3}$ (cyan lines) exhibits a more pronounced difference, as the X-ray background ionizes the IGM. By $z \sim 16$, the entire gas becomes ionized, and the electron fraction exceeds 10^{-3}. In the bottom panel, the volume-filling factor of metals is depicted for two thresholds, 10^{-4} and 10^{-2} $Z/Z_{\odot}$. The enrichment of gas with metals begins around $z \sim 20$ with the explosion of the first Pop III stars. The volume of mildly polluted gas ($> 10^{-4}$) increases over time and reaches ~ 0.01. High-metallicity gases, on the other hand, are confined to the center of DM halos and cover much smaller volume ($\lesssim 10^{-6}$). The enhanced Pop III stars formation in an X-ray background leads to the production of more metals, which cover a larger volume compared to the LW-only case.

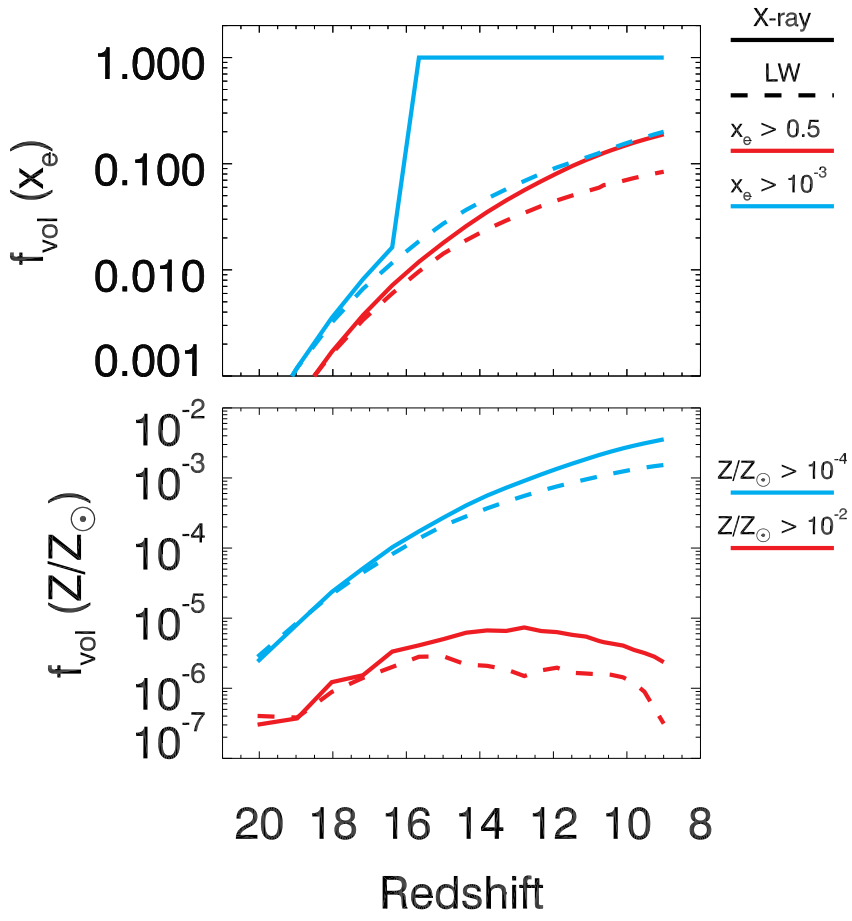

Figure 6.15: Volume filling factors. Top: Volume filling factors of ionized gas. The solid lines represent the values of the X-ray simulation (R2X) while the dashed lines represent those of the LW simulation (R2LW). The red and cyan lines depict the fractions of the gas with $x_{\rm e}$ greater than 0.5 and 10^{-3}, respectively. Notably, the volume filling factors in the X-ray simulation exceed those in the LW simulation. The most significant difference is evident in the factors for $> 10^{-3}$, as the X-ray background ionizes throughout the entire box, unlike stellar feedback. Bottom: Volume filling factors of metal-enriched gas. The format is similar to that of the top panel. By $z \sim 9$, $\sim$ 1 % of the volume is enriched with at least $Z/Z_\odot > 10^{-4}$. Highly metal-enriched gases ($Z/Z_\odot > 10^{-2}$) cover far less volume of the box ($f_{\rm vol} \lesssim 10^{-6}$).

6.4 Discussion

In this paper, we explore the impact of an X-ray background on the critical mass of halos for Pop III star formation. Unlike previous studies (Paper I, II, III, and Park et al., 2024), which focused on individual halos irradiated by X-ray/LW backgrounds with various intensities,

our approach involves computing the background radiation using the number of stars present in the simulation. This method reflects the feedback loop inherent in star formation and radiation background, where each influences the other. Our findings reveal that Pop III stars generate a weak X-ray background, altering the global characteristics of the IGM, such as the temperature, ionization fraction, and H_2 fraction. Consequently, the number of Pop III stars differs between the two simulations.

Although previous studies (R16 and Paper I) suggested a tenfold increase in Pop III star formation, such a significant difference between the two simulations is not evident in this work. We attribute this discrepancy to the influence of local stellar feedback. While the ionizing radiation of a Pop III star can evacuate gas from its host halo, inhibiting the formation of the second-generation stars within the halo, it may also have a positive feedback effect by promoting H_2 formation through ionization and facilitating the formation of other Pop III stars in other mini-halos. Although this mechanism has been explored in prior works (Ricotti et al., 2002b; Yoshida et al., 2007), it was not incorporated into the analytic study of R16 or the small-scale zoom-in simulations of Paper I and Paper II.

In simulations with higher halo densities, such as R1, local stellar feedback would be dominant over global X-ray feedback, resulting in a smaller difference between the LW-only and X-ray simulations. Conversely, simulations with lower halo densities, like R3, may exhibit a greater difference in the number density of Pop III stars with and without an X-ray background, as the influence of global X-ray feedback outweighs that of the local feedback due to large mean halo distances relative to the typical size of H II regions. Further investigations will focus on evaluating the impact of an X-ray background on the number of Pop III stars and the detectability of PISNe.

6.4.1 Future Work

In this thesis, our primary focus is on elucidating the evolution of the radiation background through on-the-fly calculations and examining its impact on gas properties and star formation within R2X and R2LW. Our future plans include extending these investigations to encompass simulations R1 and R3. Moreover, to ensure the robustness of our findings and the validity of our chosen physical parameters, we intend to conduct additional test simulations. The results of these numerical tests will presented and analyzed alongside our main findings.

Chapter 7: Conclusion

7.1 Summary

In this thesis, various aspects of Population III stars affected by external X-ray and LW radiation backgrounds were explored.

7.1.1 Critical Mass of Halos for Star Formation

In Chapter 2, we investigated the critical mass of halos, which represents the threshold above which the gas within the halo cools sufficiently for the formation of Pop III stars. This critical mass is linked to the abundance of H_2, a crucial coolant in metal-free environments that facilitates the initial collapse of gas clouds. The impact of an X-ray background on the H_2 fraction is illustrated in Fig. 2.4. Without X-rays, small halos ($M \lesssim 10^5$ $M_\odot$) cannot generate enough H_2 via collisional ionization to support the formation of Pop III stars. However, when exposed to a moderate X-ray background, these halos become capable of forming Pop III stars due to the increased production of H_2 facilitated by the H^- channel (equation 1.3). Essentially, the presence of an X-ray background reduces the critical mass by enabling the formation of Pop III stars even in low-mass halos. Conversely, LW radiation dissociates H_2, delaying the collapse of gas clouds and consequently increasing the critical mass required for star formation. Notably, an X-

ray background is particularly effective in counterbalancing the negative effects of LW radiation. When a moderate X-ray background ($J_{X0,21} = 10^{-4} - 10^{-3}$) is combined with a LW background of intensity $J_{LW,21} = 10^{-1}$, the critical mass decreases by a factor of ~ 10, leading to a proportional increase in the number of Pop III stars per volume by a similar factor. This is significant as it suggests that the presence of an X-ray background enhances the number of PISNe detected by instruments like the JWST or Nancy Grace Roman Space Telescope (NRST) (Whalen et al., 2014).

7.1.2 Mass of Pop III Stars

In Chapter 2, we examined how the mass of Pop III stars is influenced by X-ray and LW backgrounds. The mass of stars is determined by the size of the quasi-hydrostatic core. In the presence of an X-ray background, this core becomes smaller in mass thanks to the enhanced H_2 cooling as illustrated in Fig. 4.2. As the core contracts, the accretion rate onto the protostars and disk decreases (Panel f of Fig. 2.8) due to its c_s^3-dependence (equation 2.18). Since the accretion rate of the gas in a smaller cloud is lower, the central stars grow slowly and remain less massive (Fig. 2.11) following the empirical relation of Hirano et al. (2014) and Hirano et al. (2015). However, the total mass does not exhibit a clear trend with the LW radiation intensity.

7.1.3 Disk Fragmentation and Multiplicity

In Chapter 3, our focus was on investigating how X-ray radiation impacts the fragmentation of a star-forming disk and the multiplicity of Pop III stars. Building upon the findings discussed in Chapter 2, we observed that the accretion rate of gas onto the central star decreases in the

presence of an X-ray background due to its c_s^3-dependence. Consequently, this reduced accretion rate leads to the formation of a disk with a lower surface density. As a result, the disk becomes more gravitationally stable (equation (3.4)), thereby suppressing its fragmentation. In summary, an X-ray background diminishes the multiplicity of Pop III stars. Fig. 3.4 and 3.5 provide visual representations of the impacts of an X-ray background on this phenomenon.

7.1.4 Initial Mass Function

With an understanding of the X-ray effect on the mass and multiplicity of Pop III stars, we examined their IMF. The IMF of metal-free Pop III stars is top-heavy, that is, Pop III stars tend to be more massive. We represent the IMF using a power-law with an exponential cutoff (equation 3.10). The IMF is governed by two key parameters: the slope α and the cutoff mass $M_{\rm cut}$. As discussed in Chapter 2, X-rays play a role in reducing the mass of Pop III stars. Consequently, the cutoff mass is smaller in a strong X-ray background. In addition, X-ray radiation lowers the multiplicity of Pop III stars as discussed in Chapter 3. Since fewer low-mass stars form under the influence of X-rays, the slope of the IMF (α) increases, making the IMF top-heavier. The left panel of Fig. 3.11 compares the IMF in weak and strong X-ray backgrounds.

7.1.5 Radiative Feedback from Protostars

Strong UV radiation emitted by Pop III protostars triggers outflows and evaporates the protostellar disk, thereby terminating the growth of the stars (McKee and Tan, 2008). Consequently, accounting for protostellar radiation in theoretical studies of Pop III star formation becomes crucial for comprehending their mass and multiplicity. In Chapter 4, we advanced our understanding

of how X-ray and LW radiation affect the properties of Pop III stars when considering radiative feedback from protostars. Our investigation affirmed that incorporating radiative feedback impedes the growth of stars, leading to a reduction in both the mass and multiplicity of Pop III stars. Furthermore, we discovered that the formation of hierarchical binaries (binaries composed of binaries) and wide eccentric binaries is common. In an eccentric binary, the accretion onto the stars is modulated due to enhanced accretion at the pericenter resulting from tidal interaction (Toomre and Toomre, 1972). In the protostellar feedback model employed (Hosokawa and Omukai, 2009; Hosokawa et al., 2010), the protostars expand and their surfaces cool (*i.e.*, become giant stars), when the accretion rate exceeds $\sim 10^{-2}\ \mathrm{M_\odot\ yr^{-1}}$. During the giant phase, the stars become faint UV radiation but bright in the optical. This effect is depicted in Fig. 7.1. When the accretion rate is below the threshold (top right), the Pop III protostars emit UV photons, heating and ionizing the surrounding medium (top left). These Pop III stars can be observed through nebular emission lines of the surrounding medium (Oh et al., 2001). Conversely, if the accretion rate surpasses the threshold at the pericenter, the stars become faint in UV, thereby suppressing feedback (bottom left). Simultaneously, the stars become bright in the optical range, providing opportunities for direct observation of Pop III protostars (rather than through nebular lines). Although the signal falls below the detection limit of the JWST, it can be observed if a foreground galaxy cluster amplifies the light (gravitational lensing) from the stars by a factor of ~ 100 (Fig. 4.14).

7.1.6 Migration

In Chapter 3 and 4, we revealed that Pop III stars exhibit a tendency to migrate outward during their formation, resulting in the formation of wide binaries being a common occurrence.

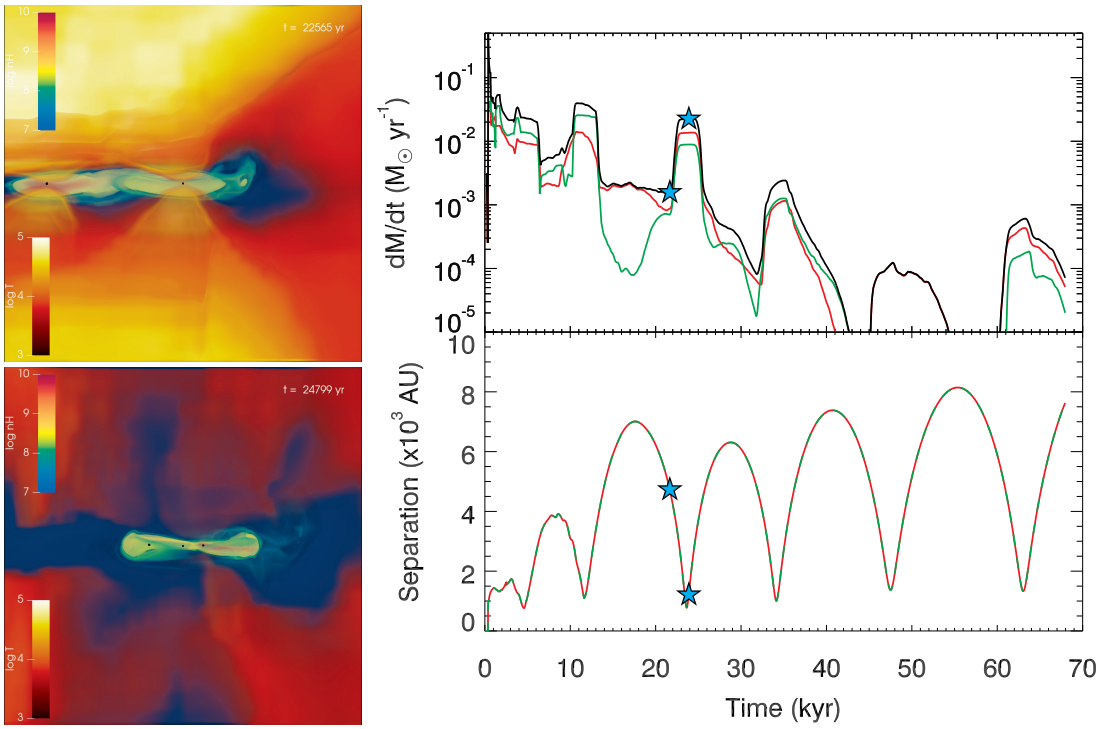

Figure 7.1: Left: Snapshots of an eccentric binary ($e \sim 0.8$) in Chapter 4. At $t \sim 22.6$ kyr (top left), intense radiative feedback from Pop III stars heat the surrounding medium. At $t \sim 24.8$ kyr, the feedback is suppressed and the surrounding medium begins to cool. Top right: The accretion rate as a function of time. The red and green lines represent the rates of individual stars, while the black line shows their sum. The two star symbols indicate the accretion rates corresponding to the two snapshots on the left. It is worth noting that the high accretion rate (the second star, $\mathrm{d}M/\mathrm{d}t \gtrsim 10^{-2}$ M$_\odot$ yr^{-1}) is the factor behind the suppression of the feedback (bottom left). Bottom right: The separation between the two stars. The accretion peak (top right) coincides with the pericenter of their orbit.

In Chapter 3, we observed that stars migrate outward more prominently in the absence of X-rays, suggesting that the primary cause of migration is the accretion of gas with high angular momentum. In the presence of an X-ray background, the lower adccretion rate leads to stars gaining less angular momentum and consequently migrating outward to a lesser extent. However, in Chapter 4, this trend becomes less distinct due to the regulatory effect of radiative feedback on gas accretion. In Chapter 5, we conducted a detailed analysis to explore the origin of outward migration. By calculating the torques exerted by various components of the system (gas disk,

other stars, accretion, and merger) on the binary, we made several key observations:

1. The gravitational force exerted by the circumstellar minidisks plays a predominant role in driving outward migration.

2. Accretion is most efficient in equal-mass binaries

3. The angular momentum of the outer gas is transferred to the binary through the minidisks.

We compared our results of Pop III binaries with metal-rich star formation (He and Ricotti, 2023) and interpreted the different directions of migration in various stellar populations as follows: In a primordial gas cloud, inefficient H_2 cooling results in the gas remaining hot, leading to rapid accretion during subsequent star formation. Consequently, protostars efficiently accrete with high angular momentum, causing outward migration. Conversely, in a metal-rich cloud, accretion occurs relatively slowly, causing protostars to migrate inward rather than outward. The frequent occurrence of wide Pop III binaries suggests a pathway for the formation of GW sources as follows: A wide eccentric BBH ($e \sim 0.9$) may form from a Pop III binary. When the orbit of the BBH is perturbed by field stars, the orbit may become more eccentric with an extremely small pericenter distance. This orbit shrinks with time as the binary loses its orbital energy at the pericenter through GW. Within the Hubble time, the BHs finally eventually merge, emitting strong GW signals detectable by VIRGO/LIGO.

7.1.7 X-ray Effects in a Cosmological Context

In Chapter 6, we revisited the critical mass of halos using cosmological zoom-in simulations. We found that an X-ray background affects the critical mass and thus the number of Pop III

stars. However, it is important to note that the intensity of the X-ray background is also affected by Pop III stars, as their remnants serve as strong X-ray sources. To account for this feedback loop, we implemented an on-the-fly calculation. We observed that PISNe produce a relatively weak X-ray radiation background until $z = 9$, and this background moderately increases the number of Pop III stars (by a factor of ~ 2). The rise in the number of Pop III stars leads to a moderate suppression of Pop II star formation due to radiative and SN feedback from Pop III stars. However, it is worth mentioning that although the X-ray background enhances Pop III star formation, its effectiveness is not as pronounced as in the previous studies (Ricotti, 2016). We hypothesize that the boost of H_2 formation in the recombination regions around Pop III stars may offset the negative LW feedback, resulting less pronounced X-ray effect observed in this work.

7.2 Future Work

In this thesis, I focused on the formation of metal-free Population III stars in X-rays and LW background. In future research, I plan to delve into the formation of extremely metal-poor stars in X-rays and LW background. This will allow for a deeper understanding of star formation in the first galaxies. Furthermore, I aim to revisit the topic addressed in Chapter 4 to refine theoretical descriptions of Pop III star formation. By revisiting and enhancing these aspects, I hope to contribute to a more comprehensive understanding of the formation and evolution of early stellar populations.

7.2.1 Structure of Bipolar H II Region around Pop III Stars at AU Scales

As highlighted in Chapter 4, protostellar radiative feedback plays a crucial role in the formation of Pop III stars. The growth of Pop III stars is self-regulated by the radiation from the protostars, thus radiative feedback must be considered in theoretical studies of Pop III stars. However, our understanding of this radiative process remains incomplete and requires refinement.

Recent research by Jaura et al. (2022) pointed out that the predicted mass of Pop III stars from numerical simulations can be influenced by assumptions regarding radiative transfer on scales smaller than the spatial resolution of the simulations. For instance, a bipolar H II region forms around a Pop III protostar because the accretion disk is opaque to the radiation from the protostar as depicted schematically in Panel a of Fig. 7.2. However, this process is often not captured in most numerical simulations due to limitations in spatial resolution. In Chapter 4, we made an assumption that photons are effectively absorbed in the unresolved disk plane (equation (4.5). With this assumption, the partially submerged sink particle emits photons in the vertical direction, effectively creating the H II region (Panel b of Fig. 7.2). As a result, radiative feedback reduces the mass of Pop III stars in our work. In contrast, Jaura et al. (2022) did not implement sub-sink physics and injected photons into the unresolved disk. They found radiation cannot penetrate the disk, leading to the absence of an H II region (Panel c). Consequently, in their study, radiative feedback does not alter the properties of Pop III stars. In this project, I aim to reconcile this discrepancy by performing high-resolution simulations and developing an improved model of radiative feedback of Pop III stars.

The project aims to address several key objectives:

1. To examine the structure of the bipolar H II region at small scales, ranging from the stellar

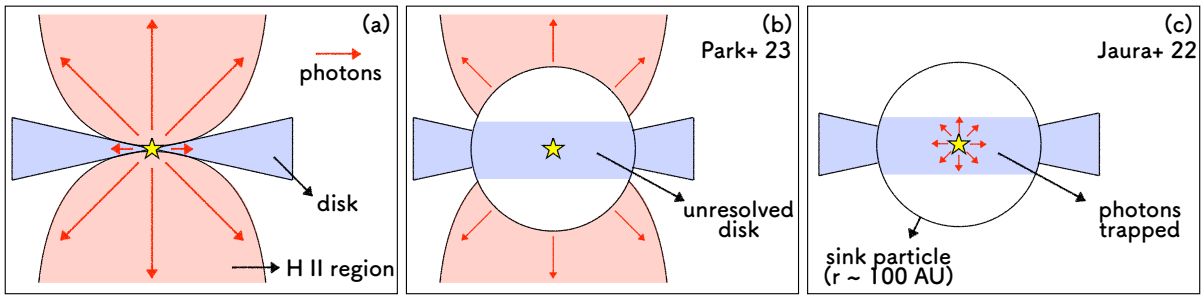

Figure 7.2: Panel a: Schematic diagram of an accretion disk (blue shaded region) and H II region (red shaded region) around a protostar (yellow symbol). Photons emitted from the protostars (red arrows) are absorbed by the disk, resulting in limited travel distance (short). However, photons emitted above and below the disk travel further (long) and contribute to the formation of the H II region. Panel b: Radiative feedback recipe utilized in the study by Park et al. (2023). The circle represents a sink particle with radius $\sim$ 100 AU. Within the sink, the disk remains unresolved. Photons are emitted from the surface of the particle. If the density at the surface exceeds a certain threshold (indicating the presence of the disk), it is assumed that all photons are absorbed within the sink, and no photons are emitted in this direction. Panel c: Feedback prescription adopted by Jaura et al. (2022). In this approach, the star emits radiation isotropically within the sink. However, the H II region around the star is unable to penetrate the dense gas within the sink, preventing its development outside the sink radius.

radius to a few hundred AU.

2. To investigate the mechanisms of radiation transfer within this region.

3. To determine the escape fractions of photons in all directions.

To achieve these goals, I will conduct simulations of Pop III protostars with a sub-AU resolution, by varying parameters such as mass, stellar radius, and accretion rates. By analyzing the simulation results, I aim to understand why properties of Pop III stars are sensitive to the sub-grid recipes, as observed in studies by Sugimura et al. (2020), Jaura et al. (2022), and Park et al. (2023). Furthermore, I will formulate or tabulate the opening angle and escape fraction across different frequency bins. This physically motivated sub-grid model will not only enhance our understanding of Pop III star formation but also serve as a valuable resource for other researchers in the field.

7.2.2 Formation of Extremely Metal-poor Stars

A recent JWST observation of the first galaxies, characterized by $Z \sim 10^{-2}\ Z_{\odot}$ (Curtis-Lake et al., 2023), suggests that stars form in a metal-poor environment in the early universe. This underscores the importance of comprehending the formation of metal-poor stars to unveil the processes involved in the formation of the first galaxies. Furthermore, the regulation of H_2 by an X-ray background may have significant implications for the formation of metal-poor stars. Therefore, it becomes imperative to explore the effects of X-ray radiation on galaxy formation, particularly in the context of metal-poor star formation. Recent observations provide additional motivation for studying this topic. JWST observations of high-redshift ($z \gtrsim 9$) galaxies indicate a surprisingly high fraction of AGN in the early universe (Juodžbalis et al., 2023; Fujimoto et al., 2023). Additionally, observations from the Hydrogen Epoch of Reionization Array (HERA) predict a non-negligible contribution from the cosmic X-ray radiation background (Abdurashidova et al., 2022).

The objective of this project is to extend the exploration of star formation in X-ray and LW radiation backgrounds, focusing specifically on the formation of low-metallicity stars. In particular, the project will concentrate on stars metallicities below $Z \sim 10^{-4}\ Z_{\odot}$. Although the metallicities of the first galaxies observed by the JWST exceed this value ($Z \sim 10^{-2}\ Z_{\odot}$, Curtis-Lake et al., 2023), this metallicity range is crucial because it represents a critical transition point in the properties of stars. This transition, as highlighted by Bromm et al. (2002) and depicted in Fig. 1.1, marks a significant shift from Pop III to Pop II star formation.

The project aims to investigate variations in the properties of stars, such as mass and multiplicity, as metallicity increases. To achieve this, a comprehensive grid of simulations will be

conducted, varying X-ray/LW intensities and metallicities. Similar to the approach taken in studies by Hirano et al. (2014) and Hirano et al. (2015), the mass of stars will be formulated. Furthermore, the IMF of stars under different X-ray radiation backgrounds and metallicities will be examined. Additionally, the project will delve into the differing migrating behaviors observed in various stellar populations.

7.2.3 Effect of X-rays on the Transition from Pop III to Pop II Star Formation

Building upon the findings of the previous project outlined in Section 7.2.2, the focus will shift towards exploring the formation of first galaxies. Specifically, I am interested in understanding the impact of an X-ray background on the transition from Pop III to Pop II star formation. To achieve this, cosmological zoom-in simulations will be performed, focusing on a region surrounding a massive DM halo, akin to the approach discussed in Chapter 6. Furthermore, the influence of other X-ray sources, such as HMXBs, AGN, and IMBHs, will be taken into account. To calculate the accretion rates of these BHs and their luminosities, a physically motivated model developed by Park and Ricotti (2011) will be utilized. Finally, simulation results will be post-processed to generate mock images of galaxies, facilitating direct comparisons with observational data.

7.3 Concluding Remarks

This thesis represents an exploration into the mysterious domain of Pop III stars, shedding light on their formation influenced by X-ray feedback. Through a systematic examination of various aspects of Pop III stars and their interactions with X-ray radiation, we have unveiled previously unseen connections that have profound implications for our understanding of the early

universe.

Our findings challenge conventional wisdom and mark a pivotal shift in our comprehension of Pop III star formation. While previous works incorporated X-ray effects into simulations (Jeon et al., 2014a; Hummel et al., 2015), they understated the role of X-rays in Pop III star formation. Our simulations, however, demonstrated that mass, multiplicity, IMF, and migration are influenced substantially by an X-ray radiation background (Chapter 2, 3, and 4). In addition, this thesis not only deepens our theoretical understanding but also bridges the gap between theory and observation. We have found the potential for directly observing Pop III stars using the JWST and NRST. As predicted by Diego (2019), Pop III stars are detectable through gravitational lensing, and recent observations of "Earendel" bolster the promise of observing Pop III stars at high redshifts. In Chapter 4, we suggested that the luminosities of Pop III protostars can surpass the detection limit of the JWST with gravitational lensing, and their variability can be observed. Furthermore, as the JWST is operating and the NRST is forthcoming, the number of Pop III stars can be estimated through observations of PISNe, as proposed by Whalen et al. (2014). Our predictions regarding the number density of Pop III stars in X-ray backgrounds, outlined in Chapter 2 and 6, lay the foundation for comparative studies between theoretical predictions and observations. Such studies may offer insight into the intensity of the X-ray radiation background in the early universe, complementing recent observations from HERA (Abdurashidova et al., 2022). Finally, we are currently modeling the infrared H2/HD line emissions from Pop III star-forming halos using the numerical simulations presented in this thesis. This aims to shed light on the observability of Pop III stars by ALMA (Atacama Large Millimeter Array).

I anticipate that this thesis, along with the subsequent studies, will establish a connection between Pop III star formation theory and observations from the JWST and NRST, thereby of-

fering valuable guidance for future surveys targeting Pop III stars and first galaxies.

Appendix A: Appendices for Chapter 2

A.1 Validation of Primordial Chemistry and Cooling in RAMSES

In Figure A.1 we show the phase diagram for one-zone calculations (cooling balances compression heating, *e.g.*, Omukai, 2001) for successive improvements of the primordial chemistry/cooling module in RAMSES. The different lines (see legend) illustrate how the original primordial cooling calculation in RAMSES is improved with the addition of each of the physical processes discussed in Section 2.2. We also compare the results with that of a former work (S20), indicated by the solid line with label "SFUMATO". Figure A.2 shows the H_2 (left panel) and electron fraction (right panel) for the same one-zone calculation. One of the major differences in this work is produced by lowering the minimum floor for the ionization fraction. As can be seen in the right panel of Figure A.2 the electron fraction is lower than 10^{-6} at $n_{\rm H} \gtrsim 10^4$ H cm^{-3}. In the original version, however, the floor is set to 10^{-6} and thus the electron fraction is always higher than this threshold. For this reason, the simulation (orange dashed line) shows the H_2 fraction abnormally higher than it is supposed to be (right panel of Figure A.1). In the current version of our code, the value of the floor is 10^{-12} and therefore the validity of the model is guaranteed up to $n_{\rm H} \sim 10^{14}$ H cm^{-3}. With three-body H_2 formation, the models are consistent with each other up to densities $n_{\rm H} \sim 10^9$ H cm^{-3} and other improvements of the physics in the high-density regime reduce the error up to $\lesssim 10^{14}$ H cm^{-3}.

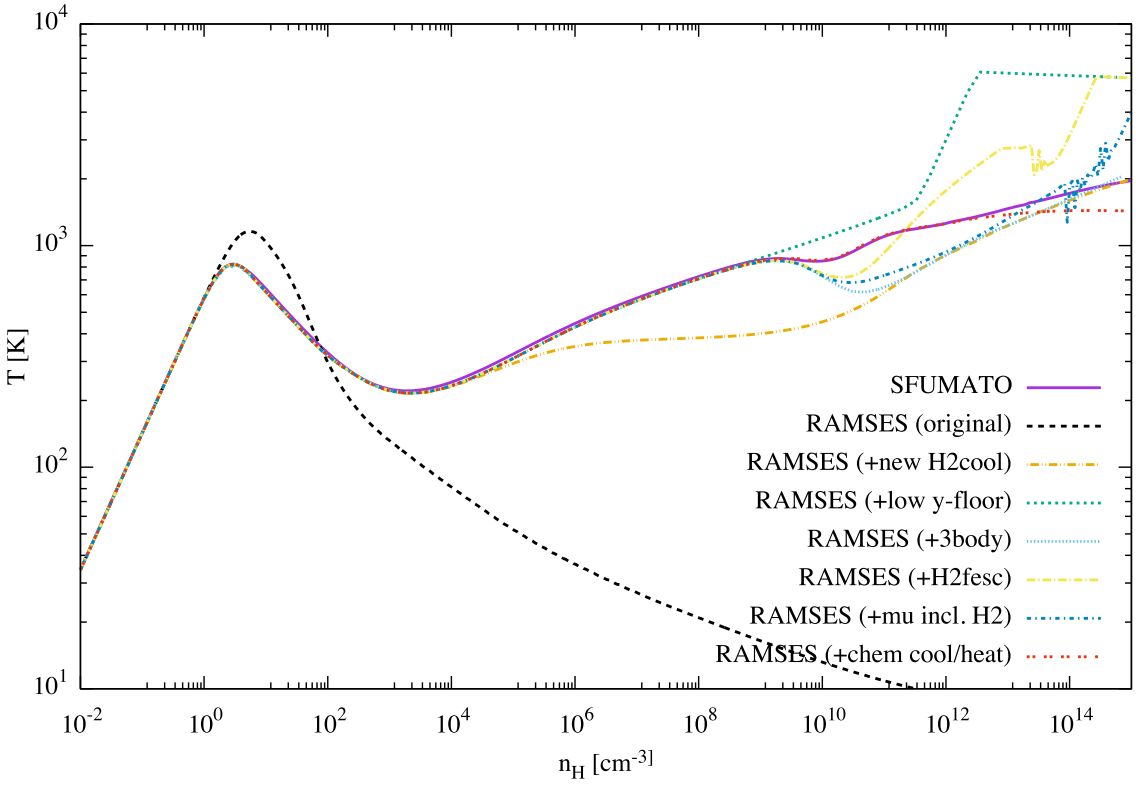

Figure A.1: Phase diagram (temperature as a function of hydrogen number density) for a one-zone calculation in which compression heating balances molecular hydrogen cooling. The different lines (see legend) refer to incremental improvements of the model with respect to the original implementation in RAMSES. The validation of the result is done by comparing our implementation in RAMSES to published results by S20 using the AMR code SFUMATO. Our results are accurate to densities $n_{\rm H} \sim 10^{12}$ H cm^{-3}, but the error remains relatively small (< 15 per cent) up to densities $n_{\rm H} \sim 10^{14}$ H cm^{-3}.

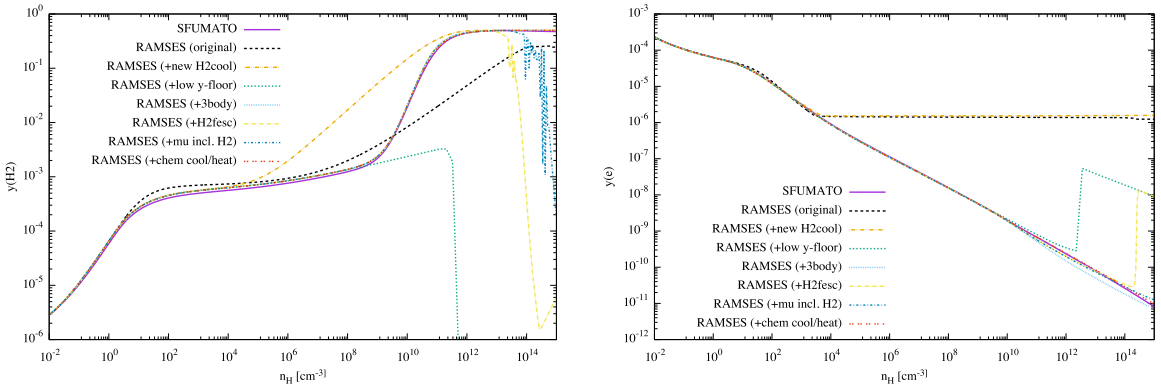

Figure A.2: Same calculations as in Figure A.1 but showing the molecular hydrogen abundance (left panel) and the electron fraction (right panel).

A.2 Number of Pop III Stars

In this section, we estimate the dependence of the number of Pop III stars on the critical mass of DM haloes. We start with the Press-Schechter formalism (Press and Schechter, 1974),

$$\frac{\mathrm{d}n_{\mathrm{halo}}}{\mathrm{d}M} = \bar{\rho}\sqrt{\frac{2}{\pi}}\frac{\delta_{\mathrm{c}}}{M^2\sigma}\frac{\mathrm{d}\ln\sigma}{\mathrm{d}\ln M}\exp\left(-\frac{\delta_{\mathrm{c}}^2}{2\sigma^2}\right), \tag{A.1}$$

where $\sigma \propto M^{-\frac{n+3}{6}}$. We are interested in the formation of Pop III stars in small haloes ($\sim 10^5 - 10^6$ $\mathrm{M}_\odot$) and the cutoff mass of the mass function is above this regime (see also Appendix A of R16). Therefore, we may assume that the index of the power spectrum is $n = -3$ and we get

$$\frac{\mathrm{d}n_{\mathrm{halo}}}{\mathrm{d}M} \propto \frac{1}{M^2}. \tag{A.2}$$

Integrating this mass function from M_{cr} to infinity and assuming one Pop III star forms in each halo give the number density of Pop III stars ($n_{\mathrm{halo}} \propto 1/M_{\mathrm{cr}}$). If the critical mass is reduced by a factor of 10 by an X-ray background, the number of Pop III stars in a given volume increases by a factor of 10.

Appendix B: Appendices for Chapter 3

B.1 Effect of X-ray Shielding

In this section, we present the result of test simulations to discuss the importance of X-ray shielding. In the test suite, we compare simulations including or excluding self-shielding for various intensities of the X-ray background and for the case without X-ray irradiation. We modeled self-shielding by reducing the ionization and heating rates of each cell by the self-shielding factor $f_{\rm shd}$ which is a function of the distance from the centre, r of the halo. For the ionization fraction of species i, the rate of change in its abundance due to the X-ray background is

$$\frac{dx_{\rm i}}{dt} = -(1 + f_{\rm ion,i})kx_{\rm i} \tag{B.1}$$

where

$$k = 4\pi \int_{I_{\rm i}}^{\infty} \frac{J_\nu}{h_{\rm P}\nu}\sigma_{\nu,{\rm i}}e^{-\tau_{\nu,{\rm i}}}d\nu. \tag{B.2}$$

In the above equations, $f_{\rm ion,i}$ is the secondary ionization factor, $I_{\rm i}$ is the ionization potential, $h_{\rm P}$ is the Planck constant, $\sigma_{\nu,{\rm i}}$ is the ionization cross-section, and $\tau_{\nu,{\rm i}}$ is the optical depth of frequency ν. As a side note, we assumed $\tau_{\nu,{\rm i}} = 0$ in the fiducial runs. To treat the self-shielding in a realistic way, the integrand in Equation (B.2) must be integrated to compute k for each cell. For simplicity,

however, we made the following approximation,

$$k \approx \left(4\pi \int_{\mathrm{I_i}}^{\infty} \frac{J_\nu}{h_\mathrm{P}\nu}\sigma_{\nu,\mathrm{i}} d\nu\right) e^{-\overline{\tau_\mathrm{i}}} = \zeta_\mathrm{i} f_\mathrm{shd}, \tag{B.3}$$

where ζ_i is constant for all cells in a given simulation and $f_\mathrm{shd} = \exp\left(-\overline{\tau_\mathrm{i}}\right)$ is the self-shielding factor. The averaged optical depth $\overline{\tau_\mathrm{i}}$ is $N_\mathrm{i}\overline{\sigma_\mathrm{i}}$. We make use of the averaged cross-section $\overline{\sigma_\mathrm{i}}$ weighted by the number of photons of the X-ray background. The cross-section is also constant throughout the entire simulation box. At each coarse timestep, we identify the centre of the halo using the on-the-fly halo finder with the friends-of-friends algorithm and the position of the densest cell. Using this, we compute the gas density profile $n_\mathrm{i}(r)$. The absorption column density for each cell is determined by its distance from the centre r:

$$N_\mathrm{i} = \int_{\mathrm{R_{vir}}}^{r} n_\mathrm{i}(r')dr'. \tag{B.4}$$

The heating by the background is treated in the same way but with the energy-weighted average cross-section.

Figure B.1 shows the gas phase diagram (temperature versus density) of all cells in Halo 1. To make the plots we adopted the same style as in Figure 6 in Hummel et al. (2015), for ease of comparison. In each panel, the cell values for the shielded and unshielded simulations are shown with blue and red dots, respectively, for a given X-ray intensity. For comparison, the gray dots show the phase diagram for the corresponding simulation without an X-ray background (that is the same in all panels). We show the phase diagram at the time when the density reaches 10^{11} H cm^{-3}. Note that this happens at different redshifts and when Halo 1 has different masses

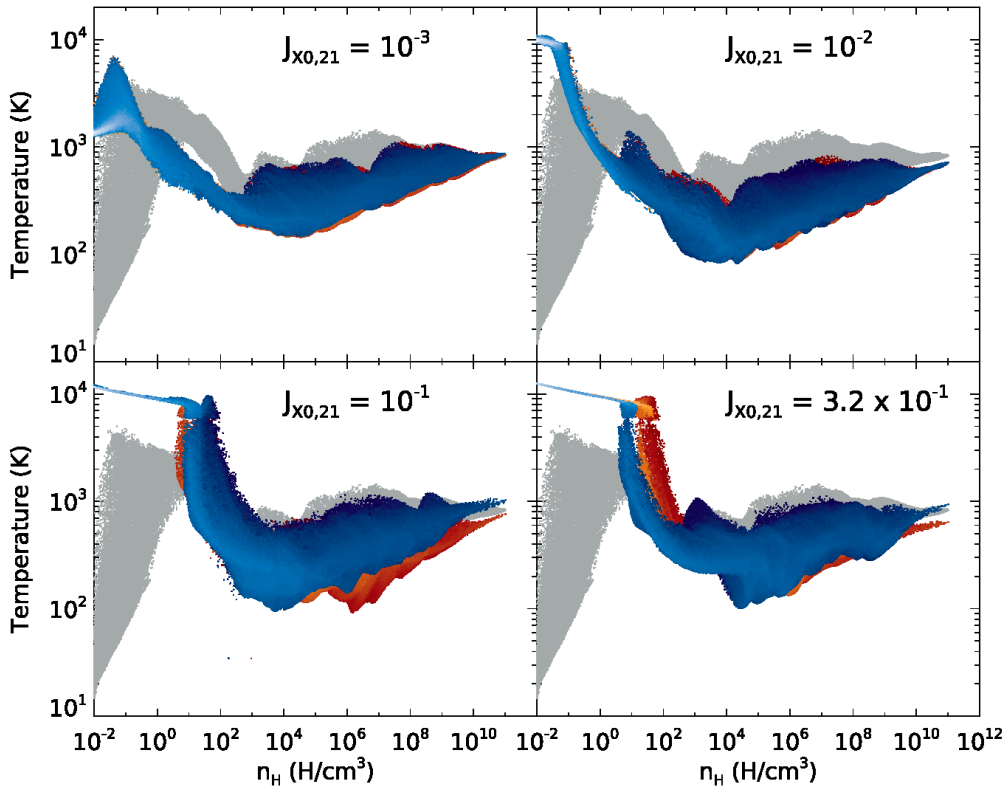

Figure B.1: Phase diagrams of test simulations. Each panel shows the temperature distribution of gas within Halo 1 in a given X-ray background. The X-ray shielding case is shown in blue, while the unshielded case is shown in red. The brightness of the color scales with the mass in each cell. For comparison, we also show the gas phase diagram for the case without X-ray background in grey. Note that $J_{X0,21} \sim 10^{-2} - 10^{-1}$ corresponds to the fiducial case (J_0) of Hummel et al. (2015) but the strong X-ray cases for the simulations in this work. The deviation at high densities due to X-ray shielding ($n_H \gtrsim 10^6$ H cm^{-3}) is pronounced only when the halo is irradiated by a very strong X-ray background (bottom two panels).

even for the 3 simulations shown in the same panel. In addition to the three strongest X-ray backgrounds ($J_{X0,21} = 10^{-3}, 10^{-2}$ and 10^{-1}) in our fiducial runs, we added to the tests suite simulations with even stronger X-ray irradiation ($J_{X0,21} = 0.32$). For the cases with strong X-ray irradiation (bottom panels), the initial gas collapse is delayed until the halo mass is $> 2 \times 10^7$ M$_\odot$ and the collapse is initiated by atomic cooling, as found previously for the strong LW background cases. As shown in Omukai (2001), however, the evolution to higher densities ($n_H \gtrsim 10^6$ H cm^{-3})

is similar to the molecular cooling case and therefore these are still valid comparisons for our tests.

The fiducial case in Hummel et al. (2015) ($J_{X0,21} = J_0$ [1]) corresponds to our cases with $J_{X0,21} \sim 10^{-2} - 10^{-1}$, that are the strongest X-ray irradiation cases in this work. We find that the differences between the simulations with and without X-ray shielding are only evident in the high-density regime, and are negligible when the background is weaker than $J_{X0,21} \sim J_0 \sim 10^{-1}$, i.e., the fiducial model in Hummel et al. (2015), as shown in the top panels of Figure B.1. When irradiated by stronger X-rays, however, high-density gas ($n_H \sim 10^{11}$ H cm^{-3}) shows a clear difference in temperature, with gas reaching higher temperature when self-shielding is included, in agreement with the results in Hummel et al. (2015). Note that Hummel et al. (2015) also finds that the importance of self-shielding depends on the X-ray intensity.

Figure B.2 shows the behaviour of the H_2 fraction in the test suite. Compared to the zero X-ray case (shown in grey), positive feedback of an X-ray background increases the overall H_2 fraction. At the high-density end ($n_H \gtrsim 10^{10}$ H cm^{-3}), however, three-body interaction becomes more important and therefore the fractions converge to 0.5 (fully molecular). At lower densities ($n_H \sim 10^4 - 10^{10}$ H cm^{-3}), the H_2 fraction grows slowly when the halo is in a weak background (top panels) or X-ray irradiation is shielded (shown in blue in bottom panels). If intense X-ray irradiation is not shielded (red in the bottom panels), however, the H^- channel alone forms H_2 effectively and is able to make the gas nearly fully molecular.

As pointed out by Hummel et al. (2015), the deviations in the gas temperature is fundamentally driven by the difference in the electron fraction and therefore molecular fraction. We

[1] They defined J_0 as the average intensity. Here it denotes the specific intensity at 1 keV normalized by 10^{-21} erg s^{-1} cm^{-2} Hz^{-1} sr^{-1}.

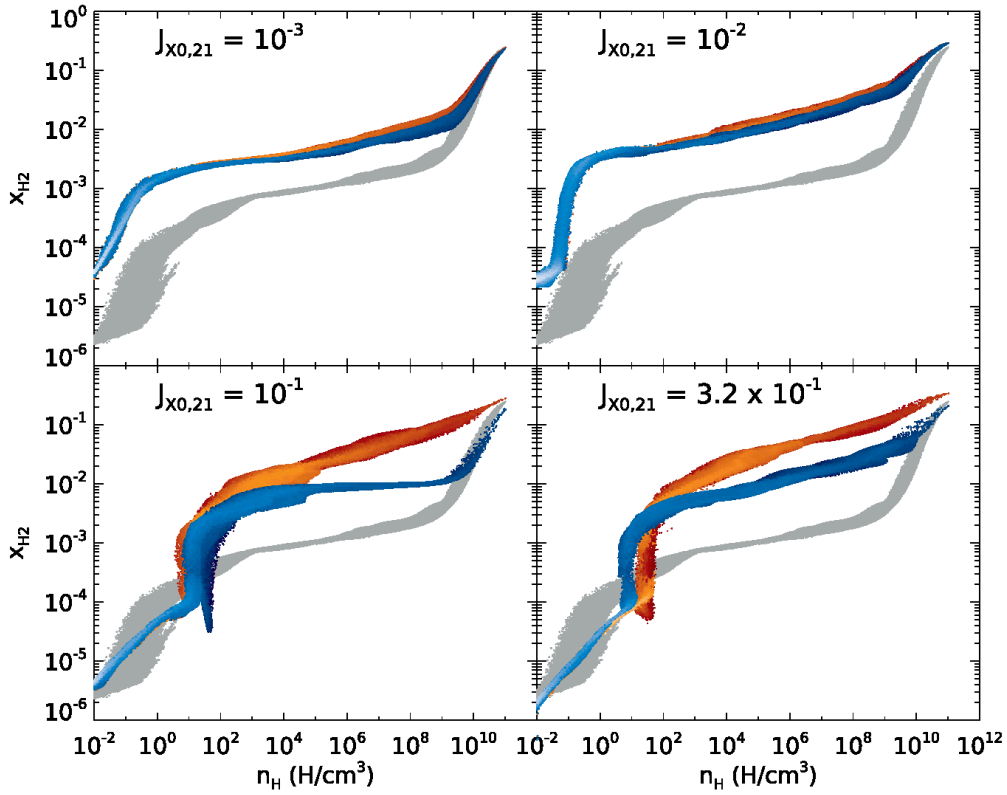

Figure B.2: Same as Figure B.1 but showing the H_2 fraction as a function of the hydrogen number density. The H_2 fraction grows slowly when irradiated by a weak X-ray background or X-rays are shielded, before it starts to increase rapidly due to three-body interactions at $n_{\rm H} \sim 10^{10}$ H cm^{-3}. If very strong X-ray irradiation is not shielded, however, the H^- channel effectively increases the H_2 fraction and makes the gas nearly fully molecular at lower densities (see bottom panels).

show the gas electron fraction in Figure B.3. In the unshielded simulation for a given background, X-rays ionize the gas efficiently and therefore the electron fraction is higher than its counterpart in the shielded case. This difference, however, is small in a weak background and only apparent in stronger ones.

We conclude that most of the results in this work and the companion paper (Paper I) are insensitive to the X-ray shielding as only a small fraction of our fiducial runs have $J_{\rm X0,21} \sim 10^{-1}$, that is the strongest X-ray intensity in the parameter range we explored. In the strongest X-ray

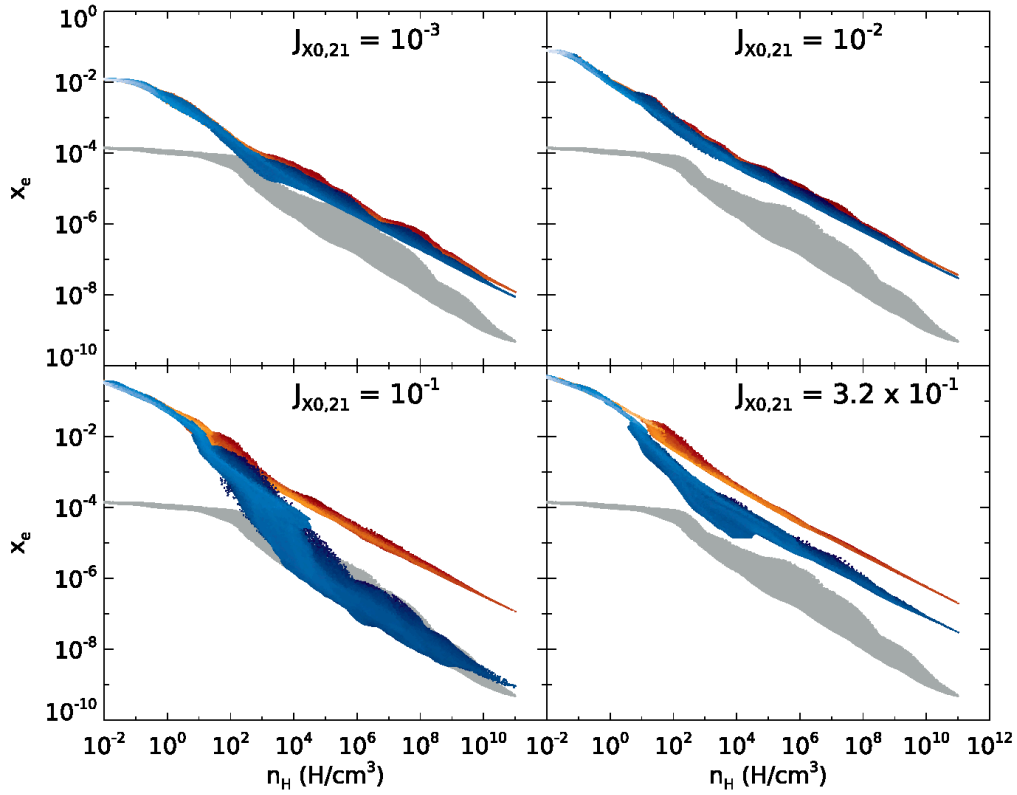

Figure B.3: Same as Figure B.1, but showing the electron fraction as a function of hydrogen number density. The deviation of the electron fraction including or neglecting self-shielding is minimal for the range of X-ray irradiation explored in our fiducial runs (top panels), but it is evident for the cases with very strong X-ray background (bottom panels, $\mathrm{J_{X0,21}} > 0.1$).

background, however, the self-shielding may potentially play a crucial role in the fragmentation of the disc and the growth of protostars. In these test simulations, we show the phase diagram when the central density reaches $n_{\mathrm{H}} = 10^{11}$ H cm^{-3}, hence it is unclear how the later evolution of the disc is affected by the shielding. We plan to explore this aspect in future works.

Appendix C: Appendices for Chapter 4

C.1 Radiative Transfer Recipes

C.1.1 Importance of X-ray Self-Shielding

The test results on the effects of X-ray self-shielding are presented in Fig. C.1. We ran a simulation with the same parameters as Run E but without including X-ray self-shielding (shown in red). We find that the sink mass is larger between $t \sim 15$ and 25 kyr when the disc is not shielded from the X-ray background. This is consistent with Hummel et al. (2015) in that the cooling is more efficient without shielding. The difference, however, is small and the results converge by $t \sim 30$ kyr. This small difference can be explained in the following way. As discussed in Paper I and Paper II properties of the stars are determined by the mass of the hydrostatic core at $n_{\rm H} \sim 10^4$ H cm^{-3} when the gas is mostly transparent to X-rays (i.e., shielding is negligible). In Paper II we have shown that X-ray shielding is important only for strong X-ray irradiation. Although a moderate X-ray background lowers the critical halo mass for star formation (Paper I), it is the opposite in an intense X-ray background where heating by X-rays is the dominant feedback. For strong X-ray irradiation the gas in a halo can condense only if it is sufficiently massive ($M > M_{\rm Jeans,IGM}$), therefore in this case the halo can be optically thick to X-rays. This is, in a sense, consistent with Hummel et al. (2015) who pointed out the dependence of shielding on halo

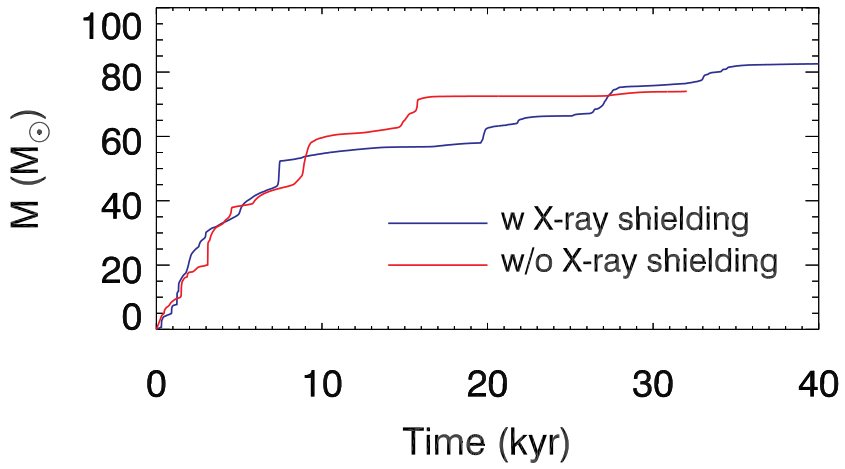

Figure C.1: Total mass in Pop III stars including (blue line) and excluding (red line) X-ray self-shielding for Run E ($J_{X0,21} = 10^{-2}$). All fiducial runs include self-shielding.

properties.

C.1.2 Protostar Formation Recipes

Fig. C.2 (1a-1d) shows snapshots of Run F with different protostar formation recipes. Protostars in the low-resolution simulation (top left) show a similar evolution to the ones in Paper I and Paper II. With a higher spatial resolution (top right) clumps reach higher densities ($\sim 10^{13}$ H cm^{-3}) and fragmentation becomes more efficient creating more protostars. When sink particles are used, however, the number of stars is reduced due to sink mergers (bottom right). The change when including RFB is not prominent as seen in the bottom left panel.

In Fig. C.2 (panel 2) we plot the total mass in Pop III stars for the different recipes shown in the left panel. One notable feature is that the total mass of the clumps is independent of the spatial resolution (red and green). The total mass of protostars tracked by sink particles (blue) is higher than the one for the clumps, suggesting that the stars in the two methods are not identical. These three cases all show a linear growth of mass due to the lack of RFB.

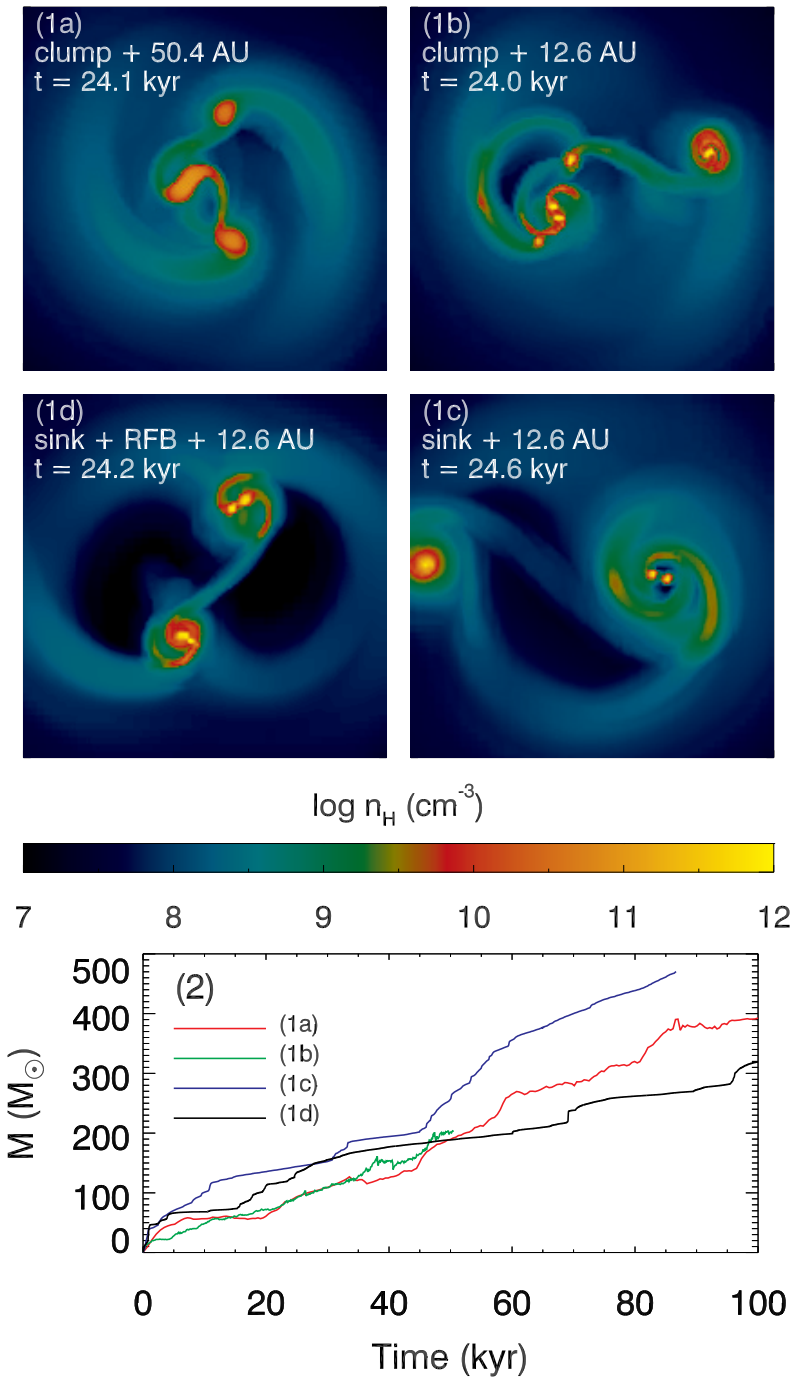

Figure C.2: Panel (1a)-(1d): Slices of the hydrogen number density of Run F with different star formation recipes. The figure shows the discs at $t \sim 24$ kyr since the formation of the first protostar. The four panels show the change with the improvement of the simulation from the top left panel in the clockwise direction. (1a): Low resolution with the clump recipe. This setting is similar to that of Paper I and Paper II. (1b): The spatial resolution is increased. (1c): Clumps are replaced by sink particles. (1d): RFB is added. This is the fiducial run. Panel (2): Evolution of the total mass in Pop III stars for the same four protostar formation recipes as in the left panel.

C.1.3 Sink Formation Threshold and Radius

In our simulations we want to resolve the Jeans length with at least $N_{\rm J} > 4$ cells to avoid numerical fragmentation (Truelove et al., 1997). Therefore we impose a refinement criterion $\Delta x = \lambda_{\rm J}/N_{\rm J}$, with $N_{\rm J} = 16$. However, when $\Delta x = \Delta x_{\rm min}$ at the maximum refinement level, the Jeans length is no longer resolved with $N_{\rm J}$ cells if the density becomes too large. To avoid this we introduce sink particles that limit the increase of the density within their radii $r_{\rm sink} = N_{\rm Sink}\Delta x_{\rm min}$ (note that inside the sinks the grid is always refined to the maximum level). A sink is formed when the peak density in a gas clump (identified by a clump finder) is above the critical density, $n_{\rm sink}$, such that

$$N_{\rm Sink}\Delta x_{\rm min} = \lambda_{\rm J} = \left(\gamma\frac{k_{\rm B}T}{\mu m_{\rm H}}\right)^{1/2}\left(\frac{1}{G m_{\rm H} n_{\rm sink}}\right)^{1/2}, \tag{C.1}$$

where $N_{\rm Sink} \leq N_{\rm J}$ is an integer. Solving for $n_{\rm sink}$ gives,

$$n_{\rm sink} \sim 1.2\times10^{12}\ {\rm cm}^{-3}\left(\frac{4}{N_{\rm Sink}}\right)^2\frac{(T/1000\ {\rm K})}{(\Delta x_{\rm min}/12.6\ {\rm AU})^2}. \tag{C.2}$$

We adopt a value $n_{\rm sink} = 10^{12}$ cm^{-3} in all our simulations, roughly corresponding to $N_{\rm Sink} = 4$, assuming $T = 1000$ K (i.e., we resolve the Jeans length with 4 cells within the sink radius. As discussed in Appendix of Paper I our chemistry and cooling implementation are valid up to $n \sim 10^{14}$ cm^{-3} and our choice of the density threshold is well below this limit.

The choice for the value of the sink radius is independent of the density threshold $n_{\rm sink}$, but it makes sense to adopt values that are comparable or multiples of the Jeans length: in our case we explore the range $4 \leq N_{\rm Sink} \leq 16$. As illustrated in Fig. C.3 adopting $N_{\rm Sink} = 4$ with our sub-sink radiation transfer recipe in C.1.4, reduces significantly the RFB efficiency with respect

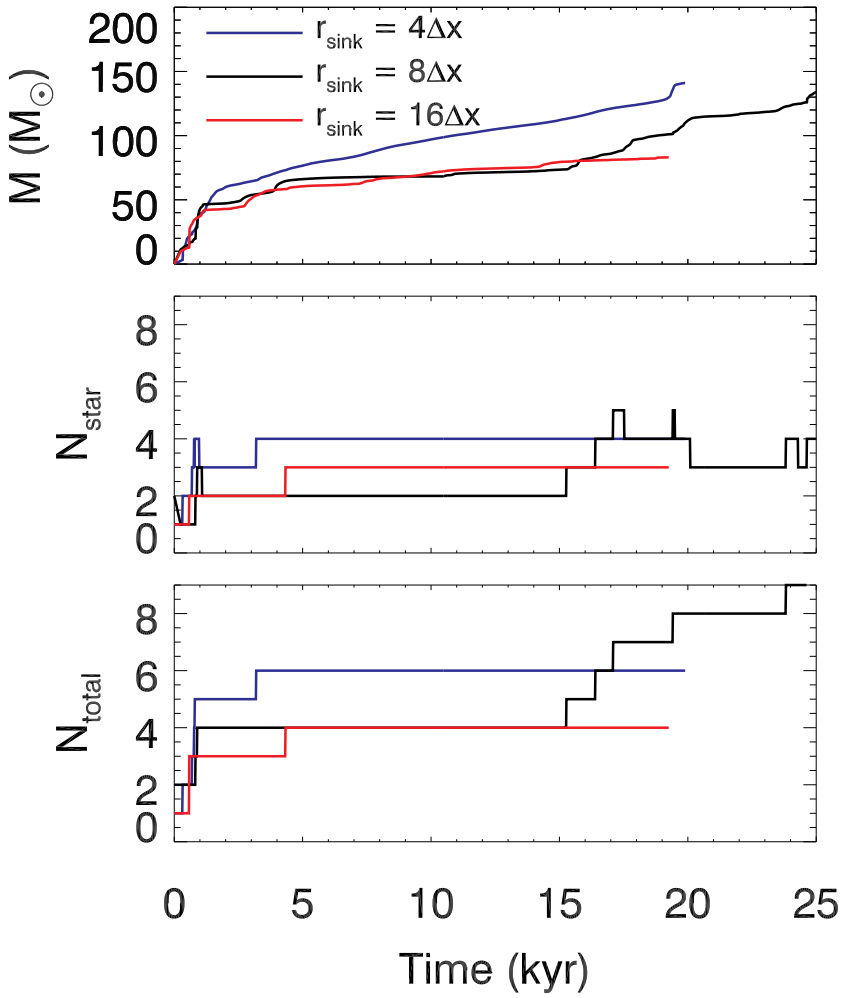

Figure C.3: Dependence of results on the assumed sink radii. The fiducial value is $8\Delta x$ where $\Delta x = 12.6$ AU. Top panel: Total mass in stars as a function of time. Middle panel: Multiplicity ($N_{\rm star}$) at a given time. Bottom panel: Total number of sinks that formed in the simulation as a function of time. This total includes the stars that have disappeared through mergers.

to using $N_{\rm Sink} = 8, 16$, producing a total mass in Pop III stars comparable to the no-FB case. The total mass in Pop III stars for $N_{\rm Sink} = 8$ and $N_{\rm Sink} = 16$ are similar, but start diverging after $t \sim 15$ kyr as more efficient feedback in the latter evaporates the gas disc. In our fiducial simulations we adopt $N_{\rm Sink} = 8$, but clearly $N_{\rm Sink}$ is a crucial parameter that determines the strength of RFB and the spatial resolution of the simulations. In Fig. C.3, we also show the number of stars (middle panel) and the total number of sinks formed (bottom panel) as a function

of time. During the first ~ 20 kyr we do not observe significant variations of multiplicity as a function of the assumed sink radius.

C.1.4 Ionizing and LW Photon Emission from Sink Particles

Pop III protostars form at the centre of sink particles, however the disc structure and dynamics inside the sink are poorly resolved. If we make a simple estimate of the size $R_{\rm S}$ (Strömgren radius) of the H II region produced by a massive star at the centre of a sink in which there is a uniform density n, we must require that $R_{\rm S}$ is greater than the sink radius for the ionizing radiation to escape the sink:

$$\left(\frac{3Q}{4\pi n^2 \alpha}\right)^{1/3} \geq r_{\rm sink}, \tag{C.3}$$

where $\alpha \approx 2 \times 10^{-10}\ T^{-3/4}\ {\rm cm^3\ s^{-1}}$ is the recombination rate. Assuming $T = 10^4$ K and an ionizing photon emission rate $Q = 10^{50}\ {\rm s^{-1}}$, we get $n \lesssim 10^8\ {\rm cm^{-3}}$. This is several orders of magnitude smaller than the $n_{\rm sink}$, hence the ionizing radiation should remain trapped inside the sink.

However, the gas inside the sink does not have a constant density. Along the disc plane, the density is comparable to $n_{\rm sink}$, however above and below the disc plane the density is much lower and, if the disc is well resolved, around the protostar the disc is thinner due to the star's gravity. For this reason, radiation can escape along bipolar H II regions above and below the disc, while being trapped along the disc direction. Because the gas structure is poorly resolved inside the sink we do not inject radiation from the star at the centre of the sink or uniformly inside the sink particle, as it likely would underestimate RFB. Instead, we inject the radiation from the star at the surface of the sink sphere, with flux in the radial direction. We adopt a sub-sink radiative transfer

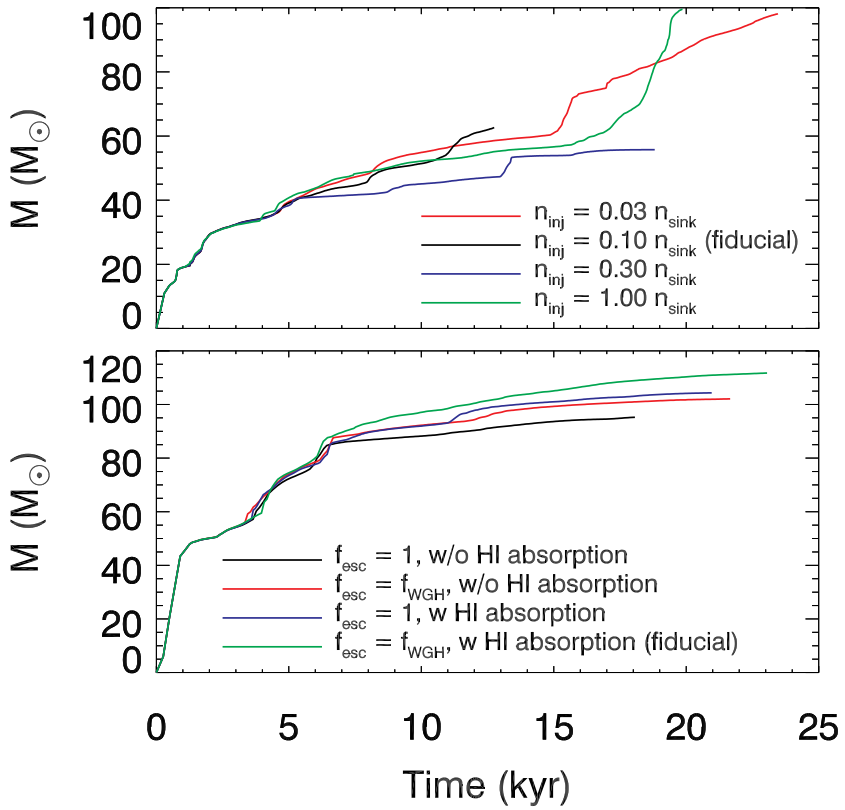

Figure C.4: Top: Test runs with different $n_{\rm inj}$. $0.1n_{\rm sink}$ is the fiducial value. Bottom: Sink mass affected by LW-related physics. The black line shows mass without a sub-sink recipe (i.e. $f_{\rm esc} = 1$) and H I absorption. Adding sub-sink recipe (i.e. $f_{\rm esc} = f_{\rm WGH}$, equation 4.5, red line) and H I absorption (blue line) alone reduce RFB and thereby increasing stars' mass. Considering both (green line) increases the mass further. We assume that LW radiation is absorbed by H_2 gas in all cases.

prescription to take into account the ionizing and LW radiation absorbed by the gas inside the sink.

Regarding H and He ionizing radiation we fully absorb the radiation for rays where the gas density at the sink radius is higher than an arbitrary threshold $n_{\rm inj} = 0.1n_{\rm sink} = 10^{11}$ cm^{-3}, since the radiation would be trapped anyway and we want to avoid photo-evaporation of the disc due to numerical effects. Test results with different density thresholds are shown in Fig. C.4 (top). The opening angle of the bipolar region where ionizing radiation escapes is not sensitive to the assumed $n_{\rm inj}$ within the explored range, and the total mass in Pop III stars does not show any clear

trend with the assumed value of $n_{\rm inj}$. However, the values of $r_{\rm sink}$ and $n_{\rm inj}$ should be considered related parameters because if $r_{\rm sink}$ is small, the gas density at the sink surface may never drop below $n_{\rm inj}$ and radiation would remain trapped.

For the LW radiation, in addition to a density threshold, we calculate the column density of the H_2 gas along rays from the centre of the sink to the sink surface and we estimate the fraction of LW photons escaping the sink in each direction due to H_2 self-shielding. In Fig. C.4 (bottom) we show how the total mass in sinks changes when including H_2 self-shielding and absorption by H I Lyman series lines (Section 4.2.6). The escape fraction of LW photons due to H_2 self-shielding alone (red line) reduces the amount of LW photons escaping from the sink surface, thereby weakening RFB and increasing the total mass in Pop III stars. The feedback effect also becomes weaker by a comparable amount due to shielding by H I resonant lines alone (blue line). The total mass in Pop III stars increases further when considering both opacity sources (green line).

C.1.5 Resolution Study

Fig. C.5 shows the dependence of the total mass (top panel), the multiplicity, and the total number of sinks (middle and bottom panels) as a function of time for three simulations with different resolutions (maximum refinement level, 15, 16 and 17). In agreement with Prole et al. (2022), we find that the total mass is rather insensitive to the spatial resolution, while the multiplicity and the total number of sinks are not convergent but increase with increasing resolution. We also found the masses of individual stars are reduced as the resolution increases (not shown here). Naively, we expect that the IMF in a higher-resolution simulation is bottom-heavier and

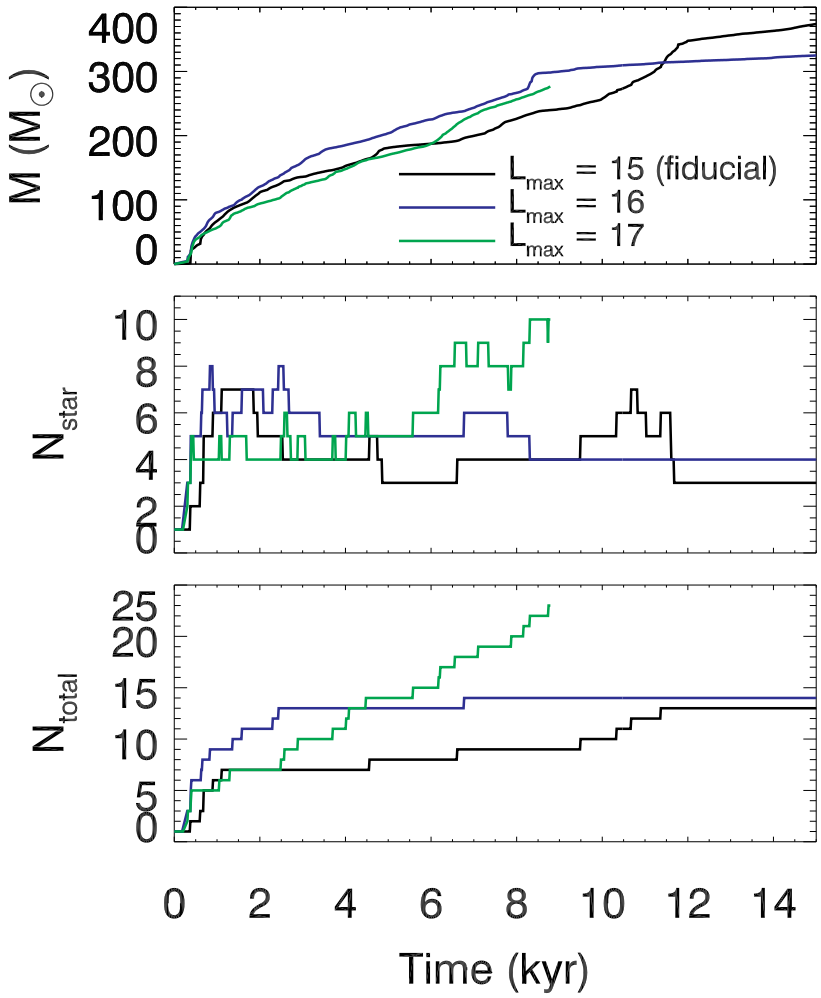

Figure C.5: Resolution study. We perform Run A with the maximum AMR level 15 (fiducial), 16 and 17 (see legend). The corresponding spatial resolutions ($\Delta x_{\rm min}$) are 12.6, 6.29 and 3.15 AU, respectively. Following equation (C.2) we choose $n_{\rm sink} = 1.0 \times 10^{12}$, 4.0×10^{12} and 1.6×10^{13} H cm^{-3} and fiducial sink radius $8\Delta x_{\rm min}$. The top panel shows the total mass in sinks, the middle panel the multiplicity (taking into account mergers of sinks) and the bottom panel the total number of sinks formed as a function of time.

has a lower cutoff/peak mass than what we found here, although the role of sink mergers is harder to predict. Even with this caveat, we speculate that the trends observed with an X-ray background are robust. We also carried out a similar resolution study for Run F and, albeit less pronounced, the results follow a similar trend.

C.1.6 Reduced Speed of Light Approximation

Ignoring recombination, the speed of the ionization front is $v_{\rm I} = Q/(4\pi d^2 n)$, where d is the distance from the source. By normalizing the parameters with typical values relevant to this work, at large scales we get:

$$v_{\rm I} = 2.79 \times 10^{-4} c \left(\frac{Q_{48}}{d^2_{0.01{\rm pc}} n_7} \right). \tag{C.4}$$

Here, Q_{48} is the luminosity of the source in units 10^{48} photon s^{-1}, $d_{0.01{\rm pc}}$ is the radius of the ionization front in units of 0.01 pc, and n_7 is the gas number density in units of 10^7 cm^{-3}. Therefore at large distances, assuming $Q_{48} \sim 1 - 10$, $v_{\rm I}$ is about a factor of $3 - 30$ times slower than our fiducial value for the reduced speed of light $c_{\rm red} = 10^{-3} c$. We expect the I-front propagation speed to be similar near the sink particles because the distance decreases but the gas density increases roughly as $\sim r^{-2}$ near the sink (Larson, 1969; Penston, 1969), therefore the ionization front speed only depends on the luminosity of the source. With our sink radius of ~ 100 AU ($d_{0.01{\rm pc}} \sim 5 \times 10^{-2}$) and photon injection density threshold 10^{11} H cm^{-3} ($n_7 = 10^4$), the ionization front speed is $v_{\rm I} \sim 10^{-5} Q_{48} c$. Therefore even for $Q_{48} \sim 10 - 100$, only relevant when sinks have high mass and accretion rates, $v_{\rm I} \sim 10^{-4} - 10^{-3} c$. All the estimates above for $v_{\rm I}$ are only an upper limit for the speed, as recombination slows down the ionization front propagation speed. Indeed we have tested different values of $c_{\rm red}$ from $10^{-1} c$ to $10^{-4} c$, and did not observe significant effects on the simulations results. Interestingly the computational cost of the simulations is not reduced significantly when assuming values of $c_{\rm red}$ lower than $10^{-3} c$, hence we adopted the most conservative $c_{\rm red} = 10^{-3} c$.

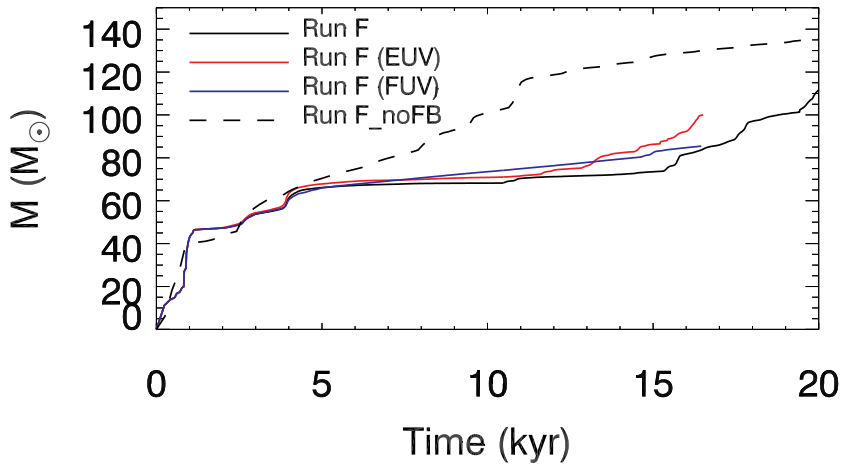

Figure C.6: Total mass in sinks in Run F affected by EUV (red), FUV (blue) and both (black solid). For comparison, noFB case is shown in a dashed line.

C.2 Relative Importance of EUV vs FUV Feedback

In Fig. C.6 we plot the total mass in sinks as a function of time in runs with different UV feedback. We find FUV (LW, red line) alone can efficiently reduce the mass unlike in Hosokawa et al. (2016). EUV-only simulation shows a similar degree of mass reduction. The mass is reduced further with the combination of two UV feedback but this further reduction seems weaker than individual feedback.

C.3 Sink Merger

In Fig. C.7 we plot the mass in Run E with and without sink merger (solid and dashed). In the fiducial run, 4 stars form and merge to leave two stars. When they merge, they are gravitationally bound to their companions. In the test run, these stars actually orbit their companions in close orbits with separations ~ 40 and 100 AU. The orbits do not expand but shrink with time possibly due to gravitational torque by the gas disc (Chon and Hosokawa, 2019) and they circularise with

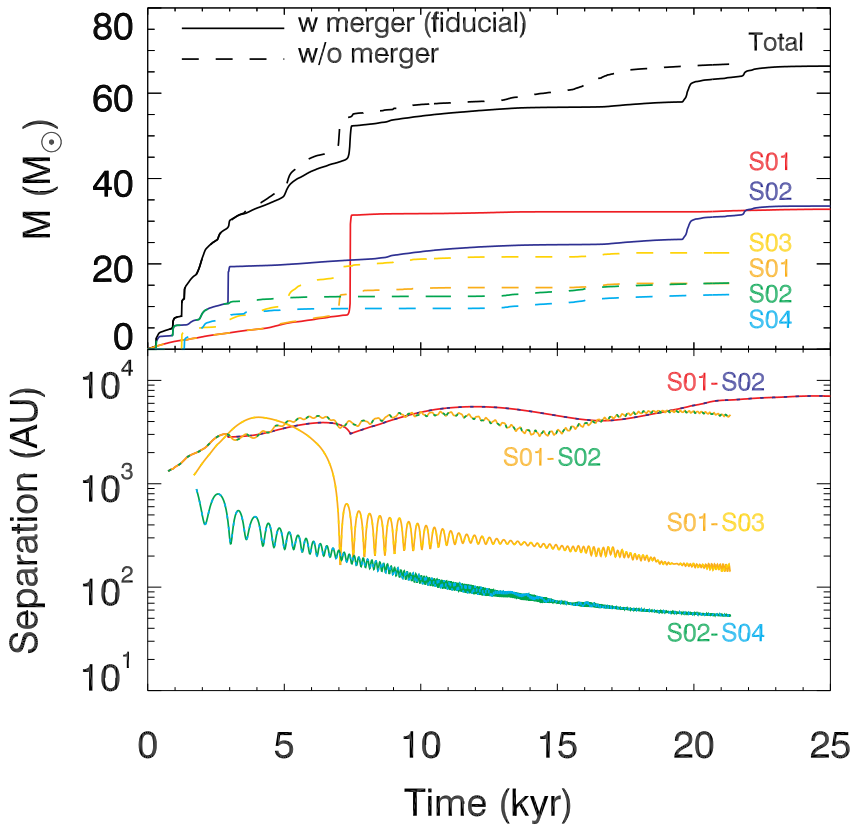

Figure C.7: Top: Masses in Run E with (solid lines) and without (dashed lines) sink mergers. The multiplicities are 2 and 4, respectively. Individual sink particles are shown in different colors. Bottom: Binary separations. In the simulation without mergers, the stars form a hierarchical binary.

time. RFB in the test run is slightly weaker than the fiducial case because the luminosity of a protostar is not a linear function of mass in the model (Hosokawa and Omukai, 2009; Hosokawa et al., 2010). Therefore the feedback strength may differ even if the total mass is the same. Even with this difference, the mass variation is insignificant. The total masses of the stars at ~ 22 kyr in the fiducial and test runs are 63.7 and 66.8 $\mathrm{M}_{\odot}$, respectively. We expect the mass of stars is not sensitive to the sink merger prescription.

Appendix D: Appendices for Chapter 5

D.1 Sink Particle Recipes

The setup of our simulations differs from those of idealised circumbinary simulations widely used in the literature (Tang et al., 2017; M19; Muñoz et al., 2020; Dempsey et al., 2020, 2021; Dittmann and Ryan, 2021, 2022). To better understand the difference and estimate the potential impacts on our conclusion, we performed numerical tests and present the results in this appendix.

D.1.1 Sink Radius

In previous works, the sink radii are kept smaller than $\lesssim 10$ % of the semimajor axis (M19; Dittmann and Ryan, 2021, 2022, 2023; Sugimura et al., 2023). The sink radius is an important parameter in a binary simulation as a too-large value might reduce the increase in the orbital angular momentum (M19). In this work, the choice of the sink radius is a more complicated matter because it determines the effect of radiative feedback. To better understand the effect of $r_{\rm sink}$ on the orbital evolution, we present the test result with different sink radii in Fig. D.1. When $r_{\rm sink} = 4\Delta x_{\rm min}$ and $8\Delta x_{\rm min}$, the binary has similar orbits. With a larger sink radius ($r = 16\Delta x_{\rm min}$), however, the stars migrate inward. We speculate that feedback plays a significant role

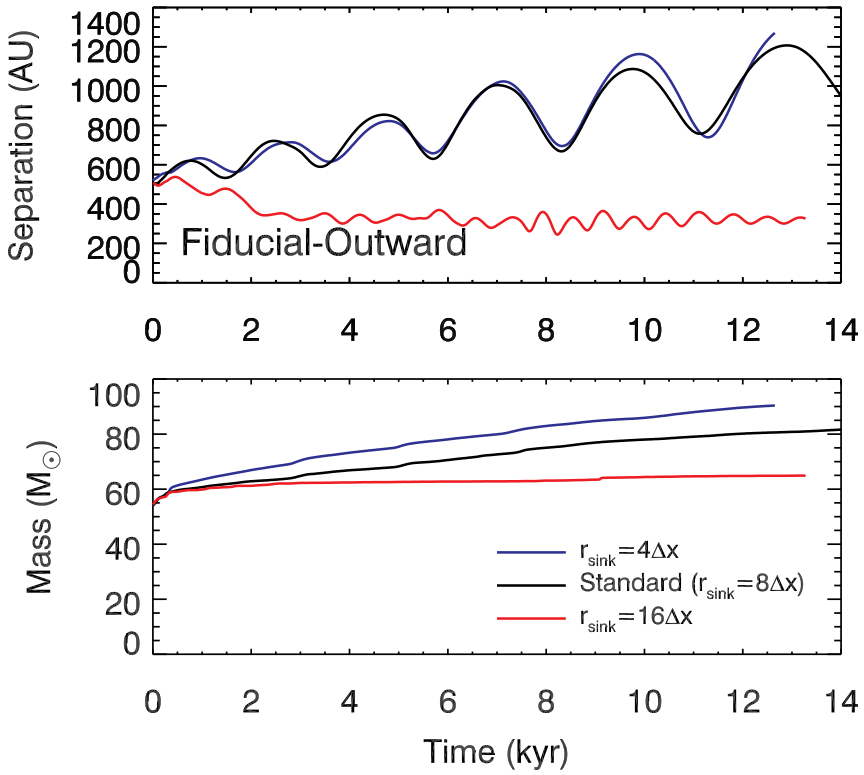

Figure D.1: Separation (top) and total mass (bottom) of binaries with different sink radii. The fiducial value adopted in this work is $r_{\rm sink} = 8\Delta x$.

in this case. As can be seen in the mass plot (bottom panel), the growth of stars is suppressed significantly due to the effective radiative feedback. However, the possibility of the numerical effect (a large sink radius leads to an increase in angular momentum, M19) is not completely ruled out. Note that our sink resolution is sufficient for wide binaries ($a_{\rm b} \gtrsim 2000$ AU) but is insufficient for close binaries. Therefore, the results of the close binaries must be interpreted with caution.

D.1.2 Softening Length

In idealised CBD simulations, two sink particles are well-controlled, and therefore the codes typically do not require a softening term when calculating interactions between sink parti-

cles. The codes developed for cosmological simulations (RAMSES or GADGET-2, Teyssier, 2002; Springel, 2005), on the other hand, often handle N-body systems in which sink particles encounter other particles frequently and therefore these codes employ softening length. As we use RAMSES in this study, we softened the gravitational force between two sink particles with the softening term ε (equation (5.5)). In this work, we choose $\varepsilon = 0.5 r_{\rm sink} = 4\Delta x_{\rm min} = 50.4$ AU. In Fiducial-Inward, the minimum separation is ~ 400 AU and is only ~ 8 times larger than the minimum separation (400 AU, Table 5.1). This causes ~ 27 % difference in the strength of the gravitational force between sinks. In this work, any two sink particles closer than 202 AU are not resolved and close binaries are beyond the scope of this paper. Rather, we focus on the formation of wide binaries and outward migration. In these binaries, the separations are even larger and the softening term becomes negligible compared to the separation. Therefore the effect of gravitational softening is insignificant in most cases. To confirm this, we present the result of the test run in Fig. D.2. We modified the code to keep the softening for gas accretion but erase the softening of the gravitational force due to other sink particles (i.e., $\varepsilon = 0$). In both Fiducial-Outward (top panel) and Fiducial-Inward (bottom panel), erasing the softening term (red lines) does not change the direction of the migration (outward to inward or vice versa). For Fiducial-Outward, the two orbits with different ε do not match perfectly. Therefore, there is a possibility that other orbital parameters (such as semimajor axis or orbital period) may change over many periods ($\gtrsim 100$ orbits). However, gravitational softening does not change our conclusions on outward migration. We admit that inward migration is more sensitive to gravitational softening. As seen in the bottom panel, we argue that it does not affect the results of our two binaries with inward migration, but we need a follow-up study with high-resolution simulations.

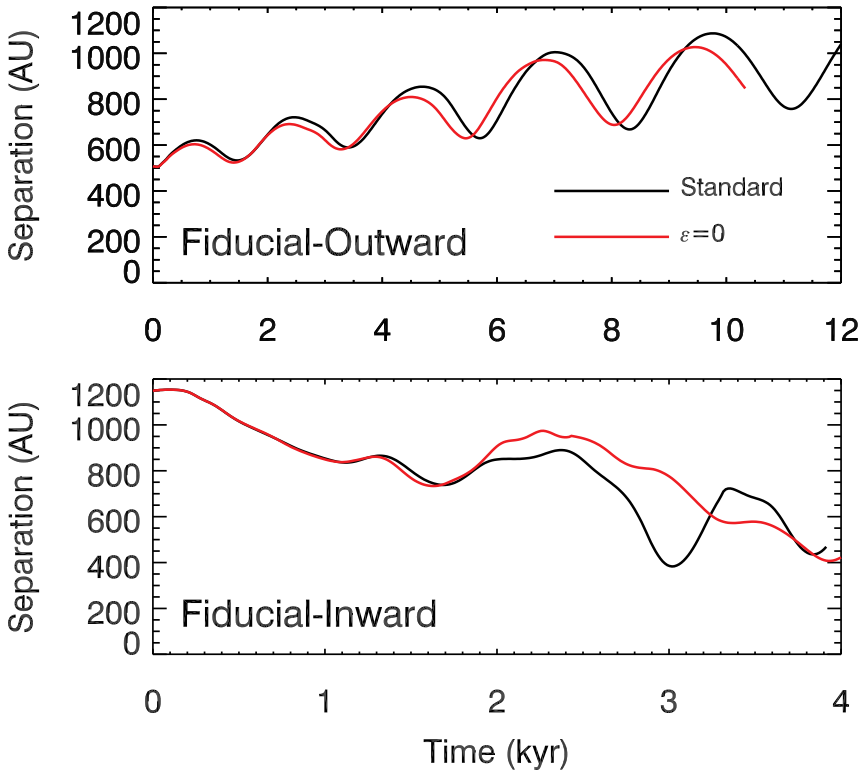

Figure D.2: The time evolution of the separations of the Fiducial-Outward (top panel) and Fiducial-Inward binaries (bottom panel) with different assumptions for sink softening lengths. Each panel compares the binary separations for the fiducial simulation ($\varepsilon = 4\Delta x_{\rm min}$, black) and the test run ($\varepsilon = 0$, red). Note that we kept the softening for gas and only changed the sink softening.

D.1.3 Accretion of Angular Momentum

Recent numerical studies demonstrated the sink particle method with mass removal may introduce an artificial torque and thus the angular momentum of the accreted gas must be conserved to prevent this (Dempsey et al., 2020; Dittmann and Ryan, 2021). We performed several test simulations and explored the impact of the accretion schemes on our conclusion. RAMSES has a built-in option to turn on the angular momentum-conserving accretion prescription described above (so-called 'no-L' accretion, Bleuler and Teyssier, 2014). This was devised to prevent the central sink from obtaining unphysically high angular momentum but this acts the same as in the

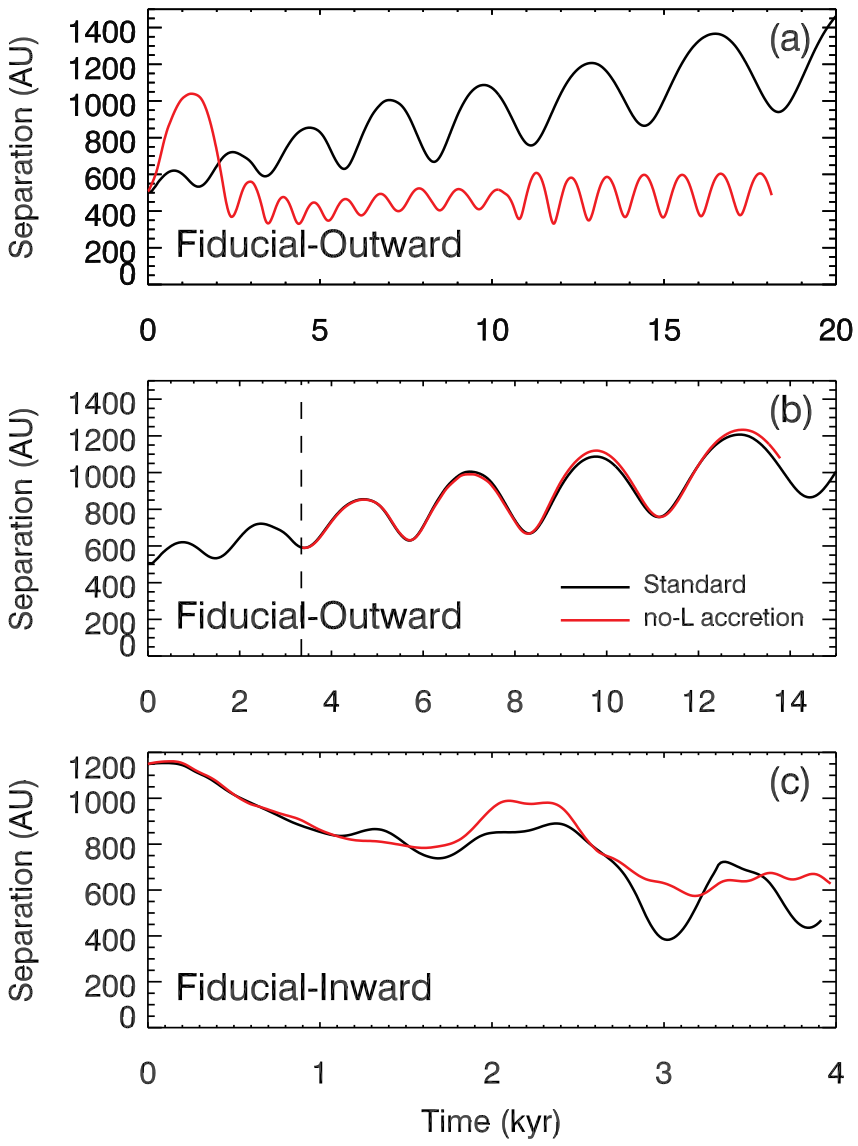

Figure D.3: Numerical tests with different accretion schemes. In the standard method (black), the sink accretes the angular momentum of the gas in addition to its mass. In 'no-L' accretion (red), on the other hand, the sink returns the tangential component of the velocity vector so that the angular momentum of the gas is conserved (Bleuler and Teyssier, 2014). Panel a: Binary separation as a function of time for the Fiducial-Outward binary. The 'no-L' option is turned on at when the binary forms ($t = 0$ kyr). Panel b: Same as Panel a but the 'no-L' accretion is turned on at $t \approx 3.3$ kyr. Panel c: The binary separation for the Fiducial-Inward binary during the first ~ 4 kyr.

works mentioned above.

In Fig. D.3, we present the results of numerical tests in three different situations. In each panel, we compare the fiducial simulation (black) and the one with 'no-L' accretion (red). In the

latter case, a sink particle returns the tangential component of the momentum to the accreted gas cells so that the angular momentum of the gas remains constant (for details, see Bleuler and Teyssier, 2014). In Panel a, we compare the time evolution of the separation of the Fiducial-Outward binary using the two accretion methods aforementioned. With 'no-L' accretion, the evolution in the first $2-3$ kyr differs significantly from the standard case. The secondary star has an eccentric orbit but is captured at the pericenter at $t \sim 2$ kyr and afterward remains in a close orbit (~ 400 AU). Note that the prescription used in the simulation affects the initial gas properties substantially and this impact is highly unpredictable. Therefore, this test is inconclusive in determining whether the accretion scheme has a long-term effect on migration. To remove this initial chaotic effect due to complicated sink formation processes, we performed another test by turning on the 'no-L' accretion at $t \sim 3$ kyr when the stars in the binary are well separated and after other sink particles disappear through mergers. The result is shown in Panel b. Unlike in the previous case, the two orbits are similar. We speculate there are two main reasons why our result is different from what was found in previous works (Dempsey et al., 2020; Dittmann and Ryan, 2021). First, the time scales of our simulations are much shorter than those in the aforementioned works. In our simulations, we followed the evolution of binaries for a few tens of orbits which correspond to the radiative feedback time scale ($\sim 10-100$ kyr Hirano et al., 2014, 2015; Sugimura et al., 2020), while the works mentioned above focus on the long-term evolution of the binary. For instance, Dittmann and Ryan (2021) evolved their binary for ~ 2000 orbits (see Fig. 2 of their work). If we run our simulations longer, hypothetically assuming that the gas supply is continuous, the change in orbital parameters may accumulate and become substantial. Second, the regulation of the density profile by the radiative feedback is likely dominant over effects related to assumptions on the angular momentum accretion scheme, unlike in the previous

numerical studies that neglect radiative feedback effects (Dempsey et al., 2020; Dittmann and Ryan, 2021). In Fiducial-Inward (Panel c), the difference is insignificant and the binary shrinks irrespectively of the assumed accretion scheme. This is because the binary has a large initial separation ($\sim$ 1200 AU) and thus is less sensitive to the accretion method.

Although different accretion schemes may cause numerical artifacts during the initial sink formation/disc fragmentation phase, our test confirms that the outward migration of Pop III stars we found in this work is physical rather than numerical. This assertion is corroborated also by other evidence. First, outward migration is also found in other studies without mass removal and thus free from artificial torque (Chon et al., 2021; Paper I; Paper II). In Paper I and Paper II we found that outward migration is common in Pop III binaries. Chon et al. (2021) focused on inward migration but found that Pop III stars may migrate outward in certain situations. Secondly, He and Ricotti (2023) used the sink particle method and found that metal-rich stars tend to migrate inward but outward migration is rare among them. We speculate this is due to the different gas properties mainly caused by the efficiency of cooling. If the artificial/numerical torque is the dominant process, they also should have found outward migration to be frequent. Finally, migration of Pop III stars is found consistently in other studies with sink particle method (Sugimura et al., 2020, 2023). We do not know whether this 'torque-free' accretion may play a role in orbital evolution for less massive systems, such as a planet orbiting a low-mass host star where radiative feedback is weaker. However, this effect is not dominant in massive Pop III binaries because strong radiative feedback regulates the gas density profile and therefore does not change the direction of migration systematically.

D.2 Non Quasi-steady State Accretion

In Fig. D.4, we plot $(\dot{a_{\rm b}}/a_{\rm b})/(\dot{M}_{\rm b}/M_{\rm b})$ which is also denoted by $(\mathrm{d}\ln a_{\rm b})/(\mathrm{d}\ln M_{\rm b})$ in the literature (Dittmann and Ryan, 2021, 2022). In a quasi-steady state disc, this value is nearly constant (Lai and Muñoz, 2023). In Fiducial-Outward (top panel), however, the rate is greater at later times. Before and after $t \sim 40$ kyr, the average rates are 2.27 and 4.21, respectively thereby suggesting the disc is not in a quasi-steady state like in typical CBD simulations. Note that the number of orbits covered in our simulations is smaller than the one required to reach the quasi-steady state (~ 100 orbits, M19). In addition, the late-time evolution (~ 60 kyr) is affected by the gravitational force of another sink particle (S11).

D.3 Reference Frame

Unlike in idealised simulations where a binary is fixed at the center of the box, binaries in our simulations drift and orbit the CoM of the entire system. The binaries are also accelerated by external forces but we did not consider this effect because the force on the CoM does not exert torque as seen below. Here, we will consider two reference frames: unprimed (unaccelerated) and primed (accelerated). The origins of both frames are at the CoM. In the unprimed frame, the force on the CoM is,

$$M_{\rm b}\boldsymbol{a} = m_1\boldsymbol{a}_1 + m_2\boldsymbol{a}_2 = \boldsymbol{F}_1 + \boldsymbol{F}_2 = \boldsymbol{F}, \tag{D.1}$$

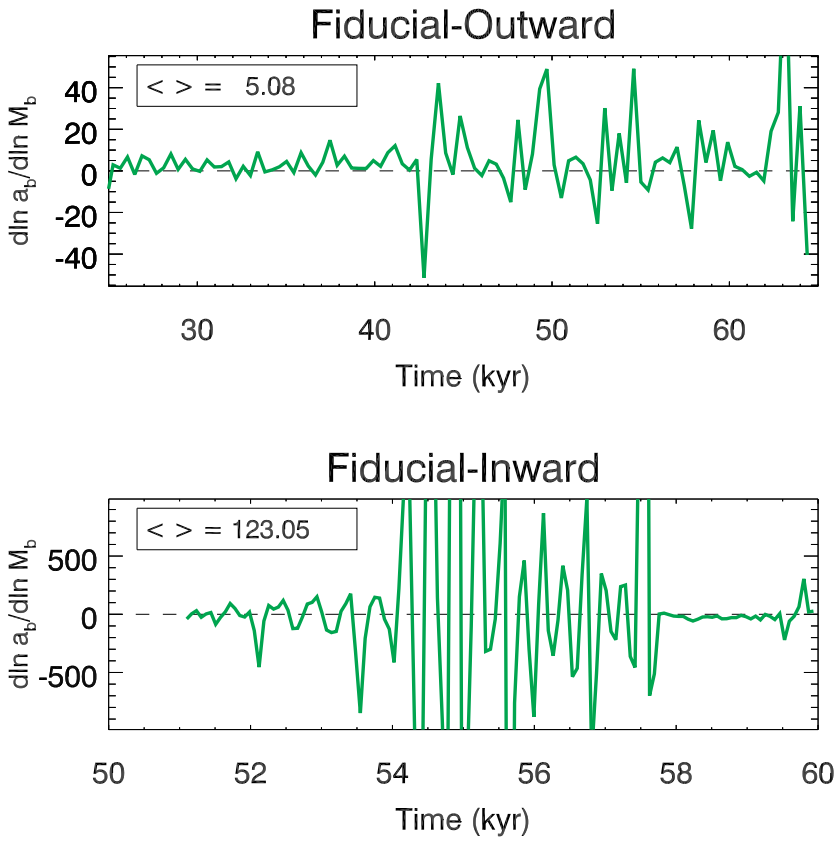

Figure D.4: $\mathrm{d}\ln a_\mathrm{b}/\mathrm{d}\ln M_\mathrm{b}$ of Fiducial-Outward (top) and Fiducial-Inward (bottom). A large increase in the rate in the bottom panel is caused by a close encounter and merger between sink particles meaning that the disc is not a quasi-steady state.

where the subscripts mean individual sink particles, $\boldsymbol{a}$ is the acceleration, and $M_\mathrm{b} = m_1 + m_2$.

The acceleration of Sink i in the primed frame is,

$$\boldsymbol{a}_i' = \boldsymbol{a}_i - \boldsymbol{a}. \tag{D.2}$$

Therefore, the force on the same sink is,

$$\boldsymbol{F}_i' = m_i \boldsymbol{a}_i' = m_i \boldsymbol{a}_i - m_i \boldsymbol{a} = m_i \boldsymbol{a}_i - \frac{m_i}{M_\mathrm{b}} \boldsymbol{F}. \tag{D.3}$$

Finally, the torque on the CoM in the primed frame is,

$$
\begin{aligned}
\boldsymbol{\tau}' &= \boldsymbol{r}_1 \times \boldsymbol{F}'_1 + \boldsymbol{r}_2 \times \boldsymbol{F}'_2 \\
&= \boldsymbol{r}_1 \times \left(\boldsymbol{F}_1 - \frac{m_1}{M_\mathrm{b}} \boldsymbol{F} \right) + \boldsymbol{r}_2 \times \left(\boldsymbol{F}_2 - \frac{m_2}{M_\mathrm{b}} \boldsymbol{F} \right) \\
&= \boldsymbol{r}_1 \times \boldsymbol{F}_1 + \boldsymbol{r}_2 \times \boldsymbol{F}_2 - \left(\frac{m_1}{M_\mathrm{b}} \boldsymbol{r}_1 \times \boldsymbol{F} + \frac{m_2}{M_\mathrm{b}} \boldsymbol{r}_2 \times \boldsymbol{F} \right) \\
&= \boldsymbol{\tau} - \frac{1}{M_\mathrm{b}} \left(m_1 \boldsymbol{r}_1 + m_2 \boldsymbol{r}_2 \right) \times \boldsymbol{F} \\
&= \boldsymbol{\tau}.
\end{aligned}
\tag{D.4}
$$

Since the torques in the two frames are identical, we used the simple approach without subtracting force on the CoM.

Bibliography

B. P. Abbott, R. Abbott, T. D. Abbott, M. R. Abernathy, F. Acernese, K. Ackley, C. Adams, T. Adams, P. Addesso, R. X. Adhikari, V. B. Adya, C. Affeldt, M. Agathos, K. Agatsuma, N. Aggarwal, O. D. Aguiar, L. Aiello, A. Ain, P. Ajith, B. Allen, A. Allocca, P. A. Altin, S. B. Anderson, W. G. Anderson, K. Arai, M. A. Arain, M. C. Araya, C. C. Arceneaux, J. S. Areeda, N. Arnaud, K. G. Arun, S. Ascenzi, G. Ashton, M. Ast, S. M. Aston, P. Astone, P. Aufmuth, C. Aulbert, S. Babak, P. Bacon, M. K. M. Bader, P. T. Baker, F. Baldaccini, G. Ballardin, S. W. Ballmer, J. C. Barayoga, S. E. Barclay, B. C. Barish, D. Barker, F. Barone, B. Barr, L. Barsotti, M. Barsuglia, D. Barta, J. Bartlett, M. A. Barton, I. Bartos, R. Bassiri, A. Basti, J. C. Batch, C. Baune, V. Bavigadda, M. Bazzan, B. Behnke, M. Bejger, C. Belczynski, A. S. Bell, C. J. Bell, B. K. Berger, J. Bergman, G. Bergmann, C. P. L. Berry, D. Bersanetti, A. Bertolini, J. Betzwieser, S. Bhagwat, R. Bhandare, I. A. Bilenko, G. Billingsley, J. Birch, R. Birney, O. Birnholtz, S. Biscans, A. Bisht, M. Bitossi, C. Biwer, M. A. Bizouard, J. K. Blackburn, C. D. Blair, D. G. Blair, R. M. Blair, S. Bloemen, O. Bock, T. P. Bodiya, M. Boer, G. Bogaert, C. Bogan, A. Bohe, P. Bojtos, C. Bond, F. Bondu, R. Bonnand, B. A. Boom, R. Bork, V. Boschi, S. Bose, Y. Bouffanais, A. Bozzi, C. Bradaschia, P. R. Brady, V. B. Braginsky, M. Branchesi, J. E. Brau, T. Briant, A. Brillet, M. Brinkmann, V. Brisson, P. Brockill, A. F. Brooks, D. A. Brown, D. D. Brown, N. M. Brown, C. C. Buchanan, A. Buikema, T. Bulik, H. J. Bulten, A. Buonanno, D. Buskulic, C. Buy, R. L. Byer, M. Cabero, L. Cadonati, G. Cagnoli, C. Cahillane, J. C. Bustillo, T. Callister, E. Calloni, J. B. Camp, K. C. Cannon, J. Cao, C. D. Capano, E. Capocasa, F. Carbognani, S. Caride, J. Casanueva Diaz, C. Casentini, S. Caudill, M. Cavaglià, F. Cavalier, R. Cavalieri, G. Cella, C. B. Cepeda, L. C. Baiardi, G. Cerretani, E. Cesarini, R. Chakraborty, T. Chalermsongsak, S. J. Chamberlin, M. Chan, S. Chao, P. Charlton, E. Chassande-Mottin, H. Y. Chen, Y. Chen, C. Cheng, A. Chincarini, A. Chiummo, H. S. Cho, M. Cho, J. H. Chow, N. Christensen, Q. Chu, S. Chua, S. Chung, G. Ciani, F. Clara, J. A. Clark, F. Cleva, E. Coccia, P. F. Cohadon, A. Colla, C. G. Collette, L. Cominsky, M. Constancio, A. Conte, L. Conti, D. Cook, T. R. Corbitt, N. Cornish, A. Corsi, S. Cortese, C. A. Costa, M. W. Coughlin, S. B. Coughlin, J. P. Coulon, S. T. Countryman, P. Couvares, E. E. Cowan, D. M. Coward, M. J. Cowart, D. C. Coyne, R. Coyne, K. Craig, J. D. E. Creighton, T. D. Creighton, J. Cripe, S. G. Crowder, A. M. Cruise, A. Cumming, L. Cunningham, E. Cuoco, T. Dal Canton, S. L. Danilishin, S. D'Antonio, K. Danzmann, N. S. Darman, C. F. Da Silva Costa, V. Dattilo, I. Dave, H. P. Daveloza, M. Davier, G. S. Davies, E. J. Daw, R. Day, S. De, D. DeBra, G. Debreczeni, J. Degallaix, M. De Laurentis, S. Deléglise, W. Del Pozzo, T. Denker, T. Dent, H. Dereli, V. Dergachev, R. T. DeRosa, R. De Rosa, R. DeSalvo, S. Dhurandhar, M. C. Díaz, L. Di Fiore, M. Di Giovanni,

A. Di Lieto, S. Di Pace, I. Di Palma, A. Di Virgilio, G. Dojcinoski, V. Dolique, F. Donovan, K. L. Dooley, S. Doravari, R. Douglas, T. P. Downes, M. Drago, R. W. P. Drever, J. C. Driggers, Z. Du, M. Ducrot, S. E. Dwyer, T. B. Edo, M. C. Edwards, A. Effler, H. B. Eggenstein, P. Ehrens, J. Eichholz, S. S. Eikenberry, W. Engels, R. C. Essick, T. Etzel, M. Evans, T. M. Evans, R. Everett, M. Factourovich, V. Fafone, H. Fair, S. Fairhurst, X. Fan, Q. Fang, S. Farinon, B. Farr, W. M. Farr, M. Favata, M. Fays, H. Fehrmann, M. M. Fejer, D. Feldbaum, I. Ferrante, E. C. Ferreira, F. Ferrini, F. Fidecaro, L. S. Finn, I. Fiori, D. Fiorucci, R. P. Fisher, R. Flaminio, M. Fletcher, H. Fong, J. D. Fournier, S. Franco, S. Frasca, F. Frasconi, M. Frede, Z. Frei, A. Freise, R. Frey, V. Frey, T. T. Fricke, P. Fritschel, V. V. Frolov, P. Fulda, M. Fyffe, H. A. G. Gabbard, J. R. Gair, L. Gammaitoni, S. G. Gaonkar, F. Garufi, A. Gatto, G. Gaur, N. Gehrels, G. Gemme, B. Gendre, E. Genin, A. Gennai, J. George, L. Gergely, V. Germain, A. Ghosh, A. Ghosh, S. Ghosh, J. A. Giaime, K. D. Giardina, A. Giazotto, K. Gill, A. Glaefke, J. R. Gleason, E. Goetz, R. Goetz, L. Gondan, G. González, J. M. G. Castro, A. Gopakumar, N. A. Gordon, M. L. Gorodetsky, S. E. Gossan, M. Gosselin, R. Gouaty, C. Graef, P. B. Graff, M. Granata, A. Grant, S. Gras, C. Gray, G. Greco, A. C. Green, R. J. S. Greenhalgh, P. Groot, H. Grote, S. Grunewald, G. M. Guidi, X. Guo, A. Gupta, M. K. Gupta, K. E. Gushwa, E. K. Gustafson, R. Gustafson, J. J. Hacker, B. R. Hall, E. D. Hall, G. Hammond, M. Haney, M. M. Hanke, J. Hanks, C. Hanna, M. D. Hannam, J. Hanson, T. Hardwick, J. Harms, G. M. Harry, I. W. Harry, M. J. Hart, M. T. Hartman, C. J. Haster, K. Haughian, J. Healy, J. Heefner, A. Heidmann, M. C. Heintze, G. Heinzel, H. Heitmann, P. Hello, G. Hemming, M. Hendry, I. S. Heng, J. Hennig, A. W. Heptonstall, M. Heurs, S. Hild, D. Hoak, K. A. Hodge, D. Hofman, S. E. Hollitt, K. Holt, D. E. Holz, P. Hopkins, D. J. Hosken, J. Hough, E. A. Houston, E. J. Howell, Y. M. Hu, S. Huang, E. A. Huerta, D. Huet, B. Hughey, S. Husa, S. H. Huttner, T. Huynh-Dinh, A. Idrisy, N. Indik, D. R. Ingram, R. Inta, H. N. Isa, J. M. Isac, M. Isi, G. Islas, T. Isogai, B. R. Iyer, K. Izumi, M. B. Jacobson, T. Jacqmin, H. Jang, K. Jani, P. Jaranowski, S. Jawahar, F. Jiménez-Forteza, W. W. Johnson, N. K. Johnson-McDaniel, D. I. Jones, R. Jones, R. J. G. Jonker, L. Ju, K. Haris, C. V. Kalaghatgi, V. Kalogera, S. Kandhasamy, G. Kang, J. B. Kanner, S. Karki, M. Kasprzack, E. Katsavounidis, W. Katzman, S. Kaufer, T. Kaur, K. Kawabe, F. Kawazoe, F. Kéfélian, M. S. Kehl, D. Keitel, D. B. Kelley, W. Kells, R. Kennedy, D. G. Keppel, J. S. Key, A. Khalaidovski, F. Y. Khalili, I. Khan, S. Khan, Z. Khan, E. A. Khazanov, N. Kijbunchoo, C. Kim, J. Kim, K. Kim, N.-G. Kim, N. Kim, Y. M. Kim, E. J. King, P. J. King, D. L. Kinzel, J. S. Kissel, L. Kleybolte, S. Klimenko, S. M. Koehlenbeck, K. Kokeyama, S. Koley, V. Kondrashov, A. Kontos, S. Koranda, M. Korobko, W. Z. Korth, I. Kowalska, D. B. Kozak, V. Kringel, B. Krishnan, A. Królak, C. Krueger, G. Kuehn, P. Kumar, R. Kumar, L. Kuo, A. Kutynia, P. Kwee, B. D. Lackey, M. Landry, J. Lange, B. Lantz, P. D. Lasky, A. Lazzarini, C. Lazzaro, P. Leaci, S. Leavey, E. O. Lebigot, C. H. Lee, H. K. Lee, H. M. Lee, K. Lee, A. Lenon, M. Leonardi, J. R. Leong, N. Leroy, N. Letendre, Y. Levin, B. M. Levine, T. G. F. Li, A. Libson, T. B. Littenberg, N. A. Lockerbie, J. Logue, A. L. Lombardi, L. T. London, J. E. Lord, M. Lorenzini, V. Loriette, M. Lormand, G. Losurdo, J. D. Lough, C. O. Lousto, G. Lovelace, H. Lück, A. P. Lundgren, J. Luo, R. Lynch, Y. Ma, T. MacDonald, B. Machenschalk, M. MacInnis, D. M. Macleod, F. Magaña-Sandoval, R. M. Magee, M. Mageswaran, E. Majorana, I. Maksimovic, V. Malvezzi, N. Man, I. Mandel, V. Mandic, V. Mangano, G. L. Mansell, M. Manske, M. Mantovani, F. Marchesoni, F. Marion, S. Márka, Z. Márka, A. S. Markosyan, E. Maros, F. Martelli, L. Martellini, I. W. Martin, R. M. Martin, D. V. Martynov, J. N. Marx, K. Mason, A. Masserot, T. J. Massinger, M. Masso-Reid, F. Matichard, L. Matone,

N. Mavalvala, N. Mazumder, G. Mazzolo, R. McCarthy, D. E. McClelland, S. McCormick, S. C. McGuire, G. McIntyre, J. McIver, D. J. McManus, S. T. McWilliams, D. Meacher, G. D. Meadors, J. Meidam, A. Melatos, G. Mendell, D. Mendoza-Gandara, R. A. Mercer, E. Merilh, M. Merzougui, S. Meshkov, C. Messenger, C. Messick, P. M. Meyers, F. Mezzani, H. Miao, C. Michel, H. Middleton, E. E. Mikhailov, L. Milano, J. Miller, M. Millhouse, Y. Minenkov, J. Ming, S. Mirshekari, C. Mishra, S. Mitra, V. P. Mitrofanov, G. Mitselmakher, R. Mittleman, A. Moggi, M. Mohan, S. R. P. Mohapatra, M. Montani, B. C. Moore, C. J. Moore, D. Moraru, G. Moreno, S. R. Morriss, K. Mossavi, B. Mours, C. M. Mow-Lowry, C. L. Mueller, G. Mueller, A. W. Muir, A. Mukherjee, D. Mukherjee, S. Mukherjee, N. Mukund, A. Mullavey, J. Munch, D. J. Murphy, P. G. Murray, A. Mytidis, I. Nardecchia, L. Naticchioni, R. K. Nayak, V. Necula, K. Nedkova, G. Nelemans, M. Neri, A. Neunzert, G. Newton, T. T. Nguyen, A. B. Nielsen, S. Nissanke, A. Nitz, F. Nocera, D. Nolting, M. E. N. Normandin, L. K. Nuttall, J. Oberling, E. Ochsner, J. O'Dell, E. Oelker, G. H. Ogin, J. J. Oh, S. H. Oh, F. Ohme, M. Oliver, P. Oppermann, R. J. Oram, B. O'Reilly, R. O'Shaughnessy, C. D. Ott, D. J. Ottaway, R. S. Ottens, H. Overmier, B. J. Owen, A. Pai, S. A. Pai, J. R. Palamos, O. Palashov, C. Palomba, A. Pal-Singh, H. Pan, Y. Pan, C. Pankow, F. Pannarale, B. C. Pant, F. Paoletti, A. Paoli, M. A. Papa, H. R. Paris, W. Parker, D. Pascucci, A. Pasqualetti, R. Passaquieti, D. Passuello, B. Patricelli, Z. Patrick, B. L. Pearlstone, M. Pedraza, R. Pedurand, L. Pekowsky, A. Pele, S. Penn, A. Perreca, H. P. Pfeiffer, M. Phelps, O. Piccinni, M. Pichot, M. Pickenpack, F. Piergiovanni, V. Pierro, G. Pillant, L. Pinard, I. M. Pinto, M. Pitkin, J. H. Poeld, R. Poggiani, P. Popolizio, A. Post, J. Powell, J. Prasad, V. Predoi, S. S. Premachandra, T. Prestegard, L. R. Price, M. Prijatelj, M. Principe, S. Privitera, R. Prix, G. A. Prodi, L. Prokhorov, O. Puncken, M. Punturo, P. Puppo, M. Pürrer, H. Qi, J. Qin, V. Quetschke, E. A. Quintero, R. Quitzow-James, F. J. Raab, D. S. Rabeling, H. Radkins, P. Raffai, S. Raja, M. Rakhmanov, C. R. Ramet, P. Rapagnani, V. Raymond, M. Razzano, V. Re, J. Read, C. M. Reed, T. Regimbau, L. Rei, S. Reid, D. H. Reitze, H. Rew, S. D. Reyes, F. Ricci, K. Riles, N. A. Robertson, R. Robie, F. Robinet, A. Rocchi, L. Rolland, J. G. Rollins, V. J. Roma, J. D. Romano, R. Romano, G. Romanov, J. H. Romie, D. Rosińska, S. Rowan, A. Rüdiger, P. Ruggi, K. Ryan, S. Sachdev, T. Sadecki, L. Sadeghian, L. Salconi, M. Saleem, F. Salemi, A. Samajdar, L. Sammut, L. M. Sampson, E. J. Sanchez, V. Sandberg, B. Sandeen, G. H. Sanders, J. R. Sanders, B. Sassolas, B. S. Sathyaprakash, P. R. Saulson, O. Sauter, R. L. Savage, A. Sawadsky, P. Schale, R. Schilling, J. Schmidt, P. Schmidt, R. Schnabel, R. M. S. Schofield, A. Schönbeck, E. Schreiber, D. Schuette, B. F. Schutz, J. Scott, S. M. Scott, D. Sellers, A. S. Sengupta, D. Sentenac, V. Sequino, A. Sergeev, G. Serna, Y. Setyawati, A. Sevigny, D. A. Shaddock, T. Shaffer, S. Shah, M. S. Shahriar, M. Shaltev, Z. Shao, B. Shapiro, P. Shawhan, A. Sheperd, D. H. Shoemaker, D. M. Shoemaker, K. Siellez, X. Siemens, D. Sigg, A. D. Silva, D. Simakov, A. Singer, L. P. Singer, A. Singh, R. Singh, A. Singhal, A. M. Sintes, B. J. J. Slagmolen, J. R. Smith, M. R. Smith, N. D. Smith, R. J. E. Smith, E. J. Son, B. Sorazu, F. Sorrentino, T. Souradeep, A. K. Srivastava, A. Staley, M. Steinke, J. Steinlechner, S. Steinlechner, D. Steinmeyer, B. C. Stephens, S. P. Stevenson, R. Stone, K. A. Strain, N. Straniero, G. Stratta, N. A. Strauss, S. Strigin, R. Sturani, A. L. Stuver, T. Z. Summerscales, L. Sun, P. J. Sutton, B. L. Swinkels, M. J. Szczepańczyk, M. Tacca, D. Talukder, D. B. Tanner, M. Tápai, S. P. Tarabrin, A. Taracchini, R. Taylor, T. Theeg, M. P. Thirugnanasambandam, E. G. Thomas, M. Thomas, P. Thomas, K. A. Thorne, K. S. Thorne, E. Thrane, S. Tiwari, V. Tiwari, K. V. Tokmakov, C. Tomlinson, M. Tonelli, C. V. Torres, C. I. Torrie, D. Töyrä, F. Travasso, G. Traylor, D. Trifirò, M. C.

Tringali, L. Trozzo, M. Tse, M. Turconi, D. Tuyenbayev, D. Ugolini, C. S. Unnikrishnan, A. L. Urban, S. A. Usman, H. Vahlbruch, G. Vajente, G. Valdes, M. Vallisneri, N. van Bakel, M. van Beuzekom, J. F. J. van den Brand, C. Van Den Broeck, D. C. Vander-Hyde, L. van der Schaaf, J. V. van Heijningen, A. A. van Veggel, M. Vardaro, S. Vass, M. Vasúth, R. Vaulin, A. Vecchio, G. Vedovato, J. Veitch, P. J. Veitch, K. Venkateswara, D. Verkindt, F. Vetrano, A. Viceré, S. Vinciguerra, D. J. Vine, J. Y. Vinet, S. Vitale, T. Vo, H. Vocca, C. Vorvick, D. Voss, W. D. Vousden, S. P. Vyatchanin, A. R. Wade, L. E. Wade, M. Wade, S. J. Waldman, M. Walker, L. Wallace, S. Walsh, G. Wang, H. Wang, M. Wang, X. Wang, Y. Wang, H. Ward, R. L. Ward, J. Warner, M. Was, B. Weaver, L. W. Wei, M. Weinert, A. J. Weinstein, R. Weiss, T. Welborn, L. Wen, P. Weßels, T. Westphal, K. Wette, J. T. Whelan, S. E. Whitcomb, D. J. White, B. F. Whiting, K. Wiesner, C. Wilkinson, P. A. Willems, L. Williams, R. D. Williams, A. R. Williamson, J. L. Willis, B. Willke, M. H. Wimmer, L. Winkelmann, W. Winkler, C. C. Wipf, A. G. Wiseman, H. Wittel, G. Woan, J. Worden, J. L. Wright, G. Wu, J. Yablon, I. Yakushin, W. Yam, H. Yamamoto, C. C. Yancey, M. J. Yap, H. Yu, M. Yvert, A. ZadroŻny, L. Zangrando, M. Zanolin, J. P. Zendri, M. Zevin, F. Zhang, L. Zhang, M. Zhang, Y. Zhang, C. Zhao, M. Zhou, Z. Zhou, X. J. Zhu, M. E. Zucker, S. E. Zuraw, J. Zweizig, LIGO Scientific Collaboration, and Virgo Collaboration. Observation of Gravitational Waves from a Binary Black Hole Merger. *Phys. Rev. Lett*, 116:061102, Feb. 2016.

B. P. Abbott, R. Abbott, T. D. Abbott, F. Acernese, K. Ackley, C. Adams, T. Adams, P. Addesso, R. X. Adhikari, V. B. Adya, C. Affeldt, M. Afrough, B. Agarwal, M. Agathos, K. Agatsuma, N. Aggarwal, O. D. Aguiar, L. Aiello, A. Ain, P. Ajith, B. Allen, G. Allen, A. Allocca, P. A. Altin, A. Amato, A. Ananyeva, S. B. Anderson, W. G. Anderson, S. V. Angelova, S. Antier, S. Appert, K. Arai, M. C. Araya, J. S. Areeda, N. Arnaud, K. G. Arun, S. Ascenzi, G. Ashton, M. Ast, S. M. Aston, P. Astone, D. V. Atallah, P. Aufmuth, C. Aulbert, K. AultONeal, C. Austin, A. Avila-Alvarez, S. Babak, P. Bacon, M. K. M. Bader, S. Bae, P. T. Baker, F. Baldaccini, G. Ballardin, S. W. Ballmer, S. Banagiri, J. C. Barayoga, S. E. Barclay, B. C. Barish, D. Barker, K. Barkett, F. Barone, B. Barr, L. Barsotti, M. Barsuglia, D. Barta, S. D. Barthelmy, J. Bartlett, I. Bartos, R. Bassiri, A. Basti, J. C. Batch, M. Bawaj, J. C. Bayley, M. Bazzan, B. Bécsy, C. Beer, M. Bejger, I. Belahcene, A. S. Bell, B. K. Berger, G. Bergmann, J. J. Bero, C. P. L. Berry, D. Bersanetti, A. Bertolini, J. Betzwieser, S. Bhagwat, R. Bhandare, I. A. Bilenko, G. Billingsley, C. R. Billman, J. Birch, R. Birney, O. Birnholtz, S. Biscans, S. Biscoveanu, A. Bisht, M. Bitossi, C. Biwer, M. A. Bizouard, J. K. Blackburn, J. Blackman, C. D. Blair, D. G. Blair, R. M. Blair, S. Bloemen, O. Bock, N. Bode, M. Boer, G. Bogaert, A. Bohe, F. Bondu, E. Bonilla, R. Bonnand, B. A. Boom, R. Bork, V. Boschi, S. Bose, K. Bossie, Y. Bouffanais, A. Bozzi, C. Bradaschia, P. R. Brady, M. Branchesi, J. E. Brau, T. Briant, A. Brillet, M. Brinkmann, V. Brisson, P. Brockill, J. E. Broida, A. F. Brooks, D. A. Brown, D. D. Brown, S. Brunett, C. C. Buchanan, A. Buikema, T. Bulik, H. J. Bulten, A. Buonanno, D. Buskulic, C. Buy, R. L. Byer, M. Cabero, L. Cadonati, G. Cagnoli, C. Cahillane, J. Calderón Bustillo, T. A. Callister, E. Calloni, J. B. Camp, M. Canepa, P. Canizares, K. C. Cannon, H. Cao, J. Cao, C. D. Capano, E. Capocasa, F. Carbognani, S. Caride, M. F. Carney, J. Casanueva Diaz, C. Casentini, S. Caudill, M. Cavaglià, F. Cavalier, R. Cavalieri, G. Cella, C. B. Cepeda, P. Cerdá-Durán, G. Cerretani, E. Cesarini, S. J. Chamberlin, M. Chan, S. Chao, P. Charlton, E. Chase, E. Chassande-Mottin, D. Chatterjee, K. Chatziioannou, B. D. Cheeseboro, H. Y. Chen, X. Chen, Y. Chen, H. P. Cheng, H. Chia, A. Chincarini, A. Chiummo,

T. Chmiel, H. S. Cho, M. Cho, J. H. Chow, N. Christensen, Q. Chu, A. J. K. Chua, S. Chua, A. K. W. Chung, S. Chung, G. Ciani, R. Ciolfi, C. E. Cirelli, A. Cirone, F. Clara, J. A. Clark, P. Clearwater, F. Cleva, C. Cocchieri, E. Coccia, P. F. Cohadon, D. Cohen, A. Colla, C. G. Collette, L. R. Cominsky, M. Constancio, L. Conti, S. J. Cooper, P. Corban, T. R. Corbitt, I. Cordero-Carrión, K. R. Corley, N. Cornish, A. Corsi, S. Cortese, C. A. Costa, M. W. Coughlin, S. B. Coughlin, J. P. Coulon, S. T. Countryman, P. Couvares, P. B. Covas, E. E. Cowan, D. M. Coward, M. J. Cowart, D. C. Coyne, R. Coyne, J. D. E. Creighton, T. D. Creighton, J. Cripe, S. G. Crowder, T. J. Cullen, A. Cumming, L. Cunningham, E. Cuoco, T. Dal Canton, G. Dálya, S. L. Danilishin, S. D'Antonio, K. Danzmann, A. Dasgupta, C. F. Da Silva Costa, V. Dattilo, I. Dave, M. Davier, D. Davis, E. J. Daw, B. Day, S. De, D. DeBra, J. Degallaix, M. De Laurentis, S. Deléglise, W. Del Pozzo, N. Demos, T. Denker, T. Dent, R. De Pietri, V. Dergachev, R. De Rosa, R. T. DeRosa, C. De Rossi, R. DeSalvo, O. de Varona, J. Devenson, S. Dhurandhar, M. C. Díaz, L. Di Fiore, M. Di Giovanni, T. Di Girolamo, A. Di Lieto, S. Di Pace, I. Di Palma, F. Di Renzo, Z. Doctor, V. Dolique, F. Donovan, K. L. Dooley, S. Doravari, I. Dorrington, R. Douglas, M. Dovale Álvarez, T. P. Downes, M. Drago, C. Dreissigacker, J. C. Driggers, Z. Du, M. Ducrot, P. Dupej, S. E. Dwyer, T. B. Edo, M. C. Edwards, A. Effler, H. B. Eggenstein, P. Ehrens, J. Eichholz, S. S. Eikenberry, R. A. Eisenstein, R. C. Essick, D. Estevez, Z. B. Etienne, T. Etzel, M. Evans, T. M. Evans, M. Factourovich, V. Fafone, H. Fair, S. Fairhurst, X. Fan, S. Farinon, B. Farr, W. M. Farr, E. J. Fauchon-Jones, M. Favata, M. Fays, C. Fee, H. Fehrmann, J. Feicht, M. M. Fejer, A. Fernandez-Galiana, I. Ferrante, E. C. Ferreira, F. Ferrini, F. Fidecaro, D. Finstad, I. Fiori, D. Fiorucci, M. Fishbach, R. P. Fisher, M. Fitz-Axen, R. Flaminio, M. Fletcher, H. Fong, J. A. Font, P. W. F. Forsyth, S. S. Forsyth, J. D. Fournier, S. Frasca, F. Frasconi, Z. Frei, A. Freise, R. Frey, V. Frey, E. M. Fries, P. Fritschel, V. V. Frolov, P. Fulda, M. Fyffe, H. Gabbard, B. U. Gadre, S. M. Gaebel, J. R. Gair, L. Gammaitoni, M. R. Ganija, S. G. Gaonkar, C. Garcia-Quiros, F. Garufi, B. Gateley, S. Gaudio, G. Gaur, V. Gayathri, N. Gehrels, G. Gemme, E. Genin, A. Gennai, D. George, J. George, L. Gergely, V. Germain, S. Ghonge, A. Ghosh, A. Ghosh, S. Ghosh, J. A. Giaime, K. D. Giardina, A. Giazotto, K. Gill, L. Glover, E. Goetz, R. Goetz, S. Gomes, B. Goncharov, G. González, J. M. Gonzalez Castro, A. Gopakumar, M. L. Gorodetsky, S. E. Gossan, M. Gosselin, R. Gouaty, A. Grado, C. Graef, M. Granata, A. Grant, S. Gras, C. Gray, G. Greco, A. C. Green, E. M. Gretarsson, P. Groot, H. Grote, S. Grunewald, P. Gruning, G. M. Guidi, X. Guo, A. Gupta, M. K. Gupta, K. E. Gushwa, E. K. Gustafson, R. Gustafson, O. Halim, B. R. Hall, E. D. Hall, E. Z. Hamilton, G. Hammond, M. Haney, M. M. Hanke, J. Hanks, C. Hanna, M. D. Hannam, O. A. Hannuksela, J. Hanson, T. Hardwick, J. Harms, G. M. Harry, I. W. Harry, M. J. Hart, C. J. Haster, K. Haughian, J. Healy, A. Heidmann, M. C. Heintze, H. Heitmann, P. Hello, G. Hemming, M. Hendry, I. S. Heng, J. Hennig, A. W. Heptonstall, M. Heurs, S. Hild, T. Hinderer, D. Hoak, D. Hofman, K. Holt, D. E. Holz, P. Hopkins, C. Horst, J. Hough, E. A. Houston, E. J. Howell, Y. M. Hu, E. A. Huerta, D. Huet, B. Hughey, S. Husa, S. H. Huttner, T. Huynh-Dinh, N. Indik, R. Inta, G. Intini, H. N. Isa, J. M. Isac, M. Isi, B. R. Iyer, K. Izumi, T. Jacqmin, K. Jani, P. Jaranowski, S. Jawahar, F. Jiménez-Forteza, W. W. Johnson, N. K. Johnson-McDaniel, D. I. Jones, R. Jones, R. J. G. Jonker, L. Ju, J. Junker, C. V. Kalaghatgi, V. Kalogera, B. Kamai, S. Kandhasamy, G. Kang, J. B. Kanner, S. J. Kapadia, S. Karki, K. S. Karvinen, M. Kasprzack, M. Katolik, E. Katsavounidis, W. Katzman, S. Kaufer, K. Kawabe, F. Kéfélian, D. Keitel, A. J. Kemball, R. Kennedy, C. Kent, J. S. Key, F. Y. Khalili, I. Khan, S. Khan, Z. Khan, E. A. Khazanov, N. Kijbunchoo, C. Kim, J. C. Kim, K. Kim, W. Kim,

W. S. Kim, Y. M. Kim, S. J. Kimbrell, E. J. King, P. J. King, M. Kinley-Hanlon, R. Kirchhoff, J. S. Kissel, L. Kleybolte, S. Klimenko, T. D. Knowles, P. Koch, S. M. Koehlenbeck, S. Koley, V. Kondrashov, A. Kontos, M. Korobko, W. Z. Korth, I. Kowalska, D. B. Kozak, C. Krämer, V. Kringel, B. Krishnan, A. Królak, G. Kuehn, P. Kumar, R. Kumar, S. Kumar, L. Kuo, A. Kutynia, S. Kwang, B. D. Lackey, K. H. Lai, M. Landry, R. N. Lang, J. Lange, B. Lantz, R. K. Lanza, A. Lartaux-Vollard, P. D. Lasky, M. Laxen, A. Lazzarini, C. Lazzaro, P. Leaci, S. Leavey, C. H. Lee, H. K. Lee, H. M. Lee, H. W. Lee, K. Lee, J. Lehmann, A. Lenon, M. Leonardi, N. Leroy, N. Letendre, Y. Levin, T. G. F. Li, S. D. Linker, T. B. Littenberg, J. Liu, R. K. L. Lo, N. A. Lockerbie, L. T. London, J. E. Lord, M. Lorenzini, V. Loriette, M. Lormand, G. Losurdo, J. D. Lough, C. O. Lousto, G. Lovelace, H. Lück, D. Lumaca, A. P. Lundgren, R. Lynch, Y. Ma, R. Macas, S. Macfoy, B. Machenschalk, M. MacInnis, D. M. Macleod, I. Magaña Hernandez, F. Magaña-Sandoval, L. Magaña Zertuche, R. M. Magee, E. Majorana, I. Maksimovic, N. Man, V. Mandic, V. Mangano, G. L. Mansell, M. Manske, M. Mantovani, F. Marchesoni, F. Marion, S. Márka, Z. Márka, C. Markakis, A. S. Markosyan, A. Markowitz, E. Maros, A. Marquina, P. Marsh, F. Martelli, L. Martellini, I. W. Martin, R. M. Martin, D. V. Martynov, K. Mason, E. Massera, A. Masserot, T. J. Massinger, M. Masso-Reid, S. Mastrogiovanni, A. Matas, F. Matichard, L. Matone, N. Mavalvala, N. Mazumder, R. McCarthy, D. E. McClelland, S. McCormick, L. McCuller, S. C. McGuire, G. McIntyre, J. McIver, D. J. McManus, L. McNeill, T. McRae, S. T. McWilliams, D. Meacher, G. D. Meadors, M. Mehmet, J. Meidam, E. Mejuto-Villa, A. Melatos, G. Mendell, R. A. Mercer, E. L. Merilh, M. Merzougui, S. Meshkov, C. Messenger, C. Messick, R. Metzdorff, P. M. Meyers, H. Miao, C. Michel, H. Middleton, E. E. Mikhailov, L. Milano, A. L. Miller, B. B. Miller, J. Miller, M. Millhouse, M. C. Milovich-Goff, O. Minazzoli, Y. Minenkov, J. Ming, C. Mishra, S. Mitra, V. P. Mitrofanov, G. Mitselmakher, R. Mittleman, D. Moffa, A. Moggi, K. Mogushi, M. Mohan, S. R. P. Mohapatra, M. Montani, C. J. Moore, D. Moraru, G. Moreno, S. Morisaki, S. R. Morriss, B. Mours, C. M. Mow-Lowry, G. Mueller, A. W. Muir, A. Mukherjee, D. Mukherjee, S. Mukherjee, N. Mukund, A. Mullavey, J. Munch, E. A. Muñiz, M. Muratore, P. G. Murray, K. Napier, I. Nardecchia, L. Naticchioni, R. K. Nayak, J. Neilson, G. Nelemans, T. J. N. Nelson, M. Nery, A. Neunzert, L. Nevin, J. M. Newport, G. Newton, K. K. Y. Ng, T. T. Nguyen, D. Nichols, A. B. Nielsen, S. Nissanke, A. Nitz, A. Noack, F. Nocera, D. Nolting, C. North, L. K. Nuttall, J. Oberling, G. D. O'Dea, G. H. Ogin, J. J. Oh, S. H. Oh, F. Ohme, M. A. Okada, M. Oliver, P. Oppermann, R. J. Oram, B. O'Reilly, R. Ormiston, L. F. Ortega, R. O'Shaughnessy, S. Ossokine, D. J. Ottaway, H. Overmier, B. J. Owen, A. E. Pace, J. Page, M. A. Page, A. Pai, S. A. Pai, J. R. Palamos, O. Palashov, C. Palomba, A. Pal-Singh, H. Pan, H.-W. Pan, B. Pang, P. T. H. Pang, C. Pankow, F. Pannarale, B. C. Pant, F. Paoletti, A. Paoli, M. A. Papa, A. Parida, W. Parker, D. Pascucci, A. Pasqualetti, R. Passaquieti, D. Passuello, M. Patil, B. Patricelli, B. L. Pearlstone, M. Pedraza, R. Pedurand, L. Pekowsky, A. Pele, S. Penn, C. J. Perez, A. Perreca, L. M. Perri, H. P. Pfeiffer, M. Phelps, O. J. Piccinni, M. Pichot, F. Piergiovanni, V. Pierro, G. Pillant, L. Pinard, I. M. Pinto, M. Pirello, M. Pitkin, M. Poe, R. Poggiani, P. Popolizio, E. K. Porter, A. Post, J. Powell, J. Prasad, J. W. W. Pratt, G. Pratten, V. Predoi, T. Prestegard, M. Prijatelj, M. Principe, S. Privitera, R. Prix, G. A. Prodi, L. G. Prokhorov, O. Puncken, M. Punturo, P. Puppo, M. Pürrer, H. Qi, V. Quetschke, E. A. Quintero, R. Quitzow-James, F. J. Raab, D. S. Rabeling, H. Radkins, P. Raffai, S. Raja, C. Rajan, B. Rajbhandari, M. Rakhmanov, K. E. Ramirez, A. Ramos-Buades, P. Rapagnani, V. Raymond, M. Razzano, J. Read, T. Regimbau, L. Rei, S. Reid, D. H. Reitze, W. Ren, S. D. Reyes,

F. Ricci, P. M. Ricker, S. Rieger, K. Riles, M. Rizzo, N. A. Robertson, R. Robie, F. Robinet, A. Rocchi, L. Rolland, J. G. Rollins, V. J. Roma, J. D. Romano, R. Romano, C. L. Romel, J. H. Romie, D. Rosińska, M. P. Ross, S. Rowan, A. Rüdiger, P. Ruggi, G. Rutins, K. Ryan, S. Sachdev, T. Sadecki, L. Sadeghian, M. Sakellariadou, L. Salconi, M. Saleem, F. Salemi, A. Samajdar, L. Sammut, L. M. Sampson, E. J. Sanchez, L. E. Sanchez, N. Sanchis-Gual, V. Sandberg, J. R. Sanders, B. Sassolas, B. S. Sathyaprakash, P. R. Saulson, O. Sauter, R. L. Savage, A. Sawadsky, P. Schale, M. Scheel, J. Scheuer, J. Schmidt, P. Schmidt, R. Schnabel, R. M. S. Schofield, A. Schönbeck, E. Schreiber, D. Schuette, B. W. Schulte, B. F. Schutz, S. G. Schwalbe, J. Scott, S. M. Scott, E. Seidel, D. Sellers, A. S. Sengupta, D. Sentenac, V. Sequino, A. Sergeev, D. A. Shaddock, T. J. Shaffer, A. A. Shah, M. S. Shahriar, M. B. Shaner, L. Shao, B. Shapiro, P. Shawhan, A. Sheperd, D. H. Shoemaker, D. M. Shoemaker, K. Siellez, X. Siemens, M. Sieniawska, D. Sigg, A. D. Silva, L. P. Singer, A. Singh, A. Singhal, A. M. Sintes, B. J. J. Slagmolen, B. Smith, J. R. Smith, R. J. E. Smith, S. Somala, E. J. Son, J. A. Sonnenberg, B. Sorazu, F. Sorrentino, T. Souradeep, A. P. Spencer, A. K. Srivastava, K. Staats, A. Staley, M. Steinke, J. Steinlechner, S. Steinlechner, D. Steinmeyer, S. P. Stevenson, R. Stone, D. J. Stops, K. A. Strain, G. Stratta, S. E. Strigin, A. Strunk, R. Sturani, A. L. Stuver, T. Z. Summerscales, L. Sun, S. Sunil, J. Suresh, P. J. Sutton, B. L. Swinkels, M. J. Szczepańczyk, M. Tacca, S. C. Tait, C. Talbot, D. Talukder, D. B. Tanner, M. Tápai, A. Taracchini, J. D. Tasson, J. A. Taylor, R. Taylor, S. V. Tewari, T. Theeg, F. Thies, E. G. Thomas, M. Thomas, P. Thomas, K. A. Thorne, E. Thrane, S. Tiwari, V. Tiwari, K. V. Tokmakov, K. Toland, M. Tonelli, Z. Tornasi, A. Torres-Forné, C. I. Torrie, D. Töyrä, F. Travasso, G. Traylor, J. Trinastic, M. C. Tringali, L. Trozzo, K. W. Tsang, M. Tse, R. Tso, L. Tsukada, D. Tsuna, D. Tuyenbayev, K. Ueno, D. Ugolini, C. S. Unnikrishnan, A. L. Urban, S. A. Usman, H. Vahlbruch, G. Vajente, G. Valdes, M. Vallisneri, N. van Bakel, M. van Beuzekom, J. F. J. van den Brand, C. Van Den Broeck, D. C. Vander-Hyde, L. van der Schaaf, J. V. van Heijningen, A. A. van Veggel, M. Vardaro, V. Varma, S. Vass, M. Vasúth, A. Vecchio, G. Vedovato, J. Veitch, P. J. Veitch, K. Venkateswara, G. Venugopalan, D. Verkindt, F. Vetrano, A. Viceré, A. D. Viets, S. Vinciguerra, D. J. Vine, J. Y. Vinet, S. Vitale, T. Vo, H. Vocca, C. Vorvick, S. P. Vyatchanin, A. R. Wade, L. E. Wade, M. Wade, R. Walet, M. Walker, L. Wallace, S. Walsh, G. Wang, H. Wang, J. Z. Wang, W. H. Wang, Y. F. Wang, R. L. Ward, J. Warner, M. Was, J. Watchi, B. Weaver, L. W. Wei, M. Weinert, A. J. Weinstein, R. Weiss, L. Wen, E. K. Wessel, P. Weßels, J. Westerweck, T. Westphal, K. Wette, J. T. Whelan, S. E. Whitcomb, B. F. Whiting, C. Whittle, D. Wilken, D. Williams, R. D. Williams, A. R. Williamson, J. L. Willis, B. Willke, M. H. Wimmer, W. Winkler, C. C. Wipf, H. Wittel, G. Woan, J. Woehler, J. Wofford, K. W. K. Wong, J. Worden, J. L. Wright, D. S. Wu, D. M. Wysocki, S. Xiao, H. Yamamoto, C. C. Yancey, L. Yang, M. J. Yap, M. Yazback, H. Yu, H. Yu, M. Yvert, A. ZadroŻny, M. Zanolin, T. Zelenova, J. P. Zendri, M. Zevin, L. Zhang, M. Zhang, T. Zhang, Y. H. Zhang, C. Zhao, M. Zhou, Z. Zhou, S. J. Zhu, X. J. Zhu, A. B. Zimmerman, M. E. Zucker, J. Zweizig, LIGO Scientific Collaboration, and Virgo Collaboration. GW170814: A Three-Detector Observation of Gravitational Waves from a Binary Black Hole Coalescence. *Phys. Rev. Lett*, 119:141101, Oct. 2017.

Z. Abdurashidova, J. E. Aguirre, P. Alexander, Z. S. Ali, Y. Balfour, R. Barkana, A. P. Beardsley, G. Bernardi, T. S. Billings, J. D. Bowman, R. F. Bradley, P. Bull, J. Burba, S. Carey, C. L. Carilli, C. Cheng, D. R. DeBoer, M. Dexter, E. de Lera Acedo, J. S. Dillon, J. Ely, A. Ewall-Wice,

N. Fagnoni, A. Fialkov, R. Fritz, S. R. Furlanetto, K. Gale-Sides, B. Glendenning, D. Gorthi, B. Greig, J. Grobbelaar, Z. Halday, B. J. Hazelton, S. Heimersheim, J. N. Hewitt, J. Hickish, D. C. Jacobs, A. Julius, N. S. Kern, J. Kerrigan, P. Kittiwisit, S. A. Kohn, M. Kolopanis, A. Lanman, P. La Plante, T. Lekalake, D. Lewis, A. Liu, Y.-Z. Ma, D. MacMahon, L. Malan, C. Malgas, M. Maree, Z. E. Martinot, E. Matsetela, A. Mesinger, J. Mirocha, M. Molewa, M. F. Morales, T. Mosiane, J. B. Muñoz, S. G. Murray, A. R. Neben, B. Nikolic, C. D. Nunhokee, A. R. Parsons, N. Patra, S. Pieterse, J. C. Pober, Y. Qin, N. Razavi-Ghods, I. Reis, J. Ringuette, J. Robnett, K. Rosie, M. G. Santos, S. Sikder, P. Sims, C. Smith, A. Syce, N. Thyagarajan, P. K. G. Williams, and H. Zheng. HERA Phase I Limits on the Cosmic 21 cm Signal: Constraints on Astrophysics and Cosmology during the Epoch of Reionization. *ApJ*, 924:51, Jan. 2022.

M. Abe, H. Yajima, S. Khochfar, C. Dalla Vecchia, and K. Omukai. Formation of the first galaxies in the aftermath of the first supernovae. *MNRAS*, 508:3226–3238, Dec. 2021.

T. Abel, G. L. Bryan, and M. L. Norman. The Formation of the First Star in the Universe. *Science*, 295:93–98, Jan. 2002.

K. Ahn, H. Xu, M. L. Norman, M. A. Alvarez, and J. H. Wise. Spatially Extended 21 cm Signal from Strongly Clustered Uv and X-Ray Sources in the Early Universe. *ApJ*, 802:8, Mar. 2015.

P. J. Armitage and P. Natarajan. Accretion during the Merger of Supermassive Black Holes. *ApJ*, 567:L9–L12, Mar. 2002.

M. Asplund, N. Grevesse, A. J. Sauval, and P. Scott. The Chemical Composition of the Sun. *ARA&A*, 47:481–522, Sept. 2009.

M. R. Bate. Predicting the properties of binary stellar systems: the evolution of accreting protobinary systems. *MNRAS*, 314:33–53, May 2000.

M. C. Begelman, M. Volonteri, and M. J. Rees. Formation of supermassive black holes by direct collapse in pre-galactic haloes. *MNRAS*, 370:289–298, July 2006.

P. S. Behroozi, R. H. Wechsler, and H.-Y. Wu. The ROCKSTAR Phase-space Temporal Halo Finder and the Velocity Offsets of Cluster Cores. *ApJ*, 762:109, Jan. 2013.

A. Bleuler and R. Teyssier. Towards a more realistic sink particle algorithm for the RAMSES CODE. *MNRAS*, 445:4015–4036, Dec. 2014.

A. Bleuler, R. Teyssier, S. Carassou, and D. Martizzi. PHEW: a parallel segmentation algorithm for three-dimensional AMR datasets. Application to structure detection in self-gravitating flows. *ComAC*, 2:5, June 2015.

H. Bondi. On spherically symmetrical accretion. *MNRAS*, 112:195, Jan. 1952.

H. Bondi and F. Hoyle. On the mechanism of accretion by stars. *MNRAS*, 104:273, Jan. 1944.

W. B. Bonnor. Boyle's Law and gravitational instability. *MNRAS*, 116:351, Jan. 1956.

R. J. Bouwens, M. Stefanon, P. A. Oesch, G. D. Illingworth, T. Nanayakkara, G. Roberts-Borsani, I. Labbé, and R. Smit. Newly Discovered Bright z $\sim$ 9-10 Galaxies and Improved Constraints on Their Prevalence Using the Full CANDELS Area. *ApJ*, 880:25, July 2019.

V. Bromm. Formation of the first stars. *Rep. Prog. Phys.*, 76:112901, Nov. 2013.

V. Bromm and A. Loeb. Formation of the First Supermassive Black Holes. *ApJ*, 596:34–46, Oct. 2003.

V. Bromm and N. Yoshida. The First Galaxies. *ARA&A*, 49:373–407, Sept. 2011.

V. Bromm, R. P. Kudritzki, and A. Loeb. Generic Spectrum and Ionization Efficiency of a Heavy Initial Mass Function for the First Stars. *ApJ*, 552:464–472, May 2001.

V. Bromm, P. S. Coppi, and R. B. Larson. The Formation of the First Stars. I. The Primordial Star-forming Cloud. *ApJ*, 564:23–51, Jan. 2002.

G. Bruzual and S. Charlot. Stellar population synthesis at the resolution of 2003. *MNRAS*, 344: 1000–1028, Oct. 2003. ADS Bibcode: 2003MNRAS.344.1000B.

G. Chabrier. Galactic Stellar and Substellar Initial Mass Function. *PASP*, 115:763–795, July 2003.

P. Chang, L. E. Strubbe, K. Menou, and E. Quataert. Fossil gas and the electromagnetic precursor of supermassive binary black hole mergers. *MNRAS*, 407:2007–2016, Sept. 2010.

G. Chiaki and J. H. Wise. Triggered Population III star formation: the effect of H2 self-shielding. *MNRAS*, Feb. 2023.

G. Chiaki, H. Susa, and S. Hirano. Metal-poor star formation triggered by the feedback effects from Pop III stars. *MNRAS*, 475:4378–4395, Apr. 2018.

S. Chon and T. Hosokawa. Forming Pop III binaries in self-gravitating discs: how to keep the orbital angular momentum. *MNRAS*, 488:2658–2672, Sept. 2019.

S. Chon, S. Hirano, T. Hosokawa, and N. Yoshida. Cosmological Simulations of Early Black Hole Formation: Halo Mergers, Tidal Disruption, and the Conditions for Direct Collapse. *ApJ*, 832:134, Dec. 2016.

S. Chon, K. Omukai, and R. Schneider. Transition of the initial mass function in the metal-poor environments. *MNRAS*, 508:4175–4192, Dec. 2021.

P. C. Clark, S. C. O. Glover, R. S. Klessen, and V. Bromm. Gravitational Fragmentation in Turbulent Primordial Gas and the Initial Mass Function of Population III Stars. *ApJ*, 727:110, Feb. 2011a.

P. C. Clark, S. C. O. Glover, R. J. Smith, T. H. Greif, R. S. Klessen, and V. Bromm. The Formation and Fragmentation of Disks Around Primordial Protostars. *Science*, 331:1040, Feb. 2011b.

B. Commerçon, M. González, R. Mignon-Risse, P. Hennebelle, and N. Vaytet. Discs and outflows in the early phases of massive star formation: Influence of magnetic fields and ambipolar diffusion. *A&A*, 658:A52, Feb. 2022.

T. J. Cox, P. Jonsson, R. S. Somerville, J. R. Primack, and A. Dekel. The effect of galaxy mass ratio on merger-driven starbursts. *MNRAS*, 384:386–409, Feb. 2008.

A. Crida, A. Morbidelli, and F. Masset. On the width and shape of gaps in protoplanetary disks. *Icarus*, 181:587–604, Apr. 2006.

E. Curtis-Lake, S. Carniani, A. Cameron, S. Charlot, P. Jakobsen, R. Maiolino, A. Bunker, J. Witstok, R. Smit, J. Chevallard, C. Willott, P. Ferruit, S. Arribas, N. Bonaventura, M. Curti, F. D'Eugenio, M. Franx, G. Giardino, T. J. Looser, N. Lützgendorf, M. V. Maseda, T. Rawle, H.-W. Rix, B. Rodríguez del Pino, H. Übler, M. Sirianni, A. Dressler, E. Egami, D. J. Eisenstein, R. Endsley, K. Hainline, R. Hausen, B. D. Johnson, M. Rieke, B. Robertson, I. Shivaei, D. P. Stark, S. Tacchella, C. C. Williams, C. N. A. Willmer, R. Bhatawdekar, R. Bowler, K. Boyett, Z. Chen, A. de Graaff, J. M. Helton, R. E. Hviding, G. C. Jones, N. Kumari, J. Lyu, E. Nelson, M. Perna, L. Sandles, A. Saxena, K. A. Suess, F. Sun, M. W. Topping, I. E. B. Wallace, and L. Whitler. Spectroscopic confirmation of four metal-poor galaxies at z = 10.3-13.2. *Nature Astronomy*, 7:622–632, May 2023.

L. del Valle and M. Volonteri. The effect of AGN feedback on the migration time-scale of supermassive black holes binaries. *MNRAS*, 480:439–450, Oct. 2018.

A. M. Dempsey, D. Muñoz, and Y. Lithwick. Inner Boundary Condition in Quasi-Lagrangian Simulations of Accretion Disks. *ApJ*, 892:L29, Apr. 2020.

A. M. Dempsey, D. J. Muñoz, and Y. Lithwick. Outward Migration of Super-Jupiters. *ApJ*, 918: L36, Sept. 2021.

J. M. Diego. The Universe at extreme magnification. *A&A*, 625:A84, May 2019.

B. Diemer. COLOSSUS: A Python Toolkit for Cosmology, Large-scale Structure, and Dark Matter Halos. *ApJS*, 239:35, Dec. 2018.

A. J. Dittmann and G. Ryan. Preventing Anomalous Torques in Circumbinary Accretion Simulations. *ApJ*, 921:71, Nov. 2021.

A. J. Dittmann and G. Ryan. A survey of disc thickness and viscosity in circumbinary accretion: Binary evolution, variability, and disc morphology. *MNRAS*, 513:6158–6176, July 2022.

A. J. Dittmann and G. Ryan. The Evolution of Accreting Binaries: from Brown Dwarfs to Supermassive Black Holes, Oct. 2023. Publication Title: arXiv e-prints ADS Bibcode: 2023arXiv231007758D.

D. J. D'Orazio and P. C. Duffell. Orbital Evolution of Equal-mass Eccentric Binaries due to a Gas Disk: Eccentric Inspirals and Circular Outspirals. *ApJ*, 914:L21, June 2021.

B. T. Draine. *Physics of the Interstellar and Intergalactic Medium*. Princeton Univ. Press, Jan. 2011.

B. T. Draine and F. Bertoldi. Structure of Stationary Photodissociation Fronts. *ApJ*, 468:269, Sept. 1996.

P. C. Duffell, D. D'Orazio, A. Derdzinski, Z. Haiman, A. MacFadyen, A. L. Rosen, and J. Zrake. Circumbinary Disks: Accretion and Torque as a Function of Mass Ratio and Disk Viscosity. *ApJ*, 901:25, Sept. 2020.

R. Ebert. Über die Verdichtung von H I-Gebieten. Mit 5 Textabbildungen. *Z. Astrophys.*, 37:217, Jan. 1955.

A. Escala, R. B. Larson, P. S. Coppi, and D. Mardones. The Role of Gas in the Merging of Massive Black Holes in Galactic Nuclei. II. Black Hole Merging in a Nuclear Gas Disk. *ApJ*, 630:152–166, Sept. 2005.

X. Fan, M. A. Strauss, R. H. Becker, R. L. White, J. E. Gunn, G. R. Knapp, G. T. Richards, D. P. Schneider, J. Brinkmann, and M. Fukugita. Constraining the Evolution of the Ionizing Background and the Epoch of Reionization with z˜6 Quasars. II. A Sample of 19 Quasars. *ApJ*, 132, July 2006.

B. D. Farris, P. Duffell, A. I. MacFadyen, and Z. Haiman. Binary Black Hole Accretion from a Circumbinary Disk: Gas Dynamics inside the Central Cavity. *ApJ*, 783:134, Mar. 2014.

S. L. Finkelstein, M. Bagley, M. Song, R. Larson, C. Papovich, M. Dickinson, K. D. Finkelstein, A. M. Koekemoer, N. Pirzkal, R. S. Somerville, L. Y. A. Yung, P. Behroozi, H. Ferguson, M. Giavalisco, N. Grogin, N. Hathi, T. A. Hutchison, I. Jung, D. Kocevski, L. Kawinwanichakij, S. Rojas-Ruiz, R. Ryan, G. F. Snyder, and S. Tacchella. A Census of the Bright z = 8.5-11 Universe with the Hubble and Spitzer Space Telescopes in the CANDELS Fields. *ApJ*, 928:52, Mar. 2022.

S. L. Finkelstein, M. B. Bagley, H. C. Ferguson, S. M. Wilkins, J. S. Kartaltepe, C. Papovich, L. Y. A. Yung, P. A. Haro, P. Behroozi, M. Dickinson, D. D. Kocevski, A. M. Koekemoer, R. L. Larson, A. Le Bail, A. M. Morales, P. G. Pérez-González, D. Burgarella, R. Davé, M. Hirschmann, R. S. Somerville, S. Wuyts, V. Bromm, C. M. Casey, A. Fontana, S. Fujimoto, J. P. Gardner, M. Giavalisco, A. Grazian, N. A. Grogin, N. P. Hathi, T. A. Hutchison, S. W. Jha, S. Jogee, L. J. Kewley, A. Kirkpatrick, A. S. Long, J. M. Lotz, L. Pentericci, J. D. R. Pierel, N. Pirzkal, S. Ravindranath, R. E. Ryan, J. R. Trump, G. Yang, R. Bhatawdekar, L. Bisigello, V. Buat, A. Calabrò, M. Castellano, N. J. Cleri, M. C. Cooper, D. Croton, E. Daddi, A. Dekel, D. Elbaz, M. Franco, E. Gawiser, B. W. Holwerda, M. Huertas-Company, A. E. Jaskot, G. C. K. Leung, R. A. Lucas, B. Mobasher, V. Pandya, S. Tacchella, B. J. Weiner, and J. A. Zavala. CEERS Key Paper. I. An Early Look into the First 500 Myr of Galaxy Formation with JWST. *ApJ*, 946:L13, Mar. 2023.

R. C. Forrey. Rate of Formation of Hydrogen Molecules by Three-body Recombination during Primordial Star Formation. *ApJ*, 773:L25, Aug. 2013.

S. Fujimoto, B. Wang, J. Weaver, V. Kokorev, H. Atek, R. Bezanson, I. Labbe, G. Brammer, J. E. Greene, I. Chemerynska, P. Dayal, A. de Graaff, L. J. Furtak, P. A. Oesch, D. J. Setton, S. H. Price, T. B. Miller, C. C. Williams, K. E. Whitaker, A. Zitrin, S. E. Cutler, J. Leja, R. Pan, D. Coe, P. van Dokkum, R. Feldmann, Y. Fudamoto, A. D. Goulding, G. Khullar, D. Marchesini, M. Maseda, T. Nanayakkara, E. J. Nelson, R. Smit, M. Stefanon, and A. Weibel. UNCOVER: A NIRSpec Census of Lensed Galaxies at z=8.50-13.08 Probing a High AGN Fraction and Ionized Bubbles in the Shadow, Aug. 2023. Publication Title: arXiv e-prints ADS Bibcode: 2023arXiv230811609F.

H. Fukushima, K. Omukai, and T. Hosokawa. Upper stellar mass limit by radiative feedback at low-metallicities: metallicity and accretion rate dependence. *MNRAS*, 473:4754–4772, Feb. 2018.

D. Galli and F. Palla. The Dawn of Chemistry. *ARA&A*, 51(1):163–206, Aug. 2013.

F. A. B. Garcia, M. Ricotti, K. Sugimura, and J. Park. Star cluster formation and survival in the first galaxies. *MNRAS*, 522:2495–2515, June 2023.

S. C. O. Glover. Simulating the formation of massive seed black holes in the early Universe - II. Impact of rate coefficient uncertainties. *MNRAS*, 453:2901–2918, Nov. 2015.

S. C. O. Glover and T. Abel. Uncertainties in H2 and HD chemistry and cooling and their role in early structure formation. *MNRAS*, 388:1627–1651, Aug. 2008.

S. C. O. Glover and P. W. J. L. Brand. Radiative feedback from an early X-ray background. *MNRAS*, 340:210–226, Mar. 2003.

S. C. O. Glover, C. Federrath, M. M. Mac Low, and R. S. Klessen. Modelling CO formation in the turbulent interstellar medium. *MNRAS*, 404:2–29, May 2010.

N. Y. Gnedin. On the Proper Use of the Reduced Speed of Light Approximation. *ApJ*, 833:66, Dec. 2016.

N. Y. Gnedin, K. Tassis, and A. V. Kravtsov. Modeling Molecular Hydrogen and Star Formation in Cosmological Simulations. *ApJ*, 697:55–67, May 2009.

A. Gould and H.-W. Rix. Binary Black Hole Mergers from Planet-like Migrations. *ApJ*, 532: L29–L32, Mar. 2000.

T. H. Greif, S. C. O. Glover, V. Bromm, and R. S. Klessen. The First Galaxies: Chemical Enrichment, Mixing, and Star Formation. *ApJ*, 716:510–520, June 2010.

T. H. Greif, V. Springel, S. D. M. White, S. C. O. Glover, P. C. Clark, R. J. Smith, R. S. Klessen, and V. Bromm. Simulations on a Moving Mesh: The Clustered Formation of Population III Protostars. *ApJ*, 737:75, Aug. 2011.

T. H. Greif, V. Bromm, P. C. Clark, S. C. O. Glover, R. J. Smith, R. S. Klessen, N. Yoshida, and V. Springel. Formation and evolution of primordial protostellar systems. *MNRAS*, 424: 399–415, July 2012.

F. Haardt and P. Madau. Radiative Transfer in a Clumpy Universe. IV. New Synthesis Models of the Cosmic UV/X-Ray Background. *ApJ*, 746:125, Feb. 2012.

O. Hahn and T. Abel. Multi-scale initial conditions for cosmological simulations. *MNRAS*, 415: 2101–2121, Aug. 2011.

Z. Haiman, T. Abel, and M. J. Rees. The Radiative Feedback of the First Cosmological Objects. *ApJ*, 534:11–24, May 2000.

D. Han, T. Kimm, H. Katz, J. Devriendt, and A. Slyz. Impact of Radiation Feedback on the Formation of Globular Cluster Candidates during Cloud-Cloud Collisions. *ApJ*, 935:53, Aug. 2022.

A. Harten, P. D. Lax, and B. v. Leer. On Upstream Differencing and Godunov-Type Schemes for Hyperbolic Conservation Laws. *SIAM Rev*, 25:35–61, Jan. 1983. Publisher: Society for Industrial and Applied Mathematics.

T. Hartwig, M. Volonteri, V. Bromm, R. S. Klessen, E. Barausse, M. Magg, and A. Stacy. Gravitational waves from the remnants of the first stars. *MNRAS*, 460:L74–L78, July 2016.

C.-C. He and M. Ricotti. Massive pre-stellar cores in radiation-magneto-turbulent simulations of molecular clouds. *MNRAS*, 522:5374–5392, July 2023.

C.-C. He, M. Ricotti, and S. Geen. Simulating star clusters across cosmic time - I. Initial mass function, star formation rates, and efficiencies. *MNRAS*, 489:1880–1898, Oct. 2019.

C.-C. He, M. Ricotti, and S. Geen. Simulating star clusters across cosmic time - II. Escape fraction of ionizing photons from molecular clouds. *MNRAS*, 492:4858–4873, Mar. 2020.

R. M. Heath and C. J. Nixon. On the orbital evolution of binaries with circumbinary discs. *A&A*, 641:A64, Sept. 2020.

A. Heger and S. E. Woosley. The Nucleosynthetic Signature of Population III. *ApJ*, 567:532–543, Mar. 2002.

S. Hirano and V. Bromm. Formation and survival of Population III stellar systems. *MNRAS*, 470: 898–914, Sept. 2017.

S. Hirano, T. Hosokawa, N. Yoshida, H. Umeda, K. Omukai, G. Chiaki, and H. W. Yorke. One Hundred First Stars: Protostellar Evolution and the Final Masses. *ApJ*, 781:60, Feb. 2014.

S. Hirano, T. Hosokawa, N. Yoshida, K. Omukai, and H. W. Yorke. Primordial star formation under the influence of far ultraviolet radiation: 1540 cosmological haloes and the stellar mass distribution. *MNRAS*, 448:568–587, Mar. 2015.

D. Hollenbach and C. F. McKee. Molecule formation and infrared emission in fast interstellar shocks. I. Physical processes. *ApJS*, 41:555–592, Nov. 1979.

T. Hosokawa and K. Omukai. Evolution of Massive Protostars with High Accretion Rates. *ApJ*, 691:823–846, Jan. 2009.

T. Hosokawa, H. W. Yorke, and K. Omukai. Evolution of Massive Protostars Via Disk Accretion. *ApJ*, 721:478–492, Sept. 2010.

T. Hosokawa, K. Omukai, N. Yoshida, and H. W. Yorke. Protostellar Feedback Halts the Growth of the First Stars in the Universe. *Science*, 334:1250, Dec. 2011.

T. Hosokawa, K. Omukai, and H. W. Yorke. Rapidly Accreting Supergiant Protostars: Embryos of Supermassive Black Holes? *ApJ*, 756:93, Sept. 2012.

T. Hosokawa, S. Hirano, R. Kuiper, H. W. Yorke, K. Omukai, and N. Yoshida. Formation of Massive Primordial Stars: Intermittent UV Feedback with Episodic Mass Accretion. *ApJ*, 824: 119, June 2016.

J. A. Hummel, A. Stacy, M. Jeon, A. Oliveri, and V. Bromm. The first stars: formation under X-ray feedback. *MNRAS*, 453:4136–4147, Nov. 2015.

K. Inayoshi and Z. Haiman. Does disc fragmentation prevent the formation of supermassive stars in protogalaxies? *MNRAS*, 445:1549–1557, Dec. 2014.

K. Inayoshi and K. Omukai. Effect of cosmic ray/X-ray ionization on supermassive black hole formation. *MNRAS*, 416:2748–2759, Oct. 2011.

K. Inayoshi, E. Visbal, and Z. Haiman. The Assembly of the First Massive Black Holes. *ARA&A*, 58:27–97, Aug. 2020.

O. Jaura, S. C. O. Glover, K. M. J. Wollenberg, R. S. Klessen, S. Geen, and L. Haemmerlé. Trapping of H II regions in Population III star formation. *MNRAS*, 512:116–136, May 2022.

M. Jeon and V. Bromm. Signature of the first galaxies in JWST deep field observations. *MNRAS*, 485:5939–5950, June 2019.

M. Jeon, A. H. Pawlik, T. H. Greif, S. C. O. Glover, V. Bromm, M. Milosavljević, and R. S. Klessen. The First Galaxies: Assembly with Black Hole Feedback. *ApJ*, 754:34, July 2012.

M. Jeon, A. H. Pawlik, V. Bromm, and M. Milosavljević. Radiative feedback from high-mass X-ray binaries on the formation of the first galaxies and early reionization. *MNRAS*, 440: 3778–3796, June 2014a.

M. Jeon, A. H. Pawlik, V. Bromm, and M. Milosavljević. Recovery from Population III supernova explosions and the onset of second-generation star formation. *MNRAS*, pages 3288–3300, Nov. 2014b.

M. Jeon, V. Bromm, A. H. Pawlik, and M. Milosavljević. The first galaxies: simulating their feedback-regulated assembly. *MNRAS*, 452:1152–1170, Sept. 2015.

J. L. Johnson, C. Dalla Vecchia, and S. Khochfar. The First Billion Years project: the impact of stellar radiation on the co-evolution of Populations II and III. *MNRAS*, 428:1857–1872, Jan. 2013.

I. Juodžbalis, C. J. Conselice, M. Singh, N. Adams, K. Ormerod, T. Harvey, D. Austin, M. Volonteri, S. H. Cohen, R. A. Jansen, J. Summers, R. A. Windhorst, J. C. J. D'Silva, A. M. Koekemoer, D. Coe, S. P. Driver, B. Frye, N. A. Grogin, M. A. Marshall, M. Nonino, N. Pirzkal, A. Robotham, R. Russell E., Jr., R. Ortiz, III, S. Tompkins, C. N. A. Willmer, and H. Yan. EPOCHS VII: discovery of high-redshift ($6.5 < z < 12$) AGN candidates in JWST ERO and PEARLS data. *MNRAS*, pages 1353–1364, Oct. 2023.

H. Katz, T. Kimm, D. Sijacki, and M. G. Haehnelt. Interpreting ALMA observations of the ISM during the epoch of reionization. *MNRAS*, 468:4831–4861, July 2017.

H. Katz, T. Kimm, R. S. Ellis, J. Devriendt, and A. Slyz. The challenges of identifying Population III stars in the early Universe. *MNRAS*, 524:351–360, Sept. 2023.

T. Kimm, H. Katz, M. Haehnelt, J. Rosdahl, J. Devriendt, and A. Slyz. Feedback-regulated star formation and escape of LyC photons from mini-haloes during reionization. *MNRAS*, 466: 4826–4846, Apr. 2017.

K. Kimura, T. Hosokawa, and K. Sugimura. Growth of Massive Disks and Early Disk Fragmentation in Primordial Star Formation. *ApJ*, 911:52, Apr. 2021.

M. R. Krumholz. Star Formation in Atomic Gas. *ApJ*, 759:9, Nov. 2012.

D. Lai and D. J. Muñoz. Circumbinary Accretion: From Binary Stars to Massive Binary Black Holes. *ARA&A*, 61:517–560, Aug. 2023.

R. B. Larson. Numerical calculations of the dynamics of collapsing proto-star. *MNRAS*, 145:271, Jan. 1969.

M. A. Latif and D. R. G. Schleicher. Disc fragmentation and the formation of Population III stars. *MNRAS*, 449:77–87, May 2015.

M. A. Latif, S. Zaroubi, and M. Spaans. The impact of Lyman α trapping on the formation of primordial objects. *MNRAS*, 411:1659–1670, Mar. 2011.

M. A. Latif, D. Whalen, and S. Khochfar. The Birth Mass Function of Population III Stars. *ApJ*, 925:28, Jan. 2022.

Y.-P. Li, A. M. Dempsey, H. Li, S. Li, and J. Li. Hot Circumsingle Disks Drive Binary Black Hole Mergers in Active Galactic Nucleus Disks. *ApJ*, 928:L19, Apr. 2022.

A. Lipovka, R. Núñez-López, and V. Avila-Reese. The cooling function of HD molecule revisited. *MNRAS*, 361:850–854, Aug. 2005.

B. Liu and V. Bromm. The Population III Origin of GW190521. *ApJ*, 903:L40, Nov. 2020.

L. A. Lopez, E. Ramirez-Ruiz, D. Huppenkothen, C. Badenes, and D. A. Pooley. Using the X-ray Morphology of Young Supernova Remnants to Constrain Explosion Type, Ejecta Distribution, and Chemical Mixing. *ApJ*, 732:114, May 2011.

W. Lyra, A. Johansen, H. Klahr, and N. Piskunov. Standing on the shoulders of giants. Trojan Earths and vortex trapping in low mass self-gravitating protoplanetary disks of gas and solids. *A&A*, 493:1125–1139, Jan. 2009.

M. E. Machacek, G. L. Bryan, and T. Abel. Effects of a soft X-ray background on structure formation at high redshift. *MNRAS*, 338:273–286, Jan. 2003.

M. N. Machida, K. Omukai, T. Matsumoto, and S.-i. Inutsuka. Conditions for the Formation of First-Star Binaries. *ApJ*, 677:813–827, Apr. 2008.

R. Matsukoba, S. Z. Takahashi, K. Sugimura, and K. Omukai. Gravitational stability and fragmentation condition for discs around accreting supermassive stars. *MNRAS*, 484:2605–2619, Apr. 2019.

C. F. McKee and J. C. Tan. The Formation of the First Stars. II. Radiative Feedback Processes and Implications for the Initial Mass Function. *ApJ*, 681:771–797, July 2008.

E. Michaely and H. B. Perets. Gravitational-wave Sources from Mergers of Binary Black Holes Catalyzed by Flyby Interactions in the Field. *ApJ*, 887:L36, Dec. 2019.

E. Michaely and H. B. Perets. High rate of gravitational waves mergers from flyby perturbations of wide black hole triples in the field. *MNRAS*, 498:4924–4935, Nov. 2020.

I. F. Mirabel, M. Dijkstra, P. Laurent, A. Loeb, and J. R. Pritchard. Stellar black holes at the dawn of the universe. *A&A*, 528:A149, Apr. 2011.

R. Miranda and D. Lai. Tidal truncation of inclined circumstellar and circumbinary discs in young stellar binaries. *MNRAS*, 452:2396–2409, Sept. 2015.

M. Montesinos, J. Garrido-Deutelmoser, J. Olofsson, C. A. Giuppone, J. Cuadra, A. Bayo, M. Sucerquia, and N. Cuello. Dust trapping around Lagrangian points in protoplanetary disks. *A&A*, 642:A224, Oct. 2020.

M. S. L. Moody, J.-M. Shi, and J. M. Stone. Hydrodynamic Torques in Circumbinary Accretion Disks. *ApJ*, 875:66, Apr. 2019.

D. J. Muñoz, R. Miranda, and D. Lai. Hydrodynamics of Circumbinary Accretion: Angular Momentum Transfer and Binary Orbital Evolution. *ApJ*, 871:84, Jan. 2019.

D. J. Muñoz, D. Lai, K. Kratter, and R. Miranda. Circumbinary Accretion from Finite and Infinite Disks. *ApJ*, 889:114, Feb. 2020.

T. Nagakura and K. Omukai. Formation of Population III stars in fossil HII regions: significance of HD. *MNRAS*, 364:1378–1386, Dec. 2005.

D. Nakauchi, K. Inayoshi, and K. Omukai. Conditions for HD cooling in the first galaxies revisited: interplay between far-ultraviolet and cosmic ray feedback in Population III star formation. *MNRAS*, 442:2667–2679, Aug. 2014.

D. Nakauchi, K. Omukai, and H. Susa. Ionization degree and magnetic diffusivity in the primordial star-forming clouds. *MNRAS*, 488:1846–1862, Sept. 2019.

K. Nomoto, N. Tominaga, H. Umeda, C. Kobayashi, and K. Maeda. Nucleosynthesis yields of core-collapse supernovae and hypernovae, and galactic chemical evolution. *Nucl. Phys. A*, 777: 424–458, Oct. 2006.

S. P. Oh. Reionization by Hard Photons. I. X-Rays from the First Star Clusters. *ApJ*, 553: 499–512, June 2001.

S. P. Oh, Z. Haiman, and M. J. Rees. HE II Recombination Lines from the First Luminous Objects. *ApJ*, 553:73–77, May 2001.

K. Omukai. Primordial Star Formation under Far-Ultraviolet Radiation. *ApJ*, 546:635–651, Jan. 2001.

K. Omukai and R. Nishi. Formation of Primordial Protostars. *ApJ*, 508:141–150, Nov. 1998.

K. Omukai, T. Tsuribe, R. Schneider, and A. Ferrara. Thermal and Fragmentation Properties of Star-forming Clouds in Low-Metallicity Environments. *ApJ*, 626:627–643, June 2005.

B. W. O'Shea and M. L. Norman. Population III Star Formation in a λ CDM Universe. II. Effects of a Photodissociating Background. *ApJ*, 673:14–33, Jan. 2008.

F. Palla, E. E. Salpeter, and S. W. Stahler. Primordial star formation - The role of molecular hydrogen. *ApJ*, 271:632–641, Aug. 1983.

J. Park, R. Smith, and S. K. Yi. Star Formation of Merging Disk Galaxies with AGN Feedback Effects. *ApJ*, 845:128, Aug. 2017.

J. Park, M. Ricotti, and K. Sugimura. Population III star formation in an X-ray background - I. Critical halo mass of formation and total mass in stars. *MNRAS*, 508:6176–6192, Dec. 2021a.

J. Park, M. Ricotti, and K. Sugimura. Population III star formation in an X-ray background - II. Protostellar discs, multiplicity, and mass function of the stars. *MNRAS*, 508:6193–6208, Dec. 2021b.

J. Park, M. Ricotti, and K. Sugimura. Population III star formation in an X-ray background: III. Periodic radiative feedback and luminosity induced by elliptical orbits. *MNRAS*, 521:5334–5353, June 2023.

J. Park, M. Ricotti, and K. Sugimura. On the origin of outward migration of Population III stars. *MNRAS*, 528:6895–6914, Mar. 2024.

K. Park and M. Ricotti. Accretion onto Intermediate-mass Black Holes Regulated by Radiative Feedback. I. Parametric Study for Spherically Symmetric Accretion. *ApJ*, 739:2, Sept. 2011.

M. V. Penston. Dynamics of self-gravitating gaseous spheres-III. Analytical results in the free-fall of isothermal cases. *MNRAS*, 144:425, Jan. 1969.

Planck Collaboration, N. Aghanim, Y. Akrami, M. Ashdown, J. Aumont, C. Baccigalupi, M. Ballardini, A. J. Banday, R. B. Barreiro, N. Bartolo, S. Basak, R. Battye, K. Benabed, J. P. Bernard, M. Bersanelli, P. Bielewicz, J. J. Bock, J. R. Bond, J. Borrill, F. R. Bouchet, F. Boulanger, M. Bucher, C. Burigana, R. C. Butler, E. Calabrese, J. F. Cardoso, J. Carron, A. Challinor, H. C. Chiang, J. Chluba, L. P. L. Colombo, C. Combet, D. Contreras, B. P. Crill, F. Cuttaia, P. de Bernardis, G. de Zotti, J. Delabrouille, J. M. Delouis, E. Di Valentino, J. M. Diego, O. Doré, M. Douspis, A. Ducout, X. Dupac, S. Dusini, G. Efstathiou, F. Elsner, T. A. Enßlin, H. K. Eriksen, Y. Fantaye, M. Farhang, J. Fergusson, R. Fernandez-Cobos, F. Finelli, F. Forastieri, M. Frailis, A. A. Fraisse, E. Franceschi, A. Frolov, S. Galeotta, S. Galli, K. Ganga, R. T. Génova-Santos, M. Gerbino, T. Ghosh, J. González-Nuevo, K. M. Górski, S. Gratton, A. Gruppuso, J. E. Gudmundsson, J. Hamann, W. Handley, F. K. Hansen, D. Herranz, S. R. Hildebrandt, E. Hivon, Z. Huang, A. H. Jaffe, W. C. Jones, A. Karakci, E. Keihänen, R. Keskitalo, K. Kiiveri, J. Kim, T. S. Kisner, L. Knox, N. Krachmalnicoff, M. Kunz, H. Kurki-Suonio, G. Lagache, J. M. Lamarre, A. Lasenby, M. Lattanzi, C. R. Lawrence, M. Le Jeune, P. Lemos, J. Lesgourgues, F. Levrier, A. Lewis, M. Liguori, P. B. Lilje, M. Lilley, V. Lindholm, M. López-Caniego, P. M. Lubin, Y. Z. Ma, J. F. Macías-Pérez, G. Maggio, D. Maino, N. Mandolesi, A. Mangilli, A. Marcos-Caballero, M. Maris, P. G. Martin, M. Martinelli, E. Martínez-González, S. Matarrese, N. Mauri, J. D. McEwen, P. R. Meinhold, A. Melchiorri, A. Mennella, M. Migliaccio, M. Millea, S. Mitra, M. A. Miville-Deschênes, D. Molinari, L. Montier, G. Morgante, A. Moss, P. Natoli, H. U. Nørgaard-Nielsen, L. Pagano, D. Paoletti, B. Partridge, G. Patanchon, H. V. Peiris, F. Perrotta, V. Pettorino, F. Piacentini, L. Polastri, G. Polenta, J. L. Puget, J. P. Rachen, M. Reinecke, M. Remazeilles, A. Renzi, G. Rocha, C. Rosset, G. Roudier, J. A. Rubiño-Martín, B. Ruiz-Granados, L. Salvati, M. Sandri, M. Savelainen, D. Scott, E. P. S. Shellard, C. Sirignano, G. Sirri, L. D. Spencer, R. Sunyaev, A. S. Suur-Uski, J. A. Tauber, D. Tavagnacco, M. Tenti, L. Toffolatti, M. Tomasi, T. Trombetti, L. Valenziano, J. Valiviita, B. Van Tent, L. Vibert, P. Vielva, F. Villa, N. Vittorio, B. D. Wandelt, I. K. Wehus, M. White, S. D. M. White, A. Zacchei, and A. Zonca. Planck 2018 results. VI. Cosmological parameters. *A&A*, 641:A6, Sept. 2020.

W. H. Press and P. Schechter. Formation of Galaxies and Clusters of Galaxies by Self-Similar Gravitational Condensation. *ApJ*, 187:425–438, Feb. 1974.

L. R. Prole, P. C. Clark, R. S. Klessen, and S. C. O. Glover. Fragmentation-induced starvation in Population III star formation: a resolution study. *MNRAS*, 510:4019–4030, Mar. 2022.

J. A. Regan and M. G. Haehnelt. Pathways to massive black holes and compact star clusters in pre-galactic dark matter haloes with virial temperatures $>\tilde{}$10000K. *MNRAS*, 396:343–353, June 2009.

J. A. Regan, J. H. Wise, B. W. O'Shea, and M. L. Norman. The emergence of the first star-free atomic cooling haloes in the Universe. *MNRAS*, 492:3021–3031, Feb. 2020.

A. J. Richings, J. Schaye, and B. D. Oppenheimer. Non-equilibrium chemistry and cooling in the diffuse interstellar medium - II. Shielded gas. *MNRAS*, 442:2780–2796, Aug. 2014.

M. Ricotti. Late gas accretion on to primordial minihaloes: a model for Leo T, dark galaxies and extragalactic high-velocity clouds. *MNRAS*, 392:L45–L49, Jan. 2009.

M. Ricotti. X-ray twinkles and Population III stars. *MNRAS*, 462:601–609, Oct. 2016.

M. Ricotti and J. P. Ostriker. X-ray pre-ionization powered by accretion on the first black holes - I. A model for the WMAP polarization measurement. *MNRAS*, 352:547–562, Aug. 2004.

M. Ricotti, N. Y. Gnedin, and J. M. Shull. Feedback from Galaxy Formation: Production and Photodissociation of Primordial H2. *ApJ*, 560:580–591, Oct. 2001.

M. Ricotti, N. Y. Gnedin, and J. M. Shull. The Fate of the First Galaxies. I. Self-consistent Cosmological Simulations with Radiative Transfer. *ApJ*, 575:33–48, Aug. 2002a.

M. Ricotti, N. Y. Gnedin, and J. M. Shull. The Fate of the First Galaxies. II. Effects of Radiative Feedback. *ApJ*, 575:49–67, Aug. 2002b.

M. Ricotti, J. P. Ostriker, and N. Y. Gnedin. X-ray pre-ionization powered by accretion on the first black holes - II. Cosmological simulations and observational signatures. *MNRAS*, 357: 207–219, Feb. 2005.

M. Ricotti, N. Y. Gnedin, and J. M. Shull. The Fate of the First Galaxies. III. Properties of Primordial Dwarf Galaxies and Their Impact on the Intergalactic Medium. *ApJ*, 685:21–39, Sept. 2008.

M. Ricotti, O. H. Parry, and N. Y. Gnedin. A Common Origin for Globular Clusters and Ultra-faint Dwarfs in Simulations of the First Galaxies. *ApJ*, 831:204, Nov. 2016.

J. Rosdahl, J. Blaizot, D. Aubert, T. Stranex, and R. Teyssier. RAMSES-RT: radiation hydrodynamics in the cosmological context. *MNRAS*, 436:2188–2231, Dec. 2013.

G. B. Rybicki and A. P. Lightman. *Radiative Processes in Astrophysics*. John Wiley & Sons, Ltd, June 1986.

C. Safranek-Shrader, M. Milosavljević, and V. Bromm. Star formation in the first galaxies - II. Clustered star formation and the influence of metal line cooling. *MNRAS*, 438:1669–1685, Feb. 2014.

E. E. Salpeter. The Luminosity Function and Stellar Evolution. *ApJ*, 121:161, Jan. 1955.

D. Schaerer. On the properties of massive Population III stars and metal-free stellar populations. *A&A*, 382:28–42, July 2002.

C. Shang, G. L. Bryan, and Z. Haiman. Supermassive black hole formation by direct collapse: keeping protogalactic gas H_2 free in dark matter haloes with virial temperatures $T_{\rm vir} \gtrsim 10^4$ K. *MNRAS*, 402:1249–1262, Feb. 2010.

R. K. Sheth and G. Tormen. Large-scale bias and the peak background split. *MNRAS*, 308: 119–126, Sept. 1999.

J. M. Shull. Heating and ionization by X-ray photoelectrons. *ApJ*, 234:761–764, Dec. 1979.

J. M. Shull and M. E. van Steenberg. X-ray secondary heating and ionization in quasar emission-line clouds. *ApJ*, 298:268–274, Nov. 1985.

B. Smith, S. Sigurdsson, and T. Abel. Metal cooling in simulations of cosmic structure formation. *MNRAS*, 385:1443–1454, Apr. 2008.

R. J. Smith, S. C. O. Glover, P. C. Clark, T. Greif, and R. S. Klessen. The effects of accretion luminosity upon fragmentation in the early universe. *MNRAS*, 414:3633–3644, July 2011.

V. Springel. The cosmological simulation code GADGET-2. *MNRAS*, 364:1105–1134, Dec. 2005.

A. Stacy and V. Bromm. Constraining the statistics of Population III binaries. *MNRAS*, 433: 1094–1107, Aug. 2013.

A. Stacy and V. Bromm. The First Stars: A Low-mass Formation Mode. *ApJ*, 785:73, Apr. 2014.

A. Stacy, T. H. Greif, and V. Bromm. The first stars: formation of binaries and small multiple systems. *MNRAS*, 403:45–60, Mar. 2010.

A. Stacy, T. H. Greif, and V. Bromm. The first stars: mass growth under protostellar feedback. *MNRAS*, 422:290–309, May 2012.

A. Stacy, V. Bromm, and A. T. Lee. Building up the Population III initial mass function from cosmological initial conditions. *MNRAS*, 462:1307–1328, Oct. 2016.

K. Sugimura and M. Ricotti. Structure and instability of the ionization fronts around moving black holes. *MNRAS*, 495, July 2020.

K. Sugimura, K. Omukai, and A. K. Inoue. The critical radiation intensity for direct collapse black hole formation: dependence on the radiation spectral shape. *MNRAS*, 445:544–553, Nov. 2014.

K. Sugimura, T. Matsumoto, T. Hosokawa, S. Hirano, and K. Omukai. The Birth of a Massive First-star Binary. *ApJ*, 892:L14, Mar. 2020.

K. Sugimura, T. Matsumoto, T. Hosokawa, S. Hirano, and K. Omukai. Formation of Massive and Wide First-star Binaries in Radiation Hydrodynamic Simulations. *ApJ*, 959:17, Dec. 2023.

H. Susa. The Mass of the First Stars. *ApJ*, 773:185, Aug. 2013.

H. Susa. Merge or Survive: Number of Population III Stars per Minihalo. *ApJ*, 877:99, June 2019.

H. Susa, K. Hasegawa, and N. Tominaga. The Mass Spectrum of the First Stars. *ApJ*, 792:32, Sept. 2014.

Y. Tang, A. MacFadyen, and Z. Haiman. On the orbital evolution of supermassive black hole binaries with circumbinary accretion discs. *MNRAS*, 469:4258–4267, Aug. 2017.

M. Tegmark, J. Silk, M. J. Rees, A. Blanchard, T. Abel, and F. Palla. How Small Were the First Cosmological Objects? *ApJ*, 474:1, Jan. 1997.

R. Teyssier. Cosmological hydrodynamics with adaptive mesh refinement. A new high resolution code called RAMSES. *A&A*, 385:337–364, Apr. 2002.

C. Tiede and D. J. D'Orazio. Eccentric binaries in retrograde discs. *MNRAS*, 527:6021–6037, Jan. 2024.

C. Tiede, J. Zrake, A. MacFadyen, and Z. Haiman. Gas-driven Inspiral of Binaries in Thin Accretion Disks. *ApJ*, 900:43, Sept. 2020.

A. Toomre. On the gravitational stability of a disk of stars. *ApJ*, 139:1217–1238, May 1964.

A. Toomre and J. Toomre. Galactic Bridges and Tails. *ApJ*, 178:623–666, Dec. 1972.

J. K. Truelove, R. I. Klein, C. F. McKee, J. H. Holliman, II, L. H. Howell, and J. A. Greenough. The Jeans Condition: A New Constraint on Spatial Resolution in Simulations of Isothermal Self-gravitational Hydrodynamics. *ApJ*, 489:L179–L183, Nov. 1997.

M. J. Turk, T. Abel, and B. O'Shea. The Formation of Population III Binaries from Cosmological Initial Conditions. *Science*, 325:601, July 2009.

E. Vanzella, F. Loiacono, P. Bergamini, U. Meštrić, M. Castellano, P. Rosati, M. Meneghetti, C. Grillo, F. Calura, M. Mignoli, M. Bradač, A. Adamo, G. Rihtaršič, M. Dickinson, M. Gronke, A. Zanella, F. Annibali, C. Willott, M. Messa, E. Sani, A. Acebron, A. Bolamperti, A. Comastri, R. Gilli, K. I. Caputi, M. Ricotti, C. Gruppioni, S. Ravindranath, A. Mercurio, V. Strait, N. Martis, R. Pascale, G. B. Caminha, M. Annunziatella, and M. Nonino. An extremely metal-poor star complex in the reionization era: Approaching Population III stars with JWST. *Astronomy and Astrophysics*, 678:A173, Oct. 2023.

A. Venkatesan, M. L. Giroux, and J. M. Shull. Heating and Ionization of the Intergalactic Medium by an Early X-Ray Background. *ApJ*, 563:1–8, Dec. 2001.

D. A. Verner, G. J. Ferland, K. T. Korista, and D. G. Yakovlev. Atomic Data for Astrophysics. II. New Analytic FITS for Photoionization Cross Sections of Atoms and Ions. *ApJ*, 465:487, July 1996.

B. Welch, D. Coe, J. M. Diego, A. Zitrin, E. Zackrisson, P. Dimauro, Y. Jiménez-Teja, P. Kelly, G. Mahler, M. Oguri, F. X. Timmes, R. Windhorst, M. Florian, S. E. de Mink, R. J. Avila, J. Anderson, L. Bradley, K. Sharon, A. Vikaeus, S. McCandliss, M. Bradač, J. Rigby, B. Frye, S. Toft, V. Strait, M. Trenti, S. Sharma, F. Andrade-Santos, and T. Broadhurst. A highly magnified star at redshift 6.2. *Nature*, 603:815–818, Mar. 2022a.

B. Welch, D. Coe, E. Zackrisson, S. E. de Mink, S. Ravindranath, J. Anderson, G. Brammer, L. Bradley, J. Yoon, P. Kelly, J. M. Diego, R. Windhorst, A. Zitrin, P. Dimauro, Y. Jiménez-Teja, Abdurro'uf, M. Nonino, A. Acebron, F. Andrade-Santos, R. J. Avila, M. B. Bayliss, A. Benítez, T. Broadhurst, R. Bhatawdekar, M. Bradač, G. B. Caminha, W. Chen, J. Eldridge, E. Farag, M. Florian, B. Frye, S. Fujimoto, S. Gomez, A. Henry, T. Y. Y. Hsiao, T. A. Hutchison, B. L.

James, M. Joyce, I. Jung, G. Khullar, R. L. Larson, G. Mahler, N. Mandelker, S. McCandliss, T. Morishita, R. Newshore, C. Norman, K. O'Connor, P. A. Oesch, M. Oguri, M. Ouchi, M. Postman, J. R. Rigby, R. E. Ryan, Jr., S. Sharma, K. Sharon, V. Strait, L.-G. Strolger, F. X. Timmes, S. Toft, M. Trenti, E. Vanzella, and A. Vikaeus. JWST Imaging of Earendel, the Extremely Magnified Star at Redshift z = 6.2. *ApJ*, 940:L1, Nov. 2022b.

D. Whalen, B. W. O'Shea, J. Smidt, and M. L. Norman. How the First Stars Regulated Local Star Formation. I. Radiative Feedback. *ApJ*, 679:925–941, June 2008.

D. J. Whalen, J. Smidt, W. Even, S. E. Woosley, A. Heger, M. Stiavelli, and C. L. Fryer. Finding the First Cosmic Explosions. III. Pulsational Pair-instability Supernovae. *ApJ*, 781:106, Feb. 2014.

J. H. Wise and T. Abel. Resolving the Formation of Protogalaxies. III. Feedback from the First Stars. *ApJ*, 685:40–56, Sept. 2008.

J. H. Wise, M. J. Turk, M. L. Norman, and T. Abel. The Birth of a Galaxy: Primordial Metal Enrichment and Stellar Populations. *ApJ*, 745:50, Jan. 2012.

J. Wolcott-Green and Z. Haiman. Suppression of HD cooling in protogalactic gas clouds by Lyman-Werner radiation. *MNRAS*, 412:2603–2616, Apr. 2011.

J. Wolcott-Green and Z. Haiman. H2 self-shielding with non-LTE rovibrational populations: implications for cooling in protogalaxies. *MNRAS*, 484:2467–2473, Apr. 2019.

J. Wolcott-Green, Z. Haiman, and G. L. Bryan. Photodissociation of H2 in protogalaxies: modelling self-shielding in three-dimensional simulations. *MNRAS*, 418:838–852, Dec. 2011.

K. M. J. Wollenberg, S. C. O. Glover, P. C. Clark, and R. S. Klessen. Formation sites of Population III star formation: The effects of different levels of rotation and turbulence on the fragmentation behaviour of primordial gas. *MNRAS*, 494:1871–1893, May 2020.

H. Xu, J. H. Wise, and M. L. Norman. Population III Stars and Remnants in High-redshift Galaxies. *ApJ*, 773:83, Aug. 2013. ADS Bibcode: 2013ApJ...773...83X.

H. Xu, K. Ahn, J. H. Wise, M. L. Norman, and B. W. O'Shea. Heating the Intergalactic Medium by X-Rays from Population III Binaries in High-redshift Galaxies. *ApJ*, 791:110, Aug. 2014.

H. Xu, K. Ahn, M. L. Norman, J. H. Wise, and B. W. O'Shea. X-Ray Background at High Redshifts from Pop III Remnants: Results from Pop III Star Formation Rates in the Renaissance Simulations. *ApJ*, 832:L5, Nov. 2016.

N. Yoshida, S. P. Oh, T. Kitayama, and L. Hernquist. Early Cosmological H II/He III Regions and Their Impact on Second-Generation Star Formation. *ApJ*, 663:687–707, July 2007.

N. Yoshida, K. Omukai, and L. Hernquist. Protostar Formation in the Early Universe. *Science*, 321:669, Aug. 2008.

J. Zrake, C. Tiede, A. MacFadyen, and Z. Haiman. Equilibrium Eccentricity of Accreting Binaries. *ApJ*, 909:L13, Mar. 2021.